Stefan Purkhart, BSc

Statistics of Nanoflares and their Contribution to Coronal Heating using SDO/AIA Differential Emission Measure Analysis

MASTER'S THESIS

to achieve the university degree of

Master of Science

Master's degree programme: Physics

submitted to

Graz University of Technology

Supervisor

Univ.-Prof. Dr. Astrid Veronig
Institute of Physics
University of Graz

Graz, July 2021

AFFIDAVIT

I declare that I have authored this thesis independently, that I have not used other than the declared sources/resources, and that I have explicitly indicated all material which has been quoted either literally or by content from the sources used. The text document uploaded to TUGRAZonline is identical to the present master's thesis.

Date, Signature

Abstract

We study the energy distributions of nanoflares in quiet Sun regions, using Differential Emission Measure (DEM) analysis of observations from the 6 EUV filters of the Atmospheric Imaging Assembly (AIA) onboard the Solar Dynamics Observatory (SDO). In total, we analyzed 30 sets of AIA/SDO image series distributed evenly between the years 2011 and 2018 to characterize the nanoflare frequency distribution and their contribution to coronal heating throughout different levels of solar activity during solar cycle 24. Each series covers a $400'' \times 400''$ field-of-view close to disc center over an observation time of two hours at the full AIA cadence of 12 seconds. DEM analysis was used to derive the emission measure and temperature evolution for each pixel. The nanoflare frequency distribution as a function of thermal nanoflare energy was then extracted from the DEM results for each data set by a threshold-based algorithm developed for the AIA data characteristics. We find that the combined nanoflare frequencies follow a power-law distribution with a power-law index $\alpha = 2.26$ that covers five orders of magnitude in event energies (10^{23} to $10^{28}\,\mathrm{erg}$). The power-law index obtained from individual data sets shows only minimal variation over the multi-year period and no significant correlation to solar activity. The steep slope ($\alpha > 2$) suggests that the dominant energy contribution resides in the small flare events (nanoflares). However, we find that the combined global energy flux ($3.2 \times 10^3\,\mathrm{erg\,cm^{-2}\,s^{-1}}$) from all detected events is about two orders of magnitude too small to account for the heating requirement of the solar corona ($3 \times 10^5\,\mathrm{erg\,cm^{-2}\,s^{-1}}$). The observed global energy flux from individual data sets also shows no correlation to the solar cycle. Additionally, we investigate the spatial distribution of energy flux and event counts per pixel and find clusters of high activity and high flux (up to $3 \times 10^4\,\mathrm{erg\,cm^{-2}\,s^{-1}}$) surrounded by extended regions of lower activity where the observed flux drops by up to two orders of magnitude. Comparisons with magnetograms from the Helioseismic and Magnetic Imager (HMI) reveal that the high-activity clusters are located mainly in the magnetic network, preferentially in mixed flux regions of opposite polarities.

Kurzfassung

Diese Arbeit untersucht die Energieverteilungen von Nanoflares in ruhigen Sonnenregionen anhand der Differential Emission Measure (DEM) Analyse von Aufnahmen der 6 EUV-Filter des Atmospheric Imaging Assembly (AIA) an Bord des Solar Dynamics Observatory (SDO). Insgesamt werden 30 Datensätze von AIA/SDO-Bildserien analysiert, die gleichmäßig zwischen den Jahren 2011 und 2018 verteilt sind, um die Häufigkeitsverteilung von Nanoflares und ihren Beitrag zur koronalen Heizung während verschiedener Sonnenaktivitätsstufen des Sonnenzyklus 24 zu charakterisieren. Jede Bildserie deckt ein $400'' \times 400''$-Sichtfeld nahe dem Zentrum der Sonnenscheibe über eine Beobachtungszeit von zwei Stunden bei der vollen AIA-Kadenz von 12 Sekunden ab. Die DEM-Analyse wurde verwendet, um die Entwicklung des Emissionsmaßes und der Temperatur für jedes Pixel abzuleiten. Die Häufigkeitsverteilung der Nanoflares als Funktion ihrer thermischen Energie wurde aus den DEM-Ergebnissen für jeden Datensatz durch einen schwellenwertbasierten Algorithmus extrahiert, der speziell für die Eigenschaften der AIA-Daten entwickelt wurde. Die kombinierten Nanoflarefrequenzen aller Datensätze folgen einem Potenzgesetz mit einem Exponenten von $\alpha = 2.26$. Dieses erstreckt sich über fünf Größenordnungen an Eventenergien (10^{23} to $10^{28}\,\mathrm{erg}$). Der aus den individuellen Datensätzen gewonnene Exponent zeigt nur minimale Schwankungen über den beobachteten Zeitraum und keine signifikante Korrelation zur Sonnenaktivität. Der steile Anstieg ($\alpha > 2$) der Verteilungen deutet darauf hin, dass der dominante Energiebeitrag von den kleinen Flares (Nanoflares) kommt. Allerdings ist der gesamte Energiefluss ($3.2 \times 10^3\,\mathrm{erg\,cm^{-2}\,s^{-1}}$) aus allen detektierten Ereignissen etwa zwei Größenordnungen zu klein, um den Energiebedarf der Sonnenkorona ($3 \times 10^5\,\mathrm{erg\,cm^{-2}\,s^{-1}}$) zu decken. Der beobachtete Energiefluss aus einzelnen Datensätzen zeigt ebenfalls keine Korrelation zum Sonnenzyklus. Die Untersuchung der räumlichen Verteilung des Energieflusses und der Ereignisanzahl pro Pixel ergab Cluster mit hoher Aktivität und hohem Energiefluss (bis zu $3 \times 10^4\,\mathrm{erg\,cm^{-2}\,s^{-1}}$), umgeben von ausgedehnten Regionen mit geringerer Aktivität, in denen der beobachtete Energiefluss um bis zu zwei Größenordnungen abfällt. Vergleiche mit Magnetogrammen des Helioseismic and Magnetic Imager (HMI) zeigen, dass sich die Aktivitätscluster hauptsächlich im magnetischen Netzwerk befinden und bevorzugt in Regionen mit magnetischer Flussdichte entgegengesetzter Polarität auftreten.

Acknowledgement

I would like to express my deepest gratitude to Univ. -Prof. Dr. Astrid Veronig, my thesis supervisor, for her patient guidance, helpful advice, and valuable critiques. Her insights and expertise were invaluable during the writing of this thesis.
Further, I would like to thank Jonas Saqri, MSc, for his helpful comments and suggestions, especially regarding the differential emission measure analysis.
This thesis used the infrastructure and resources of the Department for Geophysics, Astrophysics and Meteorology (IGAM) at the Institute of Physics of the University of Graz. I thank Roland Maderbacher and Klaus Huber for maintaining the IT infrastructure, software installations, the server farm, and providing technical support whenever I needed it.
Special thanks to my parents and friends for their continuous encouragement and support at every stage of my studies and to Caro for her unparalleled patience and warmth during the writing of this thesis.

Contents

1 Introduction

The corona is our Sun's outermost atmospheric layer and is characterized by a plasma temperature of about 1 to $2\,\mathrm{MK}$. This is much hotter than the solar surface, which has an effective temperature of about $5700\,\mathrm{K}$. Multiple theories aim to explain this unexpected temperature rise through different energy sources and heating mechanisms, all with various degrees of success. To date, we still do not possess a comprehensive understanding of all involved processes and their connections. This long-standing absence of a full explanation has motivated the term *coronal heating problem*, capturing one of the most challenging mysteries in solar physics.

One promising idea involves the build-up of free magnetic energy due to the footpoint motions of flux tubes and the subsequent release through magnetic reconnection. The resulting plasma heating is visible as small-scale brightenings, called nanoflares, in extreme ultraviolet (EUV) solar images. One of the essential factors used to verify the robustness of this theory involves the power-law distribution of nanoflare energies and their occurrence frequency. The steepness of the distribution, spanning multiple orders of magnitude, determines the relative contribution of small and large flares to the total power input. However, the exact determination of this power-law and other nanoflare properties has proven to be a difficult task. The involved high uncertainties are the results of many assumptions made in event detection and energy calculation, as well as insufficient resolution and low cadence of the used image series.

For the nanoflare study presented in this thesis, we used high spatial and temporal resolution EUV images taken in six wavelength channels by the Atmospheric Imaging Assembly (AIA) onboard the Solar Dynamics Observatory (SDO). We applied Differential Emission Measure (DEM) analysis, utilizing the inversion code by Hannah and Kontar (2012), to obtain detailed emission measure and temperature evolution for all pixels in a selected field of view. To extract information about the energy and frequency of nanoflares from the DEM results, we modified a simple threshold-based event definition, based on the algorithm in Krucker and Benz (1998), to account for AIA data characteristics. The resulting method allows tuning of three crucial parameters that alter the event detection and combination behavior.

This thesis is structured as follows. Chapter 2 provides a short general introduction of the Sun, its structure, and variability. The coronal heating problem is discussed in further detail in chapter 3, where we give a short historical overview, followed by an evaluation of the required energy and an overview of the two main heating theory categories. Chapter 4 introduces the AIA instrument, its capabilities, and data processing routines. Further, the chapter gives an overview of all data sets used in the method development and final analysis. The method development itself is presented in detail in chapter 5. It includes an introduction to DEM analysis and an investigation of different parameters that alter the DEM results. Subsequently, crucial components of the nanoflare detection method are laid out, including the energy calculation, event detection and threshold, event combination, and finally, the frequency analysis with the power-law fit. We analyzed the extracted power-law and many other nanoflare properties from differently tuned methods and across 30 data sets spaced evenly throughout 2011 to 2018, covering a large portion of solar cycle 24. The obtained results are presented in chapter 6 and cover the nanoflare frequency distributions, the energy flux, and statistics of active pixels, event frequency, and area. The results and their implications are summarized and discussed in chapter 7, and we give a conclusion in chapter 8.

2 The Sun

The Sun, a typical G-type star at about the halfway point of its main-sequence lifetime, is the single most influential body in our solar system. It formed 4.6 billion years ago out of an element-rich cosmic cloud that was probably disturbed by some outside event and started collapsing under its own gravity (Foukal, 2004). $99.8\,\%$ of the total mass of the solar system is now concentrated in the Sun. The four giant planets Jupiter, Saturn, Uranus, and Neptune further account for $>99\,\%$ of the remaining mass. The tiny fraction remaining are the four terrestrial planets including earth, the dwarf planets, moons, asteroids, and comets. The Sun's immense mass and resulting gravity, compared to everything else in its vicinity, binds the whole solar system together and defines most of its dynamics (Hanslmeier, 2020).

Maybe even more vital for us, the enormous gravity of such a concentrated mass provides the conditions necessary to fuse Hydrogen into Helium, releasing enormous amounts of energy in the process. This mechanism turns the Sun also into the dominant energy source for the rest of the solar system, fueling many subsequent phenomena. On earth, this energy drives critical processes like our weather and climate and provides the foundation for the existence of complex life. We are highly dependent on this massive sphere of plasma, and what happens on the Sun can have direct consequences for our life on earth, especially as humanity becomes increasingly more dependent on technology and develops a renewed interest in space exploration. It is therefore wise to study the Sun in great detail and further our understanding of its structure and dynamics as well as its influence on the rest of the solar system (Hanslmeier, 2020).

The work presented in this thesis is nested in one of the many mysteries remaining in solar physics. Specifically, the high temperature of the solar corona and the search for mechanisms providing the necessary energy. Before discussing this surprisingly hard to solve conundrum commonly summarized by the keyword *Coronal Heating Problem*, this chapter aims to provide a compact overview of the necessary theory. We cover the energy production through nuclear fusion, the resulting interior and atmospheric structure, the fundamental theories governing the interaction of the Sun's plasma and magnetic field, as well as dynamic phenomena that arise from the cyclic behavior of this magnetic field.

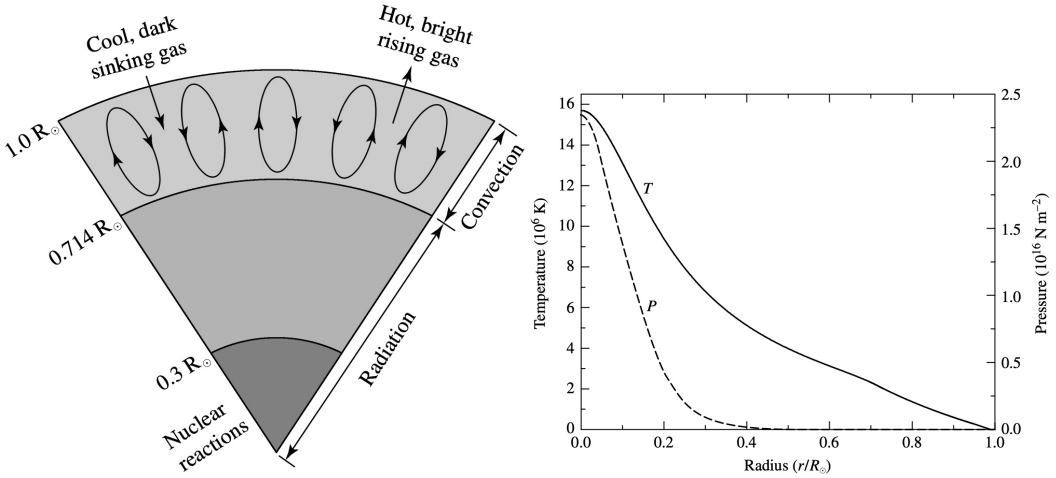

Fig. 2.1.: Illustration of the solar interior (left) divided into three distinct regions (core, radiation zone and convection zone) and the temperature and pressure profiles along the solar radius from the core to the surface (right). Distance from the center is given as a fraction of the Sun's radius ($R_\odot$). From Carroll and Ostlie (2006).

2.1 The Solar Structure

The Sun is commonly divided into an interior region and an atmosphere based on the region's optical depth. In this model, the atmosphere is loosely defined as the optically thin (optical thickness less than unity) outer region of the Sun where approximations concerning photon diffusion are no longer valid, and line emission and absorption have to be taken into account. It is also the region of the Sun that light can escape from, making it directly observable to us. On the other hand, the interior is the optically thick sphere beneath, where those approximations are justified. Light emitted in these optically thick layers can not freely escape from the Sun. The transition from optically thick to thin happens in a layer with a width of only about $600\,\mathrm{km}$. This small extension relative to the solar radius gives the Sun its seemingly sharp edge in the visible (Carroll and Ostlie, 2006).

2.1.1 The Solar Interior

The core is the innermost solar region and extends from the Sun's center to about $30\,\%$ of its radius. Here the temperature ($\approx$15 MK), pressure ($\approx 2.3 \times 10^{16}\,\mathrm{N\,m^{-2}}$) and density ($\approx 1.5 \times 10^{5}\,\mathrm{kg\,m^{-3}}$) are highest throughout the solar interior and can sustain energy production through nuclear fusion. The consequent outward flow of this released energy defines the rest of the solar structure and is also the fundamental driver behind all dynamic phenomena. Figure 2.1 shows an illustration of the solar interior divided into the core and the subsequent convection and radiation zones,

named after their dominant energy transport method. It also shows the decreasing temperature and pressure profiles along the solar radius, from the center to the surface. The energy produced through fusion in the core flows outward according to this decreasing temperature gradient (Carroll and Ostlie, 2006).

In the Sun, the proton-proton (p-p) chain is the dominant nuclear fusion process. It starts by fusing two protons (p) into deuterium ($^2\mathrm{H}$) while releasing a positron (e^+) and an electron neutrino (ν_e) (Foukal, 2004).

$$\mathrm{p} + \mathrm{p} \rightarrow {}^2\mathrm{H} + \mathrm{e}^+ + \nu_\mathrm{e} + 1.442\,\mathrm{MeV} \tag{2.1}$$

This first step is the limiting factor of the whole reaction. It requires a collision of two protons with sufficient energy to overcome the coulomb barrier and the simultaneous beta decay of one of the involved protons into a neutron, since the $^2\mathrm{He}$ nucleus, consisting of two protons, is highly unstable (Foukal, 2004). Classical calculations show that the mean kinetic energy of protons in the core is about 500 times lower than the required energy to overcome this barrier. However, the quantum mechanical tunnel effect lowers this requirement and makes the process reasonably likely under conditions found in the solar core. Even with this correction, the average lifetime of protons before they fuse into deuterium only approaches 10^{10} years in the center of the core. This estimate moves to even longer time scales further away from the center, where temperature and density are lower. Despite this low probability, about 6×10^4 reactions per cubic centimeter occur every second due to the core's very high density (Severino, 2017).

The deuterium produced through the first part of the total reaction will subsequently fuse with another proton to form the helium isotope $^3_2\mathrm{He}$. This step happens much faster within about $10\,\mathrm{s}$ and emits a γ-ray in the process (Foukal, 2004).

$${}^2\mathrm{H} + \mathrm{p} \rightarrow {}^3\mathrm{He} + \gamma + 5.494\,\mathrm{MeV} \tag{2.2}$$

Lastly, there are four different paths to produce the final fusion product $^4_2\mathrm{He}$. In the Sun, most is produced through the following p-p I branch, where two $^3_2\mathrm{He}$ nuclei combine to form $^4_2\mathrm{He}$ and two protons (Foukal, 2004).

$${}^3_2\mathrm{He} + {}^3_2\mathrm{He} \rightarrow {}^4_2\mathrm{He} + 2\mathrm{p} + 12.86\,\mathrm{MeV} \tag{2.3}$$

In Summary, four protons and two electrons fuse into one $^4_2\mathrm{He}$ nucleus and release a total energy of $26.732\,\mathrm{MeV}$ through the created particles and γ-rays. This energy is equivalent to a helium core's mass defect relative to the sum of the original protons and electrons. $2\,\%$ of the energy released in the p-p chain gets carried off by neutrinos, which are very unlikely to interact again with solar particles and will therefore not contribute to the heating of the Sun (Foukal, 2004).

Only about $1\,\%$ of the total energy produced in the Sun's core comes from another fusion process called the CNO cycle. It uses carbon (C), nitrogen (N), and oxygen (O) as catalysts and needs higher temperatures to become more efficient and produce significant energy (Foukal, 2004).

At first, the energy produced in the core gets transported outwards by radiation to about $70\,\%$ of the solar radius, and this region is therefore called the radiation zone (Severino, 2017). Because of the high density, the γ-rays produced by nuclear fusion can not travel far in the Sun's core before interacting with the surrounding plasma. A vital interaction process is the inelastic Compton scattering of these high-energy photons on free electrons. With each scattering process, the energy of the photon gets reduced, and its propagation direction changes. Combined with the short mean free path between interactions, this leads to a very slow random-walk-like outward transport of the energy (Murdin, 2001). The temperature drops from $7\,\mathrm{MK}$ to about $2\,\mathrm{MK}$ in the radiation zone (Carroll and Ostlie, 2006).

The tachocline is a transition layer between the radiation zone and the convection zone where the Sun stops rotating as one solid sphere. Instead, different latitudes and layers start to rotate at different speeds (see Figure 2.2). This phenomenon, referred to as solar differential rotation, is likely an essential ingredient of the Sun's magnetic field and its dynamics (Hanslmeier, 2020; Hathaway, 2015).

In the convection zone, the radiative temperature gradient becomes steeper than the adiabatic temperature gradient, resulting in instability in the subsequent layers. This instability results in a switch of the dominant heat transfer from radiation to convective motions of the plasma (Carroll and Ostlie, 2006). The material in the low layers of the convection zone gets heated and consequently expands. Because of the resulting low density compared to its surroundings, the heated material will rise up to near the surface, where it releases the stored energy and cools again. The cooled and contracted cell will sink again and repeat the process (Hanslmeier, 2020). This convective energy transport results in a temperature profile from $2\,\mathrm{MK}$ at the lowest extent of the convection zone to about $5800\,\mathrm{K}$ at the solar surface (Carroll and Ostlie, 2006).

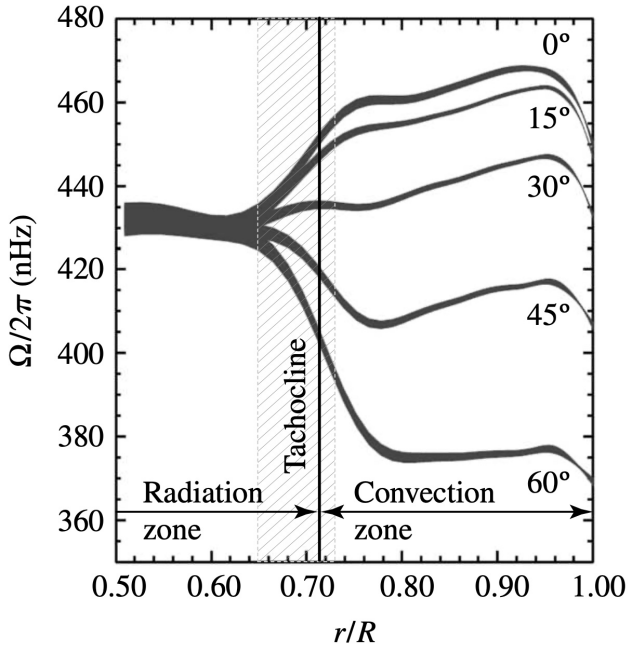

Fig. 2.2.: Rotation period over depth for a selection of solar latitudes. Adapted by Carroll and Ostlie (2006) from a figure courtesy of NSF's National Solar Observatory. Results are derived from GONG (Global Oscillation Network Group) observations of solar oscillations originally published by Thompson et al. (1996).

2.1.2 The Solar Atmosphere

The solar atmosphere is also divided into various regions, each with its own characteristics. Figure 2.3 shows an illustration of all layers as a function of radial distance to the surface, more specifically, the layer where the optical depth in the visible reaches unity ($\tau_{500} = 1$). Additionally, temperature and density profiles throughout the atmosphere are shown, and the formation heights for a selection of spectral lines are marked.

Nearly all visible light originates at the bottom of the atmosphere in a region called the photosphere. The average optical depth at which this solar flux originates has a value of about $\tau = 2/3$ (Eddington approximation). Since the change from optically thin to thick takes place in a very narrow region, the solar flux is well defined as black body radiation corresponding to the effective temperature ($5777\,\mathrm{K}$) at this specific optical depth (Carroll and Ostlie, 2006). The temperature and density continue to drop with increasing distance from the surface until the temperature reaches a minimum of $4400\,\mathrm{K}$ at the height of about $525\,\mathrm{km}$, the top of the photosphere (Hanslmeier, 2020).

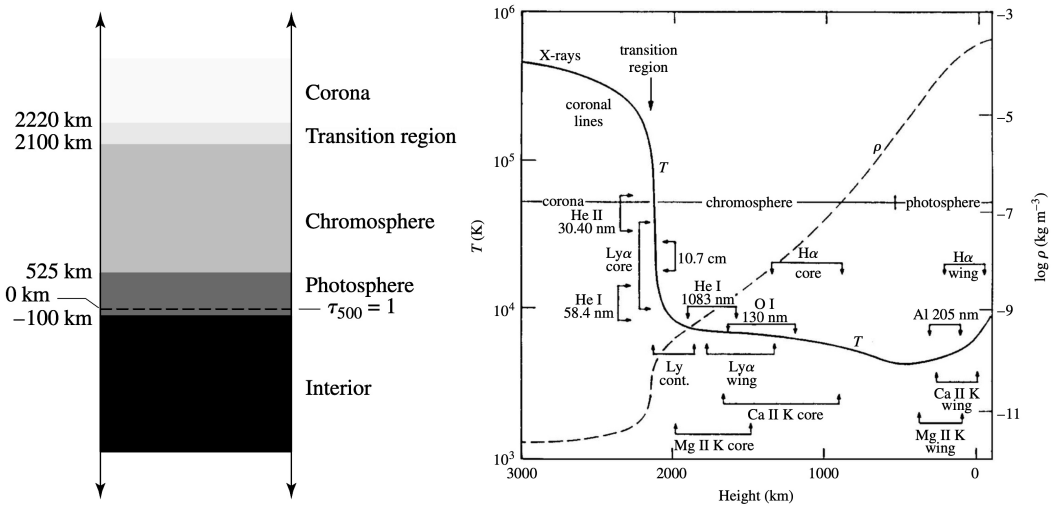

Fig. 2.3.: An illustration of solar atmosphere layers (left) with distances given relative to the height where $\tau_{500} = 1$. The temperature (solid line) and density (dashed line) profiles in the atmosphere as a function of altitude above the solar surface (right). Altitude ranges are marked that can be observed at different wavelengths. Figure adapted by Carroll and Ostlie (2006) from Murdin (2001).

The chromosphere lies just above the photosphere and has a thickness of approximately $1500\,\mathrm{km}$. The temperature rises again from its minimum at the top of the photosphere to the order of $10^4\,\mathrm{K}$, while the particle density continues to drop from $10^{15}\,\mathrm{cm}^{-3}$ at the minimum temperature layer to $10^{11}\,\mathrm{cm}^{-3}$ at a hight of about $2000\,\mathrm{km}$. Even though the chromosphere is much hotter than the photosphere, it does not contribute a lot to the total radiation because of this much lower density (Foukal, 2004). To make the chromosphere visible, we can observe the Sun at the core of strong absorption lines like $\mathrm{H}\alpha$ or CaII H and K. In these spectral lines, the opacity is greatly enhanced, which reduces the geometric depth we can see into the atmosphere. This means that instead of the photosphere, we observe the higher chromospheric layers (Mullan, 2009).

In a thin layer above the chromosphere with an approximate thickness of some $100\,\mathrm{km}$, called the transition region, the temperature rapidly rises from some $10^4\,\mathrm{K}$ to about $10^5\,\mathrm{K}$ and then continues rising more slowly to over $10^6\,\mathrm{K}$. Simultaneously the density decreases to even lower levels (Carroll and Ostlie, 2006). Due to inhomogeneities in the solar atmosphere from a range of phenomena, the transition region is not a perfectly spherical shell. Instead, it exists at different heights depending on the local atmospheric structure (Mullan, 2009).

The transition region marks the boundary to the outermost atmospheric layer, the solar corona. This very faint region compared to the rest of the solar atmosphere can normally only be seen when the solar disc is occulted because the underlying

atmospheric regions are much brighter. The left image in Figure 2.4 shows a picture of the corona taken during an eclipse when the moon occults the bright solar disc. However, when observed in the proper wavelength regimes like EUV, soft X-ray, or radio, the corona appears very bright compared to the underlying photosphere and chromosphere due to its much higher temperature. Therefore, we can use space-bound solar telescopes to take images in these wavelengths and continuously observe the corona even above the solar disc (Aschwanden, 2004). One such instrument is the Atmospheric Imaging Assembly (AIA) onboard the Solar Dynamics Observatory (SDO), which was used in this study and will be introduced in more detail in section 4.1. An image taken with this instrument in the extreme ultraviolet (EUV) can be seen on the right-hand side of Figure 2.4. It shows the highly variable nature of the solar corona, which can be roughly divided into three regions according to activity and magnetic field configuration: Active regions, quiet Sun regions, and coronal holes (Aschwanden, 2004).

Active regions are located around strong magnetic fields and are often visible as sunspot groups in the visible. Due to the bipolar nature of such sunspot groups, we conclude that the magnetic field lines are mostly closed. Constant magnetic activity in these regions fuels many dynamic processes like flares and coronal mass ejections. Heated plasma flows upward along the closed magnetic loops, making them brighter in the EUV than the background and giving the active regions their unique appearance. Quiet Sun regions are the remaining areas with closed magnetic field lines that are not considered active. However, the definition of active is ambiguous, and the boundary between active and quiet Sun is therefore not well defined. The quiet Sun, in fact, features many dynamic phenomena such as the nanoflares we analyzed in this thesis. Active should therefore only be seen as a relative term. Finally, coronal holes are regions of open magnetic field lines. Plasma can thus more easily escape (solar wind), making these regions much less dense. Their lower density makes them appear darker than the quiet corona, where hot plasma is trapped by the closed magnetic field lines (Aschwanden, 2004).

The particle density in the corona is extremely low, in the range of $10^6\,\mathrm{cm}^{-3}$ in the upper corona and $10^9\,\mathrm{cm}^{-3}$ at the base of quiet regions. In flare loops it can reach $10^{11}\,\mathrm{cm}^{-3}$. Because of the high temperature, all coronal plasma is fully ionized, but the temperature is not homogeneous. Instead, the corona consists of numerous over-dense structures that are filled with hot plasma, which is a result of the plasma being confined to the magnetic field lines, only able to flow along them and not across (Aschwanden, 2004). The theoretical reason for this phenomenon is discussed in more detail in the following section 2.2. Consequently, the coronal magnetic field is very well visible since it gets highlighted by this efficient spread of hot plasma along a field line and the constrained flow between different field lines, a 13 orders of magnitude difference in thermal conduction efficiency (Priest, 1984).

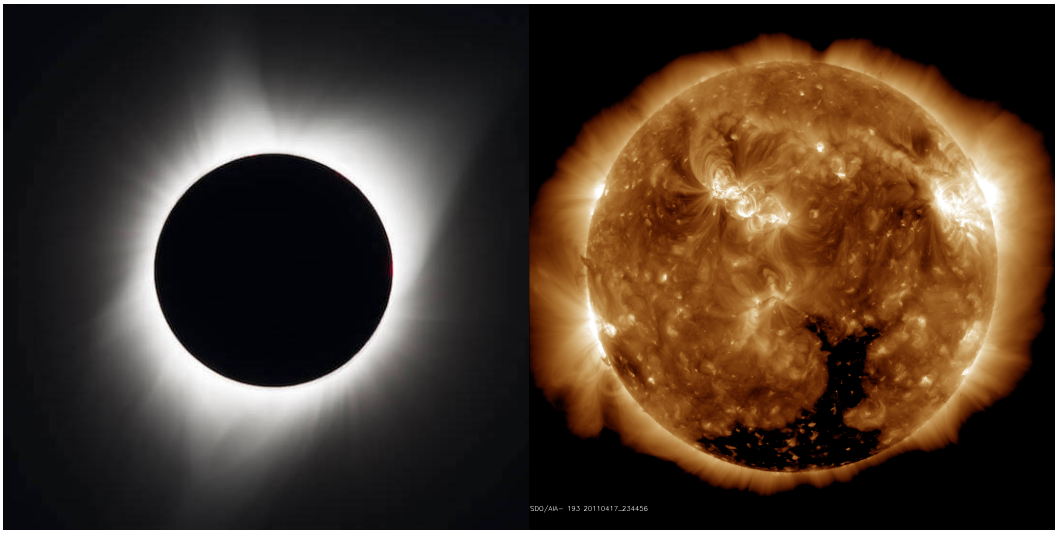

Fig. 2.4.: An image of the solar corona taken during the eclipse of 2017 form Madras, Oregon (left). From NASA/Aubrey Gemignani[1]. An EUV 193 Å image taken from space with the AIA/SDO instrument (right). Regions of various activity are visible including bright active regions with coronal loops, a dark coronal hole extending from the south pole and intermediate quiet Sun regions.

This restriction results in the characteristic loop structure of the corona (Parnell and De Moortel, 2012). The effect that cross-field diffusion is not possible also implies that those magnetic structures can only be heated from the chromospheric foot-points, which results in many different plasma temperatures inside of loops (Aschwanden, 2004).

2.2 Magnetic Fields and Reconnection

The Sun consists mainly of plasma, a state of matter where ionized atoms with positive electric charge and negative free electrons coexist in an unbound state. While this plasma is usually quasi-neutral on large scales because the overall charges cancel, it is locally charged and highly conductive. As a result, the Sun's magnetic field influences its properties and dynamics. Additionally, the movement of a charged particle in the plasma generates currents that affect all other charged particles in the surrounding. These interactions lead to much more complicated phenomena compared to a simple uncharged gas (Mullan, 2009). The relations between magnetic field, electric field, charges, and currents in a plasma follow Maxwell's equations (in CGS units):

[1] https://www.nasa.gov/image-feature/2017-total-solar-eclipse

$$\nabla \cdot \mathbf{E} = 4\pi\rho_E \tag{2.4}$$

$$\nabla \cdot \mathbf{B} = 0 \tag{2.5}$$

$$\nabla \times \mathbf{E} = -\frac{1}{c}\frac{\partial \mathbf{B}}{\partial t} \tag{2.6}$$

$$\nabla \times \mathbf{B} = \frac{1}{c}\frac{\partial \mathbf{E}}{\partial t} + 4\pi\mathbf{j} \tag{2.7}$$

where E is the electric field, B the magnetic field, ρ_E the electric charge density, **j** the electric current density, and c the speed of light (Aschwanden, 2004).

To describe also the plasma motions, the Maxwell equations are combined with the mass, momentum, and energy conservation laws (Navier-Stokes equations) from hydrodynamics. The resulting theory is called magnetohydrodynamics (MHD) and describes the behavior of an electrically and magnetically influenced fluid and the interaction with a surrounding field (Mullan, 2009). Since one fundamental assumption of MHD is that the involved plasma motions happen at speeds much slower than the speed of light ($v \ll c$), the term $(1/c)(\partial\mathbf{E}/\partial t)$ in Eq. 2.7 can be neglected (Aschwanden, 2004). In the frame of reference of an observer, a plasma moving with speed **v** feels an electric field component $(1/c)(\mathbf{v} \times \mathbf{B})$ in addition to the rest electric field **E**. Ohm's law states that the current density is then proportional to the total electric field times the electric conductivity constant σ:

$$\mathbf{j} = \sigma(\mathbf{E} + \frac{1}{c}\mathbf{v} \times \mathbf{B}) \tag{2.8}$$

A magnetic field gives rise to a magnetic pressure with magnitude $p_m = B^2/8\pi$, in addition to the gas pressure. However, the force exerted by this magnetic pressure acts only in the direction perpendicular to the magnetic field and not along the field lines. Since the magnetic pressure has the same dimensions as an energy density and is also often referred to as the magnetic energy density (Mullan, 2009).

By eliminating the electric field and the current density from the description of the magnetic field one arrives at the induction equation that describes how the magnetic field changes with time in a moving plasma:

$$\frac{\partial \mathbf{B}}{\partial t} = \nabla \times (\mathbf{v} \times \mathbf{B}) + \eta\nabla^2\mathbf{B} \tag{2.9}$$

with the magnetic diffusivity $\eta = c^2/4\pi\sigma$. The first term ($\nabla \times (\mathbf{v} \times \mathbf{B})$) is called the

convection term and the second term ($\eta\nabla^2\mathbf{B}$) is called the diffusion term (Aschwanden, 2004). The Reynolds number (R_m) is then defined as the ratio of convection term to diffusion term:

$$R_m = \frac{\text{convection}}{\text{diffusion}} = \frac{\nabla \times (\mathbf{v} \times \mathbf{B})}{\eta\nabla^2\mathbf{B}} = \frac{v_0 l_0}{\eta} \tag{2.10}$$

with the the typical length scale l_0 and the typical speed v_0 of the plasma (Aschwanden, 2004). The induction equation can be approximated for two extremes of plasma conditions, depending on the Reynolds number:

$$R_m \gg 1: \quad \frac{\partial \mathbf{B}}{\partial t} \approx \nabla \times (\mathbf{v} \times \mathbf{B}) \tag{2.11}$$

$$R_m \ll 1: \quad \frac{\partial \mathbf{B}}{\partial t} \approx \eta\nabla^2\mathbf{B} \tag{2.12}$$

Under conditions where $R_m \ll 1$, the time evolution of the magnetic field is governed by the diffusion term. It is proportional to the second spatial derivative of the field and describes the decay of the magnetic field over time. The typical timescale for a magnetic field to leak out of a conducting medium is $\tau_d = l_0^2/\eta$. The magnetic energy is removed by resistive dissipation (Foukal, 2004; Aschwanden, 2004). According to Eq. 2.10 such conditions are possible if either the diffusivity η is large (small conductivity) or the involved length scales and speeds are low.

In the solar corona, we have conditions with $R_m \gg 1$. Due to the very high conductivity $\sigma \to \infty$, the diffusivity η goes to zero. Additionally, the typical length scales are large. In such conditions, the diffusion term can be neglected and the magnetic flux ($\Phi = \int \mathbf{B} d\mathbf{A}$) enclosed by a fluid parcel remains constant. Magnetic flux can neither enter nor leave the parcel. Thus plasma and embedded magnetic field lines have to move together, and we describe this state as "frozen-in" (Mullan, 2009). Depending on the exact conditions, either the plasma motions can dominate the magnetic field, or the magnetic field can dominate the plasma. Which one is the case is determined by the plasma-β parameter, which is given by the ratio of the gas pressure and the magnetic pressure (Aschwanden, 2004):

$$\beta = \frac{p_g}{p_m} = \frac{nkT}{B^2/8\pi} \tag{2.13}$$

If $\beta \gg 1$, the plasma motions dominate the magnetic field. Such conditions are present in the convection zone and the photosphere, and the magnetic field has to follow the convective motions and the differential solar rotation. On the other hand, if $\beta \ll 1$, the magnetic field dominates the plasma motions, as observed in the solar corona. Plasma can only move along field lines which highlights the magnetic field structure of the corona as described in the previous section (Aschwanden, 2004).

A potential field **B(r)** is defined as any magnetic field that can be expressed as the gradient of a magnetic scalar potential function $\phi(\mathbf{r})$ of the solar plasma:

$$\mathbf{B(r)} = \nabla\phi(\mathbf{r}) \tag{2.14}$$

Inserting this relation into Eq. 2.8, it follows that in such a magnetic potential field, the current density vanishes ($\mathbf{j} = \mathbf{0}$), and it is therefore also called a current-free magnetic field (Aschwanden, 2004). A force-free field is a magnetic field configuration where the Lorentz force is zero ($\mathbf{F} = \mathbf{j} \times \mathbf{B} = 0$), which means currents are only allowed to flow along the field lines. Such fields are commonly encountered in the chromosphere and corona, where we have frozen-in conditions ($R_m \gg 1$) and a dominant magnetic pressure ($\beta \ll 1$) (Foukal, 2004). A force-free field configuration can be interpreted as a deviation from the potential field. One example of a possible deviation is a sheared arcade. This refers to a sequence of equally sized loops with a common axis of curvature, where one side of footpoints is shifted parallel to the neutral line. This shift results in a shearing motion where the shearing angle is directly proportional to the non-potentiality of the arcades magnetic field (Aschwanden, 2004). The free magnetic energy is the energy difference between the non-potential force-free field and the hypothetical potential field without currents and can be released if frozen-in conditions are (locally) broken (Foukal, 2004).

Magnetic reconnection is a restructuring of the magnetic field that changes its topology and releases non-potential energy in the process. The free energy is converted into thermal energy, particle acceleration, and plasma motions. While this energy release could happen in a slow and steady process, it is usually observed as a fast, violent process in events like flares and coronal mass ejections. In the Sweet-Parker model of quasi-static magnetic reconnection (Sweet, 1958; Parker, 1957), two sets of oppositely directed magnetic fields that get into close proximity form a dynamic boundary between them. According to Faraday's law, the strong opposing magnetic fields are associated with a strong current in this boundary called the current sheet. Such a field configuration can, for instance, happen when new magnetic flux is pushed towards a preexisting one or when new emerging flux pushes upward through the chromosphere against a preexisting coronal field. Since the

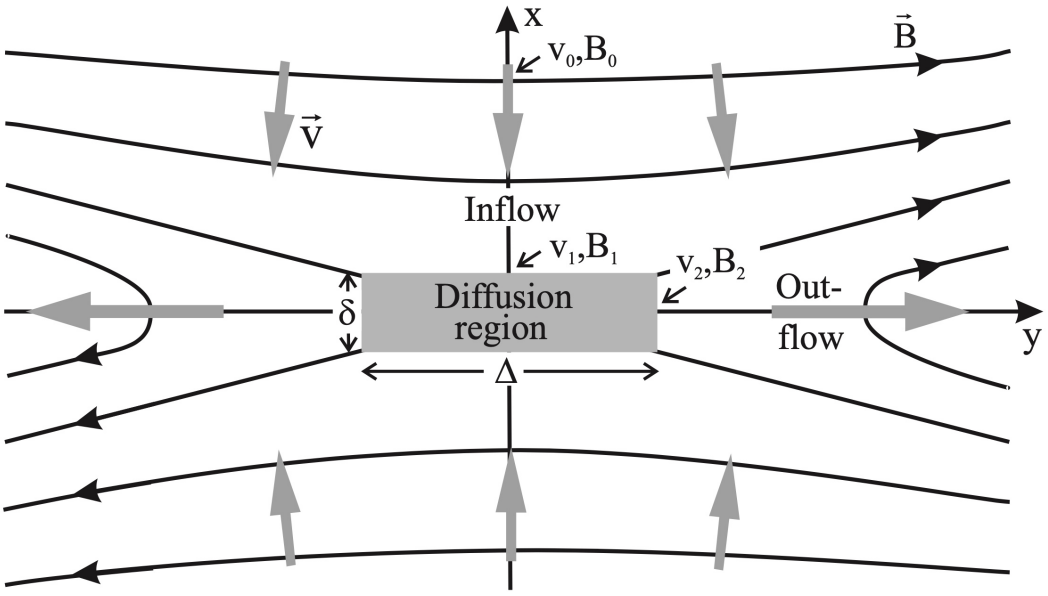

Fig. 2.5.: The basic model of (2D) magnetic reconnection. Shown are the inflows (x-direction) from the two regions of opposite magnetic polarity, the central diffusion region where magnetic fields are reconnected, and the resulting outflows (y-direction). From Schindler and Hornig (2000).

magnetic field needs to transition continuously between polarities at the boundary between both field regions of opposite polarity, the magnetic field has to drop to zero at the boundary. As a result of the missing magnetic pressure, the thermal pressure in the neutral boundary layer has to be higher compared to both sides. Since the involved length scales are short in the central region, the plasma is no longer frozen-in and can flow across field lines. This region where frozen-in is locally broken is called the diffusion region. The plasma that flows into the diffusion region from both polarities is channeled towards outflow regions parallel to the boundary layer. Here plasma-$\beta < 1$ and magnetic flux is frozen-in again. The extent of the diffusion region is at first limited by the finite area of the first contact and then further constrained by the resulting outflow of plasma. The whole process can reach an equilibrium between outward-directed magnetic tension, inward-directed magnetic pressure, and thermal pressure. A standing slow shock forms on both polarity sides, with stationary outflows between them. The thin diffusion region is located in the middle (Aschwanden, 2004). Figure 2.5 shows an illustration of this basic steady magnetic reconnection model.

Large diffusion regions will become unstable and are susceptible to secondary tearing. This leads to unsteady reconnection modes that are very likely to occur in solar flares. Some examples are tearing instability, coalescence instability, X-type collapse, resistive 3D reconnection, or collisionless reconnection (Aschwanden, 2004).

2.3 The Solar Cycle

The term solar cycle refers to the observed periodic change of many solar phenomena with a period of about 11 years and has its origin in the cyclic behavior of the Sun's magnetic field. The main record of solar activity comes from the observations of sunspot numbers on the solar disk that became possible with the invention of the telescope around 1610 (Hathaway, 2015). A possible cyclic behavior was first mentioned in 1776 but only truly discovered much later by Schwabe (1844).

Sunspot observations in white light show a dark central region called the umbra and a slightly less dark surrounding region called the penumbra (Foukal, 2004). Figure 2.6 shows a white light image of the solar disc with multiple sunspots taken at the Kanzelhöhe Observatory in Austria. Sunspots are the result of strong magnetic fields, reaching field strengths of 2 to $3\,\mathrm{kG}$, that penetrate the solar photosphere in the form of locally concentrated, mostly vertical flux tubes (Aschwanden, 2004). Since sunspots remain relatively stable for an extended period, the flux tube has to be in horizontal pressure equilibrium. Considering the principles of magneto-statics, the combined thermal and magnetic pressure inside a flux tube has to balance the outside thermal pressure. The horizontal pressure equilibrium inside a sunspot is therefore given as (Aschwanden, 2004):

$$p_E = p_0 + \frac{B_0^2}{8\pi} \tag{2.15}$$

where p_E is the external pressure, p_0 is the inside thermal pressure, and $\frac{B_0^2}{8\pi}$ is the inside magnetic pressure given by the inside magnetic field strength B_0.

If we assume a constant density inside and outside the vertical flux tube, it follows that the inside temperature has to be lower than in the surrounding plasma. This lower temperature can be understood in terms of a restricted heat transfer. The strong vertical magnetic field inside a sunspot inhibits convection because the plasma is frozen-in and horizontal plasma flow is not possible. Radiation can still transport heat, but it is much less effective. Consequently, the plasma inside a sunspot has to be much cooler than the surrounding plasma (Mullan, 2009). A typically measured temperature inside a sunspot is $\approx 4500\,\mathrm{K}$, at least $1000\,\mathrm{K}$ colder than regular photospheric plasma. Therefore, sunspots emit less radiation than their surroundings and appear darker (Aschwanden, 2004). Because the density in the solar atmosphere decreases with distance to the surface in the solar atmosphere, magnetic flux tubes have to expand outward with height, rapidly

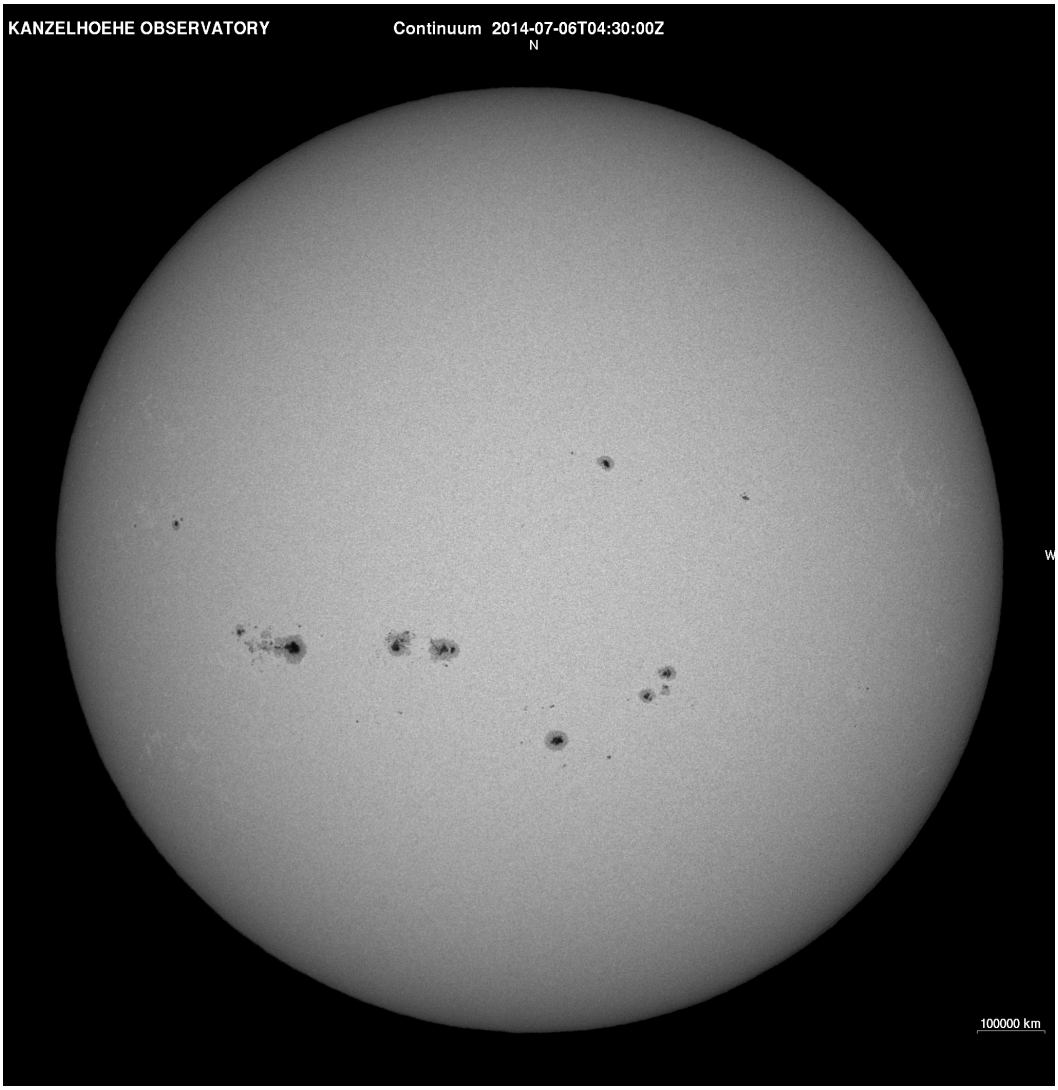

Fig. 2.6.: White light image of the Sun shows the solar disc with multiple dark sunspots. The image was taken at Kanzelhöhe Observatory in Austria[2].

growing in geometric expansion and creating what is called the magnetic canopy structure (Aschwanden, 2004).

In order to allow for a better study and comparison of the number of sunspots, Swiss Astronomer Rudolf Wolf introduced his relative sunspot number in 1849, given by the following equation:

$$R = k(10g + s) \tag{2.16}$$

where R is the relative sunspot number, g is the number of sunspot groups, s is the

[2] www.kso.ac.at

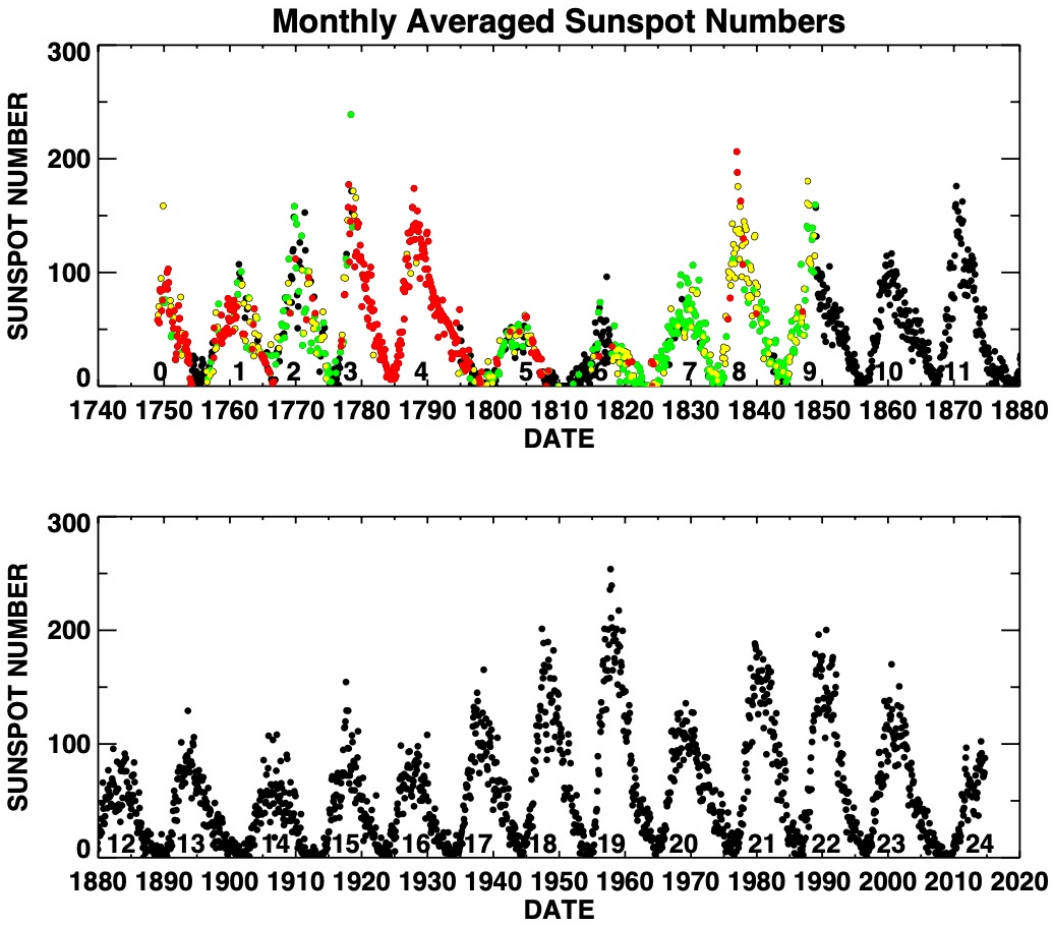

Fig. 2.7.: Monthly mean International Sunspot Number showing the cyclic behavior of the Sun and the variations in amplitude, shape and length between cycles. Colores represent various degrees of missing data. From Hathaway (2015).

number of individual spots, and k is a correction factor that accounts for different observers, telescopes, and site conditions (Foukal, 2004).

The relative sunspot number emphasizes sunspot groups that are, in general, far easier to identify than individual spots. This definition introduced by Wolf is still used for the international sunspot number (ISN) produced today through combined sunspot observations from around the globe, and continuous daily observations have been made since the introduction in 1849 (Hathaway, 2015). Past observations beginning in the early 17th century have also been reconstructed to fit this definition, and the total sunspot number record has been thoroughly recalibrated by Clette et al. (2014). Figure 2.7 shows the monthly averages of the daily sunspot numbers between 1750 until 2015 and the periodic changes due to the solar cycle.

In addition to the changes in their number, sunspots also show other cyclic behaviors. Together with their associated active region, sunspot locations migrate

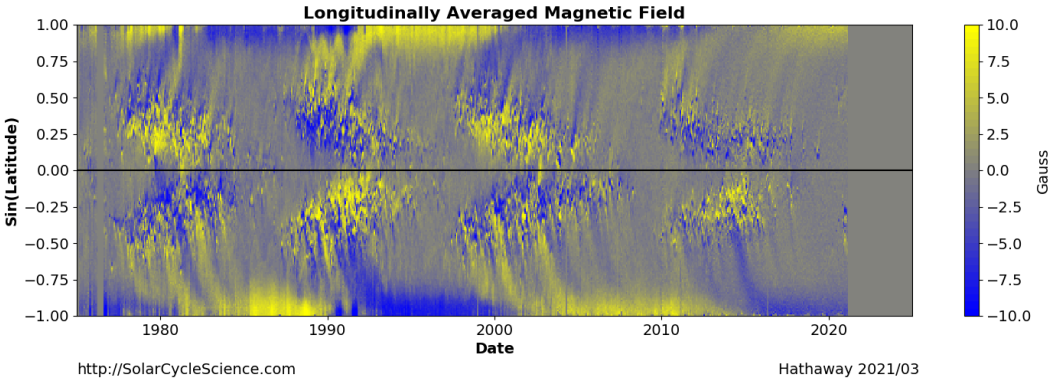

Fig. 2.8.: The magnetic butterfly diagram shows the distribution of surface magnetic field over the last four solar cycles (two Hale cycles). Shown is an updated version of the diagram published by Hathaway (2015), which is available on the solarcyclescience website[3].

from about $40°$ in latitude during the solar minimum (lowest sunspot number) down to about $10°$ when approaching the maximum (highest sunspot number). Additionally, the east-west orientation of active region magnetic fields are opposite on the northern and southern hemispheres and flip orientation with every cycle (Aschwanden, 2004). The combined effect of these phenomena is visible in Figure 2.8, known as the magnetic butterfly diagram because of its distinct form. It illustrates the regular changes of the magnetic field by plotting the surface magnetic field at a certain latitude as a function of time.

The solar cycle is believed to result from a dynamo process driven by the strong internal magnetic field in the tachocline that periodically strengthens and weakens. Buoyant magnetic flux tubes may rise from this region and emerge from the solar surface, forming the bipolar sunspot pairs and active regions. Subsequently, the differential surface rotation shears the field into a more toroidal shape until it is broken up by surface diffusion (granular convection) and is transported as fragments towards the poles by meridional flows. This weakens the toroidal field component until only a weak global poloidal field with opposite polarity to the original field is left during the solar minimum. Then, the field in the tachocline gets strengthened again by the internal dynamo and forms more buoyant flux tubes. The new solar cycle begins. A complete magnetic cycle called the Hale cycle, during which the original magnetic polarity is restored, lasts for 22 years (Aschwanden, 2004).

The total magnetic flux is at its lowest at the minimum of the solar cycle and peaks during the solar cycle maximum. The brightness in many wavelengths (e.g. X-rays, UV and radio) is modulated by the magnetic field and follows the solar cycle. Brightness in the visual wavelength range is, however, much less affected. Coronal structure, appearance, and phenomena are all heavily influenced by the strength

[3] solarcyclescience.com/solarcycle.html

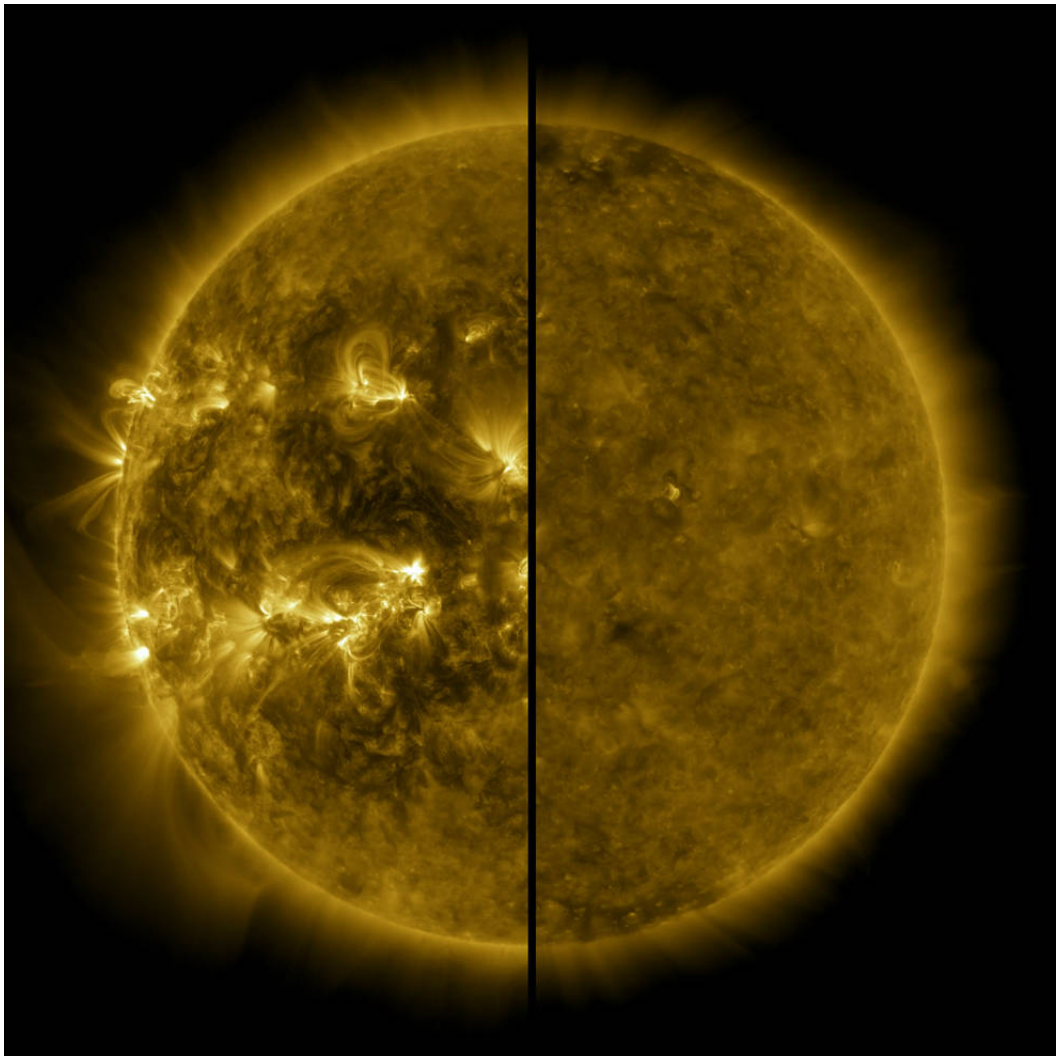

Fig. 2.9.: A split image of the corona during the maximum of the solar cycle in April 2014 (left), and during the minimum in December 2019. Both images are EUV 171 Å images taken by AIA/SDO during solar cycle 24. From NASA/SDO[4].

and dynamics of the solar magnetic field. Figure 2.9 shows the influence of the solar cycle and the consequent changes in activity level on the observed appearance of the solar corona. Both halves of the combined image were acquired with the AIA/SDO instrument in the same 171 Å EUV wavelength but about five years apart during solar cycle number 24. The left image, taken near the solar maximum, shows bright bands of active regions at low latitudes in both hemispheres. In the right image, taken during the cycle minimum in December 2019, no active regions are visible, and the corona looks much more homogenous. Only the polar coronal holes are bigger and more pronounced.

[4] www.nasa.gov/press-release/solar-cycle-25-is-here-nasa-noaa-scientists-explain-what-that-means

3 The Coronal Heating Problem

The Sun's temperature steadily decreases along its radius, from its highest at the source of energy in the core all the way to its minimum in the photosphere. This is expected and consistent with an outward flow of thermal energy. Unexpectedly, in the chromosphere, the temperature starts to rise again and then steeply increases within the transition region to finally reach millions of degrees in the corona (see section 2.1.2). Coronal temperatures are 200 to 300 times higher than in the photosphere, while the coronal density is 8 to 9 orders of magnitude lower than photospheric values. Therefore, the thermal energy density of the corona is much smaller than the energy density inside the photosphere. However, since thermal energy must flow along a decreasing temperature gradient, like in the Sun's interior, heat transfer from the photosphere to the corona cannot explain the high coronal temperatures. If only purely thermal processes were at work, we would expect the temperature to continue decreasing with increasing distance from the photosphere. Consequently, there has to be a different (kinetic) source of energy that is heating the corona. This mystery and the search for a satisfying explanation is commonly referred to as the *coronal heating problem* (Sakurai, 2017).

3.1 Discovery of the High Coronal Temperature

Although unknown at the time, the first real evidence of the high coronal temperature was obtained in 1869 by the Astronomers C.A. Young and W. Harkness. When they measured the coronal spectrum during a solar eclipse, they discovered an unfamiliar emission line at a wavelength of $530.3\,\mathrm{nm}$. This so-called green coronal line and the later found red coronal line at $637.4\,\mathrm{nm}$ are still the strongest coronal emission lines in the visible part of the spectrum, even though numerous other emission lines are known today. Their origin was initially a mystery since they did not match the emission lines of any known element in the 19th century. This changed as the Swedish physicist Edlén determined the energy levels of Fe X by measuring the ultraviolet emission of highly ionized iron in spark discharge experiments. The German physicist Grotrian then successfully matched one of the found transitions to the red corona line (Sakurai, 2017).

Since this is a forbidden transition, it does not usually occur in laboratory conditions. Electrons need much longer to get from such a metastable level to a forbidden lower energy level compared to an allowed transition. If the density is high, collisions usually let the electron escape to a different energy level before it has time to make the forbidden transition. However, in the solar corona, collisions are very infrequent due to the very low density. Electrons are left undisturbed for a sufficient amount of time to spontaneously make such a forbidden transition and produce the observed coronal lines (Carroll and Ostlie, 2006).

After this first discovery, many additional coronal lines were identified through the same process. The green line was finally matched to a transition of Fe XIV. These emission lines from highly ionized iron atoms that got ripped off 13 of their 26 electrons point to a very high temperature inside the corona. While Edlén originally arrived at a temperature of $250\,000\,\mathrm{K}$, the temperature has since been corrected to the modern value of 1 to $2\,\mathrm{MK}$, which can be determined from the relative abundances of ions. For example, Fe X is the most abundant ionization stage of iron at a temperature of $1\,\mathrm{MK}$, while Fe XIV and Fe XV are the most abundant ionization stage at a temperature of $2\,\mathrm{MK}$ (Sakurai, 2017). Figure 3.1 shows the abundance of iron ionizations (Fe V to Fe XIX) for different temperatures.

3.2 Heating Energy Requirements

The energy balance of the corona can be described by

$$n_e^2 \Lambda(T) - \mathrm{div}(\kappa_c \nabla T) = \epsilon_H \tag{3.1}$$

where n_e is the electron density, $\Lambda(T)$ the radiative loss function of an optically thin plasma, κ_c the thermal conductivity, and T the temperature (Sakurai, 2017). The first term of the energy balance equation describes the energy loss through radiation. Noticeable is the dependency on the squared electron density, which is proportional to the emission measure of an optically thin plasma, and in turn, on the observed flux. Therefore, the heating is directly proportional to the observed brightness. This would not be true for optically thick radiation (Aschwanden, 2004). The second term of the energy balance equation describes the energy loss through thermal conduction. The rate of energy loss is given by the spatial divergence of the heat flux $F = \kappa_c \nabla T$ (Mullan, 2009). ϵ_H is the required heat input per unit volume to compensate for both losses and keep the corona at a stable temperature (Sakurai, 2017).

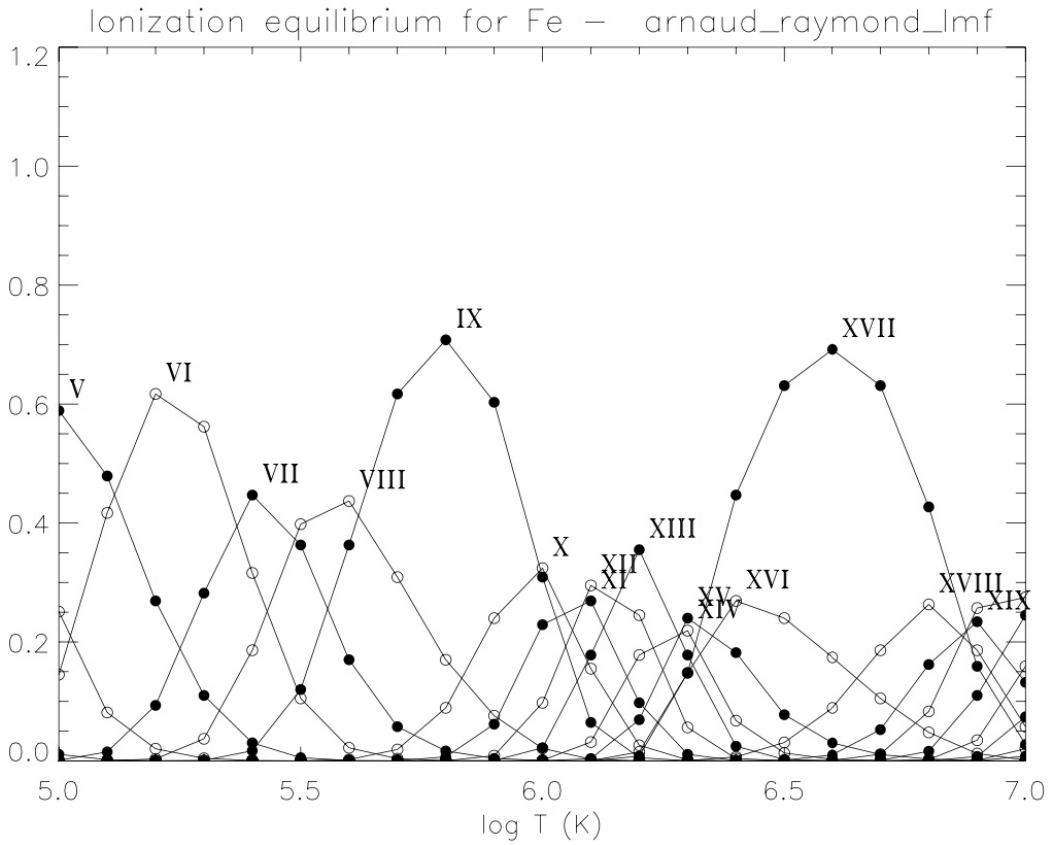

Fig. 3.1.: Ionization equilibrium for Fe V to Fe XIX in the temperature range of 10^5 to 10^7 K, using the CHIANTI database (Dere et al., 1997; Dere et al., 2019) and ionization ratios derived by Arnaud and Raymond (1992). From Aschwanden (2004).

Sakurai (2017) shows that a volumetric heating rate of 10^{-4} to $10^{-2}\,\mathrm{erg\,cm^{-3}\,s^{-1}}$ is necessary for a coronal temperature of $2\,\mathrm{MK}$, if one assumes a magnetically closed volume with constant pressure and constant ϵ_H along the loop. Aschwanden (2004) calculated a heating flux per unit area (P) at the coronal base by additionally integrating the volumetric heating rate in the vertical direction. For coronal holes ($n_e = 1 \times 10^8\,\mathrm{cm^{-3}}$ and $T = 1\,\mathrm{MK}$) he estimates that a heating rate of $P \approx 5 \times 10^3\,\mathrm{erg\,cm^{-2}\,s^{-1}}$ is required. In active regions ($n_e = 2 \times 10^9\,\mathrm{cm^{-3}}$ and $T = 2.5\,\mathrm{MK}$) his estimate rises to $P \approx 5 \times 10^6\,\mathrm{erg\,cm^{-2}\,s^{-1}}$, a 3 magnitudes increase. He sets a lower limit for the heating rate at any place of the solar surface at $P \gtrsim 3 \times 10^5\,\mathrm{erg\,cm^{-2}\,s^{-1}}$ to account for the combined energy loss. This is consistent with the values reported by Withbroe and Noyes (1977), where conduction and radiation account for a coronal energy loss of $2 \times 10^5\,\mathrm{erg\,cm^{-2}\,s^{-1}}$ and $10^5\,\mathrm{erg\,cm^{-2}\,s^{-1}}$, respectively. For comparison, in the chromosphere, the heating energy requirement even rises to $4 \times 10^6\,\mathrm{erg\,cm^{-2}\,s^{-1}}$ (Parnell and De Moortel, 2012).

A fundamental requirement of any heating theory is the inclusion of a sufficient energy source. Parnell and De Moortel (2012) make an order of magnitude argu-

ment that the magnetic flux ($2.5 \times 10^7\,\mathrm{erg\,cm^{-2}\,s^{-1}}$) generated by the movement of magnetic loop footpoints is already sufficient to provide more than enough energy to heat both the chromosphere and corona ($4.3 \times 10^6\,\mathrm{erg\,cm^{-2}\,s^{-1}}$ required). The constant emergence of new flux would provide an additional energy source of about $1 \times 10^6\,\mathrm{erg\,cm^{-2}\,s^{-1}}$, which is on its own a substantial fraction of the required energy, although about a factor of 25 less than the energy from footpoint motions. Since MHD models yield similar results, Parnell and De Moortel (2012) conclude that the solar atmosphere's heating energy clearly comes from these mechanisms, with the kinetic and magnetic energy of convective plasma at and below the photosphere being the ultimate driver for both energy sources. The theory of a photospheric energy source for atmospheric heating is widely accepted and there exist multiple different mechanisms that can then convert this provided energy into the heat required for coronal temperatures (Klimchuk, 2006).

3.3 Heating Mechanisms

For all models, the energy ultimately comes from some photospheric driver, but the coronal response to changes in this driver can be different, leading to either direct (DC) or alternating (AC) currents. Which one depends mainly on the relation between the timescales involved in the process. More specifically, the critical parameters are the timescale τ_C of changes to the photospheric driver and the characteristic timescale τ_A disturbances need to propagate along the length of the magnetic field loop. Since disturbances in the magnetic field propagate from the photosphere to the corona with the Alfvén speed, the characteristic timescale of coronal magnetic loops can be estimated as $\tau_A = L/v_A$, where L is the length of the loop and $v_A = B/\sqrt{\mu_0 \rho}$ the Alfvén speed in the loop. The Alfvén speed is dependent on the magnetic field strength B, the vacuum permeability μ_0, and the mass density ρ. AC currents are generated if τ_C is less than τ_A. Since the magnetic loop does not have enough time to respond to the photospheric disturbances fully, the energy is dissipated through waves. On the other hand, DC currents are produced if τ_C is greater than τ_A. Because disturbances happen slowly compared to the propagation time, the loop can react in a quasi-static way to any changes, becomes stressed, and builds up free magnetic energy that can be released at a later time (Aschwanden, 2004; Sakurai, 2017). Figure 3.2 shows a sketch of both AC and DC heating models and drivers.

The induced currents can then be dissipated by various processes, including Ohmic dissipation, magnetic reconnection, current cascading, and viscous turbulence for DC models. Processes for AC currents are Alfvénic resonance, resonance absorption, phase mixing, current layer formation, and turbulence (Aschwanden, 2004).

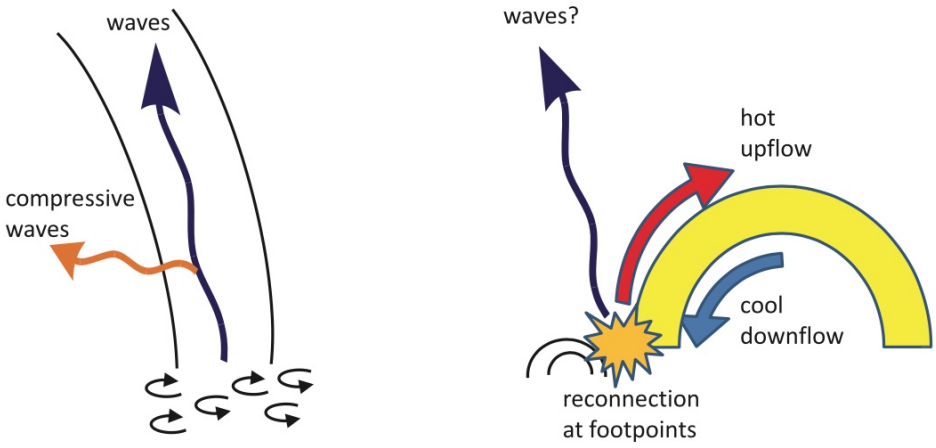

Fig. 3.2.: Schematic overview of two heating mechanisms in the solar corona. AC or wave heating driven by convective motions (left), and DC heating via magnetic reconnection and consequent up-flow of hot plasma (right). From Sakurai (2017).

The entire coronal (and chromospheric) heating process is a highly coupled system that involves many steps. Aschwanden (2001) classifies each heating model as a series of eight subprocesses, starting from the energy produced by the mechanical driver (a) and ending with the hot plasma filling coronal loops (h). Only models that give concrete predictions for this trapped hot plasma in the last step can be compared to observations. Figure 3.3 shows an overview of different heating models and the involvement of each of the eight subprocesses.

While historically, coronal heating was treated as an independent problem and a question of DC versus AC models, it has been realized that both processes are probably involved. Solving the coronal heating problem has shifted towards the question of which one dominates the heating process. Since energy and mass constantly flow between the chromosphere and the corona through the transition region, we have to treat the whole atmosphere as a highly coupled system. Therefore an extensive range of plasma properties is involved in the process, making the heating problem much more complicated than initially expected and still a topic of hot debate. It became clear that any heating model has to explain how plasma is heated to coronal temperatures and how it fills the coronal loops (Parnell and De Moortel, 2012).

3.3.1 DC Heating Models

The emergence of new magnetic flux from the solar interior into the photosphere leads to the constant formation of new coronal loops by connecting the new flux features to existing ones. Therefore, magnetic reconnection has to take place to

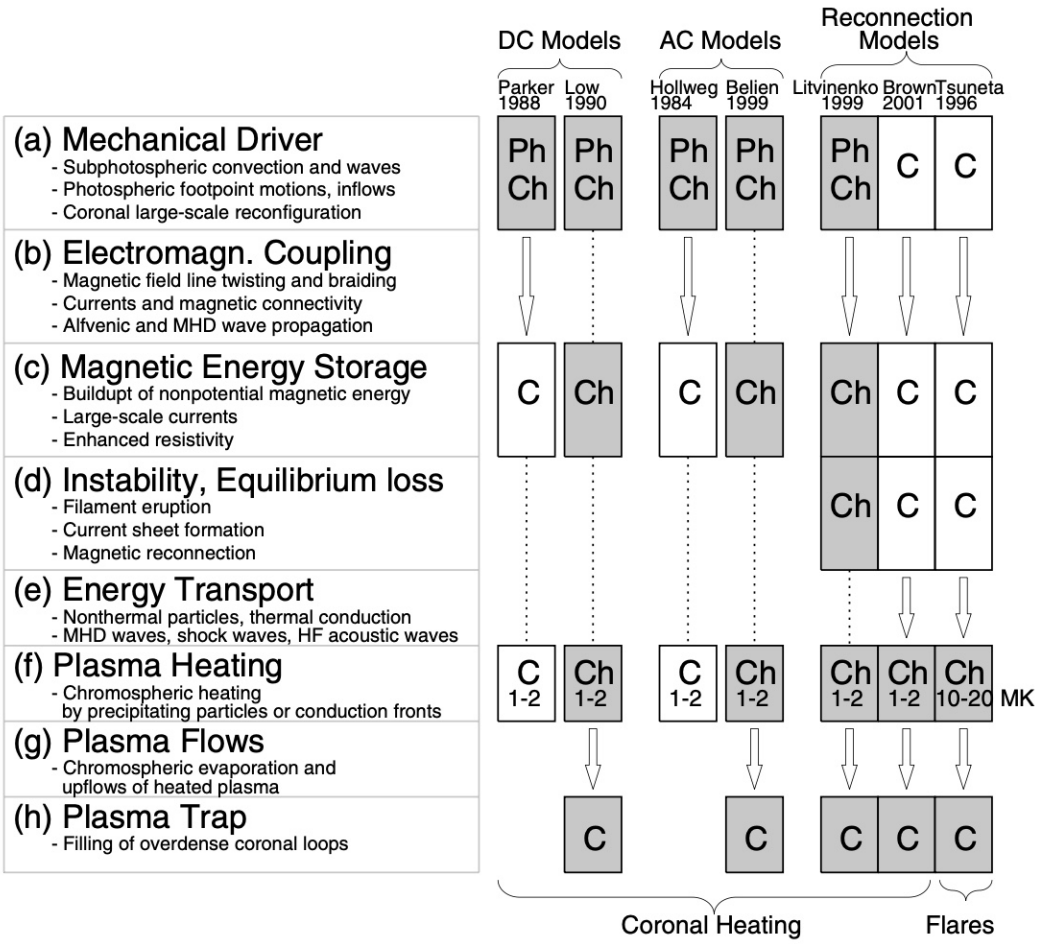

Fig. 3.3.: Coronal heating models are divided into eight subprocesses (a to h) listed and detailed on the left. The flow chart on the right shows their involvement and location for a selection of heating models with boxes marking a subprocess that is part of the model. The gray color highlights high-density regions like the photosphere (Ph), the chromosphere (Ch), and over-dense coronal loops (C). Regions of low density like the coronal background plasma (C) are left white. Arrows are used to represent transport processes between different locations, and dotted lines connect co-spatial locations. From Aschwanden (2001).

allow for this continual restructuring of the magnetic field. Magnetic reconnection is also necessary for the removal of flux from the photosphere (Parnell and De Moortel, 2012). Stress-induced magnetic reconnection, on the contrary, is the result of photospheric granular and supergranular motions that move the base of coronal field lines in a random-walk-like manner. The field lines will get twisted and wrapped around each other if the random walk step size is larger than the characteristic separation of neighboring flux tubes (Klimchuk, 2006). This process forms current sheets at the interface of misaligned flux tubes and builds up free energy until it is released and partially turned into thermal energy by tiny magnetic reconnection events. The idea was first introduced by Parker (1972) who also established the name

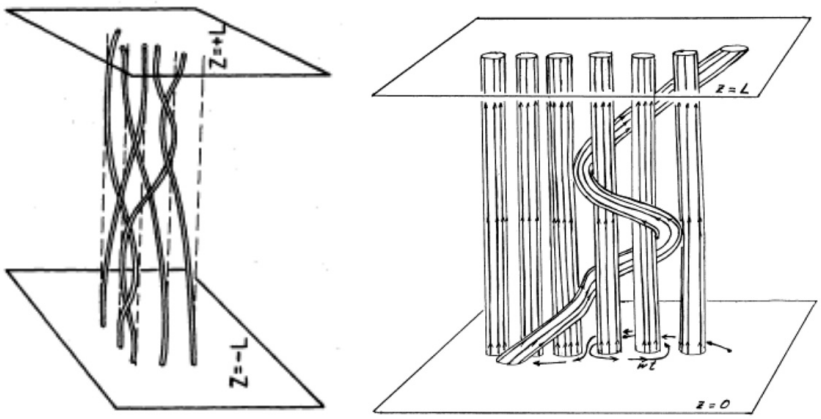

Fig. 3.4.: Two images drawn by Parker (1972) (left) and Parker (1983) (right) visualizing how random walk motions of footpoints would twist magnetic fluxtubes and lead to an entangled state where neighboring fluxtubes are wound around each other.

nanoflare for these tiny magnetic reconnection events (Aschwanden, 2004). Two of his drawings shown in Figure 3.4 illustrate how Parker imagined that footpoint motions would lead to twisted and entangled flux tubes that store free magnetic energy. Today we typically divide flare-like reconnection events into categories depending on their thermal energy content. Aschwanden (2004) gives energy (ϵ_{th}) boundaries for the three main groups and provides approximate values for their temperature (T_e) and density(n_e).

	ϵ_{th} [erg]	T_e [MK]	n_e [cm^{-3}]
Large flares:	10^{30} to 10^{33}	8 to 40	0.2 to 2×10^{11}
Microflares:	10^{27} to 10^{30}	2 to 8	0.2 to 2×10^{10}
Nanoflares:	10^{24} to 10^{27}	1 to 2	0.2 to 2×10^{9}

While large flares can be detected in hard X-ray (HXR), soft X-ray (SXR), and extreme ultraviolet (EUV) radiation, microflares will only appear in SXR and EUV, and nanoflares are only visible in the EUV. These minor events should not reach temperatures higher than about $2\,\mathrm{MK}$ but have otherwise similar characteristics to standard flares. For instance, they show an impulsive rise and decay and occur in small-scale loops (Aschwanden, 2004).

Large flares have been extensively studied. Crosby et al. (1993) determined frequency distributions of multiple hard X-ray flare parameters for 12000 flares between 1980 and 1989, and found that they follow a power-law distribution, meaning that the occurrence rate $\frac{dN}{dE}$ of flares can be expressed as a function of their energy (E), the power-law index α, and some factor (A):

$$\frac{dN}{dE} = AE^{-\alpha} \tag{3.2}$$

The observed power-law extends over three orders of magnitude of total flare energy in electrons (1×10^{29} to $1 \times 10^{32}\,\mathrm{erg}$) with a power-law index of $\alpha \approx 1.5$. Further power-laws include the parameters measured during the peak count rate of each flare, such as the count rate itself, photon flux, and electron flux, which result in slopes between -1.6 to -1.7. They did not find any power-law changes that correlated to changes in solar activity throughout the solar cycle but found variations in the overall flaring rate by a factor of 20. Veronig et al. (2002) did a statistical analysis of about 50000 soft X-ray flares from GOES observations during the years 1976 to 2000. They also find that frequency distributions of peak flux, fluence, and event duration can be characterized as power-laws over several decades and that the steepness of the power-law distributions does not reveal any significant change over the solar cycle. However, the total number of events per flare peak flux bin does change by more than an order of magnitude between times of minimum and maximum solar activity (Fig. 3.5). These findings show that the total number of flares is a strong function of the solar activity level, but the steepness of the distributions remains unchanged.

Solar flares release typical energies in the range of 10^{29} to $10^{32}\,\mathrm{erg}$, but even larger flares called superflares can be observed on other stars. Maehara et al. (2012) report observations of 365 superflares with total bolometric energies of 10^{33} to $10^{36}\,\mathrm{erg}$ on 148 solar-type stars observed from April 2009 to December 2009. They find that the frequency distribution of these superflares follows a power-law with index -2.0 to -2.3, very similar to the power-laws found in solar flares. The predicted occurrence frequency of a $10^{34}\,\mathrm{erg}$ superflares is once in 800 years, and that of an $10^{35}\,\mathrm{erg}$ superflare once in 5000 years. Shibata et al. (2013) makes an order of magnitude estimate in order to determine whether such superflares could occur on the Sun using currently known dynamo mechanisms and find that it could indeed be possible to generate a large enough sunspot for a $10^{34}\,\mathrm{erg}$ superflare within one solar cycle. An $10^{35}\,\mathrm{erg}$ flare would need an estimated 40 years to build up the necessary energy, and it is currently not clear how this amount of magnetic flux could be stored and inhibited from emergence from the base of the convection zone during the build-up process.

Figure 7.3 shows the observed superflares on solar-type stars (Maehara et al., 2012) and compares them to the solar flares (Crosby et al., 1993), as well as selected microflare (Shimizu, 1995), and nanoflare (Aschwanden et al., 2000) studies. Interestingly all distributions seem to be roughly represented by a common power-law.

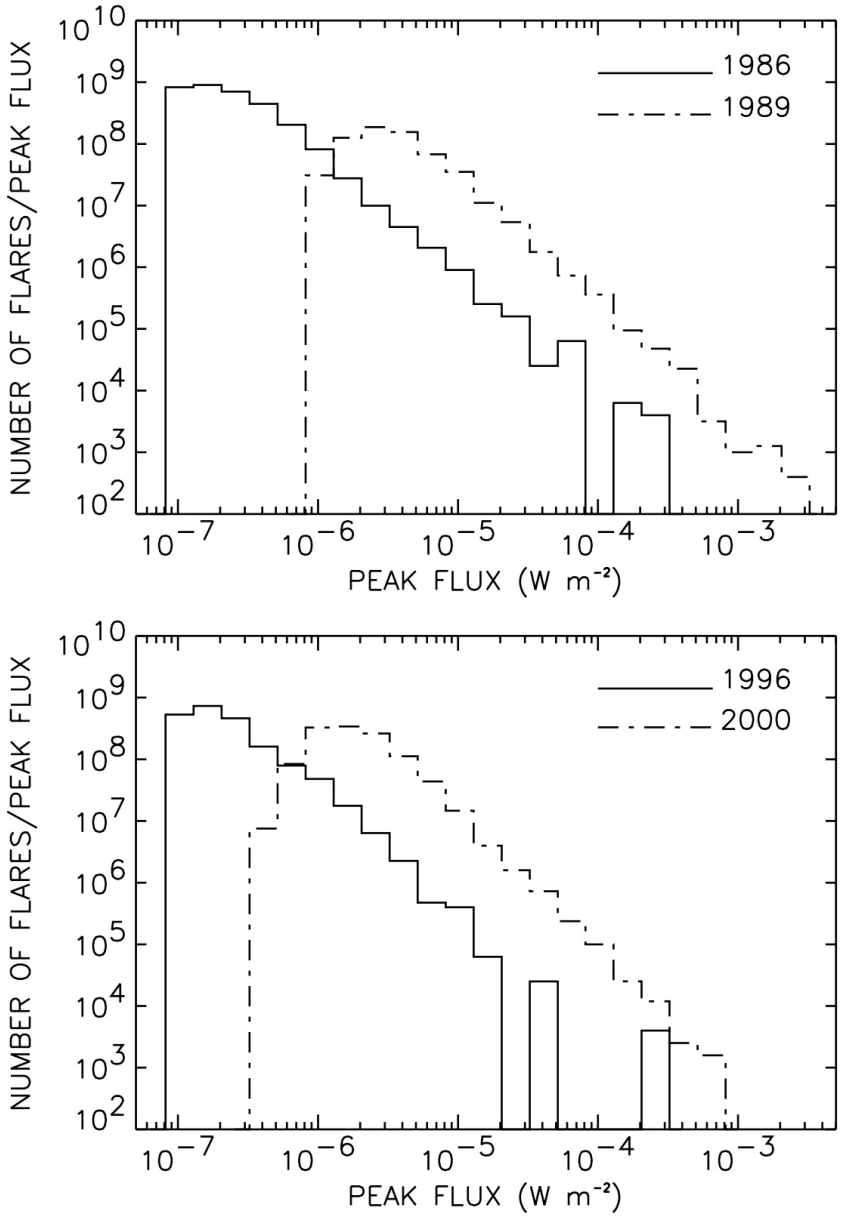

Fig. 3.5.: Flare frequency distributions as function of the peak flux calculated separately for periods of minimum (full lines) and maximum (dashed-dotted lines) activity of solar cycle 22 (top panel) and solar cycle 23 (bottom panel). From Veronig et al. (2002).

To explain the observed power-law distribution of solar flares, Lu and Hamilton (1991) first introduced the idea that the solar corona might be in a self-organized critical state that lacks any intrinsic length or time scale and would be consistent with solar flares observations at the time. They provide a sandpile as an analogous to better understand how some systems can reach such a self-organized critical state. In this gedankenexperiment, sand is added to a sandpile, which increases its slope until a critical angle is reached. Any additional sand poured over the pile will only result in a local restructuring through avalanches but keep the slope at roughly this

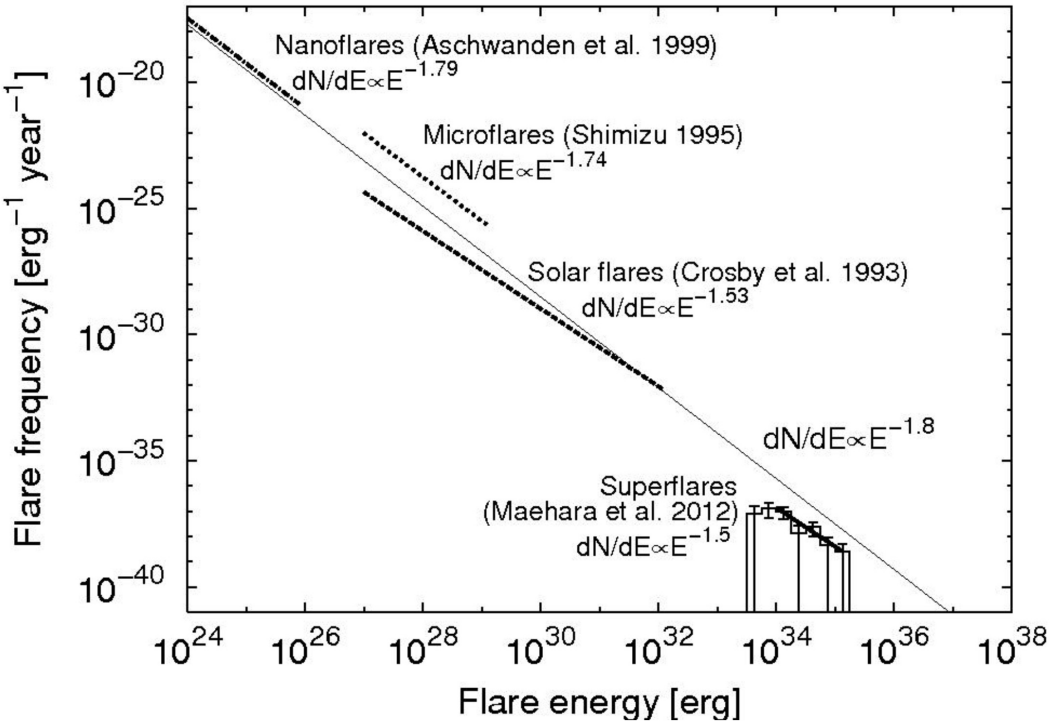

Fig. 3.6.: Frequency distribution of G-type superflares (Maehara et al., 2012) compared to solar nanoflares observed in EUV (Aschwanden et al., 2000), soft X-ray flares (Shimizu, 1995), and hard X-ray flares (Crosby et al., 1993). The thin solid line represents a power-law with index $\alpha = 1.8$. From Shibata et al. (2013).

critical value. Importantly, this resulting critical state does not depend on its history or any finely tuned parameters and enables avalanches in a wide range of sizes (from a single grain to the size of the whole system) with no characteristic length scale. The result is a power-law distribution of avalanche sizes. Any such self-organized critical state only requires the existence of a local instability that becomes active after a critical parameter is exceeded. Crossing the critical parameter threshold must also be followed by a change of the parameter at neighboring sites that can likewise cause these to exceed the critical value.

In the coronal magnetic field, this condition is fulfilled by a critical angle between adjacent field lines that must be exceeded before the stored free energy can be released. The existence of such a critical parameter means that the corona can also be driven into a self-organized critical state similar to the sandpile. Here, regions of all sizes can be on the verge of stability and produce reconnection avalanches that we observe as flares (Lu and Hamilton, 1991). The existence and exact value of such a critical parameter also have important implications for the coronal heating problem. The sheared and twisted magnetic field must be able to build up free magnetic energy until a critical amount of stress is reached that is then suddenly released. If the release mechanism switched on too early, the corona would be cooler,

and if it switched on at a higher stress level, the corona would be hotter (Klimchuk, 2006).

Energy balance considerations suggest an approximate tilt of the magnetic field at the base of the corona of $20°$ from the vertical, resulting in a misalignment angle of about $40°$ between tangled flux tubes. This matches the switch on condition of the secondary instability that sets in after the primary instability and produces intense and impulsive heating (Dahlburg et al., 2003; Dahlburg et al., 2005; Klimchuk, 2006). Additionally, the self-organized criticality model predicts that the observed power-law is unaffected by the solar cycle while the flare occurrence rate varies. This matches the discussed observations of solar flares by Crosby et al. (1993) and Veronig et al. (2002).

If the theory is correct, the classification into nanoflares, microflares, and flares may be arbitrary (as suggested by Fig. 3.6) since such a state has no preferred scale. However, this is only true if all flares originate from regions where the magnetic field is in a self-organized critical state. This does not have to be the case, and in fact, for coronal heating, the power-law of nanoflares may have to become steeper than the common power-law observed for large flares (Lu and Hamilton, 1991).

Integration of the flare occurrence rate given in Eq. 3.2 over the whole energy range (from E_{min} to E_{max}) of flares gives a function for the total energy release.

$$W(E_{min} \leq E \leq E_{max}) = \int_{E_{min}}^{E_{max}} \frac{dN}{dE} E dE = \frac{A}{2-\alpha}[E_{max}^{-\alpha+2} - E_{min}^{-\alpha+2}] \tag{3.3}$$

Hudson (1991) was the first to point out that the relative contribution of small and large flares to the total energy W critically depends on the power-law index. W diverges as $E_{min} \to 0$ if $\alpha > 2$. On the other hand, it also diverges for large E_{max} if $\alpha < 2$. However, there is a maximum energy for solar flares of about $10^{33}\,\mathrm{erg}$ due to the finite size of the Sun (Sakurai, 2017) and limits of the possible sunspot size. As discussed by Shibata et al. (2013), even larger solar flares could still be possible but have never been observed on the Sun.

Studies of large flares have shown that they do not contribute enough energy to account for coronal heating by themselves. Therefore, the basic idea of the nanoflare heating model is that the number of small events is so large compared to regular flares that together, they can provide enough energy for the million-degree temperature of the corona. Furthermore, their high frequency would provide near-constant heating, allowing the temperature to stay very stable (Sakurai, 2017).

Applied to the findings of Hudson (1991), this means that in order for small flares to contribute the majority of the total energy, the power-law has to be $\alpha > 2$. Only such a steep slope would make it possible for small events to have a significant role in coronal heating, provided they extend down to small enough energies. Otherwise, if $\alpha < 2$, the main contribution comes from larger flares, and small flares will only provide a negligible contribution to the total energy. Here it should also be noted that even if we find a steep enough slope ($\alpha > 2$), it does not guarantee a sufficient amount of nanoflares to explain coronal heating. Instead, the power-law on its own only shows if the dominant heat input comes from small or large events (Parnell and De Moortel, 2012).

Parnell and De Moortel (2012) discussed a range of flare, microflare, and nanoflare studies that where carried out near the turn of the century (Crosby et al., 1993; Shimizu, 1995; Krucker and Benz, 1998; Parnell and Jupp, 2000; Aschwanden et al., 2000; Benz and Krucker, 2002; Aschwanden and Parnell, 2002) and reported a range for the derived power-law index of $1.5 < \alpha < 2.7$. They pointed out that from these results, it remains inconclusive whether small or large flares contribute more energy to the coronal heating. The studies were done with different instruments (HXRBS/SMM, Yohkoh/SXT, SOHO/EIT, and TRACE), different detection methods were used, energies were calculated as thermal energy or radiative/conductive losses, and they also varied in other assumptions. Parnell (2004) did a systematic analysis on the influence of different assumptions regarding the flare detection and energy calculation on the power-law index and found 1200 different values in the range $1.6 < \alpha < 2.5$. Parnell and De Moortel (2012) argued that the most reasonable conclusion of these results should be that it is impossible to use direct detection of nanoflares to get exact results for the power-law. They point to studies detecting ensembles of nanoflares as an alternative.

Aschwanden (2004) also summarized the flare frequency distribution studies by Krucker and Benz (1998) and Benz and Krucker (2002) (SOHO/EIT), Parnell and Jupp (2000) (TRACE), Aschwanden et al. (2000) (TRACE), Shimizu (1995) (Yohkoh/SXT), Crosby et al. (1993) (HXRBS/SMM) and Aschwanden and Parnell (2002) (TRACE), and finds a synthesised nanoflare distribution with a power-law slope of $\alpha \approx 1.55$. Additionally he compares them to the required energy input for coronal heating. Figure 3.7 shows the results of these studies compared to the heating requirement of $P = 3 \times 10^5 \,\mathrm{erg\,cm^{-2}\,s^{-1}}$ if we assume the same power-law and an energy range from $E_{min} = 1 \times 10^{24} \,\mathrm{erg}$ to $E_{max} = 1 \times 10^{30} \,\mathrm{erg}$. The heating rate found in the observations lies about a factor of 10 below the requirement. Alternatively, the observed heating rate could also be shifted by a factor of ≈ 3 towards lower energies relative to the total energy requirement. He argued that the thermal energy of the observed events is only calculated from the observed radiation in the EUV and therefore only characterizes the energy lost due to radiation. For

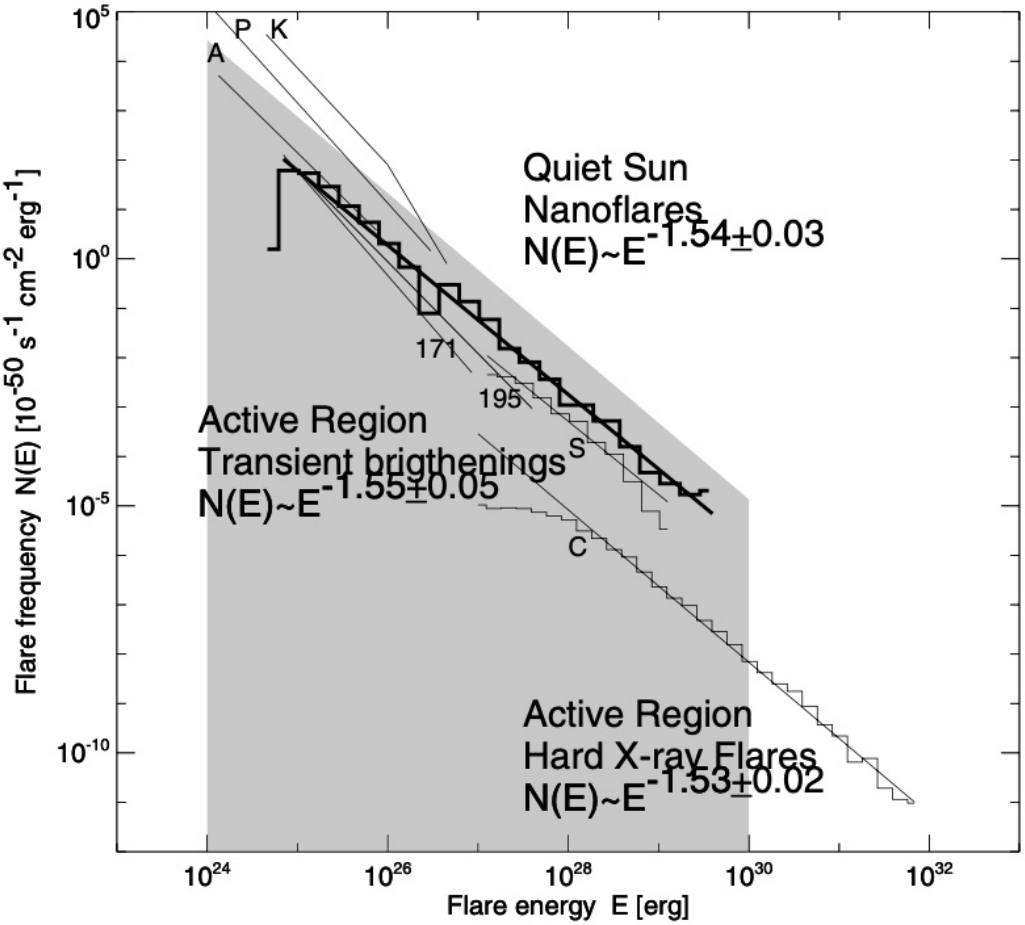

Fig. 3.7.: Frequency distributions of nanoflares in the quiet Sun, active region transient brightenings, and hard X-ray flares derived by the following studies: Krucker and Benz (1998) and Benz and Krucker (2002) (K), Parnell and Jupp (2000) (P), Aschwanden et al. (2000) (A), Shimizu (1995) (S), Crosby et al. (1993) (C) and Aschwanden and Parnell (2002) (171 and 195). Distributions of transient brightenings and hard X-ray flares are also shown. The grey area indicates the coronal heating requirement of $P = 3 \times 10^5\,\mathrm{erg\,cm^{-2}\,s^{-1}}$ for quiet Sun regions when a power-law index of $\alpha = 1.54$ (combined slope of all studies) and an energy interval of 10^{24} to $10^{30}\,\mathrm{erg}$ is assumed. From Aschwanden (2004).

the quiet Sun, this would be about a factor of 3 lower than the total energy loss of the corona. Further calculation of the total energy flux observed by the presented studies yields an observed heating rate of $0.5(2) \times 10^5\,\mathrm{erg\,cm^{-2}\,s^{-1}}$ which is about one to two-thirds of the requirement, again roughly covering the radiative losses in the quiet Sun corona. Aschwanden (2004) therefore concluded that the observed events could account for the coronal heating in quiet Sun regions if the presented distributions prove accurate. He further argued that the total observed energy flux is a better and more stable metric than the power law. Since the observed energy flux already matches the requirements, finding the actual value of the power-law index could be less critical.

It is also essential to consider where in the solar atmosphere such events may occur. The complexity of the magnetic field drops rapidly in the solar atmosphere, with more than $50\,\%$ of the flux closing down below $2.5 \times 10^6\,\mathrm{m}$ (Close et al., 2003). This suggests that most magnetic reconnection between loops probably occurs in the chromosphere (Parnell and De Moortel, 2012). However, in order to disentangle the magnetic field and keep it from building up magnetic stress indefinitely, both reconnecting flux tubes must extend above the magnetic carpet (about $5 \times 10^6\,\mathrm{m}$) (Close et al., 2003; Klimchuk, 2006). Reconnection involving a shorter carpet loop increases the tangling in the corona since it can be thought of as an additional random-walk-like movement of the footpoints (Schrijver et al., 1998). While this kind of magnetic reconnection may be necessary for the heating of the chromosphere, low-lying cold loops, and the loop footpoints, Klimchuk (2006) argues that higher altitude magnetic reconnection should have a dominant role in coronal heating. Furthermore, Klimchuk (2015) rejects the idea that chromospheric reconnection events might be a significant source of coronal plasma but points out that the generated waves may play a role in heating the corona.

Any heating model is only complete if it can also explain how the heated plasma is transported to the corona. Parnell and De Moortel (2012) described the results from 1D hydrodynamic simulations that show the evolution of plasma within a strand during the heating through an impulsive coronal event: Starting with a cool, low-density strand in equilibrium, the heat from the impulsive event is conducted rapidly along the whole strand, heating it to a maximum temperature. Density and emission change very little during this short time, leading to an underdense strand relative to the static equilibrium. During the following more prolonged evaporation phase, the event continues to supply heat which now flows into the chromosphere. This leads to an expansion and finally evaporation of chromospheric plasma that rises and fills the strand. It gets denser but remains underdense, and the emission quickly rises. Conduction starts to cool the plasma as soon as the impulsive event is over. While the emission peaks and starts to decrease again, the density continues to rise, which increases the radiative cooling until radiative and conductive cooling are balanced. In the last phase, the loop now appears overdense, and radiative cooling dominates. Density and temperature decrease slowly until reaching a threshold where catastrophic cooling rapidly reduces the density. Emission measure and the temperature finally reach their pre-event values (Parnell and De Moortel, 2012).

3.3.2 AC Heating Models

The AC/wave model was first introduced in 1948 and only included acoustic waves produced by the convective motions in the photosphere. As they propagate upwards into the chromosphere and corona, their amplitude would grow exponentially due to

the steep drop in density and form shock waves that dissipate their energy. However, it was shown that this model relied on too optimistic estimations, and it has since been extended to include magnetic waves. Since the solar atmosphere is a magnetic medium, three types of magnetic waves can form. These are fast and slow MHD waves and Alfvén waves. All three types can develop shock waves in the corona due to various phenomena and dissipate their energy (Sakurai, 2017).

However, the energy feasibility of the AC heating models is not so certain. While the solar convection does produce upwards propagating waves with an energy flux of about $1 \times 10^7 \, \mathrm{erg \, cm^{-2} \, s^{-1}}$ at the top of the convection zone (Narain and Ulmschneider, 1996), enough to account for coronal heating, most of this energy flux never reaches the corona due to the steep temperature and density gradient in the transition region (Parnell and De Moortel, 2012; Klimchuk, 2006). Acoustic and slow-mode waves can not pass sufficiently through the transition region because they form shocks and are strongly dampened, and fast-mode waves are hindered by strong refraction and reflection (Narain and Ulmschneider, 1996; Klimchuk, 2006). While Alfvén waves are best able to propagate into the corona, significant transition is only achieved in narrow frequency bands that satisfy loop resonance conditions. Sufficient flux may pass through large active region loops, but the higher resonant frequencies of smaller loops pose a problem when combined with the likely exponential photospheric power spectrum decrease at those higher frequencies (Hollweg, 1981; Hollweg, 1984; Ionson, 1982; Klimchuk, 2006). Waves created in the corona itself via the release of magnetic stress overcome these transmission problems. This may hint at a possible heating scenario with both DC and AC aspects (Klimchuk, 2006).

Historically, reconnection-based models (DC) were favored in the 1980s and early 1990s due to a lack of direct observations of waves in the solar atmosphere. However, space-based missions with EUV imagers made it possible to resolve oscillatory motions, and these observations of flows and Alfvén waves have restored the interest in the wave heating mechanisms (Parnell and De Moortel, 2012). Tomczyk et al. (2007) made the first direct observations of Alfvén waves in the coronal magnetic field using the Coronal Multi-Channel Polarimeter (CoMP) instrument in New Mexico. The estimated energy of the resolved waves was, however, not enough to heat the corona. Today the existence of waves in the corona is well documented, but it is still an open question whether they carry sufficient energy to heat the plasma to coronal temperatures (Klimchuk, 2006). AC/wave heating models will not be discussed in further detail in this thesis as it is focused on the direct observation of DC model phenomena.

4 Instruments and Data

The characteristics of Earth's atmosphere allow only the existence of two main spectral windows through which radiation can pass down to the surface, one for visible light and one for radio waves. Since the wavelengths present in the solar radiation span at least 14 orders of magnitude (from radio waves to gamma-rays), most of the contained information is lost in the atmosphere and unobtainable from ground-based observations. This especially concerns observations of the solar corona, which mainly emits in the extreme ultraviolet (EUV) and soft X-ray (SXR) wavelength domain. It has previously only been observable during solar eclipses when the moon briefly covers the bright solar disk and the faint surrounding glow of the corona becomes visible. With space telescopes, we can now explore the whole range of solar radiation and focus on any characteristic wavelength to isolate specific regions and phenomena previously invisible. However, only the simultaneous and complementary observation in multiple wavelengths allows for a complete reconstruction of the observed processes (Aschwanden, 2004), a goal realized in part through the Atmospheric Imaging Assembly.

4.1 The SDO/AIA Instrument

The data used in this study comes mainly from the Atmospheric Imaging Assembly (AIA) instrument onboard the Solar Dynamics Observatory (SDO) mission. The information provided on AIA and SDO in this chapter is extracted from the AIA instrument paper by Lemen et al. (2012): SDO, and with it the AIA instrument, orbits the Earth in a geosynchronous orbit since 11 February 2010 and is part of NASA's *Living With a Star* program. The science objectives of this mission focus on five key research areas that have shaped the design of the instrument: (1.) Energy input, storage, and release (including reconnection), (2.) Coronal heating and irradiance, (3.) Transients, (4.) Connections to geospace, and (5.) Coronal seismology.

The AIA instrument consists of four individual f/20 Cassegrain telescopes with $20\,\mathrm{cm}$ primary optics, active secondary mirrors, and a CCD sensor with 4096×4096 pixels, each corresponding to a spatial sampling of the solar disk with $0.6''$. Three telescopes can switch between different wavelength filters via a filter wheel in front of the focal plane, and the fourth telescope uses a selector mechanism to choose the

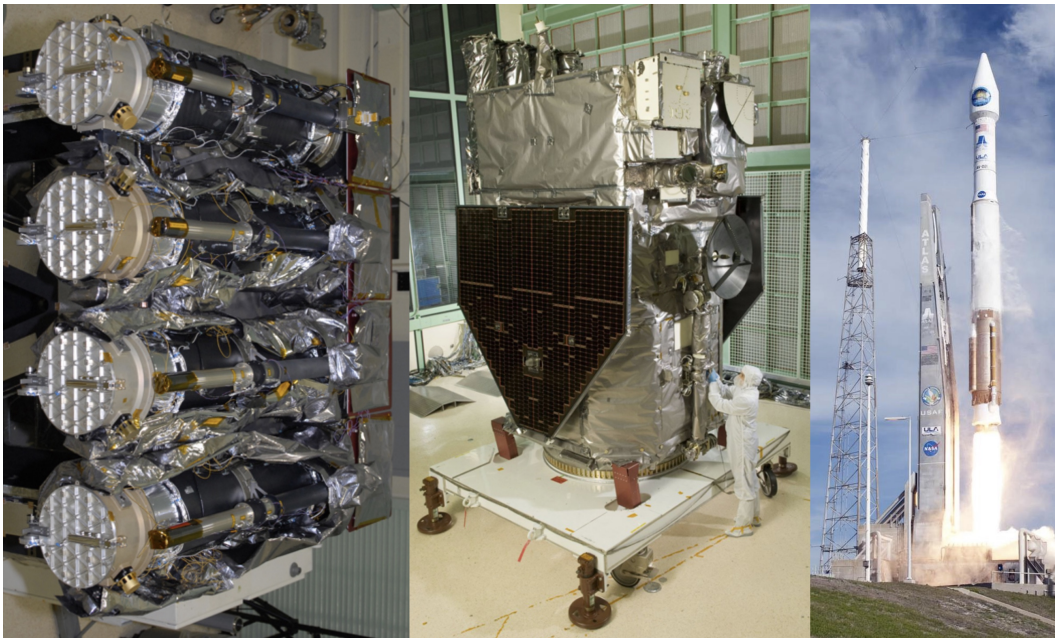

Fig. 4.1.: The four AIA telescopes (left) in the NASA Goddard Space Flight Center clean room during integration. The closed front doors protected the entrance filters from debris during launch and opened successfully in orbit. A smaller guidance telescope is mounted on each tube. SDO (middle) with a stowed solar array and high gain antenna. Parts of the four AIA telescope tubes peek out from the back of the observatory. Launch of the United Launch Alliance Atlas V rocket (right) carrying SDO to space from Launch Complex 41 on Cape Canaveral Air Force Station. From NASA/Sandra Joseph and Tony Gray[1].

observing wavelength. Every telescope tube has its own guidance telescope mounted on top that produces a constant error signal for the active secondary mirror that stabilizes the image on the CCD. Pictures of the AIA during integration, mounted on the SDO satellite, and on its way to space are shown in Figure 4.1 and a schematic layout of a telescope assembly is shown in Figure 4.2.

With this configuration, AIA produces full disc images of the Sun in multiple wavelengths with a $1.5''$ spatial resolution at a standard operating cadence of $12\,\mathrm{s}$. Narrow-band imaging using normal-incidence, multilayer-coated optics is done in seven EUV bandpasses centered on wavelengths corresponding to essential iron lines at various ionization stages and a helium line. One of the telescopes observes the Sun in the ultraviolet (UV) wavelengths $1600\,\text{Å}$ and $1700\,\text{Å}$, and in the visible for coalignment with other telescopes. Table 4.1 shows an overview of all used wavelength channels, the primary irons corresponding to each line, the region of the solar atmosphere visible in this channel, and the formation temperature. Actually, each channel is sensitive to a more extensive range of different temperatures. The

[1] sdo.gsfc.nasa.gov/gallery/itl

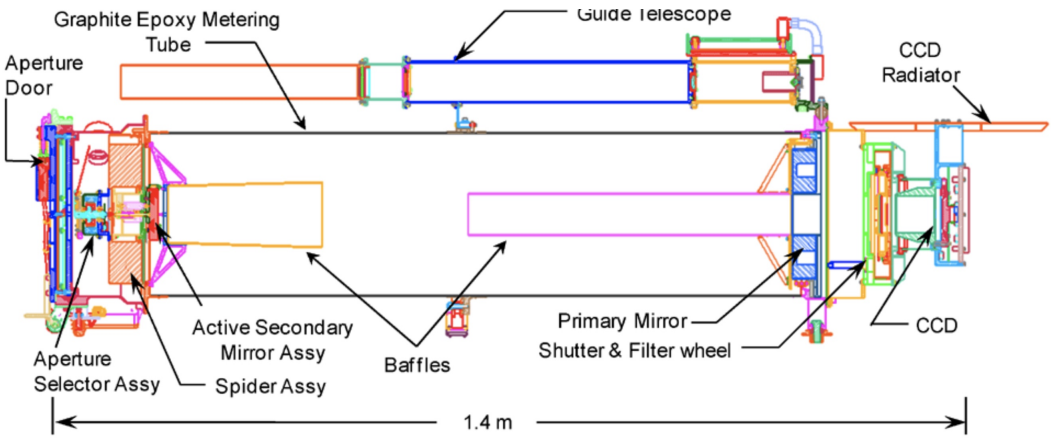

Fig. 4.2.: Schematic layout of an AIA telescope assembly. From Boerner et al. (2012).

Channel	Primary ion(s)	Region of atmosphere	Char. log(T)
4500 Å	continuum	photosphere	3.7
1700 Å	continuum	temperature minimum, photosphere	3.7
304 Å	He II	chromosphere, transition region	4.7
1600 Å	C IV + cont.	transition region, upper photosphere	5.0
171 Å	Fe IX	quiet corona, upper transition region	5.8
193 Å	Fe XII, XXIV	corona and hot flare plasma	6.2, 7.3
211 Å	Fe XIV	active-region corona	6.3
335 Å	Fe XVI	active-region corona	6.4
94 Å	Fe XVIII	flaring corona	6.8
131 Å	Fe VIII, XXI	transition region, flaring corona	5.6, 7.0

Table 4.1.: List of all AIA wavelength channel followed by the primary ion observed with this channel, the corresponding region of the atmosphere, and the characteristic temperature. From Lemen et al. (2012).

response of all six EUV wavelength channels as a function of temperature is shown in Figure 4.3.

The Helioseismic and Magnetic Imager (HMI), also on board SDO, is the second instrument used for this study. It uses the Fe I absorption line at 6173 Å to obtain Doppler shift, line-of-sight magnetic field, intensity, and vector magnetic field at the photosphere. This is done by taking a series of images at different wavelengths along the spectral line (co-tuning one Lyot element and both Michelson interferometers) and polarizations (rotating quartz waveplates) and combining them. Such an instrument differs from a spectrograph that scans across the image and is therefore known as a filtergraph (Schou et al., 2012).

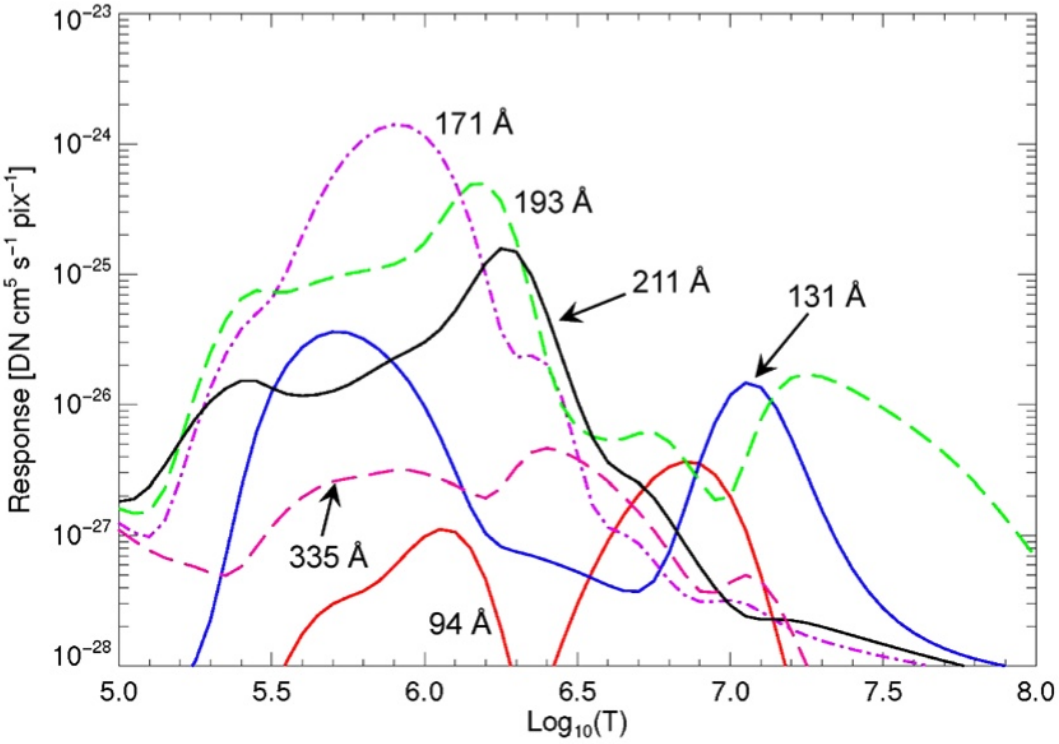

Fig. 4.3.: AIA temperature response functions for the six EUV wavelength channels with Fe ionizations as primary ions. From Lemen et al. (2012) and corresponding to Figure 11 from Boerner et al. (2012).

Gathered data from AIA and HMI is transferred from the satellite to ground stations in New Mexico and further sent to Stanford University Campus, where they are stored as level 0 data in the Joint SDO Operations Center (JSOC). Here images are processed to level 1. This includes the removal of over-scan rows and columns produced by the CCD, the removal of a dark image to account for the digital offset of the camera, read noise of the CCD and dark currents, the application of a flat-field correction of detector non-uniformities, the correction of individual permanently bad pixel, and the removal of spikes produced by energetic particles. Finally, images are flipped to have solar north at the top. These level 1 data can be exported as FITS files from the JSOC website[2].

Level 1.5 processing takes this a few steps further. All images are rotated to have solar north at 0° at the top of the image. This corrects for the slight difference in roll angle between the four different telescope tubes. The second correction accounts for the slight difference in focal length between the telescopes and scales the images to precisely $0.6''$ per pixel. Finally, images are aligned to have the Sun's center precisely at the center of the image. Since we will combine the information of six EUV wavelengths for the differential emission measure analysis, level 1.5 data preparation is crucial to ensure that all pixels overlap perfectly.

[2] http://jsoc.stanford.edu/ajax/lookdata.html

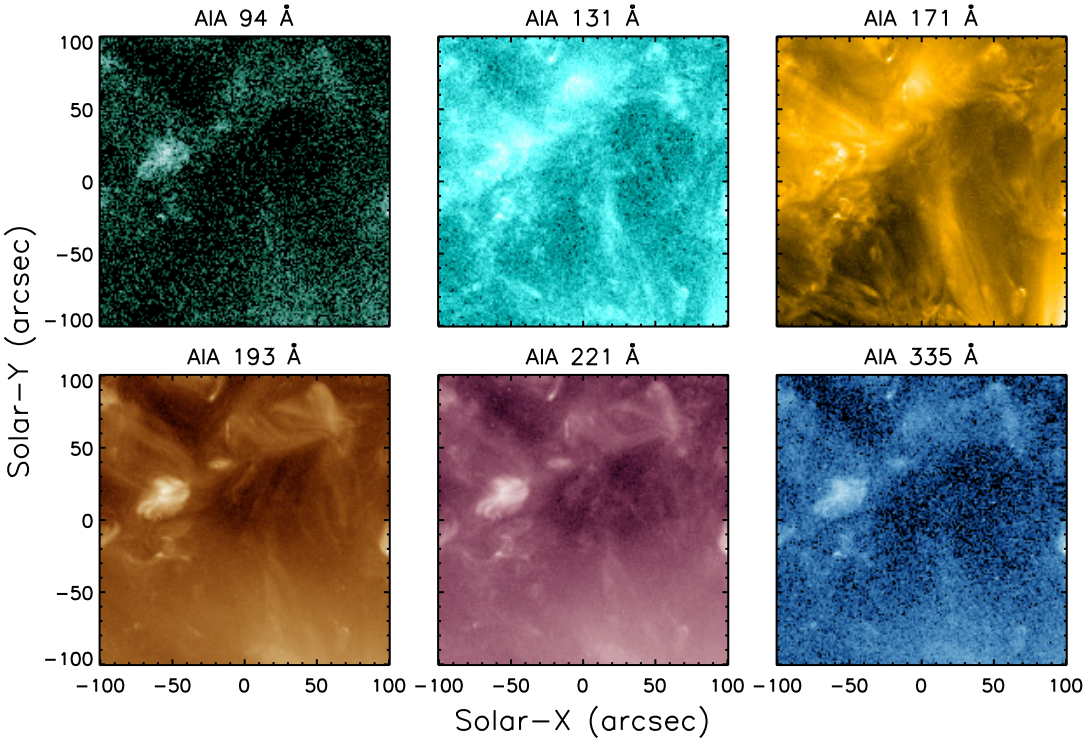

Fig. 4.4.: Images in each of the six used EUV wavelengths taken at the beginning (08:00UT) of the one hour long test data set from 01 February 2011.

4.2 Data

For the development of the event detection method presented in chapter 5, a test dataset was used. It consists of a series of AIA EUV images in the six filters required for the differential emission measure (DEM) calculation: 94, 131, 171, 193, 211 and 335 Å. All images were cropped to an $200''$ times $200''$ field of view at the center of the solar disc. The total observation time was one hour starting at 08:00UT on 01 February 2011, and the full cadence of 12 s was used. This resulted in a total of 1800 images contained in this test dataset. Figure 4.4 shows the first image during this series for each of the six wavelengths.

For the complete solar cycle analysis, multiple datasets were chosen for each year, starting in 2011 and ending in 2018. From late 2018 onwards, the DEM code produced consistently bad results. This is due to the strong in-space degradation of several AIA filters that is not fully recovered by the correction functions. Problems arise since the DEM needs a high accuracy in the counts measured in the different filters in order to reliably reconstruct the temperature-dependent emission. Data before 2011 was also found unusable for the analysis. To get a continuous distribution of data during each year, suitable data sets were searched for in February,

April, August, and November. Starting at the beginning of each month, a desired $400''$ times $400''$ field of few at the center of the solar disk was checked for quiet sun regions. Such a region had to pass the following criteria for a continuous span of two hours. Otherwise, the search continued at a later time.

- No active regions inside the region of interest, since in this study we want to investigate the nanoflare distribution in the quiet Sun region. Thus we have to ensure similar target regions for all data sets. We further note that the method developed to detect nanoflares is not capable of accurately representing large-scale events present in active regions, leading to unwanted effects.

- No pronounced coronal holes filling large areas of the observed field of view. First, as stated above, we are interested in similar target regions of the quiet Sun. Second, missing data and low count numbers in these regions hinder the accurate reconstruction of the DEM, and subsequently, the density and temperature. Smaller dark areas visible were allowed and did not affect performance.

- No (large) flares on the whole solar disc during the full time of the observation. Very bright areas can reduce the AIA exposure time, leading to low count numbers in quiet sun regions of the same image and consequently an increase in bad or missing data.

All criteria were checked before downloading using the web version of Helioviewer[3]. $171\,$Å images were mainly used to identify active regions in combination with the included cataloge. $193\,$Å images were used for the identification of coronal holes present in the region of interest. The absence of large flares during the whole two hour period was verified through the integrated event timeline. A collection of the first images for each dataset can be seen in Figure 4.5 for the $171\,$Å and in Figure 4.6 for the $193\,$Å images. Figure 4.7 shows images taken at the hotter $211\,$Å line and HMI magnetograms from the beginning of each dataset are shown in Figure 4.8. The three remaining lines at 335, 94 and $131\,$Å are shown in the appendix in Figures A.1, A.2, and 4.7, respectively.

[3] https://www.helioviewer.org

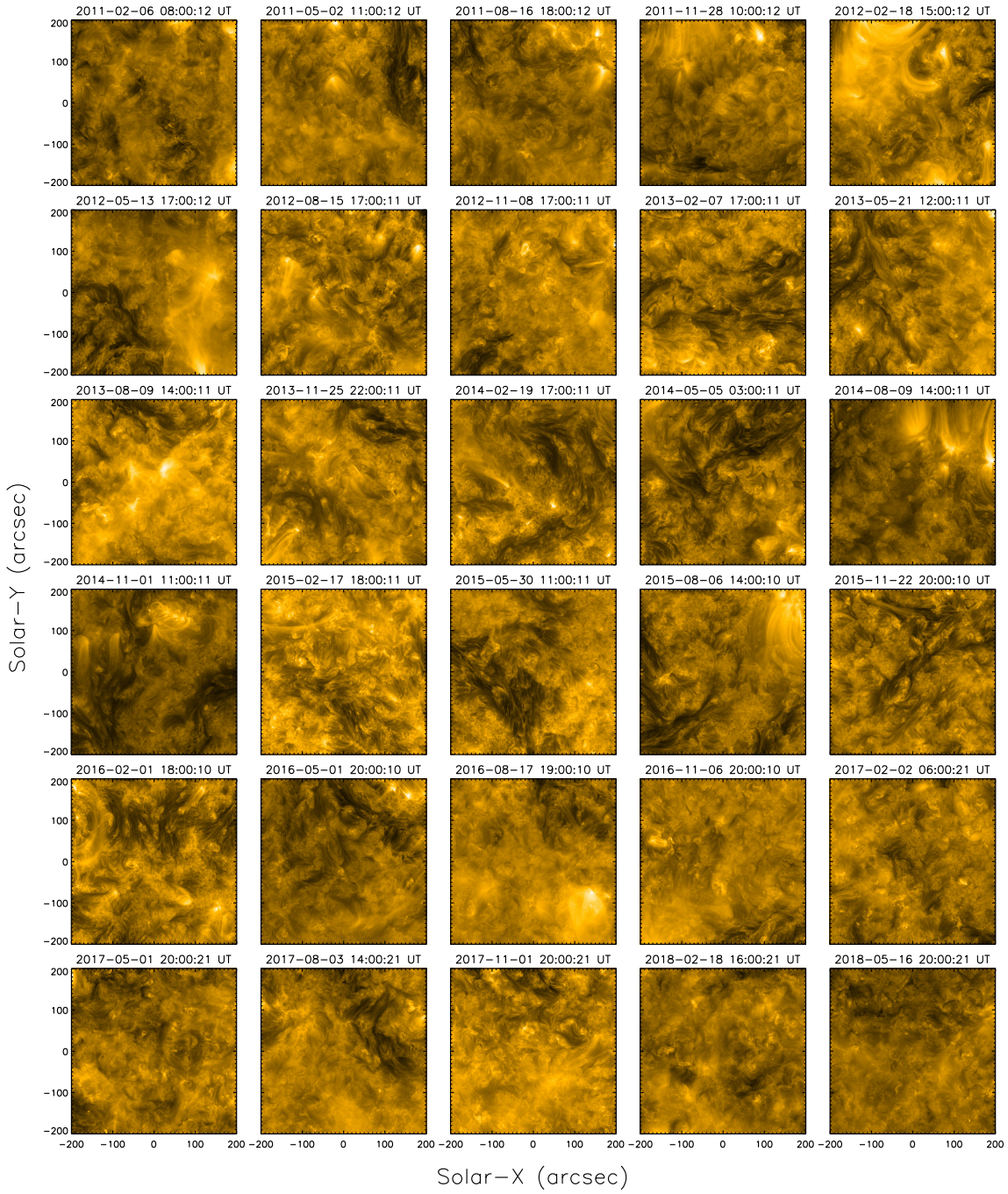

Fig. 4.5.: The first AIA 171 Å image from each data set used for the study. The start of the observation time is displayed above each image. The total data sets consist of all images taken during the interval of two hours following the shown images.

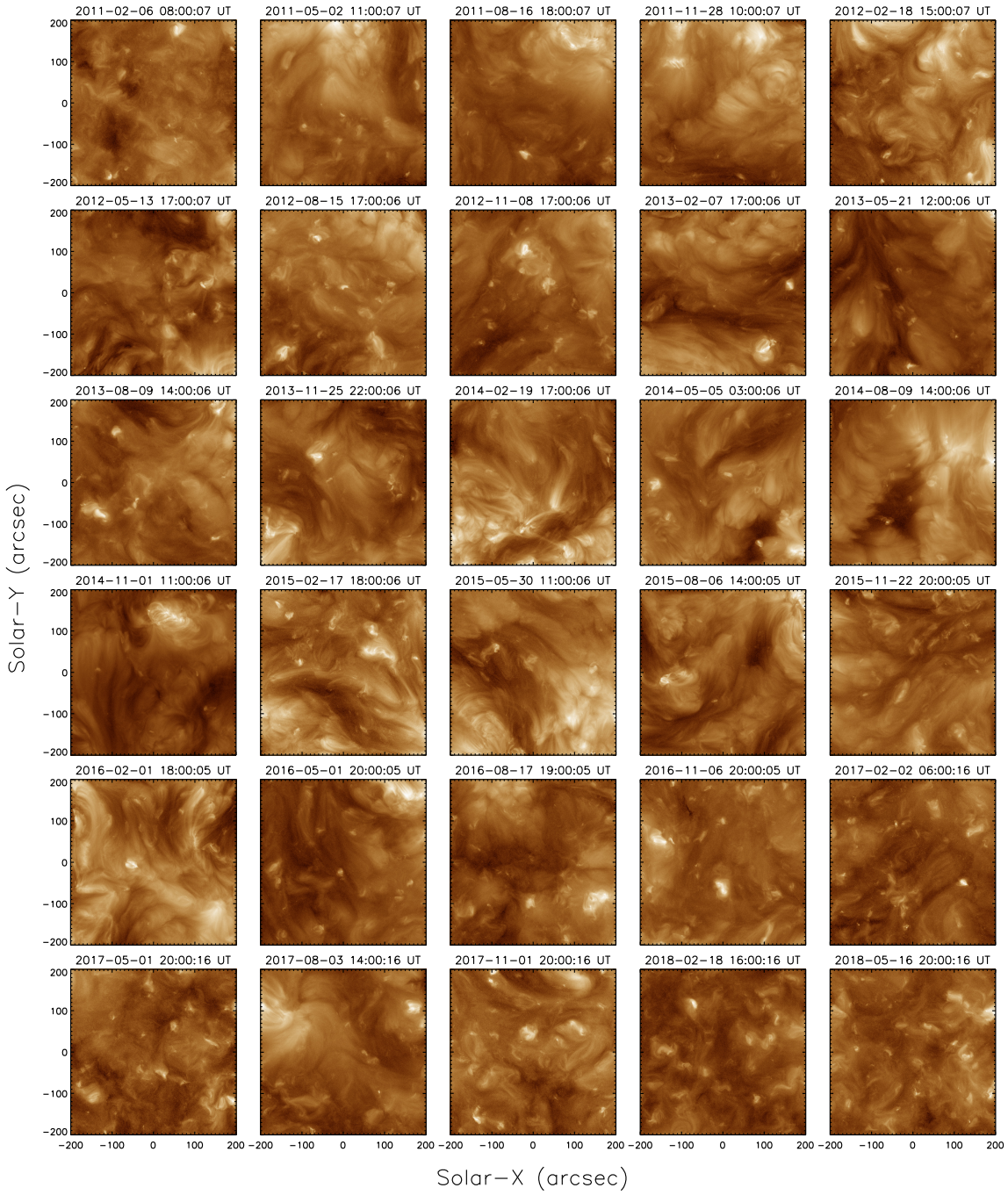

Fig. 4.6.: First AIA 193 Å image from each dataset used for the study. The start of the observation time is displayed above each image. The total data sets consist of all images taken during the interval of two hours following the shown images.

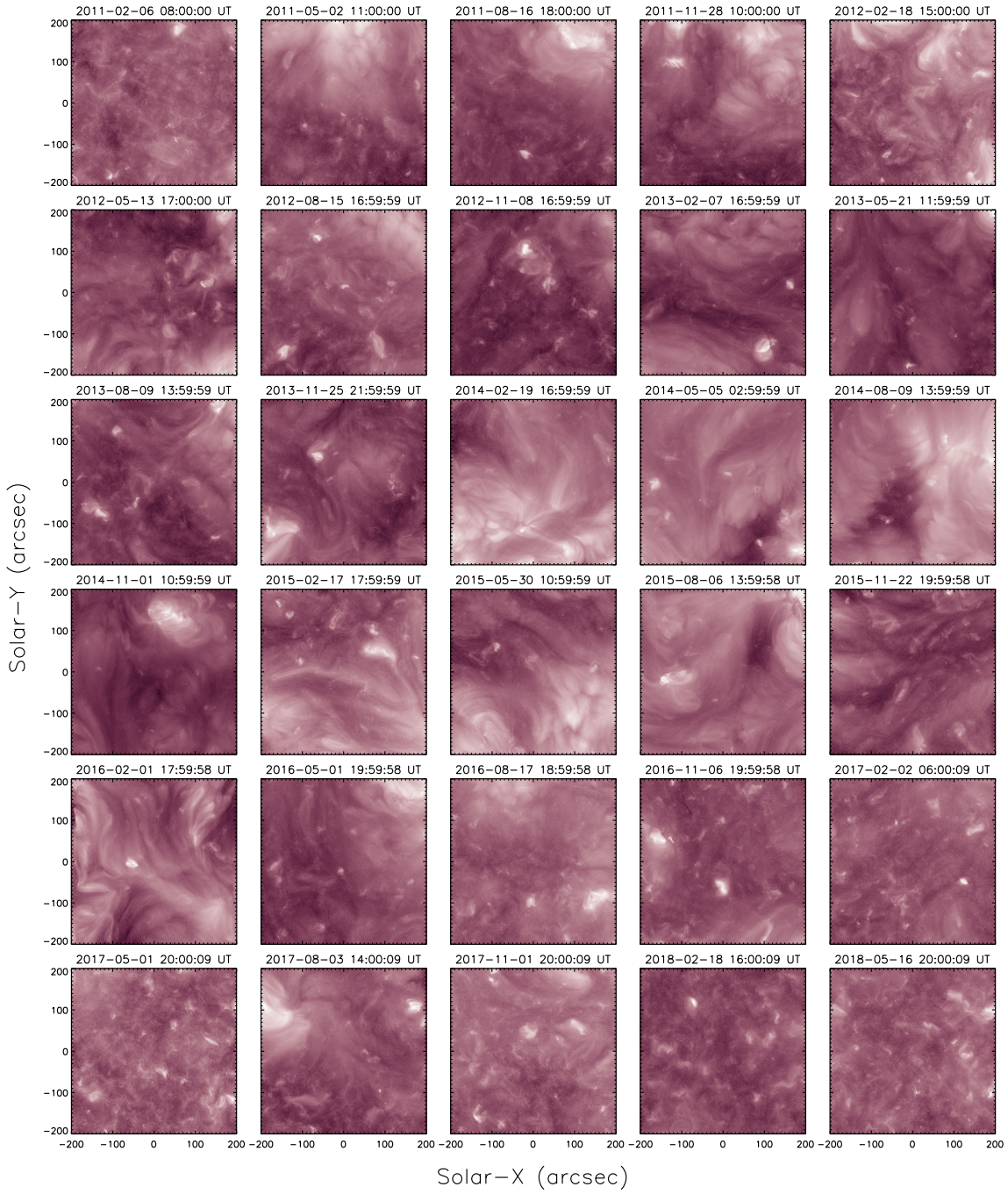

Fig. 4.7.: First AIA 211 Å image from each dataset used for the study. The start of the observation time is displayed above each image. The total data sets consist of all images taken during the interval of two hours following the shown images.

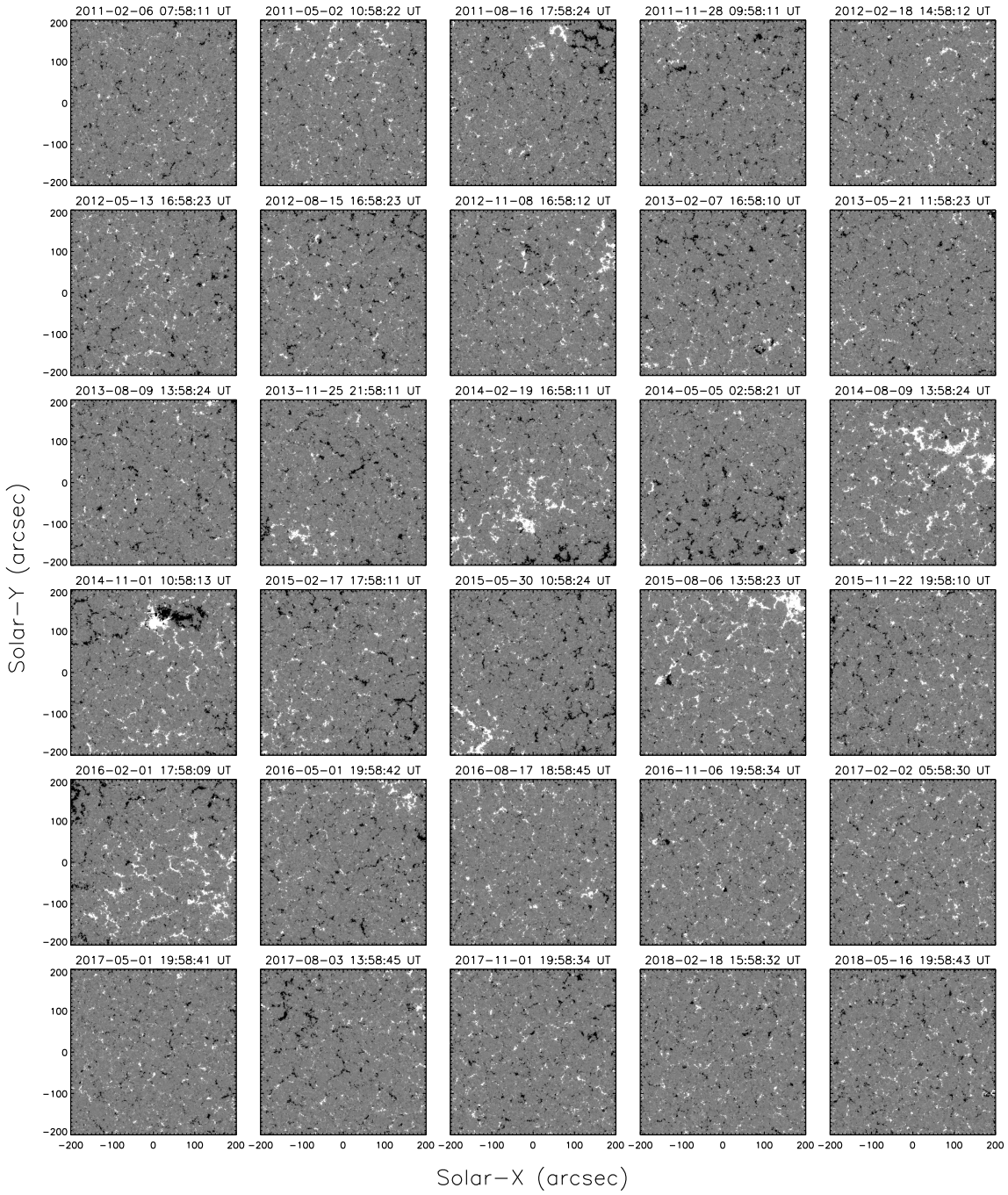

Fig. 4.8.: HMI line-of-sight magnetic field map from the beginning of each dataset used for the study. Images are saturated at $\pm 50\,\mathrm{G}$. The start of the observation time is displayed above each image.

5 Methods

This chapter describes the individual steps performed to extract a nanoflare frequency distribution from a series of AIA EUV images and discusses critical choices made in each step. Section 5.1 consists of an overview of the differential emission measure (DEM) analysis and introduces the specific code used for this study. The essential data preparation, listed in section 5.2, creates AIA images suitable for this DEM code and marks data with potentially inconsistent results. The final image binning reduces the number of pixels that deliver no DEM results and the needed computation time. In section 5.3.1, we discuss these effects for a selection of different binning factors. The final DEM results are further dependent on several parameters that have to be provided by the user. We focus on the effects of the chosen temperature range and the number of bins and present the results in section 5.3.2. The DEM profiles obtained for each "super-pixel" (i.e. after binning) allow a straightforward calculation of the emission weighted mean temperature and the total emission measure (EM). Section 5.4 describes the subsequent thermal energy calculation from changes observed in the temperature and EM time series. We developed an adapted method that searches for events directly in each pixel's thermal energy and can be tuned for different requirements. Section 5.5 compares different event definitions and search algorithms to demonstrate their respective strengths and weaknesses. The standard deviation of pixel fluctuations has proven to be a practical basis for the required energy threshold. Finally, bordering active pixels are combined to allow for accurate detection of larger event areas.

5.1 Differential Emission Measure

The differential emission measure (DEM) expresses the amount of plasma along a line of sight as a function of temperature and is therefore expressed in units of $\mathrm{cm}^{-5}\,\mathrm{K}^{-1}$. Using AIA data, it can be calculated for single pixels and temperature bins ΔT using the set of measured intensities (I) in units of $\mathrm{DN/s}$ from the six EUV wavelengths channels 94, 131, 171, 193, 211 and $335\,$Å. Additionally, the instrument's temperature response function (TR) of each AIA EUV channel has to be known to solve the following set of equations (Su et al., 2018).

$$I(\lambda_i) = \sum DEM(T) \cdot \Delta T \cdot TR(\lambda_i) \tag{5.1}$$

with $i = 1$ to 6 for the different EUV wavelength filters of AIA. However, these equations are challenging to solve and do not have a unique solution. The observed flux is a convolution of the original DEM with both the involved emission processes and the instrument's response (Hannah and Kontar, 2012). Multiple codes utilizing different approaches try to reconstruct an accurate DEM from AIA EUV images. Each has its strengths and weaknesses depending on the exact use case. One common problem is that the DEM is often not well constrained by AIA data alone, primarily due to the low response at high temperatures. Consequently, the computations tend to overestimate the amount of hot plasma ($\sim 6\,\mathrm{MK}$ to tens of MK) (Su et al., 2018). For the DEM analysis performed in this study, we used the regularized inversion algorithm developed by Hannah and Kontar (2012), in the following abbreviated as HK.

While DEM reconstruction is a complicated and computationally expensive task, the acquired information allows for a wide range of different analyses. For example, a whole range of other essential plasma parameters can be calculated from a successfully extracted DEM. These include the emission measure (EM) in a specific temperature range (ΔT)

$$EM_T = DEM(T) \cdot \Delta T \tag{5.2}$$

the emission-measure-weighted mean temperature

$$T_{EM} = \frac{\sum(DEM(T) \cdot \Delta T \cdot T)}{\sum(DEM(T) \cdot \Delta T)} = \frac{\sum(EM_T \cdot T)}{\sum EM_T} \tag{5.3}$$

the estimated plasma density, thermal flux, and thermal energy (Su et al., 2018).

The input required by the HK DEM code includes a map structure of six AIA EUV wavelength channels (94, 131, 171, 193, 211 and $335\,$Å) in order, the edges of the desired temperature bins, and the AIA temperature response function. The response of the different AIA wavelength channels degrades over time and will also be different for each channel. Therefore, we always calculated the correct response function for the DEM calculations using the *aia_get_response* procedure for the beginning of the current observation series.

5.2 Data Preparation for DEM Analysis

FITS files of the desired EUV wavelengths 94, 131, 171, 193, 211 and 335 Å were downloaded from JSOC[1] as level 1 data at the full cadence of 12 seconds. Either as full images or using the available *im_patch* processing procedure to extract a tracked subframe before downloading. Depending on the requested field of view, the latter method can greatly reduce download time and data size while leaving the data itself unchanged at level 1. The same subsequent data processing steps can therefore be applied to both the full-size images and the subframes. Downloading only the needed part of the images has proved to be especially useful for the large solar cycle data set. The data preparation and analysis described in the following sections utilize the SolarSoftWare[2] (SSW) data analysis environment built on the IDL programming language.

SSW's *read_sdo* procedure first obtains the wavelength and the exact observation time of all images included in a data set. Each AIA 193 Å image found is used as a seed for building a complete EUV map structure. The algorithm searches for images of the other five required wavelengths with the minimum difference in observation time relative to the reference image. The result is a series of ordered groups centered around the observation times of each included 193 Å image. If the time difference between the reference image and any of the other five images within its group exceeds ten seconds, the final DEM code result is flagged to alert the user of possible instabilities in the DEM results. An exposure time of fewer than 1.9 seconds in any of the six images also generates flagged results. Such low exposures are typically the result of the automatic exposure time control during flares. The resulting low count rate from the quiet sun leads to high uncertainties in the DEM result. We either omitted occasional flagged DEM results in a data set in the further analysis or searched for a new data set if extended parts of the observation series returned flagged results. Lastly, the six images are checked for the *bad data* keyword, and further calculation for this group is completely skipped if found in at least one image.

The first data processing step reads the images of accepted groups using the *read_sdo* procedure and then applies all necessary transformations required for data level 1.5 within the *aia_prep* procedure. The images are first cropped to dimensions exceeding the desired field of view by 50″ in the solar-x-direction and 10″ in the solar-y-direction to reduce data size. The *drot_map* procedure subsequently removes the effect of the solar differential rotation from the images, with the very first 193 Å image of the whole data series serving as a reference. Final cropping by the *sub_map*

[1] http://jsoc.stanford.edu/ajax/lookdata.html
[2] https://sohowww.nascom.nasa.gov/solarsoft/

procedure produces fully prepped images that could be passed to the DEM code. To improve the signal-to-noise ratio and thus the DEM results, we have added an additional step that bins the images according to a specified binning factor. Section 5.3.1 discusses the effectiveness of different factors.

5.3 DEM Code Settings

5.3.1 Spatial Binning

The HK DEM code version used requires the pixel values in all six wavelength channels to be greater than $0\,\mathrm{DN}$. Otherwise, a pixel gets omitted during the calculation. This requirement drastically reduces the number of pixels suitable for DEM calculation. Especially the $94\,$Å channel contains very low count numbers in quiet sun regions, and after processing to level 1 data, many pixels hold negative values. In the first $94\,$Å image of the test data set $37\,\%$ of all pixels have a value less or equal to $0\,\mathrm{DN}$ and can therefore not produce a DEM result. The average pixel value of the whole image is just slightly above $0\,\mathrm{DN}$ with a mean of $0.45\,\mathrm{DN}$. In the first $335\,$Å image, only $4\,\%$ of pixels are not suitable for DEM calculation and will mostly match the regions already heavily affected by the $94\,$Å image. The $131\,$Å image still has a few pixels with low count rates, but they account for only $0.01\,\%$ of the total number. 171, 193 and $211\,$Å images contain no pixels with low count rates.

Clusters of $N \times N$ pixels in the AIA maps can be binned together before the DEM calculation. The bin-factor N reduces the resolution of the images by N and consequently the total number of pixels by N^2. Binning also reduces processing time for the DEM code by about the same factor as the reduction in pixels. Furthermore, it decreases the number of pixels unusable for DEM calculation. A binned pixel holds a value equal to the mean of all combined pixels, which should tend towards a positive number for larger bin-factors. At the same time, the signal-to-noise ratio is enhanced by about N through spatial binning since the count rate increases by N^2 while the Poisson error only increases by N. Combined, fewer negative pixel values and enhanced signal-to-noise ratio result in fewer missing solutions and more stable DEM results.

Figure 5.1 shows the first AIA $94\,$Å image of the test data set with different bin-factors ($N = 2$, 4, 6, 8 and 10) applied, together with a map of the corresponding pixels that did not return a DEM solution. A bin-factor of $N = 2$ yields still large areas with missing DEM data. Especially regions with an overall lower count number are affected. With a bin-factor of $N = 4$ the missing data is already greatly reduced,

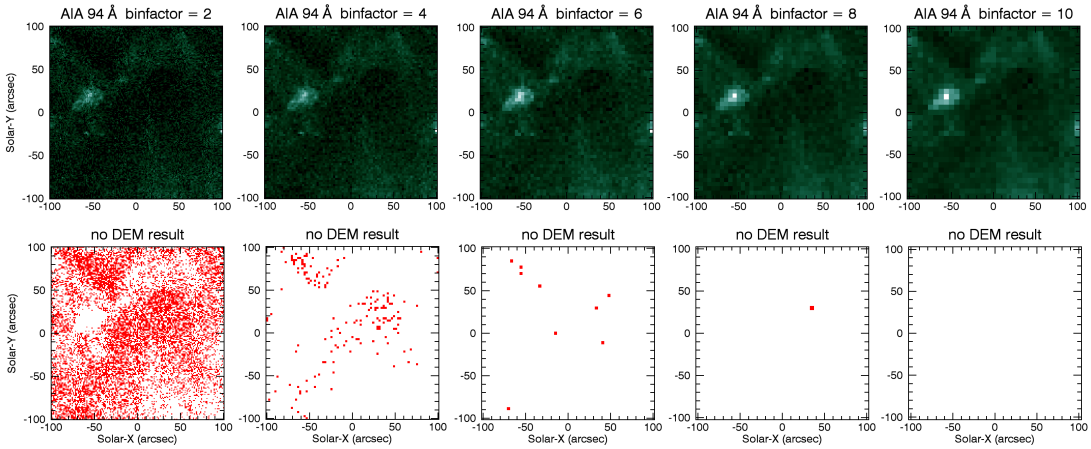

Fig. 5.1.: The top row shows the first AIA $94\,\text{Å}$ image from the test data set with different bin-factors ($N = 2$, 4, 6, 8 and 10) applied. In the bottom row locations of pixels with values less or equal to zero are shown in red.

and only the darkest regions remain affected. When we increase the bin-factor further to $N = 6$ only a few bad pixels remain. At $N = 8$ there is almost no missing data left, and $N = 10$ has non at all.

While a larger bin-factor can significantly reduce the number of unusable pixels in the DEM code analysis, the biggest drawback is the loss of spatial resolution and, consequently, a possible reduction of sensitivity for events smaller than the dimensions of the binned pixel. While some binning seems necessary to get reliable DEM results, it should be used cautiously since the detection of the smallest possible events is a critical aspect of nanoflare studies. As a compromise, we used the bin-factor of $N = 4$ for the final analysis performed in this study. It strikes a good balance between faster computation and reduction of the number of unsuitable pixels on the one hand and the capability to still detect small events on the other hand.

5.3.2 Temperature Range and Binning

The temperature bins passed to the DEM code also influence the results. We calculate the edges of the bins by evenly distributing the user-specified number of bins between the defined upper and lower bound on a logarithmic temperature scale. The importance of temperature range and number of bins can therefore be analyzed separately.

First, we investigated the effects on the DEM results when changing the temperature range. The lower temperature limit was held constant at $0.2\,\text{MK}$ and only the upper temperature boundary was set to different values of 5, 8, 10 and $15\,\text{MK}$.

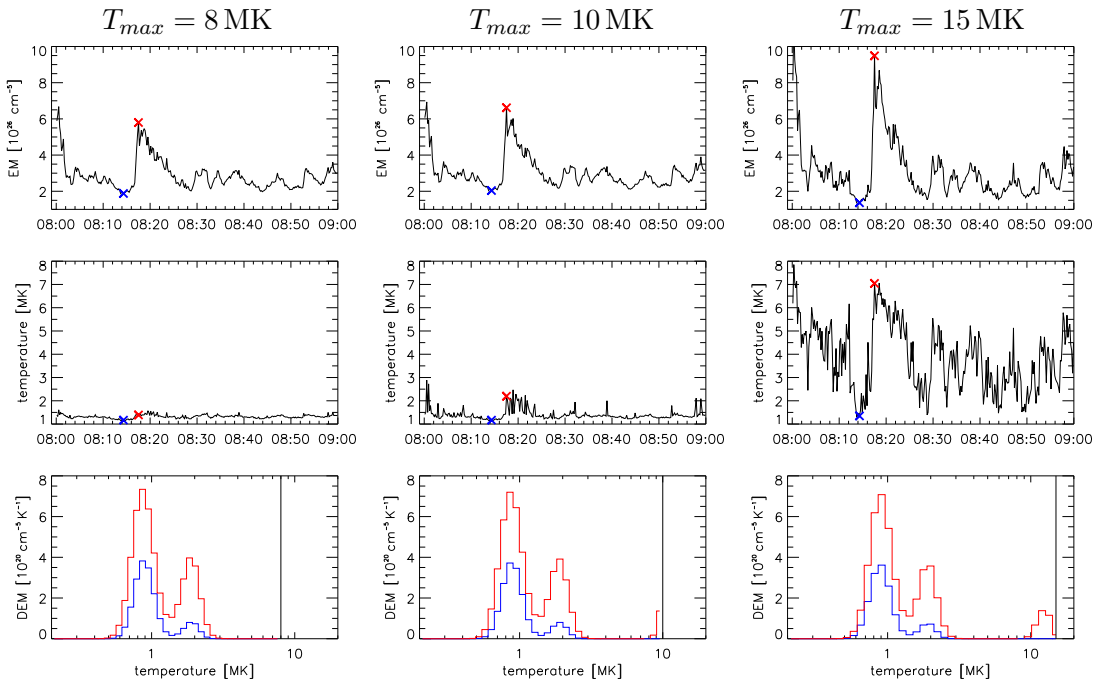

Fig. 5.2.: DEM results of the same pixel at about $x = -23''$ and $y = 84''$ in heliocentric coordinates but with different upper limits for the used temperature bins. The time evolution of the reconstructed total emission measure (EM) and EM-weighted mean temperature over one hour are shown in the top and middle panels, respectively. The bottom panel shows the DEM profile at the two marked time steps, before and during an event. The left column shows results for an upper limit of $8\,\mathrm{MK}$, the middle column for $10\,\mathrm{MK}$, and the right column for $15\,\mathrm{MK}$. All temperature ranges were divided into 40 bins evenly spaced along the logarithmic temperature axis.

The number of bins was also constant at $40\,\mathrm{bins}$. Figure 5.2 shows the result for a selected pixel of the test data set at $x = -23''$ and $y = 84''$ in heliocentric coordinates. The most noticeable change is the increased DEM profile above $10\,\mathrm{MK}$ for the higher temperature limits. It is present primarily during sharp rises of the EM and can completely disappear in low EM phases. In more energetic regions, it is visible at all times during the observation. Consequently, the weighted temperature increases when the DEM code receives a temperature limit above $10\,\mathrm{MK}$. Additionally, this increases the temperature change observed during an event. In the EM time series, the peak value nearly doubles. Simultaneously, the background level remains similar to values derived from lower temperature limits, leading to an increase of the EM change during the event. Combined, both effects would lead to an overestimation of the involved energy. We will, therefore, treat any DEM results at temperatures above $10\,\mathrm{MK}$ as possible artifacts of the DEM calculation and not as a physical reality. To suppress any influence from possible false results at high temperatures, we have set the upper limit at $8\,\mathrm{MK}$ for the rest of our nanoflare study.

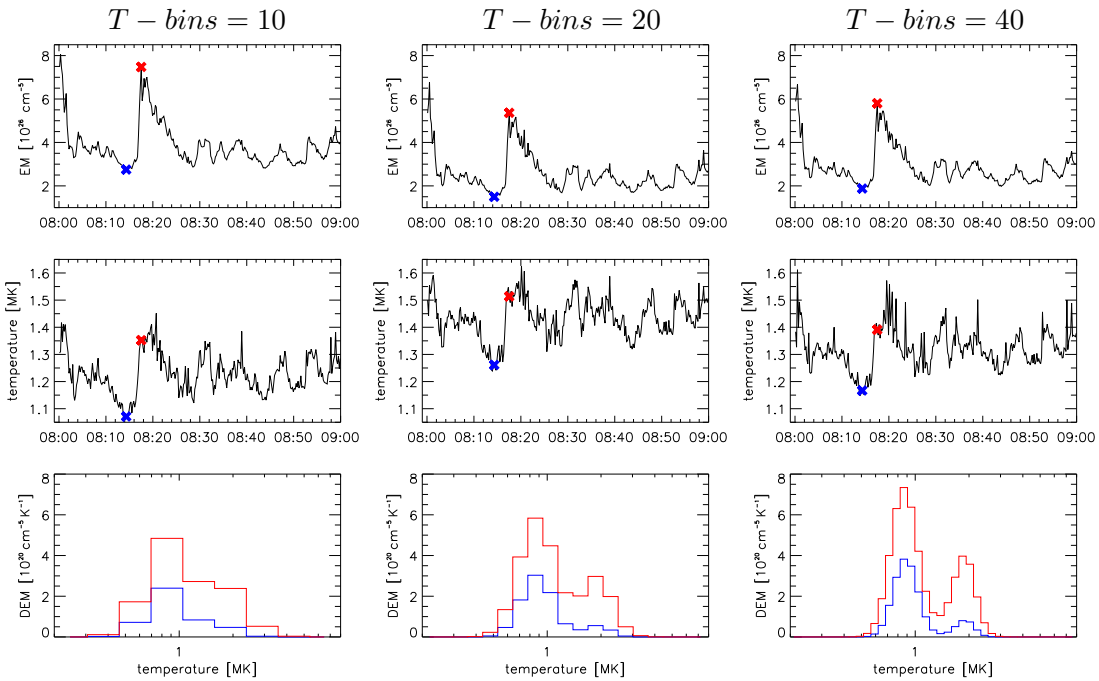

Fig. 5.3.: DEM results of the same pixel at about $x = -23''$ and $y = 84''$ in heliocentric coordinates with the same temperature range (0.2 to $8\,\mathrm{MK}$) but with a different number of temperature bins. Evolution of the total emission measure (EM) and EM-weighted mean temperature are shown in the top and middle panels, respectively. The bottom panel shows the DEM profile at the two marked time steps, before and during an event. The left column contains results from 10 bins, the middle from 20 bins, and the right from 40 bins spaced equally in logarithmic temperature.

Next, we analyzed the influence of the number of temperature bins on the DEM results. The temperature range has been held constant at the previously determined interval of 0.2 to $8\,\mathrm{MK}$. Since only the mean EM and EM-weighted mean temperature will be used to calculate an event's energy, a high temperature resolution in the DEM results might be unnecessary. Figure 5.3 shows the differences between selected numbers of 10, 20 and 40 temperature bins, again for the pixel at $x = -23''$ and $y = 84''$ inside the test data set. No significant quality in the EM and weighted temperature evolution is lost when reducing the number of bins from 40 to 20. However, a significant shift in the temperature level with unexplained cause can be seen. Since we are only interested in EM and temperature changes (difference between peak and minimum) for the event energy calculation, this change does not have much effect on the calculated event energy. Reducing the number of temperature bins to half its original value (40 to 20) also decreases the necessary computing time for the DEM calculation by about a factor of two. A further reduction to 10 temperature bins is also shown but was decided to be a too large tradeoff. While EM and temperature evolution look similar, the DEM loses much detail that could be useful for future analysis. Therefore, 20 temperature bins were used in the remaining study.

5.4 Energy Map Time Series

The following equation describes the change in thermal energy during an observed event.

$$E_{th} = 3k_B \Delta T \sqrt{\Delta M A s_{eff}} \tag{5.4}$$

where k_B is the Boltzmann constant, ΔT the temperature change, ΔM the increase in emission measure, A the observed area of the event, and s_{eff} a model parameter representing the line of sight thickness (Benz and Krucker, 2002). If the increase in emission measure and temperature during all events are known, equation 5.4 gives a reasonable estimate on their relative energy released during the event. However, the calculated energy is subject to a number of assumptions and consequently quite uncertain, as discussed by Benz and Krucker (2002).

In past nanoflare studies (see Benz and Krucker (2002), Aschwanden (2004), and Parnell and De Moortel (2012) for a selection), the EM and temperature evolution in each pixel was determined using a simple line ratio, with data provided by either EUV Imaging Telescope (EIT) (Delaboudinière et al., 1995) onboard the Solar and Heliospheric Observatory (SOHO) or the Transition Region and Coronal Explorer (TRACE) (Handy et al., 1999). A common method developed for the detection of nanoflares first searches the time evolution of EM(t) for local peaks. Its value is then compared to a preceding minimum or a defined background level. If the observed difference exceeds a defined threshold, the peak is accepted as an event, and the energy can be calculated from the observed change in EM and temperature using equation 5.4. Benz and Krucker (2002) observed that contrary to previous assumptions, it is the change in EM that primarily determines the resulting energy and not the change in temperature.

For this study, a slight variation of this procedure has been used. We first calculated for each pixel an energy time series by using equation 5.4 but with the absolute values of EM and temperature determined through the DEM analysis. Missing data points resulting from missing or flagged DEM results were replaced by interpolated values from the pixels energy evolution. This procedure allows us to search the energy evolution for local peaks directly and immediately determine the event energy from the difference between the identified event peak and a preceding minimum. Section 5.5 explains the exact process in more detail. Figure 5.4 displays an example of EM and weighted temperature results from the DEM analysis and the calculated energy map.

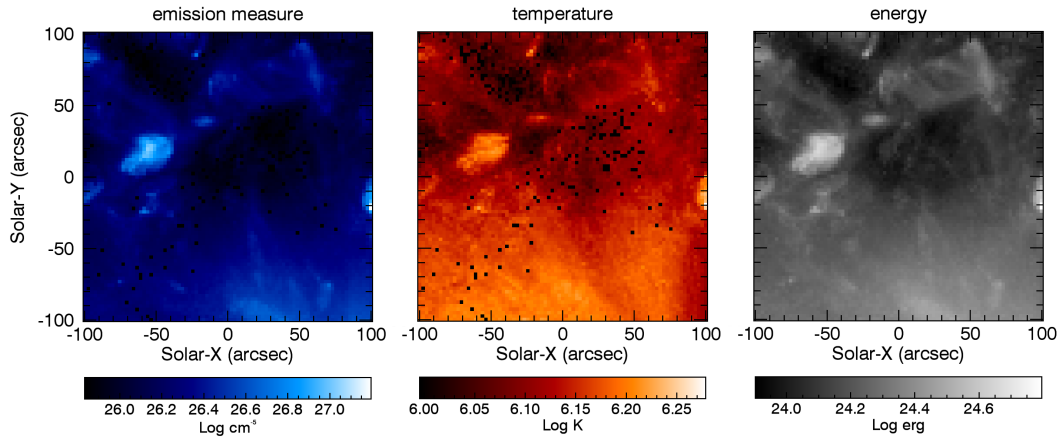

Fig. 5.4.: Emission measure map (left), temperature map (middle) and thermal energy map (right) at the beginning of the test data set. A few missing pixels without DEM results are visible in the EM and temperature maps. In the energy map these missing pixels have been removed by temporal interpolation.

Figure 5.5 shows the EM and temperature evolution derived for a selected pixel and the calculated energy time series. It confirms that the EM dominates all changes in the energy evolution. We can consequently expect to find the same local peaks whether we search in the EM or directly in the energy curves. However, the energy map simplifies the event search by first merging all relevant data. This reduces the complexity and makes it possible to efficiently define a threshold on the event energy itself that reflects the combined noise fluctuations from EM and temperature. More detail on this threshold is provided in section 5.5.1.

The energy map is initially calculated using a constant effective height s_{eff}. Benz and Krucker (2002) estimated a value of $500\,\mathrm{km}$ by assuming that the lowest observable event extends to about the spatial extent of a pixel. The EIT images and the binned AIA images from our study have similar spatial resolutions. The bin-factor of N=4 results in a $2.4''$ pixel resolution for AIA, while EIT's resolution is $2.6''$. Therefore, we used the same effective height estimate for the initial energy calculation. However, a fixed effective height may not be reasonable since it is expected to change proportional to the event size. Therefore, an alternative method scales the effective height with the square root of the detected event area (A). This approach increases the derived energy for larger events and, in turn, reduces the power-law index of the energy distribution. Benz and Krucker (2002) find that the $\sqrt{A}$ method is more plausible for studies comparing events over multiple energy ranges. We correct the initial energy for this influence of the event area after the event combination (section 5.6). The initial energy estimate for an event is multiplied by a factor determined by the number of combined pixels (N), resulting in the final event energy of $E_{final} = E \cdot (N)^{1/4}$.

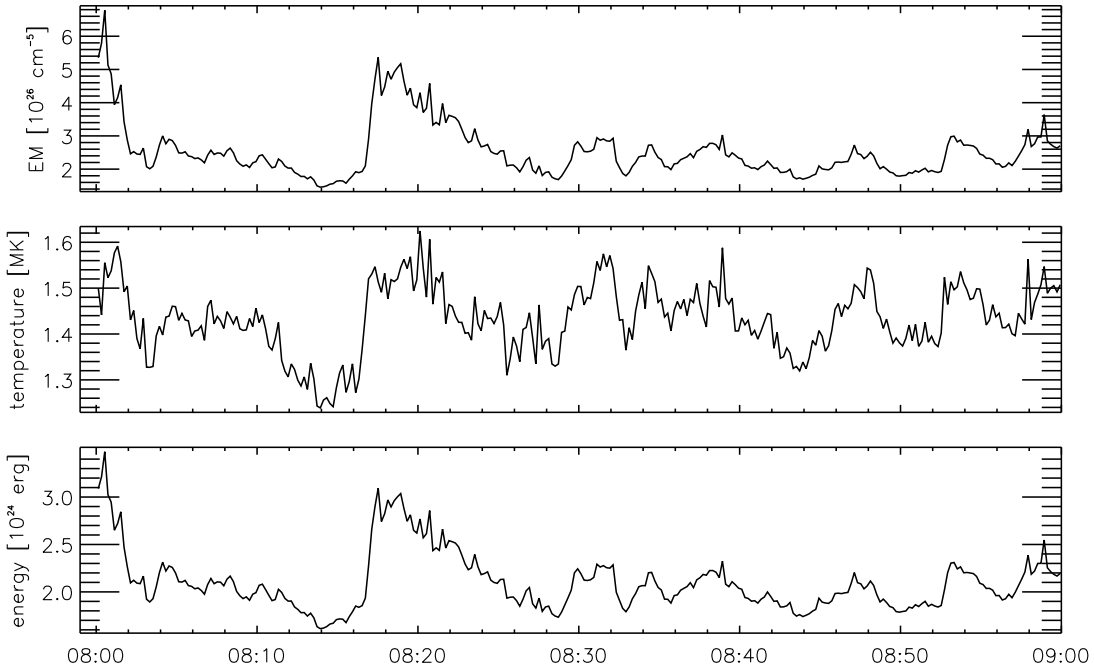

Fig. 5.5.: EM (top), temperature (middle) and thermal energy (bottom) evolution of a single pixel at $x = -23''$ and $y = 84''$ in the test data set.

5.5 Event Detection and Definition

The exact event definition is one of the most critical aspects of this kind of nanoflare study. A poorly chosen definition can favor or reduce the detection of certain event energies, changing the event distribution and, therefore, the derived power-law index. As discussed in section 3.3.1, finding the right definition was already shown to be a very difficult task with no clear solution (see Parnell (2004) and Parnell and De Moortel (2012)). Experiments with different definitions and parameters during our methods development have shown a similar variance in the final power-law index. Thus, we will not attempt to give a definitive answer for the best event definition or the exact power-law distribution. Rather, our goal was to develop a simple and tunable method that can reliably work across various data sets and produce comparable results.

As a basis, we used the event detection method developed by Krucker and Benz (1998) for EIT data (171 and $195\,$Å wavelength bands) with a spacial resolution of $2.6''$ and a temporal resolution of $127.8\,\mathrm{s}$. We modified it to allow the direct search in the energy time series and to obtain improved results with the high cadence and multi-wavelength AIA data. As with many nanoflare studies, their method starts with a search for local peaks in each pixel's EM. A background value, defined as the minimum EM since the last accepted event, is then subtracted from the peak EM. If the result exceeds a predefined threshold, the local peak counts as an event, and

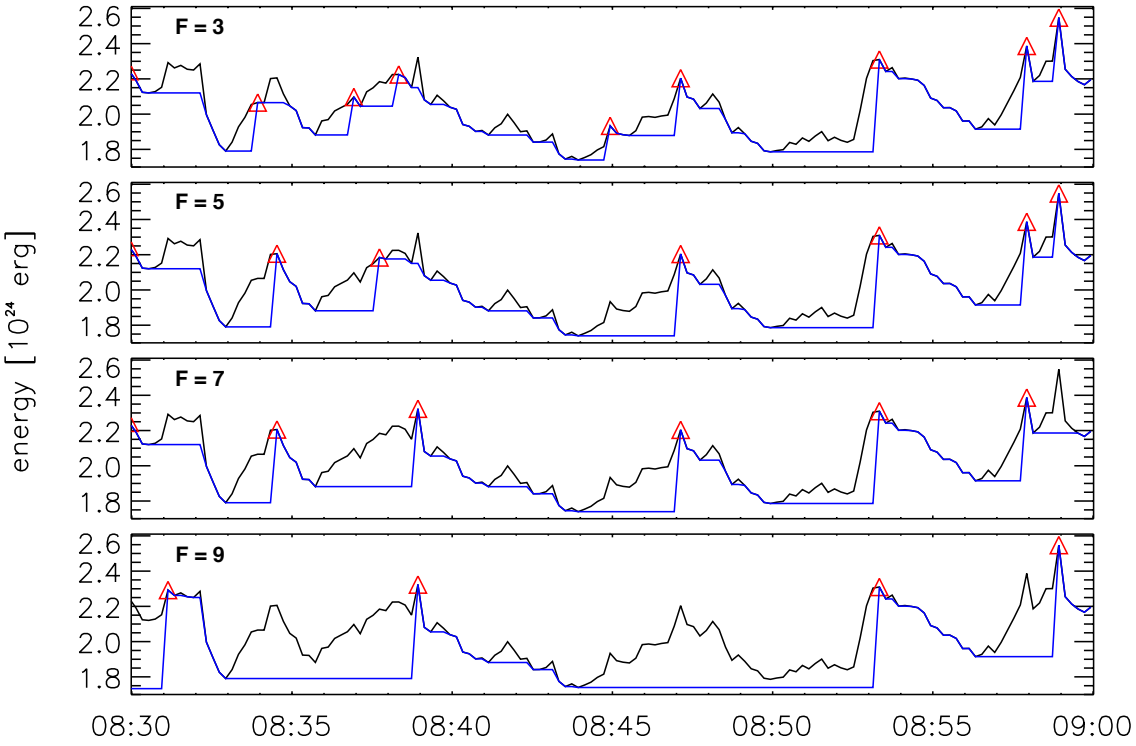

Fig. 5.6.: Original method with different thresholds $F \times \sigma$ applied to the energy evolution of a pixel at $x = -23''$ and $y = 84''$ in the test data set. The blue line represents the current minimum while the red triangles mark accepted events. σ is a constant value for each pixel (see section 5.5.1).

the energy is calculated. This seemingly simple algorithm already relies on multiple parameters and assumptions that are hard to tune correctly.

Local peaks were usually defined as time steps in a pixel's EM evolution with a higher value than the previous and the following time step. When we applied this simple definition to the high cadence AIA data, we detected numerous local peaks in an event's rising phase because of single low data values. This effect breaks up what would otherwise be considered a single large event into multiple smaller ones. Figure 5.6 shows the events extracted from the time evolution of the thermal energy content in a selected pixel by this simple method and different thresholds. Thresholds are given as a multiplication of a factor F with a fixed value σ that is calculated for each pixel and will be explained in section 5.5.1. The event peaking shortly before 8:35 UT is underestimated by the lower thresholds because of a local peak in the events rising phase. Higher thresholds more accurately represent the event's actual energy. For the second event between 8:35 UT and 8:40 UT, the various thresholds find different energies, numbers of events, and peak locations. In general, we observed that this method stops at insignificant local peaks if the threshold allows it. Once the threshold is raised, it will find new peak positions or add previously independent peaks to satisfy the larger threshold.

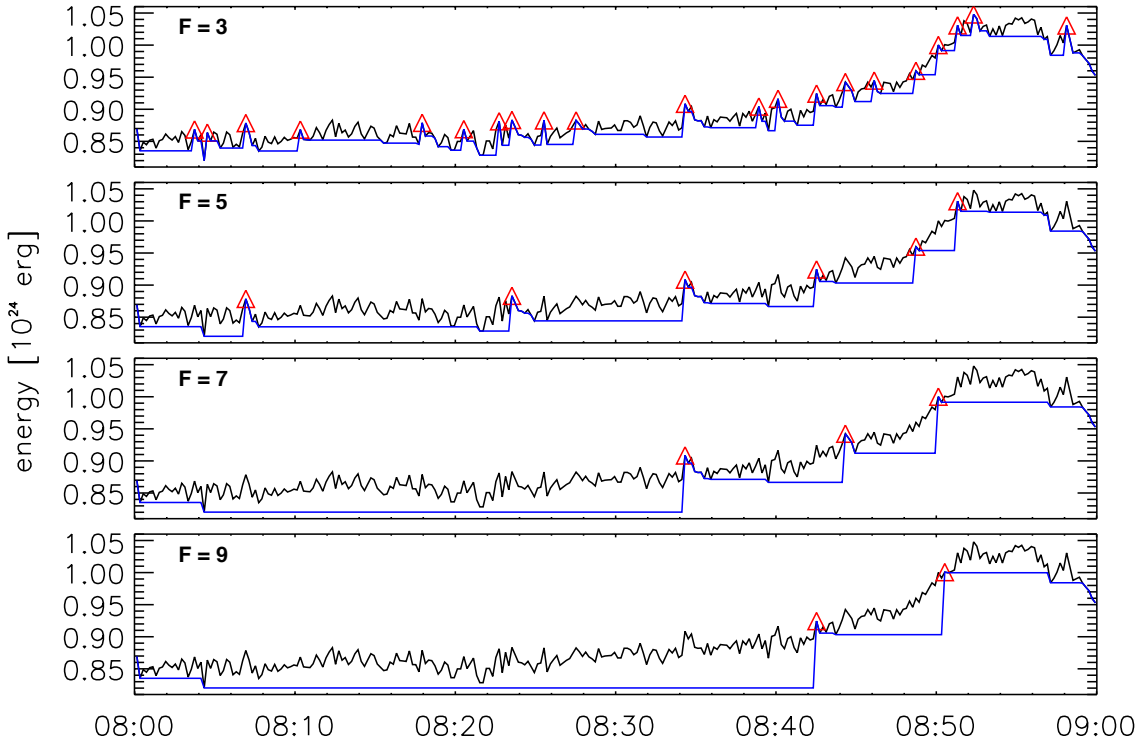

Fig. 5.7.: Original method with different thresholds $F \times \sigma$ applied to the energy evolution of a pixel at $x = -50''$ and $y = 80''$ in the test data set. The blue line represents the current minimum while the red triangles mark accepted events. σ is a constant value for each pixel (see section 5.5.1).

These inconsistencies in the determined event number and event energy result in problems for the accurate reconstruction of the nanoflare frequency distributions. The peak location's uncertainty could lead to additional problems in the following event combination that are hard to characterize.

To reduce some of these uncertainties, the definition of a local peak was expanded to include a predefined interval in units of time steps. A point along the energy time series is then marked as a local peak if it has the highest value of all data points inside the interval. This added condition prevents single low data points from creating unwanted events if the energy continues rising afterward. Intervals of up to four time steps in both directions have been tried. An interval of two time steps, i.e. $24\,\mathrm{s}$, in both directions already prevents the majority of unwanted breakups of otherwise continuous rises. Larger intervals can provide a visually even more pleasing event detection, mainly for large events. However, the sensitivity for small events may be reduced by large detection intervals.

Another problem of the original method is the detection of multiple events during slow continuous rises in the energy that is not abrupt enough to be considered a flare. The original event definition tends to dissect such continuous rises into many

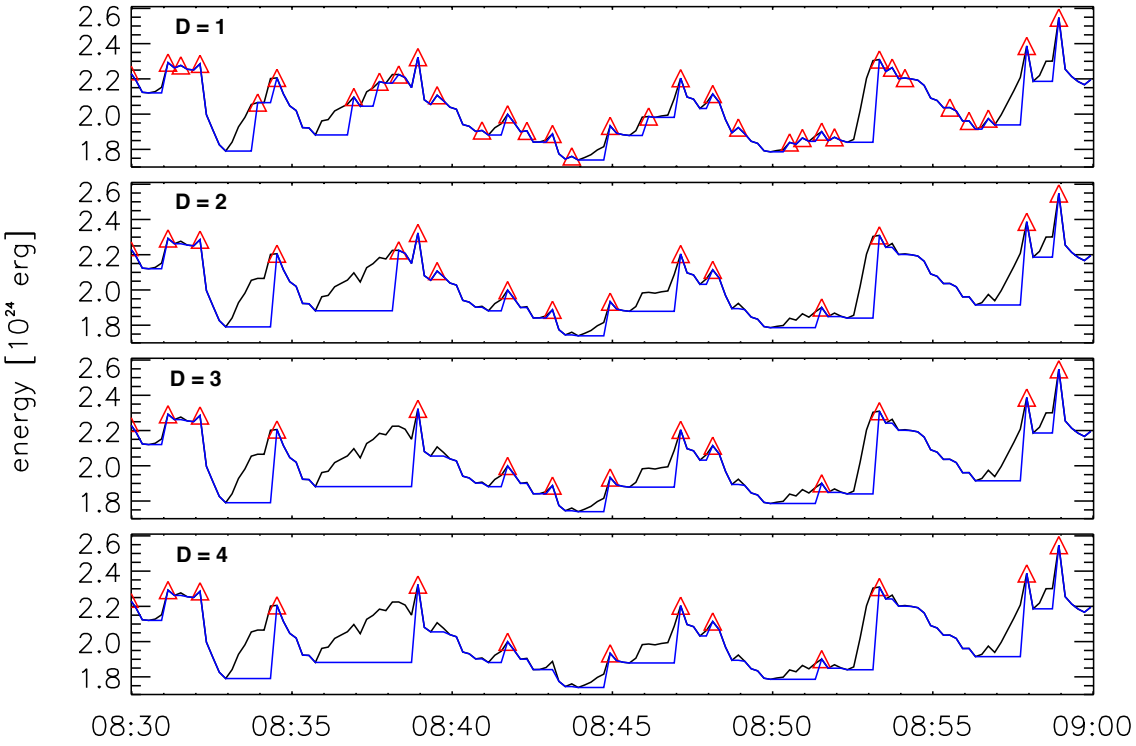

Fig. 5.8.: Adapted method with different event detection intervals D applied to the energy evolution of a pixel at $x = -23''$ and $y = 84''$ in the test data set. Local peaks are marked independent of any threshold. The blue line represents the current minimum while the red triangles mark accepted events.

small events near the threshold set. Figure 5.7 shows the energy evolution of such an occurrence and how it is divided depending on the set threshold.

We attempted to solve this problem by first running the event detection without a threshold, marking every local peak, and saving each event's energy. This method results in peak positions determined by the set detection interval and not by the threshold. Figure 5.8 shows how peaks are marked depending on the used interval. The desired threshold is then applied afterward by filtering out all events with energies below the threshold. Figure 5.9 shows the application of different thresholds to the events previously determined by a selected detection interval of two time steps. The location of the peaks remains fixed, and only small events are removed. This change indirectly controls the event's impulsiveness since the background level can also move back to higher energies, especially during slow continuous rises.

Figure 5.10 shows the results from the adapted method with a detection interval $D = 2$ and a threshold of $5 \times \sigma$ for a selection of different pixels, including the ones shown in the threshold chapter (section 5.5.1). The continuous rise in the first row gets reduced to a single event in the most significant part of the energy evolution,

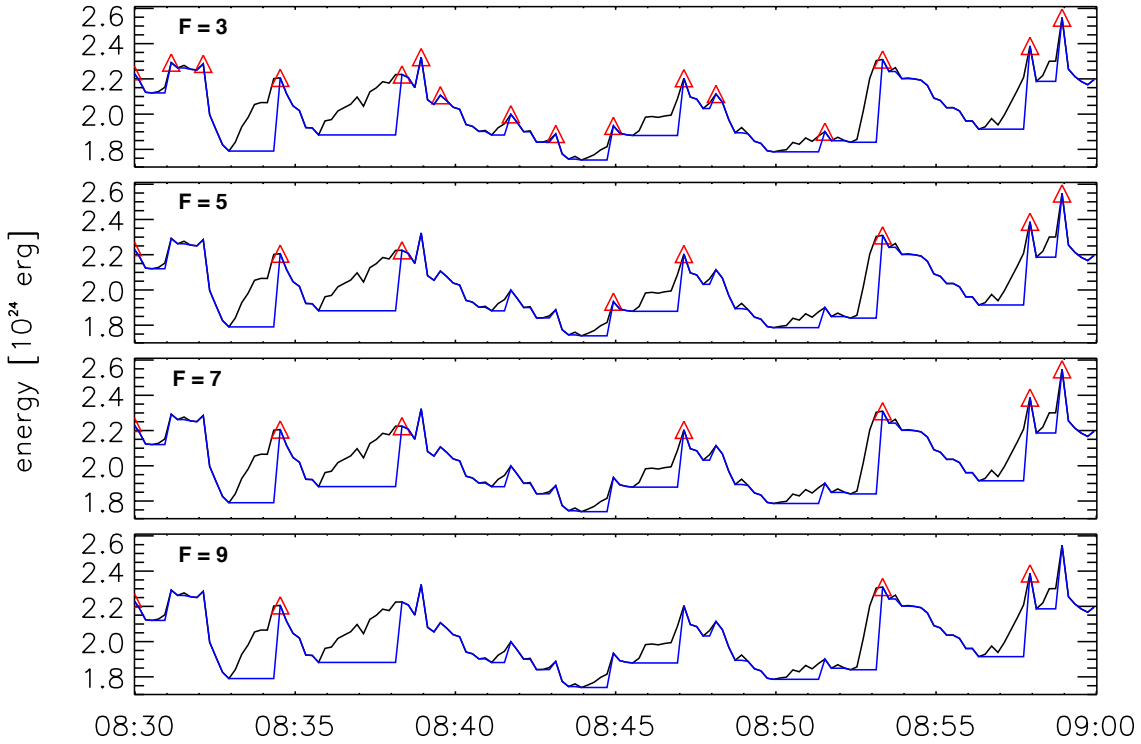

Fig. 5.9.: Adapted method with fixed event detection intervals ($D = 2$) and increasing threshold ($F \times \sigma$) applied to the energy evolution of a pixel at $x = -23''$ and $y = 84''$ in the test data set. The blue line represents the current minimum, while the red triangles mark accepted events. σ is a constant value for each pixel and is explained in section 5.5.1.

and pixels with clear peaks are marked satisfactorily. In pixels dominated by noise, no events are detected.

A further selection of event detection settings in part relevant to the final analysis presented in chapter 6 in shown in the appendix in section A.2. Decreasing the threshold to $3 \times \sigma$ increases the number of detected events significantly, and we find that many of those are probably associated to noise. Increasing the threshold to $5 \times \sigma$ and higher reduces the accepted events to the most significant ones. A detection interval set to $D = 4$ manages to find the most significant peaks even in the noise-dominated pixels.

Neither one of the described methods is perfect. While some changes produce seemingly better results, they may come with tradeoffs in other aspects. How it will affect the overall performance of finding a reliable power-law in different data sets is hard to predict from looking at single pixels. However, the adapted method seems to produce more reliable results across the various thresholds and addresses many of the original method's critical problems.

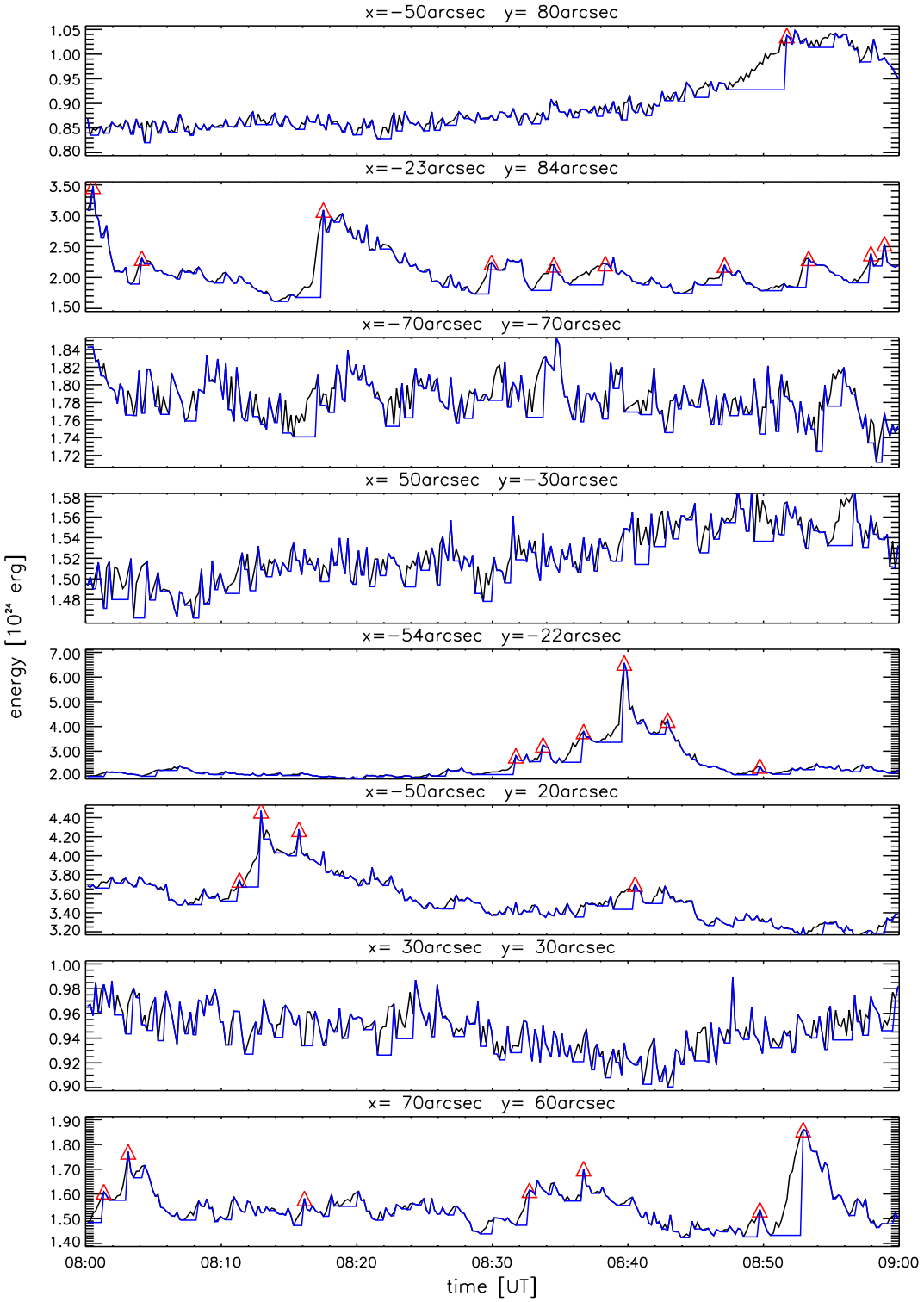

Fig. 5.10.: Adapted detection method results using an interval of $D = 1$ and a threshold factor of $F = 5$. The energy evolution (black) of seven different pixels from the test data set is shown. Pixel location for each panel is given in heliocentric coordinates at the top and the bottom six match the pixels discussed in Figures 5.11 and 5.12. The blue line shows the current value of the minimum used for event energy calculation, while red triangles mark accepted events.

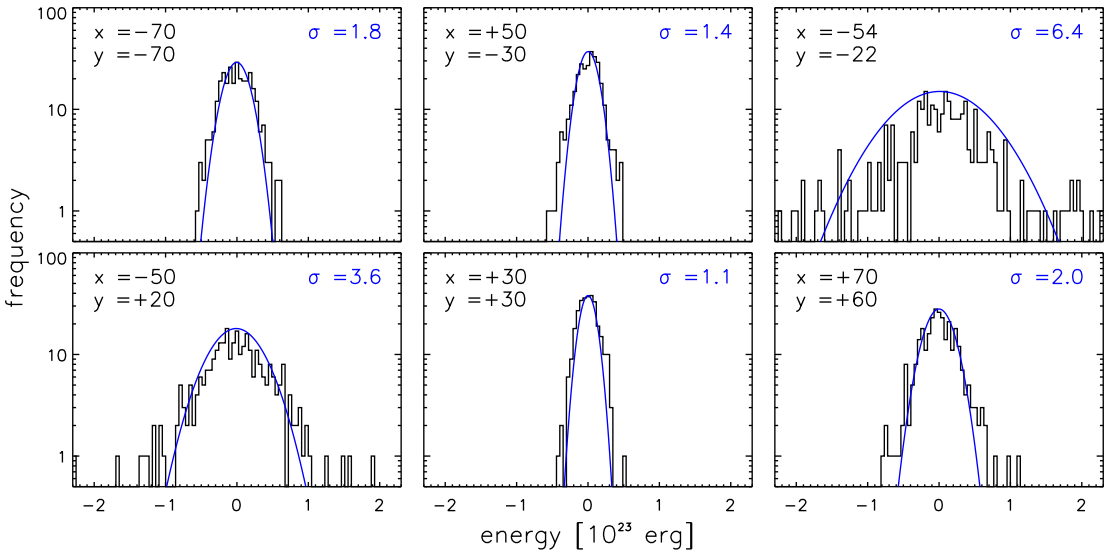

Fig. 5.11.: Distribution of changes in energy between single time steps ($12\,\mathrm{s}$) during the one hour long test data set in six different pixels (marked in Figure 5.12). x and y pixel coordinates are given in arcseconds in heliocentric coordinates. The overplotted gaussian function (blue) is determined from the standard deviation σ (given in units of $10^{22}\,\mathrm{erg}$) and mean of the data distribution.

5.5.1 Threshold

The threshold defines the lower boundary for acceptable event energies. Applying the threshold to the event map means that every detected event with an energy below the threshold is discarded and will not be involved in further processing.

A threshold can either be applied globally or locally. The global threshold uses the same energy for all detected events independent of their location. A local threshold applies only to a specific pixel. Global thresholds were found to favor pixels with higher background levels and, in turn, higher event energies. Local thresholds can take into account the background energy of an individual pixel and its noise.

We do not use the uncertainties calculated by the DEM code to derive our threshold. Instead, the standard deviation of time step to time step variations in each pixel's thermal energy evolution is used. First, we calculate for each pixel the differences between consecutive time steps over the whole data set. Then the standard deviation of these differences is calculated for the lower 90% of absolute values. This was done to capture mainly the thermal energy fluctuations due to noise and exclude any high values created by actual events.

Figure 5.11 shows histograms of the time-step to time-step variations in selected pixels. They are over-plotted with a gaussian defined by the histogram's maximum

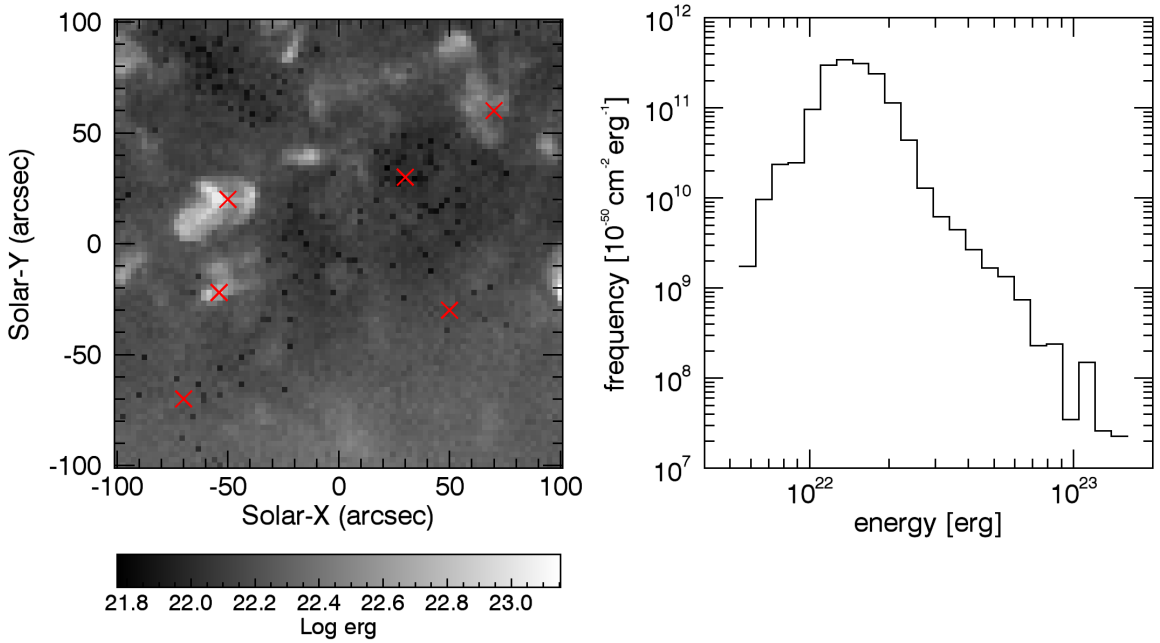

Fig. 5.12.: The left image shows the standard deviation determined for each pixel in the test data set, and the histogram of all standard deviations is shown to the right. The given frequency is normalized to the observed field of view.

count number and the mean and standard deviation calculated from the variations. Standard deviations (σ) vary from 1.1×10^{22} to 6.4×10^{22} erg in the pixels shown. Figure 5.12 shows the distribution of all sigma-values in the test data set and the selected pixels' location. They reach up to 10^{23} erg and show a maximum frequency of about 1.5×10^{22} erg. The derived local standard deviations are then multiplied by a common integer factor to get the final local thresholds. They are then applied to the previously generated event energy maps to filter out unwanted events before any further analysis.

5.6 Event Combination

Nanoflares can be more extended than the size of a single binned pixel. Consequently, we developed an algorithm that combines events in bordering pixels if they both happen during a defined time interval. In this context, bordering can either suggest a search for events in all surrounding eight pixels or just the ones in the x and y direction (a total of four). Previous nanoflare studies used both approaches, and there is no clear conclusion on which one should be preferred. Krucker and Benz (1998) only combined events from the nearest four neighbors with good results. We also found this approach sufficient for combining events that cover more than one pixel. A higher number of pixels searched for related events mainly increases

random encounters and false combinations with little benefit to detecting large-scale events. Therefore, our algorithm only searches for related events in the x and y direction and omits the diagonals.

Studies using EIT data have obtained good results by either combining only pixels that peak simultaneously or allowing combinations with the previous or following time steps. Benz and Krucker (2002) argue about the optimal time interval for event combination in studies using EIT data. They analyzed studies using intervals of ± 1 to ± 3 min between peaks and concluded that the optimal time interval is closer to ± 1 min. Using the found frequency of events in Krucker and Benz (1998) they calculate that the ± 3 min interval has a 45% chance to produce random encounters in the four bordering pixels. This chance reduces to 15% if the interval is only ± 1 mins. Since the binned AIA data has a spatial resolution of $2.4''$ compared to the $2.6''$ of the EIT instrument, a very similar argument can be made. However, it is hard to predict the implications of the much higher temporal resolution. Using the AIA image cadence of 12 seconds, we need to use an interval of ± 5 time steps to create the same ± 1 min interval.

Our visual analysis of intervals up to ± 10 time steps (± 2 min) revealed that a minimum interval of ± 3 time steps is required to combine events spanning more than a few pixels accurately. An interval of ± 5 time steps (± 1 min) improved the combination of such events further and reduced the break up of large-sale events into multiple smaller ones. ± 7 time steps only slightly improve the combination of the most significant events, and even larger intervals do not significantly improve the detection but will increase the chance for random encounters.

5.7 Event Frequency Distributions

Nanoflare frequency distributions were obtained by first creating a histogram from all combined event energies of a given data set. We divided events into 50 bins spaced evenly across the energy range 10^{22} to $10^{28}\,\mathrm{erg}$ in logarithmic representation. The number of events in each bin was normalized to its energy range, the observation time, and the area. The power-law index (α) and its standard deviation σ were then derived through a linear fit in log-log space, which corresponds to a power-law function when applied in a double logarithmic plot. IDL's *LINFIT* function fits a linear model to a provided data set by minimizing the chi-square error statistic. Additionally, measurement errors can be accounted for, resulting in different weights of each data point.

These measurement errors were derived by assuming standard Poisson error statistics for each histogram bin, equal to the square root of the number of events. We propagated this Poisson error through the normalization steps and the logarithmization of the histogram. This method results in a higher weight for bins containing a large number of events. Since the event frequency usually differs by multiple magnitudes across the full observed energy range, a weighted linear fit is determined mainly by the smaller events with significant count numbers. With just a few to even single detected events, the energy bins at high energies have virtually no effect on the resulting power law.

Alternatively, we can also omit these measurement errors, which results in a linear fit without any weights. Each positive bin in the histogram is consequently treated as an equally valid and important data point. As a result, a small number of large events can affect the steepness of the fit and the resulting power-law index. This may give unwanted significance to potentially erroneous data points since bins at high energy with few event counts contain significant uncertainties in the derived occurrence frequency. Furthermore, the event energy itself includes more potential errors from the event combination step, considering larger events generally result from combined pixels while smaller events are captured by a single pixel. On the other hand, this method produces power-law fits that visually represent the whole derived frequency distribution more accurately. Furthermore, the smaller events may also be subject to unidentified biases, which are then amplified through their influence in the weighted linear fit. We will therefore compare the results of both methods in section 6.1.

6 Results

This section presents the results obtained by the developed method when we applied it to the solar cycle data set. As described in chapter 5, our method features multiple parameters that the user can choose freely. While we have narrowed them down to a sensible range, the combination of all available options is still extensive and significantly influences the final results. In the following, we summarize the free parameters and their reasonable intervals and then examine the consequences of selecting different combinations.

The event **detection interval** ($\mathbf{D} \in \mathbb{N}$): To be accepted as a local peak, an energy value in a pixels time series has to be larger than any other energy value inside an interval of $D * 12$ seconds in either direction. Values of $D = 1$, 2, 3 and 4 have been tested (see section 5.5). $D = 1$ only accepts continuous, uninterrupted rises in energy. A single low data point during the rising phase will split an event into multiple sections. $D = 2$ solves this problem by allowing the continuation of an event after the interruption. $D = 3$ and 4 can produce visually even more pleasing results but may discriminate against smaller events.

The **threshold factor** ($\mathbf{F} \in \mathbb{N}$): The threshold ($TH$) defines the lower boundary for the acceptable event energy. We first calculate the standard deviation of energy changes between successive time steps for each pixel. The result is interpreted as a measure of noise present in each pixel (see section 5.5.1), and we then defined the final threshold via multiplication of the standard deviation (σ) with the chosen factor (F). The threshold is applied after the detection of local peaks and does not influence their position. We tested values of $F = 3$, 5, 7 and 9 and an interval of $F = 5$ to 9 has been found to produce good results. $F = 3$ results in the most found events, leading to numerous unwanted event combinations. $F = 5$ reduces the number of found events and consequently the chance of false combinations. With $F = 7$ the number of events decreases further. At $F = 9$ only a small number of events are left, but the method still produces stable results.

The event **combination interval** ($\mathbf{C} \in \mathbb{N}$): It defines the time interval, with $C * 12$ seconds in both directions, during which events found in bordering (x and y direction, not diagonals) pixels are combined. We studied the effects of $C = 0$, 1, 3, 5, 7 and 9 and found satisfactory results with values of $C = 3$ to 7 (see section 5.6).

$C = 3$ seems to be the lower acceptable boundary to connect larger events reliably. $C = 5$ leads to less breakup of large event areas into smaller ones and produced visually more pleasing results. An increase to $C = 7$ may be advantageous when combined with a high threshold factor (e.g., $F = 7$) but generally produces similar results to $C = 5$.

Because of the many possible combinations, we will not cover all of them in this analysis. Instead, we first select a reference parameter set and then observe variations caused by modifying parameters individually. This reference method consists of the most promising parameters we encountered during the method development, both separately and in combination. The event detection interval is initially set to $D = 2$, the threshold factor to $F = 5$, and the event combination interval to $C = 5$. Then those parameters are changed one at a time to $D = 1$ and 4, $F = 7$ and 9, and $C = 3$ and 7 while keeping the other two fixed at the reference values. This approach resulted in the seven different parameter combinations used in the following sections to present the results.

Section 6.1 analyses the nanoflare frequency distributions obtained by different parameter settings in the applied method. We show two different approaches for the linear fit that extracts the power-law index from the distribution. The results and any changes observed from the different event detection methods are presented separately for both fits. They are followed by an analysis of the combined power-law from all data sets. In section 6.2 we discuss the observed energy flux. First, for each pixel and each dataset individually to analyze the flux distribution across the observed field of view, and then as a mean flux for each dataset to inspect changes over the solar cycle and across different methods. We define the term active pixel in section 6.3 and investigate the distribution of detected activity in each pixel for all data sets. We inspect any changes produced by the different methods concerning the fraction of active pixels and the number of events detected in those pixels. Subsequently, comparisons of the HMI line-of-sight magnetogram, the energy flux distribution, the active pixel distribution, and three selected AIA wavelengths for a few selected data sets are shown in section 6.4. The section also includes contours on top of HMI magnetograms showing the location of areas where we observed a high mean energy flux. Section 6.5 shows the frequency of event sizes in the different data sets. Changes to the mean and total event area over the solar cycle and across methods are subsequently analyzed. Finally, section 6.6 examines the final number of events found after the combination of neighboring pixels. We investigate the total number of events as well as the fractions of events larger than a minimum area, present changes with respect to the solar cycle, and discuss the differences between the chosen methods.

6.1 Nanoflare Frequency Distributions

This section focuses on the power laws derived from the extracted nanoflare frequency distribution. As explained in section 5.7 we have used two methods for the linear fit, each with its potential strengths and weaknesses. Figure 6.1 shows the nanoflare frequency distributions throughout solar cycle 24, obtained using the reference method. The included linear fit utilizes the calculated counting errors, which are also shown in the plot but are only visible at higher energies. These high-energy bins contain only a few detected events, and the bins with the largest energies are even the result of a single event. The first four energy bins starting at the peak are excluded from the fit to reduce unwanted effects from the used threshold method. Since we incorporated a local threshold in the developed method, not all pixels become available to the event detection at the same energy (see Fig. 5.12). By moving the starting point of the fit to a higher energy bin, we can reduce the influence of this effect. As expected, the weighted fit is mostly determined by the bins at lower energies, where the occurrence frequency is much higher. It shows a very close agreement with the found event frequencies over the first order of magnitude but does not always accurately represent the derived frequency of the larger events.

Figure 6.2 shows again the nanoflare frequency distributions obtained by the reference method but fitted with a linear function without the use of individual weights. The fit starts at the same energy bin at the low end to reduce the influence from the local threshold, even though any errors would be much less pronounced without weights since these low-energy bins do not dominantly determine the fit. Additionally, the four highest energy bins are excluded because of their high uncertainty and strong effect on the non-weighted fit. While the fit might be a more accurate representation of the total distribution, it compromises on the close agreement with the smaller, lass uncertain energy bins. Overall the derived power-laws are slightly steeper and their standard deviation slightly higher than the ones from the weighted fitting method.

The nanoflare distributions obtained by the other six parameter combinations in the applied method discussed in this chapter are collectively shown in the appendix. Section A.3 shows the distributions with the weighted power-law fit, and section A.4 shows identical histograms but including the power-law fit without weights. The following sections present the derived power-laws of different sets of method parameters separately for both linear fitting methods.

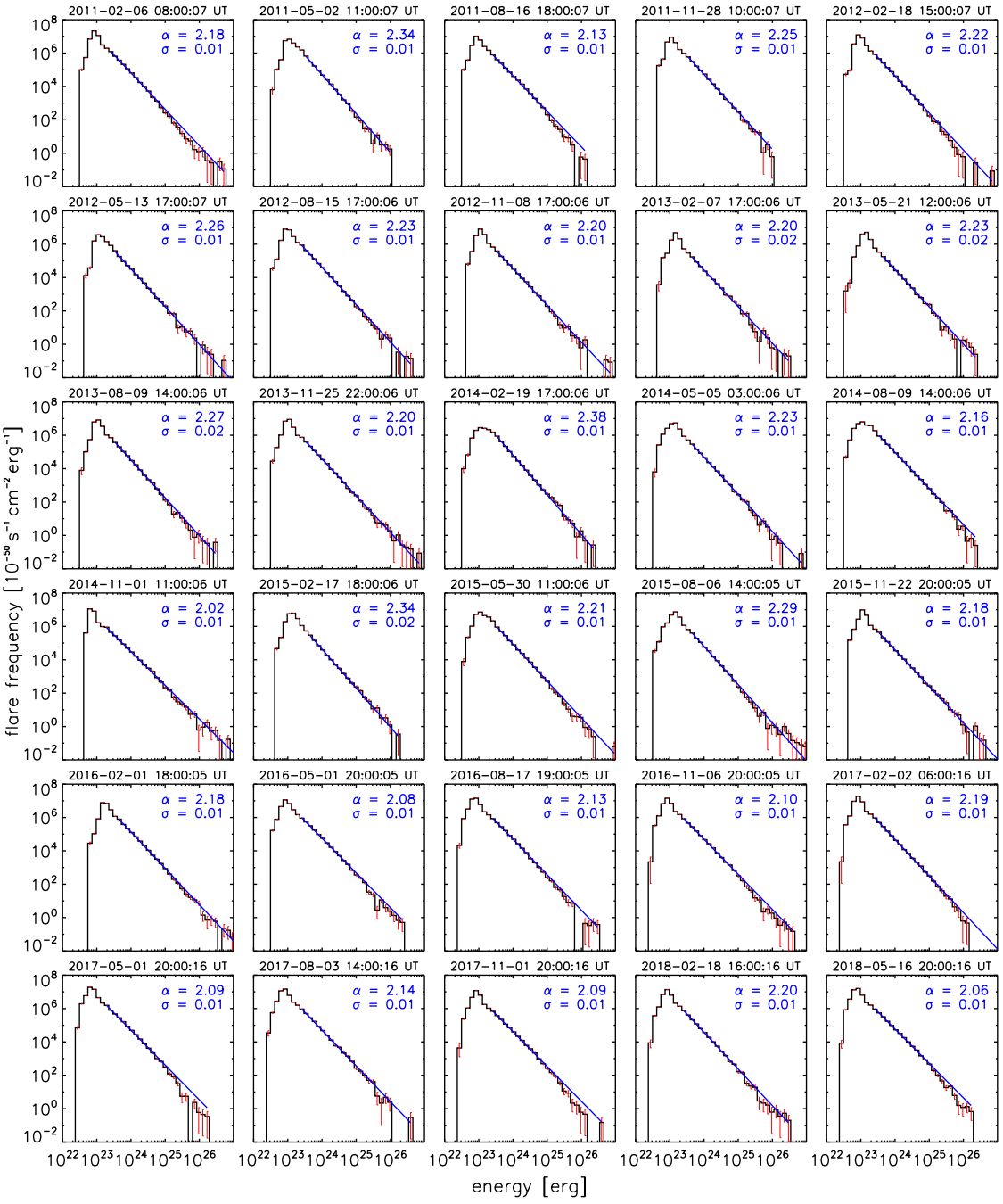

Fig. 6.1.: Nanoflare frequency distribution for each data set for the years 2011 to 2018 during solar cycle 24. Events were extracted with the detection interval set to $D = 2$, a threshold factor of $F = 5$, and a combination interval of $C = 5$, the reference set of parameters. A linear fit (blue) with weights derived from the counting errors (red) was used to extract the power-law index (α) and its fitting error (σ). The power-law fit starts four bins above the maximum number of counts and includes all positive bins at higher energies. Count numbers are normalized to the width of the energy bins, the observation duration, and the area of the observed field of view. The start date and times of each observation is given on top.

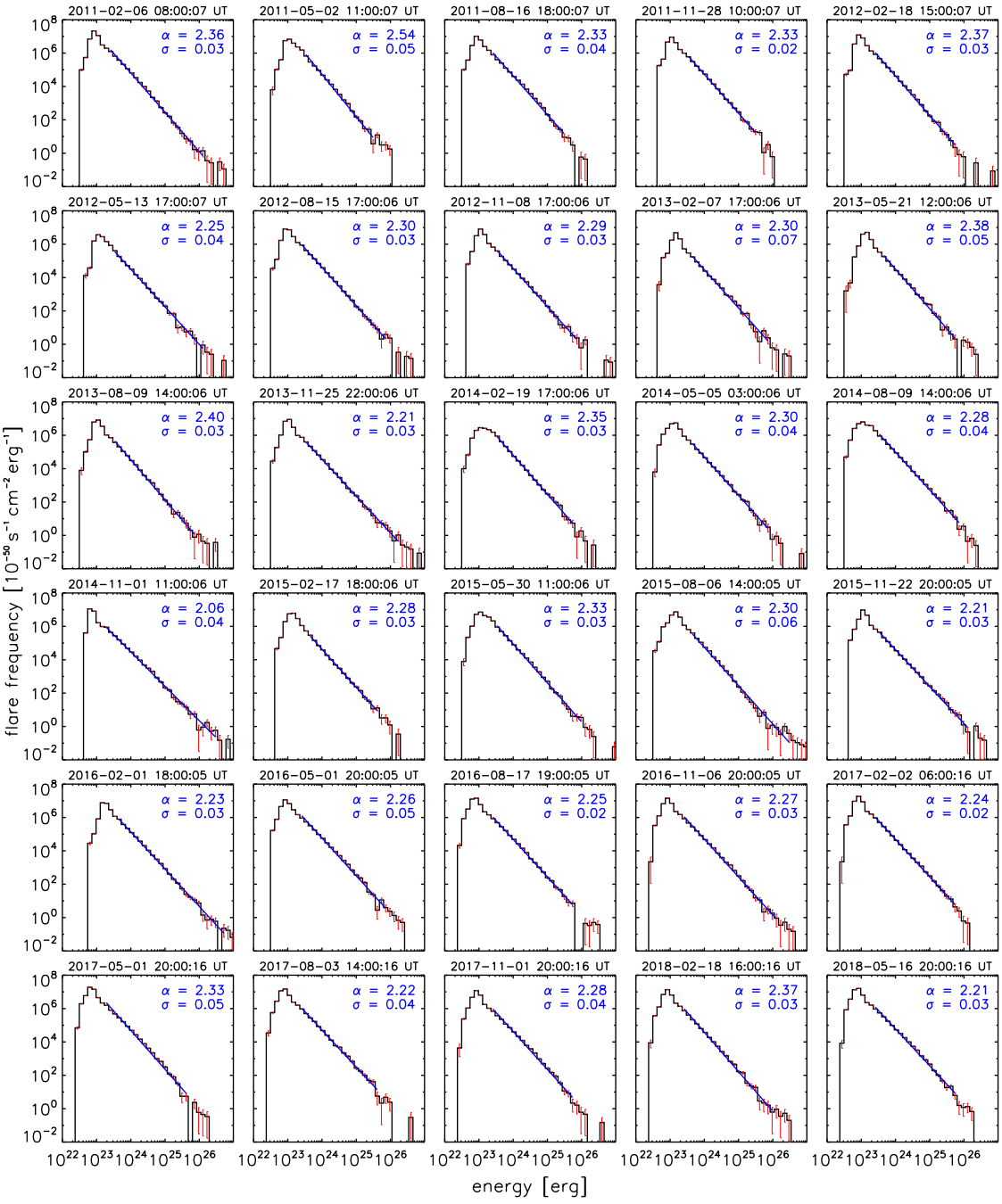

Fig. 6.2.: Same as Figure 6.1 but with a linear fit without weights fitted to the nanoflare frequency distributions extracted by the reference set of parameters.

6.1.1 Power-law Derived from Weighted Linear Fit

In this section, we focus on the power-laws obtained by a linear fit with weights (derived from the Poisson error of each histogram bin). Therefore, the results should be most representative of the lower energy range where most of the events reside, with the closest agreement to the event distribution observed in the first order of magnitude of the total fitted energy range.

Figure 6.3 shows the evolution of the power-law index α over the solar cycle for three different event detection intervals used. Their correlation to the monthly mean sunspot number, as a representation of solar activity, is also included. The reference method, with its detection interval of $D = 2$, is displayed in the middle of the plot. It is compared to two other methods using a detection interval of $D = 1$ and 4 while keeping the other two parameters fixed. Application of the detection interval of $D = 1$ (left) does not reveal any significant changes over the solar cycle and results in a correlation coefficient of $r = 0.07$. However, the result is quite different for the reference method, where the correlation coefficient gives $r = 0.52$, indicating a variation of the power-law index in phase with the solar cycle. This increase in correlation is mainly due to the now pronounced decrease of the steepness of the power-law index after the year 2016. A general trend of a steeper nanoflare frequency distribution during higher solar activity is visible. Raising the detection interval to $D = 4$ increases the correlation further to $r = 0.66$.

Figure 6.4 shows the different power-law indices produced by a change in threshold factor while keeping the detection interval fixed at $D = 2$ and the combination interval fixed at $C = 5$. The reference method with its threshold factor of $F = 5$ is shown in the left panels of the Figure. Increasing the factor to $F = 7$ results in a seemingly systematic change over the solar cycle but with a very low correlation to the sunspot number ($r = 0.19$). The power-law shows no decrease to lower than previous values after 2016, which resulted in the correlation of the selected method. Increasing the threshold further to $F = 9$ eliminates any visual pattern. A correlation coefficient of $r = 0.01$ further supports this observation. Noticeable are also the more significant fitting errors for larger threshold factors.

Figure 6.5 compares the three chosen combination intervals while keeping the detection interval fixed at $D = 2$ and the threshold factor set to $F = 5$. Reducing the combination interval to $C = 3$ produces overall steeper power-law fits and reduces the correlation to $r = 0.43$ with respect to the reference method. An increased combination interval of $C = 7$ slightly decreases the overall power-law but otherwise features little changes compared to the reference method. The correlation slightly improves to $r = 0.56$.

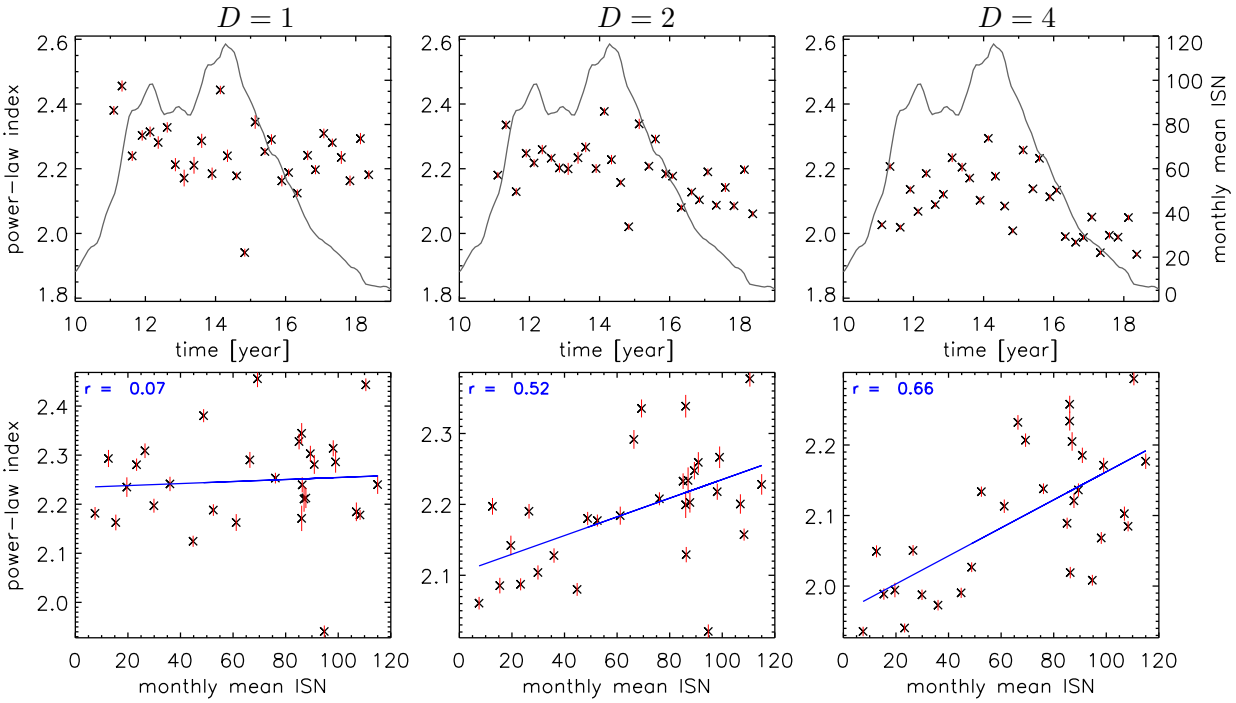

Fig. 6.3.: Power-law from linear fit with weights for different detection intervals $D = 1$, 2 and 4 (left to right). The middle panels show results from the reference method. Values extracted for each data set are plotted as a function of time (top row) together with the sunspot number (gray). Correlation to the sunspot number (bottom row), with a linear fit (blue) and correlation coefficient (r) is also shown.

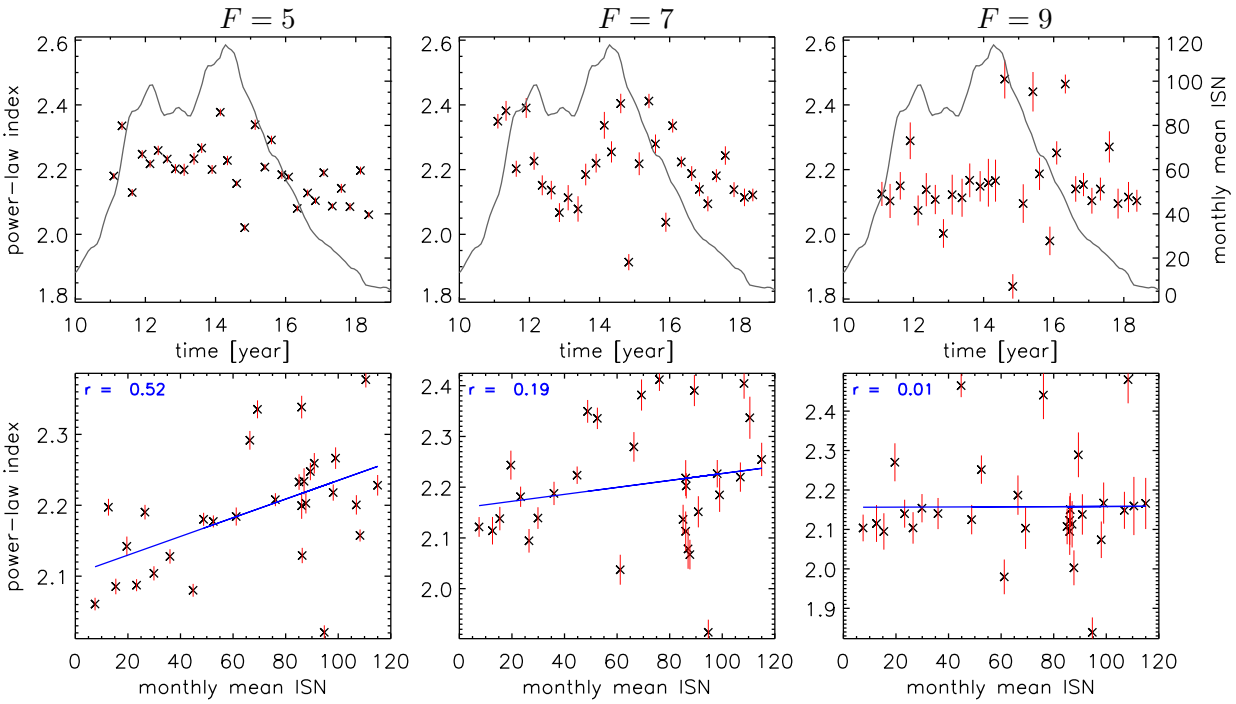

Fig. 6.4.: Same as Figure 6.3 but for different threshold factors $F = 5$, 7 and 9 (left to right). The left panels show results from the reference method.

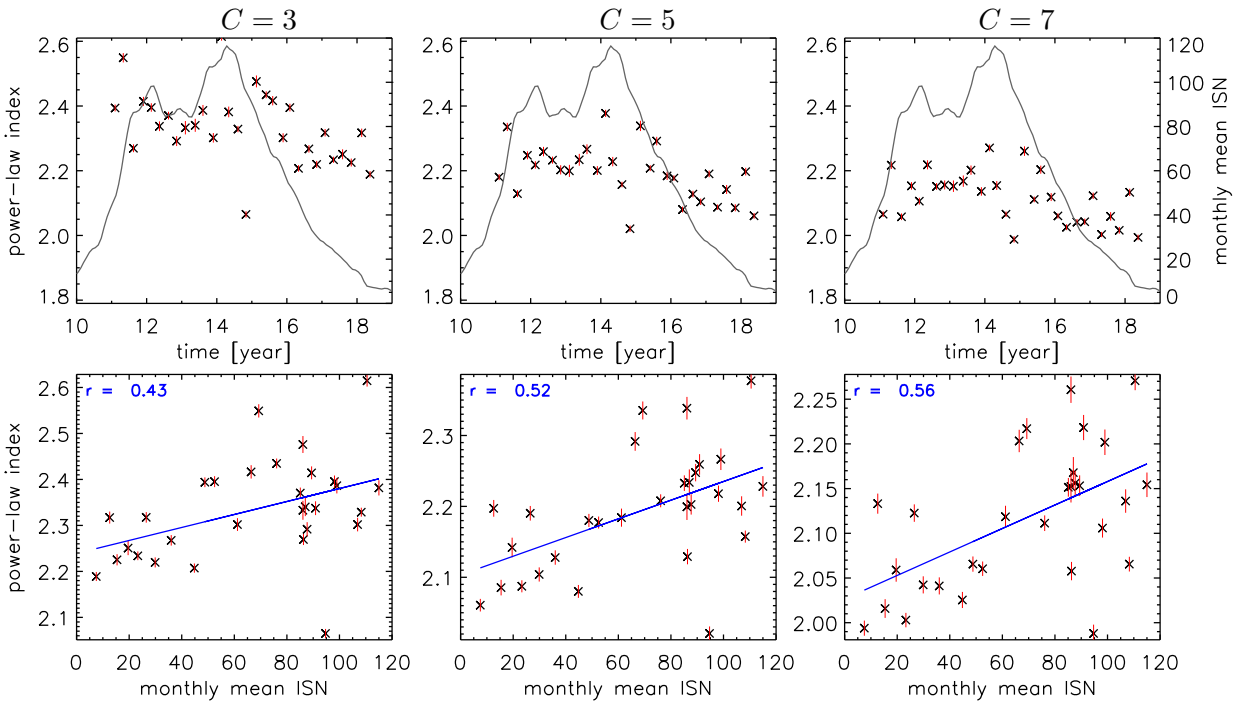

Fig. 6.5.: Same as Figure 6.3 but for different combination intervals $C = 3$, 5 and 7 (left to right). The middle panels show results from the reference method.

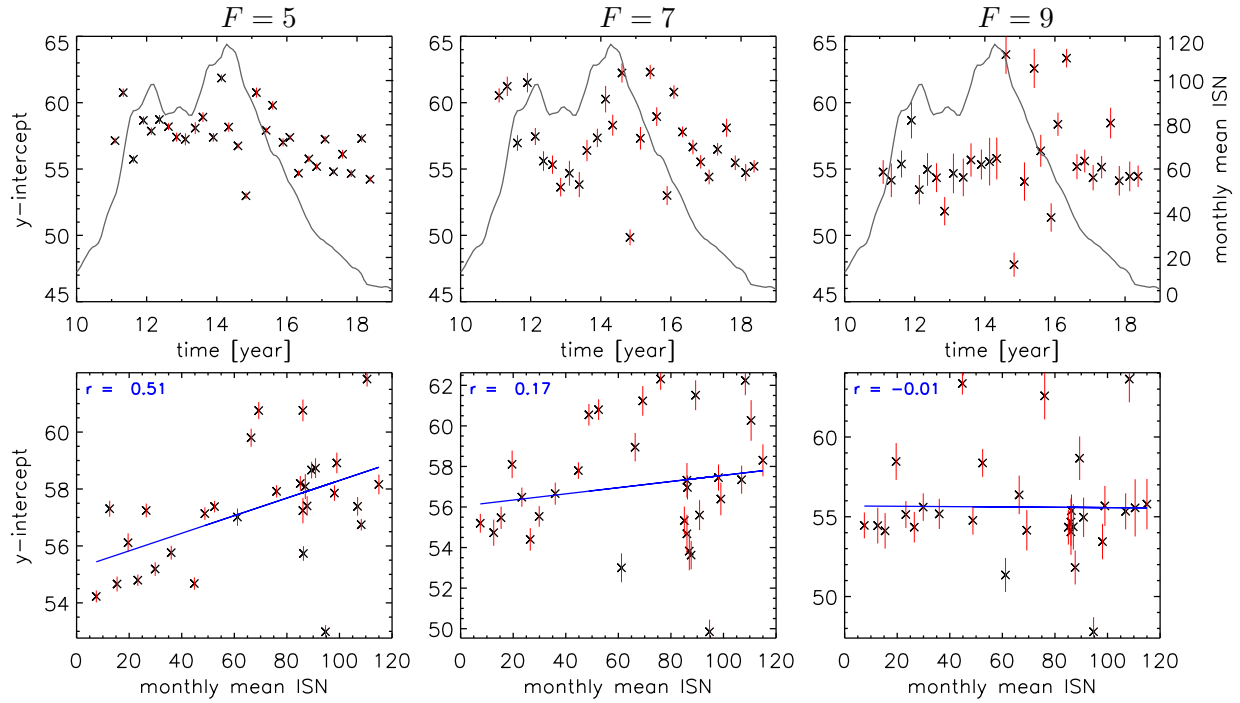

Fig. 6.6.: Y-intercept from linear fit with weights for different threshold factors $F = 5$, 7 and 9 (left to right). The left panels show results from the reference method. Values extracted for each data set are plotted as a function of time (top row) together with the sunspot number (gray). Correlation to the sunspot number (bottom row), with a linear fit (blue) and correlation coefficient (r) is also shown.

A second fitting parameter produced by the linear fit is the y-intercept point, where the linear fit crosses the y-axis. Its value is also equal to the logarithm of the factor A from equation 3.2 and is determined by the steepness and the height of the nanoflare frequency distribution. The overall height of the intersect therefore changes between methods as the amount of found events changes. However, within the same method, the variation across the solar cycle is very similar to the power-law variation and results in a similar correlation. These findings suggest that the steepness of the slope primarily defines the intercept variations, while the height of the nanoflare distribution within the same method does not play any significant role for the variations over the solar cycle. Therefore, we only show the influence of the threshold factor on this parameter in Figure 6.6 since the results are the same as already described for the power-law index.

6.1.2 Power-law Derived from Linear Fit Without Weights

The same power-law analysis as in section 6.1.1 was repeated using the values extracted by a linear fit without weights. Figure 6.7 shows the extracted power-law by methods using different detection intervals. The reference method only finds a negligible ($r = 0.12$) trend of steeper power-laws at a higher solar activity, whereas the correlation found by the weighted linear fit is $r = 0.52$. A decrease of the detection interval to $F = 3$ even reverses the overall trend ($r = -0.10$). Only the method using an interval of $F = 4$ remains at a higher correlation of $r = 0.45$ driven mainly by the slight decrease in the power-law index after 2016. The results of different threshold factors shown in Figure 6.8 contain no obvious correlation to the solar activity and the different combination intervals in Figure 6.9 also remain at low correlations of $r = 0.17$ to 0.27. Larger combination intervals, however, still show an overall reduction of power-law steepness across all data sets.

6.1.3 Combined Frequency Distributions

In Figure 6.10 we present a merged frequency distribution from all analyzed data sets during solar cycle 24. The combined data set has a total observation time of $60\,\mathrm{h}$ at a $12\,\mathrm{s}$ cadence and covers a $400''$ times $400''$ quiet-Sun field-of-view around the solar disc center. We used the reference method to extract the frequency distribution shown and fitted a power-law using a linear fit without weights. The fit has good agreement with the whole observed distribution and gives a power-law index of $\alpha = 2.26$. The detected events cover more than five orders of magnitude in energy and follow a close power-law distribution from 10^{23} to $10^{28}\,\mathrm{erg}$, covering the whole nanoflare energy range as defined by Aschwanden (2004) and even extending beyond the lower boundary for another order of magnitude.

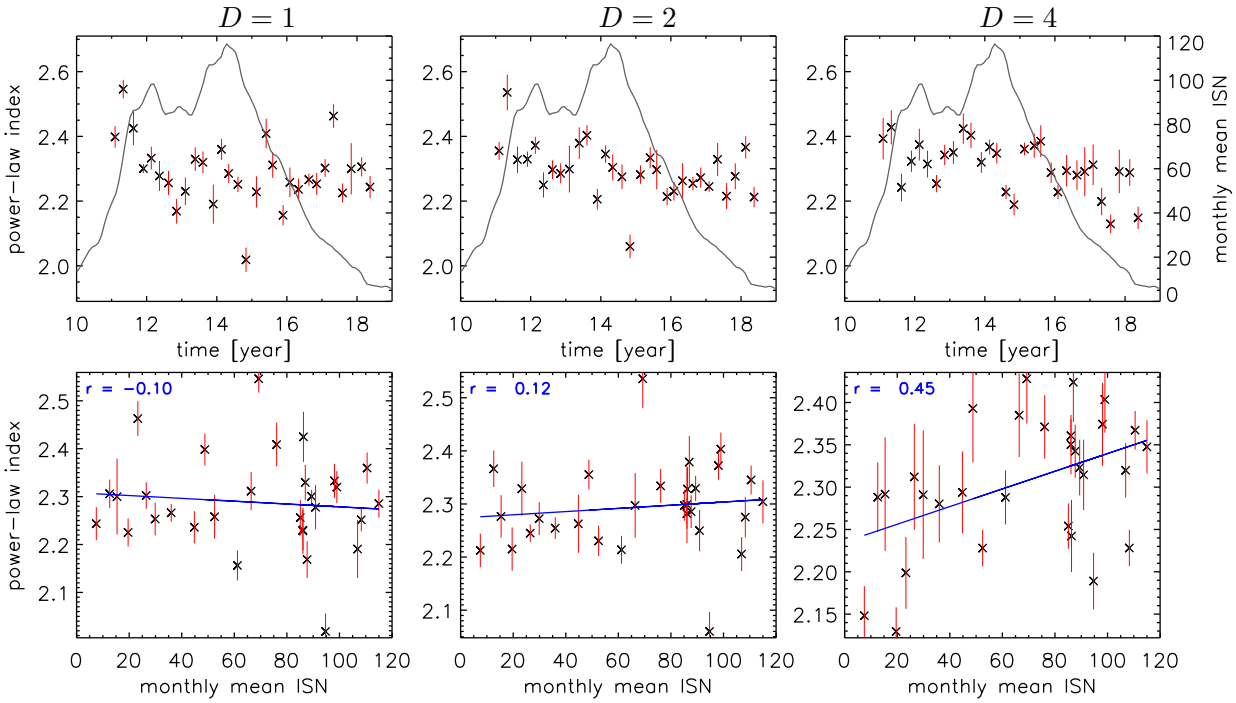

Fig. 6.7.: Power-law from linear fit without weights for different detection intervals $D = 1$, 2 and 4 (left to right). The middle panels show results from the reference method. Values extracted for each data set are plotted as a function of time (top row) together with the sunspot number (gray). Correlation to the sunspot number (bottom row), with a linear fit (blue) and correlation coefficient (r) is also shown.

The combined frequency distributions of the other sets of parameters show variations of the power-law index in the range of $\alpha = 2.16$ to 2.36. Figure 6.11 shows the difference between different detection intervals with power-law indices $\alpha = 2.20$, 2.26 and 2.33 for $D = 1$, 2 and 4, respectively. The differences are the result of changes in the event frequency in the lower energy part of the distribution. The detection interval $D = 4$ shows the most significant deviations from its linear fit across all parameter combinations. Figure 6.12 compares the frequency distributions of different threshold factors. The found power-law indices show very little variation for different threshold factors with $\alpha = 2.26$, 2.24 and 2.22 for $F = 5$, 7 and 9, respectively. Different threshold factors only result in an overall change to the event frequency without significantly changing the observed power-law index. Finally, Figure 6.13 shows changes to the frequency distribution resulting from a change in combination interval. We find power-law indices of $\alpha = 2.36$, 2.26 and 2.16, for $C = 3$, 5 and 7, respectively. Interestingly, each increase of the combination interval by two time steps reduces the observed power-law by 0.10. The changes in the frequency distribution happen only in the higher energy part while leaving the lower energy cutoff unchanged.

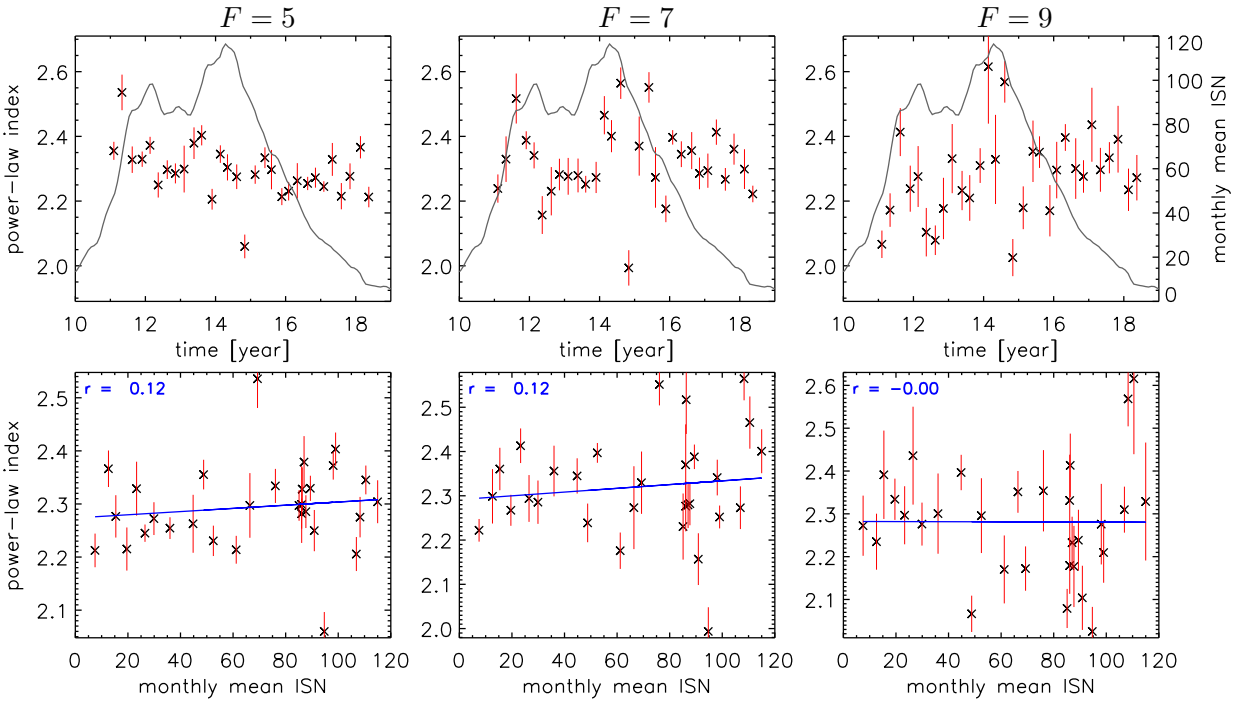

Fig. 6.8.: Same as Figure 6.7 but for different threshold factors $F = 5$, 7 and 9 (left to right). The left panels show results from the reference method.

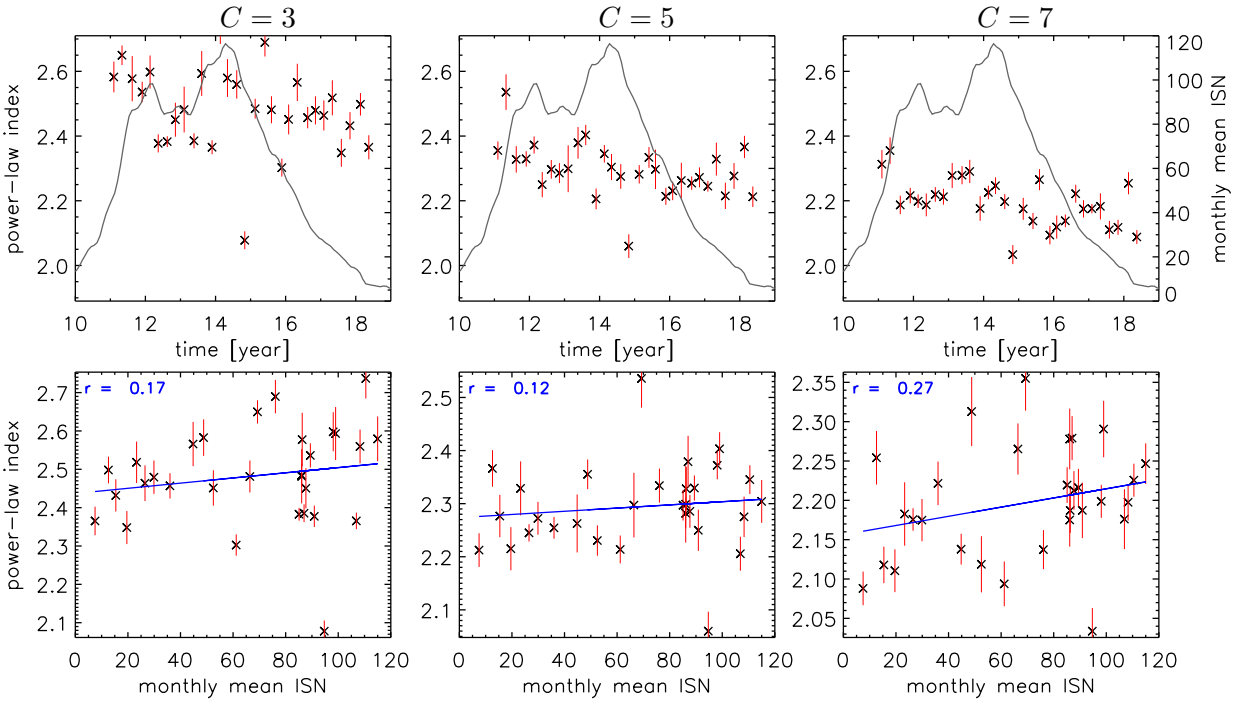

Fig. 6.9.: Same as Figure 6.7 but for different combination intervals $C = 3$, 5 and 7 (left to right). The middle panels show results from the reference method.

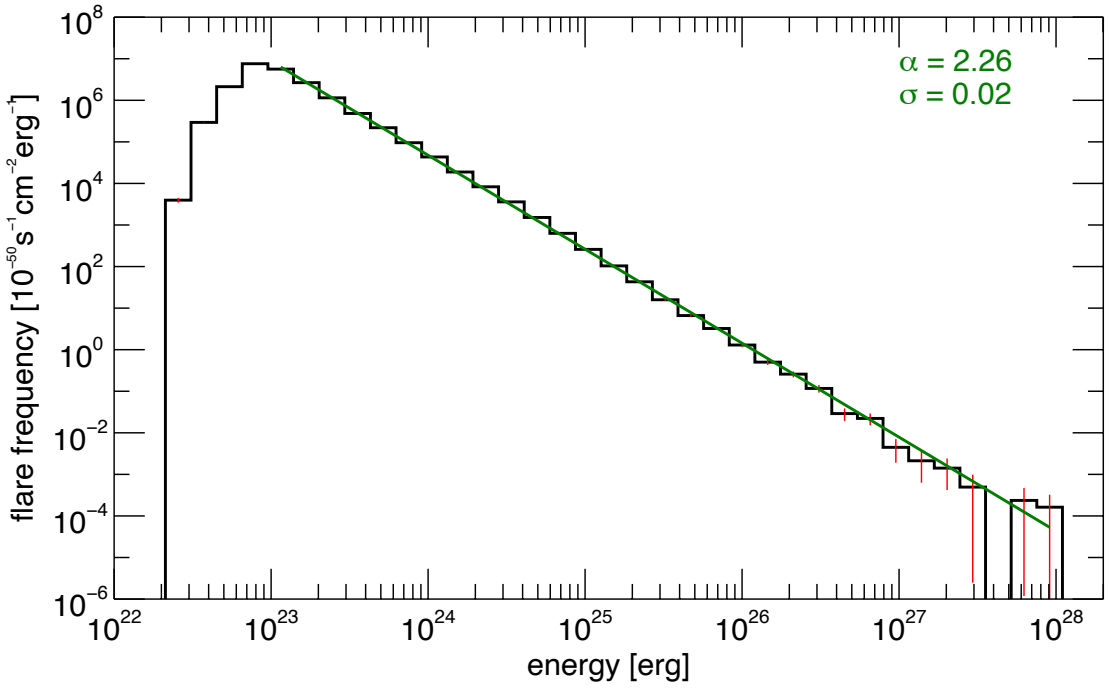

Fig. 6.10.: Combined nanoflare frequency distribution (black) from all data sets. The shown linear fit without weights (green) uses an extended fitting range compared to the individual datasets because of much better statistics. The derived standard deviation (α) and its fitting error (σ) are annotated.

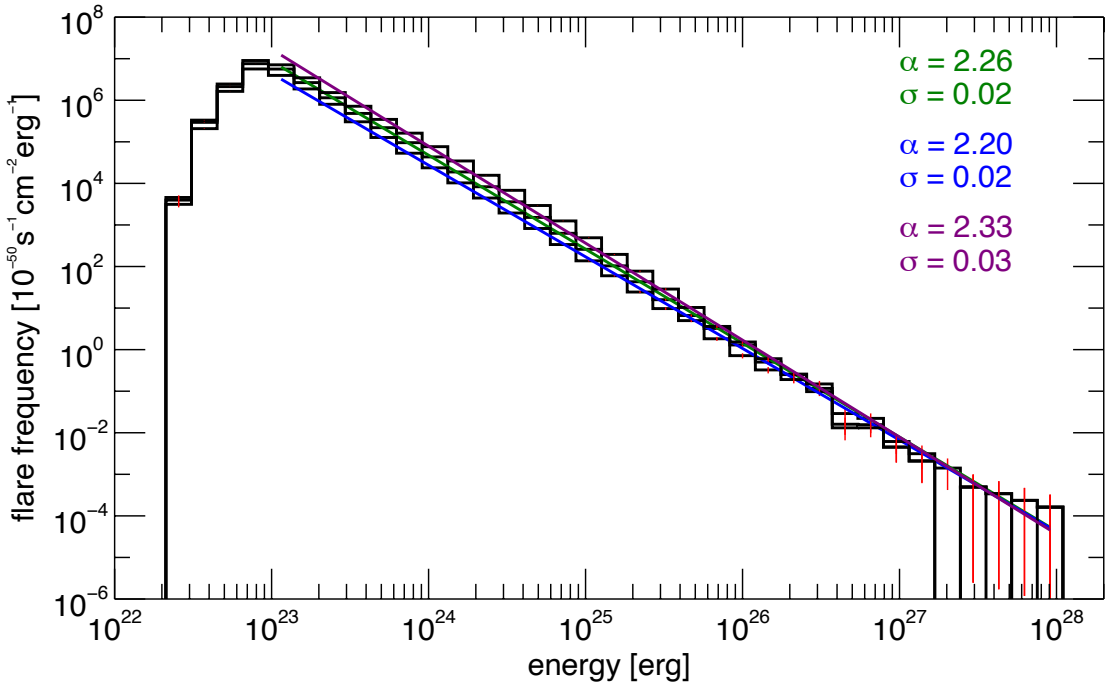

Fig. 6.11.: Same as Fig. 6.10, but showing nanoflare frequency distributions and linear fits for the different detection intervals $D = 1$ (blue), 2 (green), and 4 (purple).

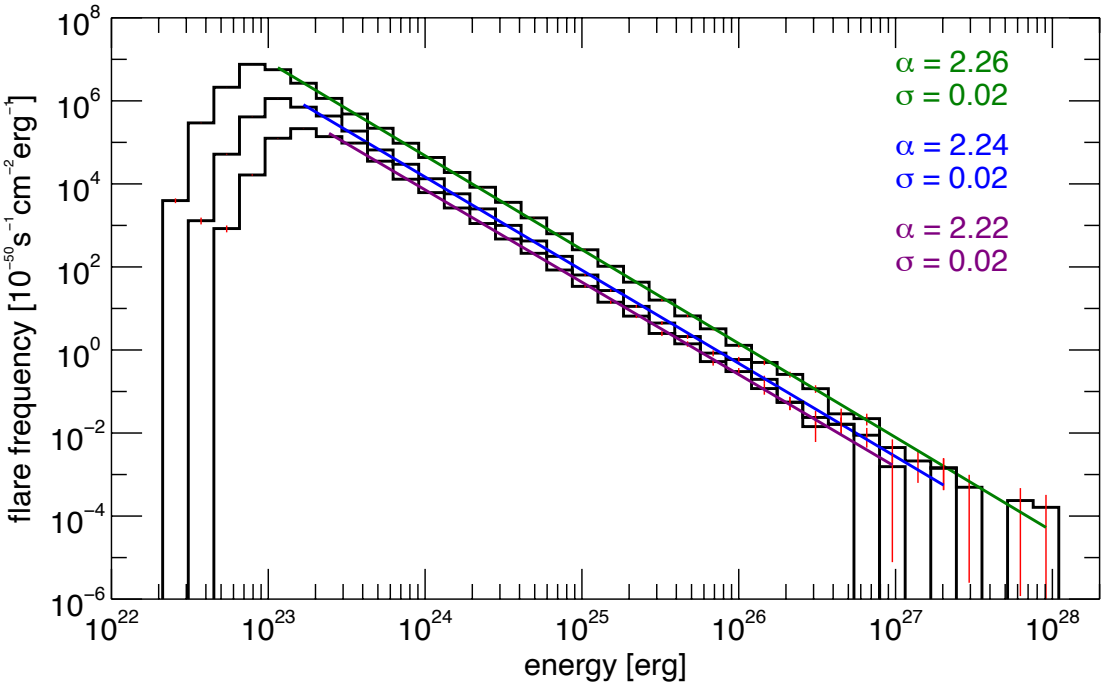

Fig. 6.12.: Same as Fig. 6.10, but showing nanoflare frequency distributions and linear fits for the different threshold factors $F = 5$ (green), 7 (blue), and 9 (purple).

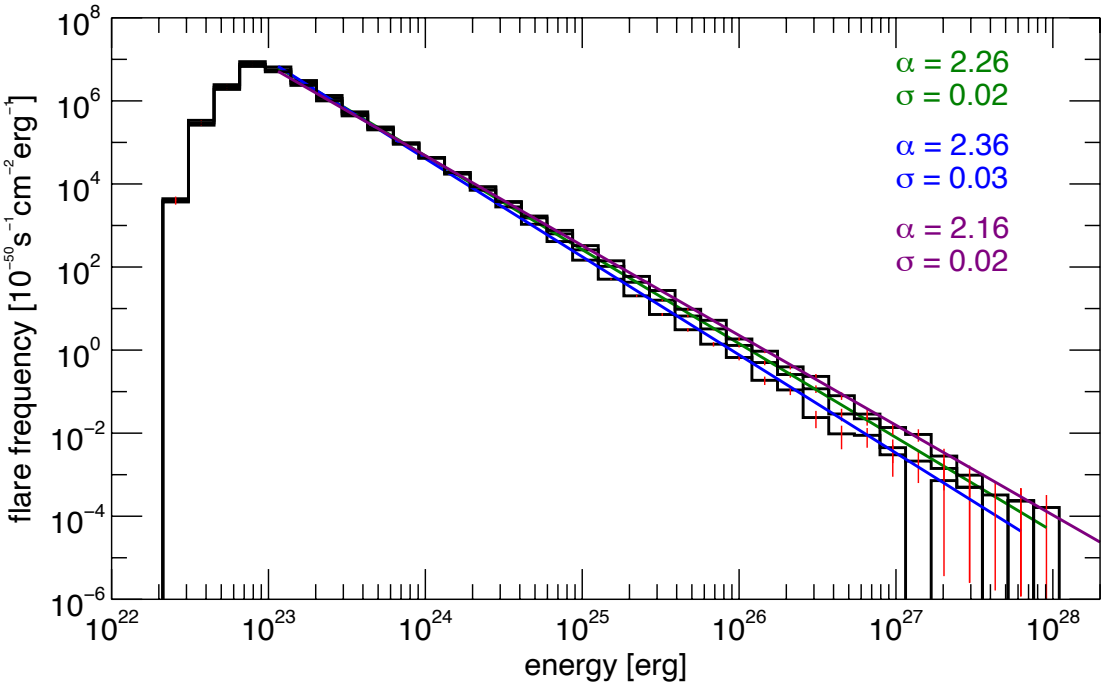

Fig. 6.13.: Same as Fig. 6.10, but showing nanoflare frequency distributions and linear fits for the different combination intervals $C = 3$ (blue), 5 (green), and 7 (purple).

6.2 Observed Energy Flux

The observed energy flux represents the detected thermal event energy normalized per unit time and area. We first added up the corrected energy of all events found during an observation series. The resulting total energy was then divided by the total observation time and the area covered in the field of view, resulting in the desired energy flux in units of $\mathrm{erg\,cm^{-2}\,s^{-1}}$. The reference method yields an energy input into the corona of 0.02×10^5 to $0.04 \times 10^5\,\mathrm{erg\,cm^{-2}\,s^{-1}}$. Only about one percent of the minimum required heating rate of $3 \times 10^5\,\mathrm{erg\,cm^{-2}\,s^{-1}}$ (section 3.2).

Figure 6.14 shows the energy flux (mean over observation time) found by the reference method for each pixel and all data sets across the solar cycle. The energy flux is evidently not distributed evenly across pixels but instead forms clusters. However, such clusters are then spread out over the whole field of view. High observed energy flux in a pixel can either be the result of a few large events or arise from the occurrence of multiple smaller events. Also, a combination of both influences is possible, especially for pixels with the highest energy flux. In addition to the smaller clusters, some data sets show large-scale structures that produce much thermal energy. Interestingly, the center regions of such large-scale structures often completely lack event observations and appear black in the images shown. Examples are the top right corner of the datasets from 2011-08-16 and 2011-11-28.

In Figure 6.15 we compare the observed energy flux for different event detection intervals and find that a larger detection interval leads to an overall increase of the detected energy flux. Therefore, large detection intervals have to either find more events or lead to higher individual event energies. Surprisingly, the detected energy flux rises slightly during the second half of the analyzed time frame, starting from about 2014. This leads to an overall trend of higher detected flux at a lower solar activity. Correlation coefficients to the sunspot number remain low in a range of $r = -0.03$ to -0.24. In Figure 6.16 the changes resulting from different threshold factors are shown. As expected, the observed energy flux decreases as the threshold is increased since a higher threshold removes more events from the observation. A threshold factor of $F = 9$ reduces the energy flux to about a tenth of the amount found with the reference method using $F = 5$. All threshold factors preserve the slight trend of higher observed energy flux at lower solar activity with a low anti-correlation to the sunspot number in the range of $r = -0.13$ to -0.21. The comparison of different combination intervals is shown in Figure 6.17. As expected, we find only minimal changes between different intervals. Independent of the used method, we find significantly higher energy flux in the data set from 2016-02-01, resulting in a strong outlier in the flux evolution. The increased energy flux that can also be seen in Figure 6.14 in the form of extended red areas.

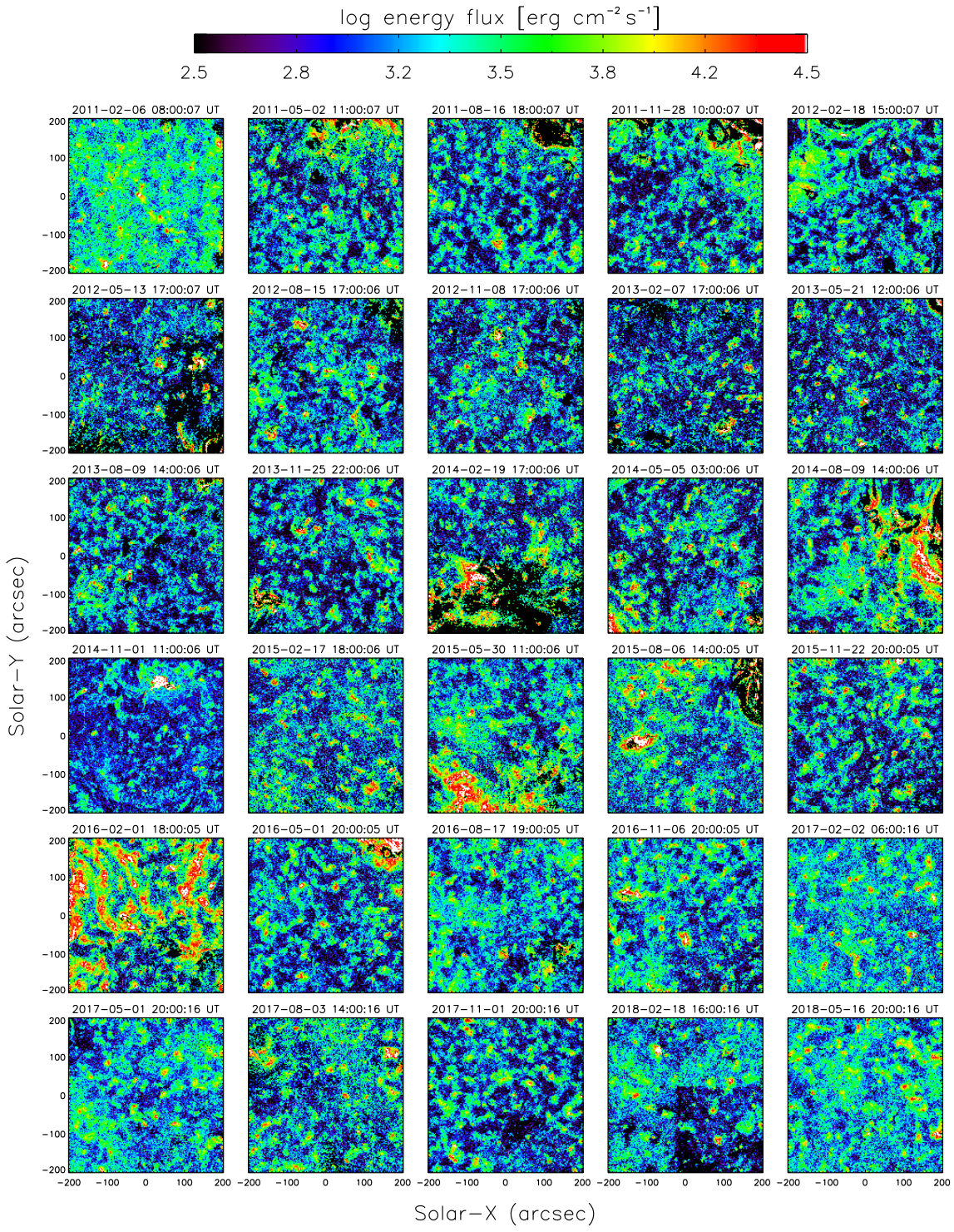

Fig. 6.14.: Spatial distribution of the derived energy flux by the reference method for each pixel in all data sets during 2011 to 2018. Flux for each pixel was calculated by averaging its total detected event energy over the two hour observation time and the area of the pixel. The beginning of each observation is given on top.

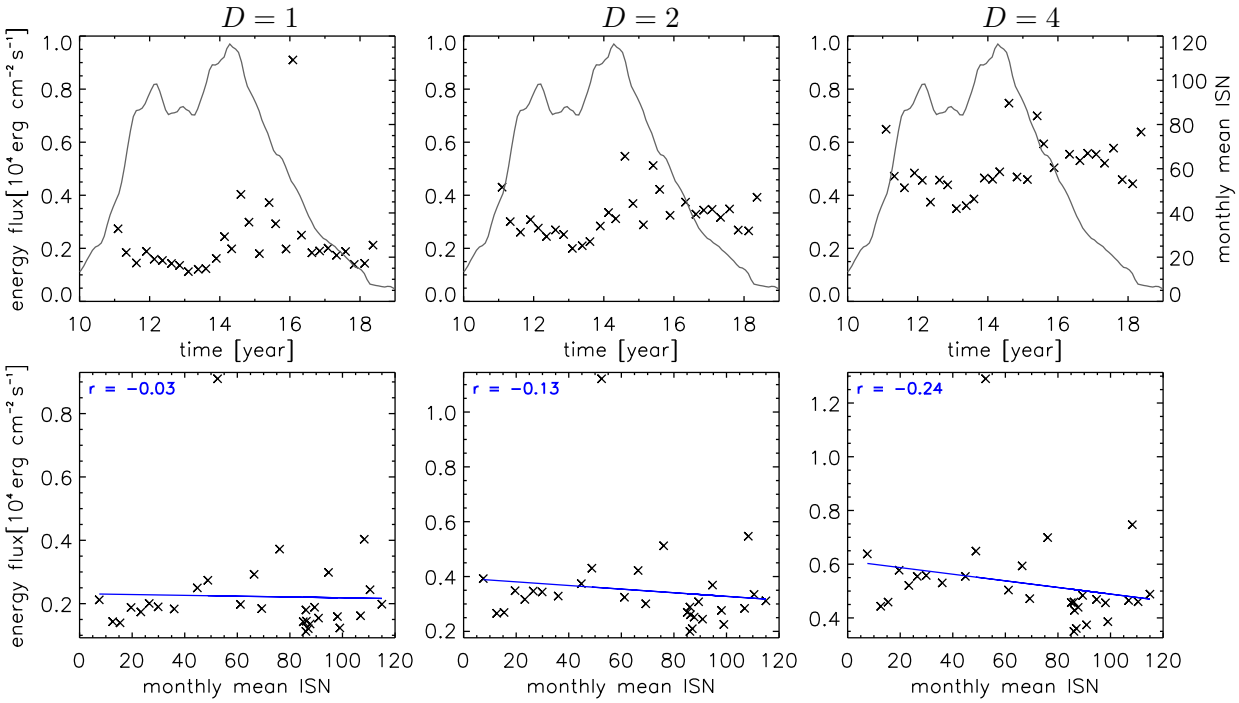

Fig. 6.15.: Energy flux for different detection intervals $D = 1$, 2 and 4 (left to right). The middle panels show results from the reference method. Values extracted for each data set are plotted as a function of time (top row) together with the sunspot number (gray). Correlation to the sunspot number (bottom row), with a linear fit (blue) and correlation coefficient (r) is also shown.

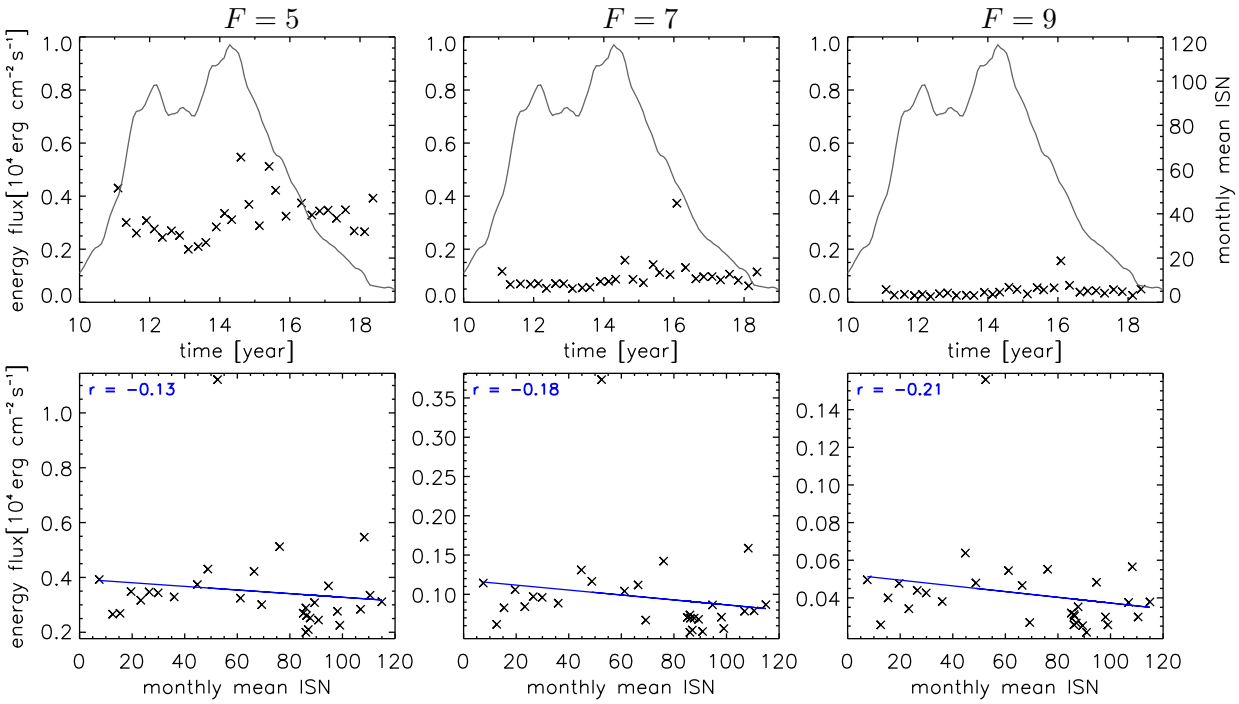

Fig. 6.16.: Same as Figure 6.15 but for different threshold factors $F = 5$, 7 and 9 (left to right). The left panels show results from the reference method.

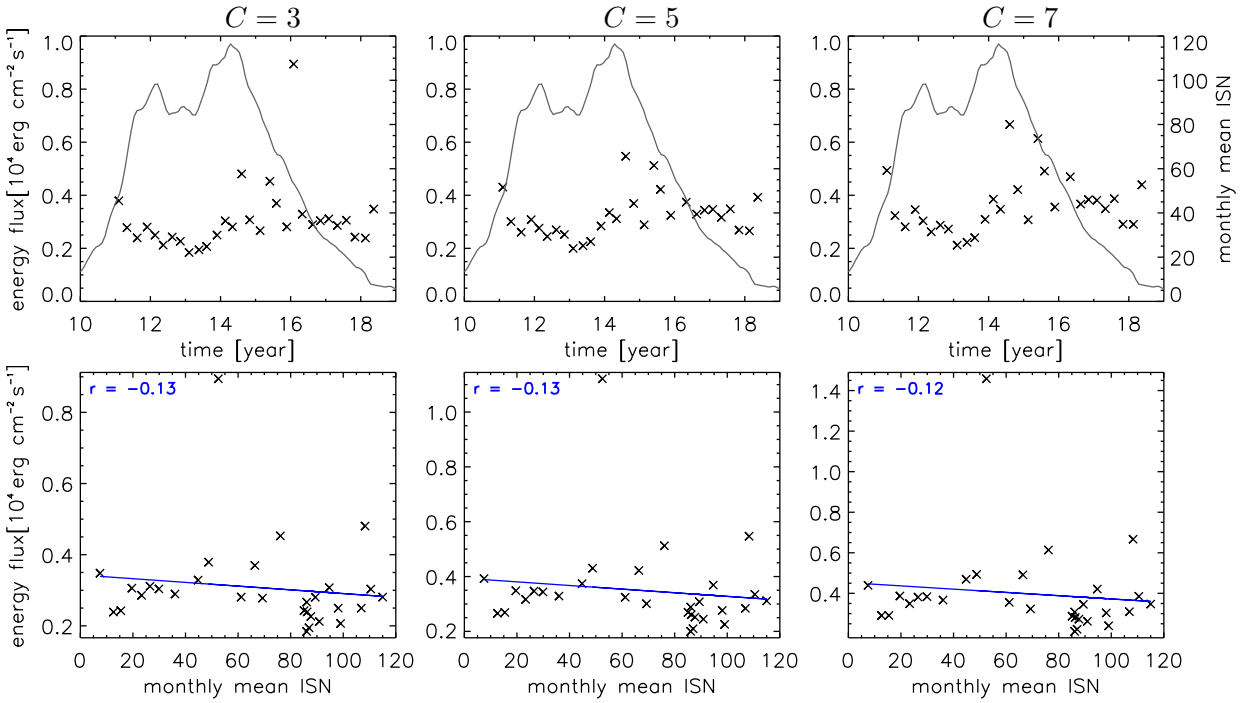

Fig. 6.17.: Same as Figure 6.15 but for different combination intervals $C = 3$, 5 and 7 (left to right). The middle panels show results from the reference method.

6.3 Statistics of Active Pixels

We define a pixel to be active if it is part of at least one event during the observations. The two interesting metrics derived from this definition are the fraction of pixels considered active during our observation and the number of event counts in active pixels. Combined, they allow us to determine whether observed events are spread evenly across the field of view or clustered in certain areas like in the spatial distribution of the energy flux (Figure 6.14). Furthermore, it highlights active pixel regions that are the source of many events independent of their individual energy.

Figure 6.18 shows the spatial distribution of active pixels and their event counts as found by the reference method for each data set. Most of the observed pixels are active as they contain at least one event. However, the number of events is not evenly distributed but instead shows clusters of high activity. There seems to be a trend towards more events in later observations, visible through the increased number of green pixel areas (7 to 10 events) with red centers (12 events and more). Areas with the most activity correlate well with areas we observed the most considerable energy flux in, but especially the extended green areas found in later data sets do not necessarily result in significant energy flux over the same region. On the other hand, there are also areas where no event is found during the two-hour-long observation. They mostly correspond to the brightest areas from the AIA images and

were previously discussed as areas with missing energy flux observations. Noticeably, the map from 2014-08-09 shows much activity in the small-scale coronal hole that covers the bottom left quadrant. Unexpectedly, there are also square areas in the lower right-hand corner of some images, most noticeable in 2018-02-18 and visible in others. They are characterized by a well-defined border where the event number suddenly drops due to reasons unknown.

Changes to the fraction of pixels considered active depending on the method parameters are shown in Figures 6.19 and 6.20. Since active pixels are determined independently of the event combination, the combination interval is not included. A higher detection interval increases the fraction of active pixels, while a higher threshold factor decreases it. The correlation to the sunspot number is $r = -0.58$ for the reference method and only varies slightly for other methods. The negative correlation confirms the observation of larger active pixel regions in later data sets. Over $80\,\%$ of pixels are active throughout all data sets analyzed by the reference method.

Concerning the number of events in active pixels, we looked at the maximum event count obtained and also calculated the mean number of events from all active pixels. Figures 6.21 and 6.22 show the maximum event count in a single pixels across methods. It is very stable towards any changes of the detection interval and stays in a range of 20 to 30 counts across all data sets. Higher thresholds lower the maximum event count in active pixels until they reach a range of 10 to 20 counts at a threshold factor of $F = 9$. We observe a slight trend of higher maximum counts at a higher solar activity. Figures 6.23 and 6.24 show the same changes but for the mean number of events found in all active pixels. With an increased detection interval, the mean event count rises across all data sets, and the observed negative correlation is enhanced up to $r = -0.55$. On the other hand, higher threshold factors lower the mean number of detected events and show no correlation to the sunspot number ($r = -0.09$ and -0.01).

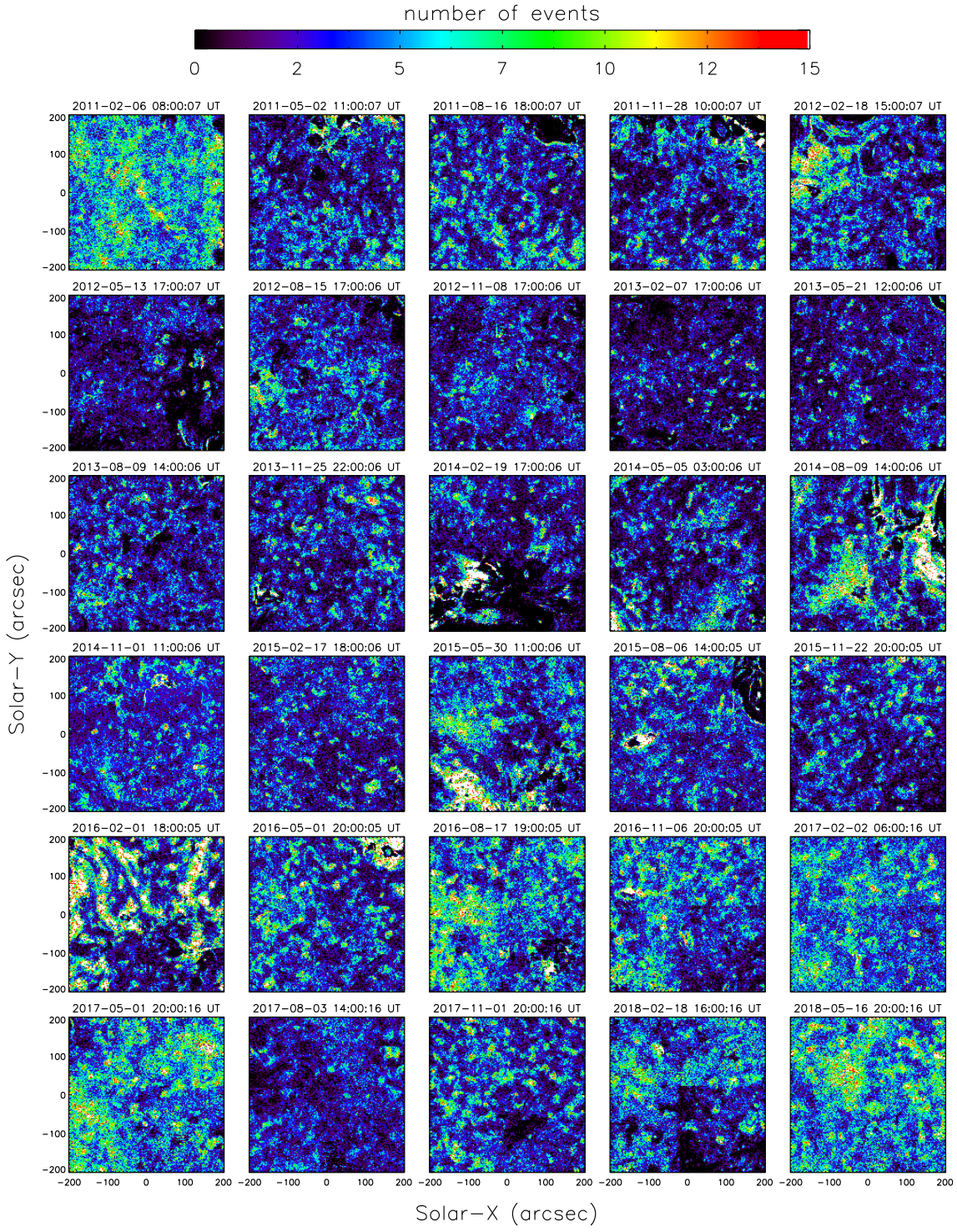

Fig. 6.18.: Spatial distribution of active Pixels found by the reference method in all data sets. Colors represent the number of events in an active pixel during the two-hour observation time. The beginning of each observation is given on top.

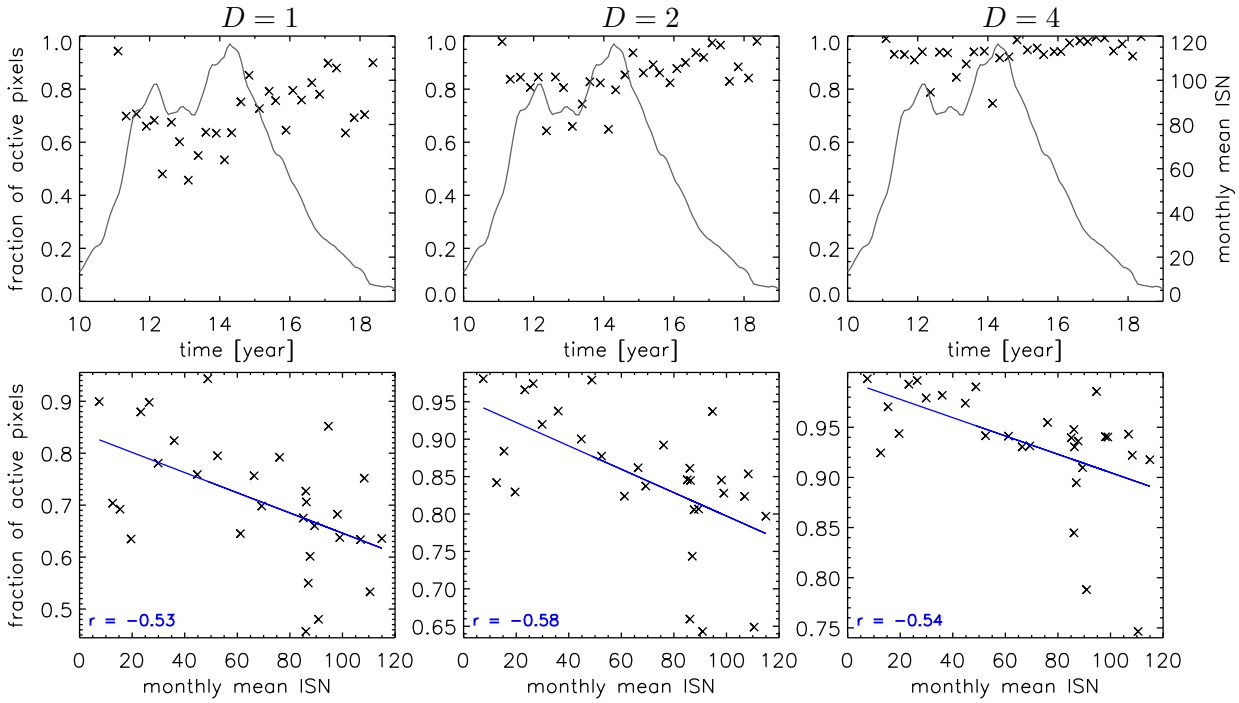

Fig. 6.19.: Fraction of active pixels for different detection intervals $D = 1$, 2 and 4 (left to right). The middle panels show results from the reference method. Values extracted for each data set are plotted as a function of time (top row) together with the sunspot number (gray). Correlation to the sunspot number (bottom row), with a linear fit (blue) and correlation coefficient (r) is also shown.

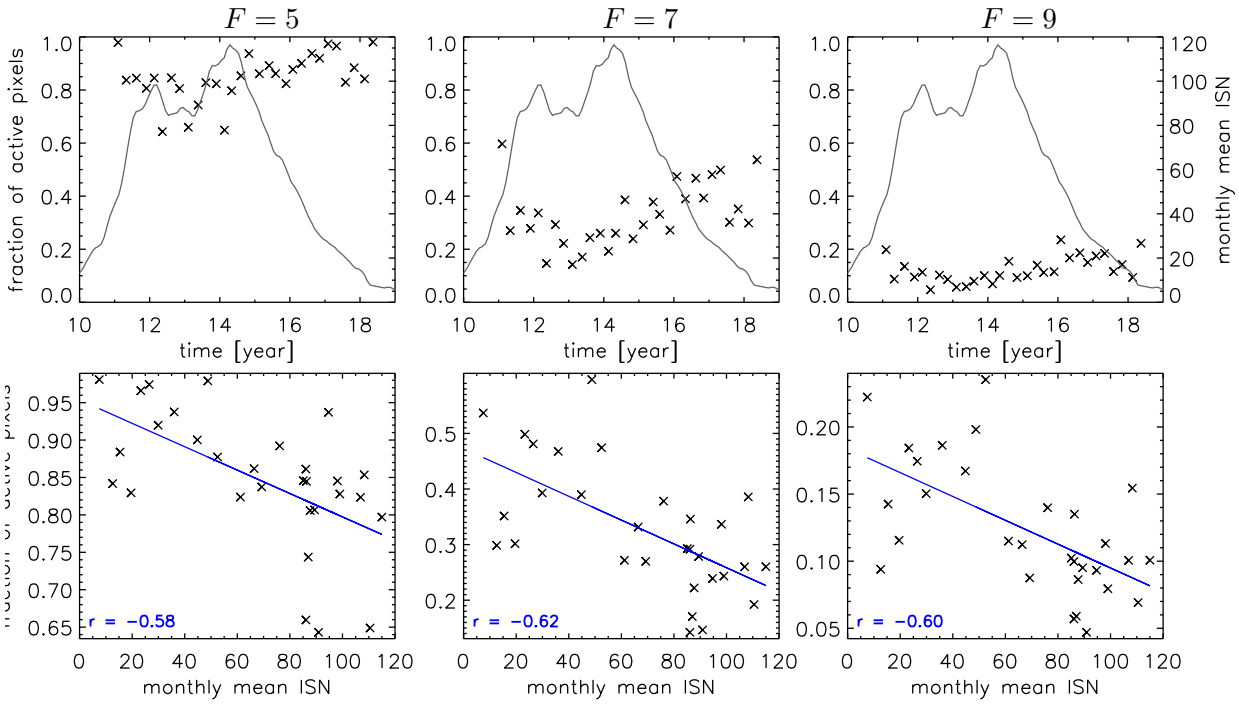

Fig. 6.20.: Same as Figure 6.19 but for different threshold factors $F = 5$, 7 and 9 (left to right). The left panels show results from the reference method.

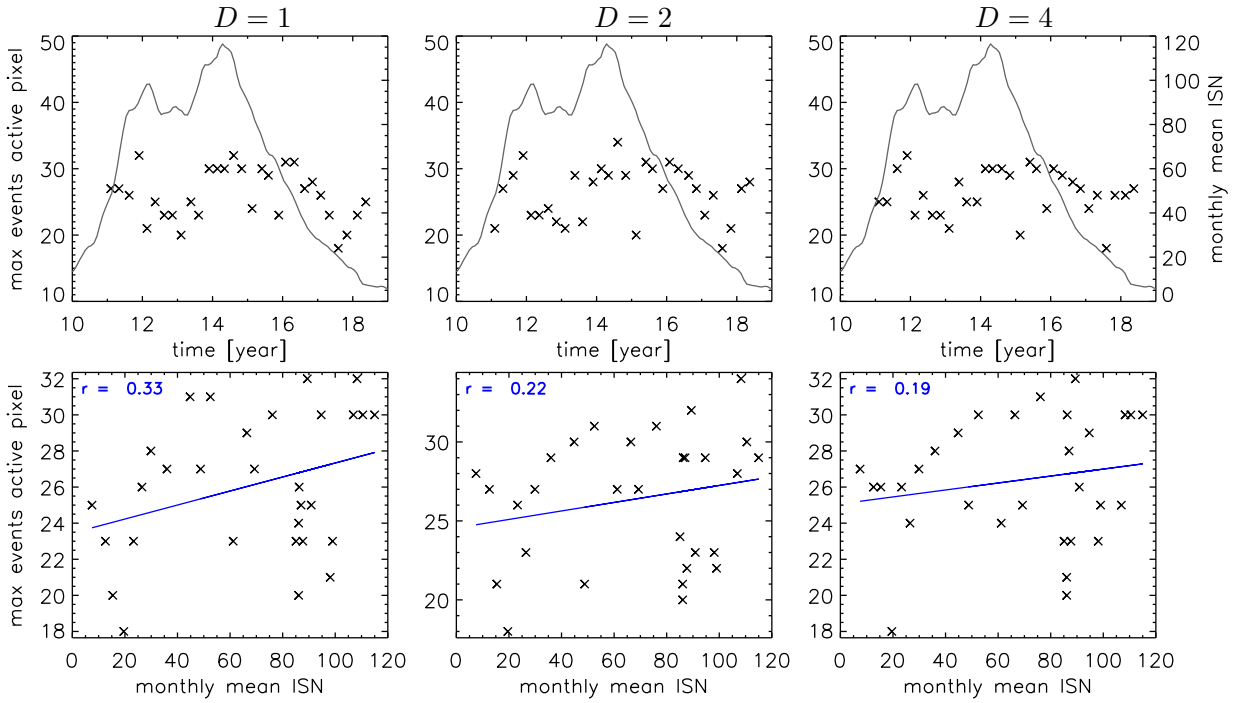

Fig. 6.21.: Maximum number of events in an active pixel for different detection intervals $D = 1$, 2 and 4 (left to right). The middle panels show results from the reference method. Values extracted for each data set are plotted as a function of time (top row) together with the sunspot number (gray). Correlation to the sunspot number (bottom row), with a linear fit (blue) and correlation coefficient (r) is also shown.

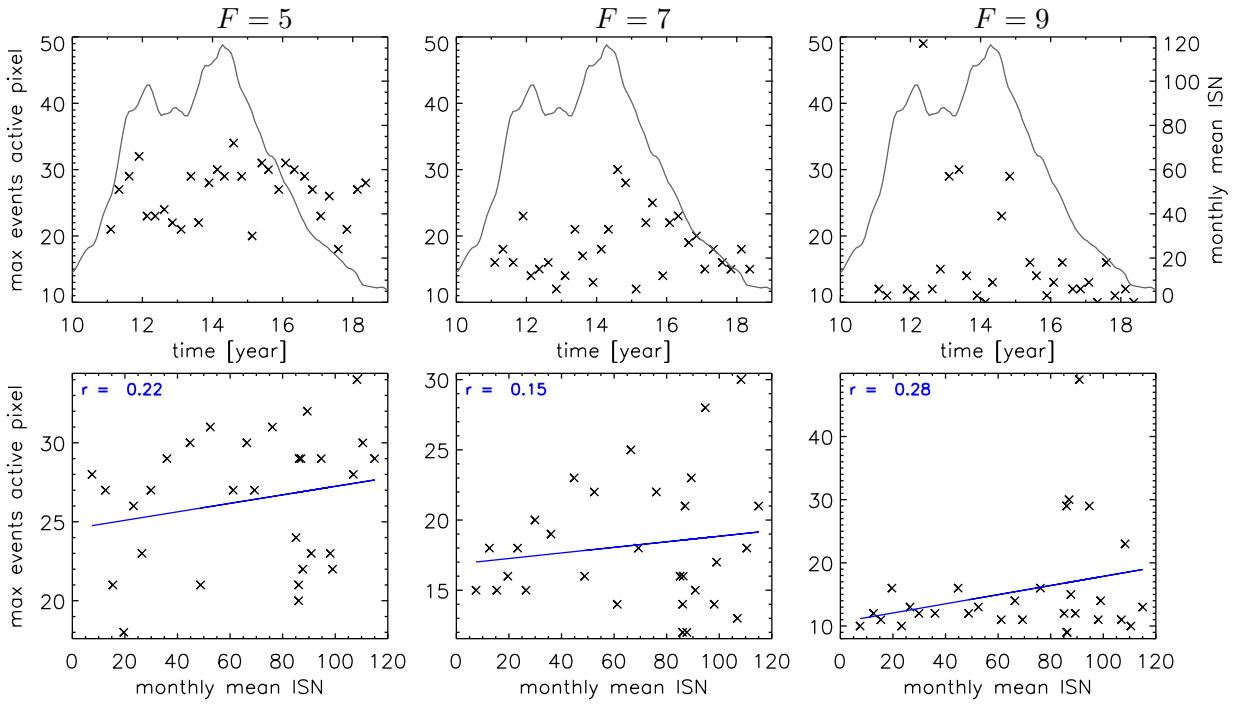

Fig. 6.22.: Same as Figure 6.21 but for different threshold factors $F = 5$, 7 and 9 (left to right). The left panels show results from the reference method.

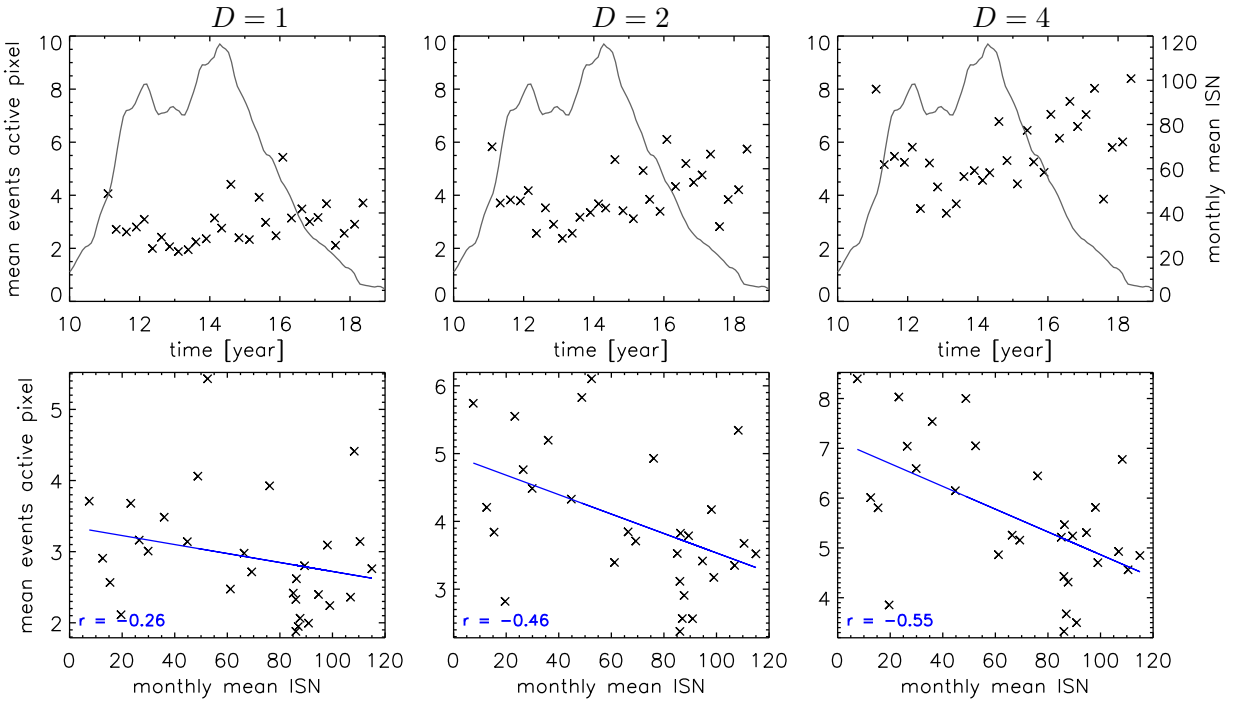

Fig. 6.23.: Mean number of events in active pixels for different detection intervals $D = 1$, 2 and 4 (left to right). The middle panels show results from the reference method. Values extracted for each data set are plotted as a function of time (top row) together with the sunspot number (gray). Correlation to the sunspot number (bottom row), with a linear fit (blue) and correlation coefficient (r) is also shown.

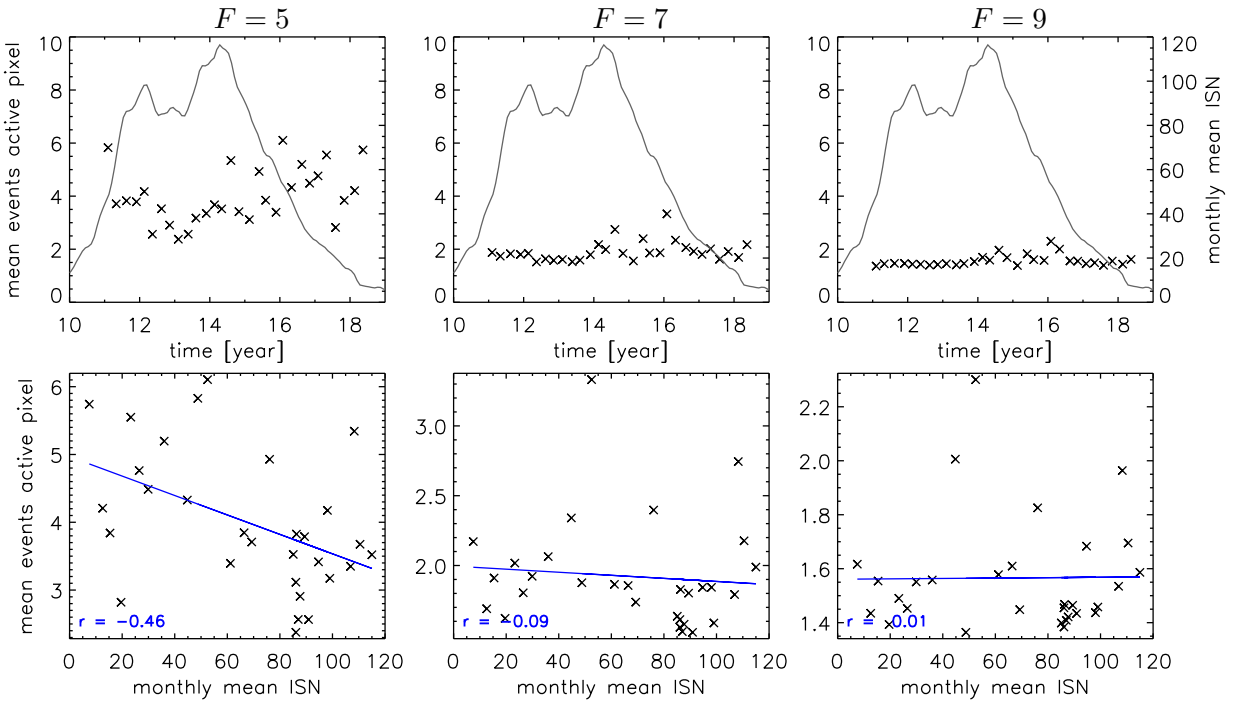

Fig. 6.24.: Same as Figure 6.23 but for different threshold factors $F = 5$, 7 and 9 (left to right). The left panels show results from the reference method.

6.4 Spatial Distribution of Nanoflares

To further analyze the spatial distribution of the observed nanoflares, we produced comparison plots between the HMI line-of-sight magnetogram, the energy flux map, the active pixels map, and three selected AIA wavelength channels (171, 193 and 211 Å). Figures 6.25 to 6.29 show these comparisons for a selection of interesting data sets, and additional plots can be found in the appendix in section A.5. In addition, we show contours of areas with a mean energy flux over two hours that exceeds $5 \times 10^3\,\mathrm{erg\,cm^{-2}\,s^{-1}}$ plotted on top of HMI magnetograms. These images can be seen in Figures 6.30 to 6.33 for selected data sets and additional plots are again provided in section A.5 of the appendix. We find that the areas with the highest energy flux tend to be located in the magnetic network, with a strong preference for boundary regions of strong opposing fields.

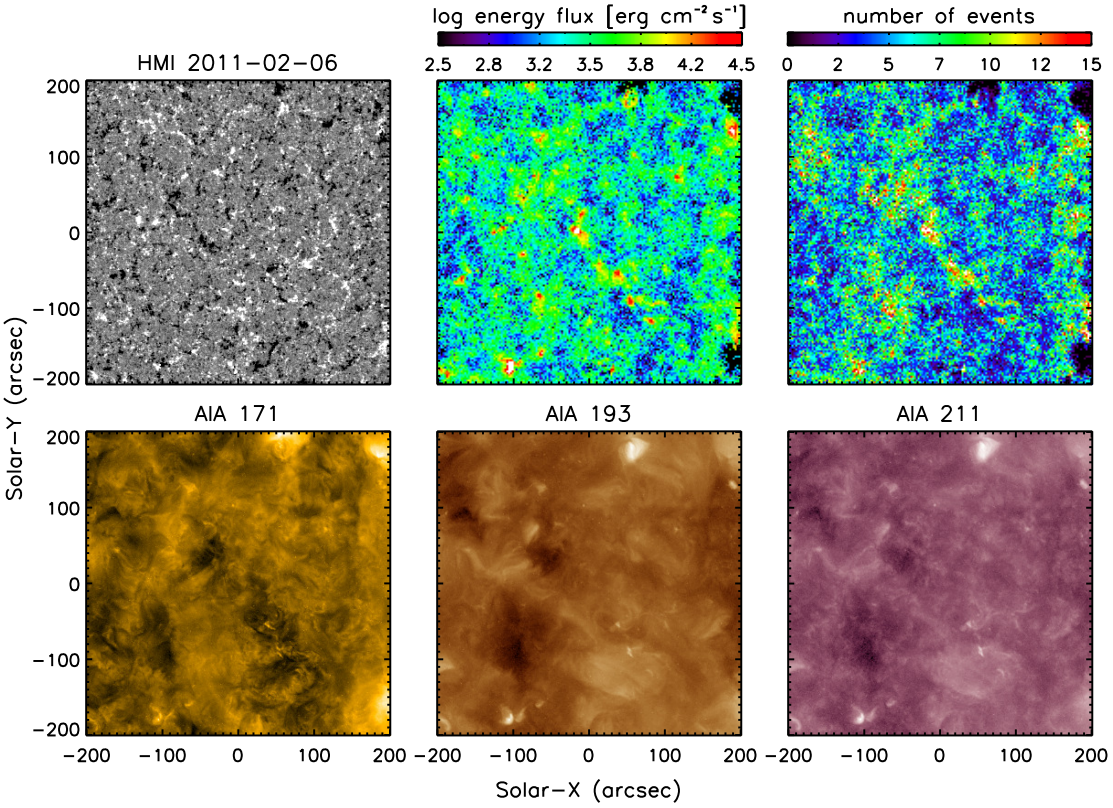

Fig. 6.25.: Comparison of the HMI line-of-sight magnetogram, the spatial distribution of energy flux and the event count, and AIA images in the 171, 193 and 211 Å wavelength bands. Energy flux and event count were extracted by the reference set of parameters and the energy flux in each pixel is given as the mean over the two hours observation time. The date of the data series is given on top of the HMI magnetogram.

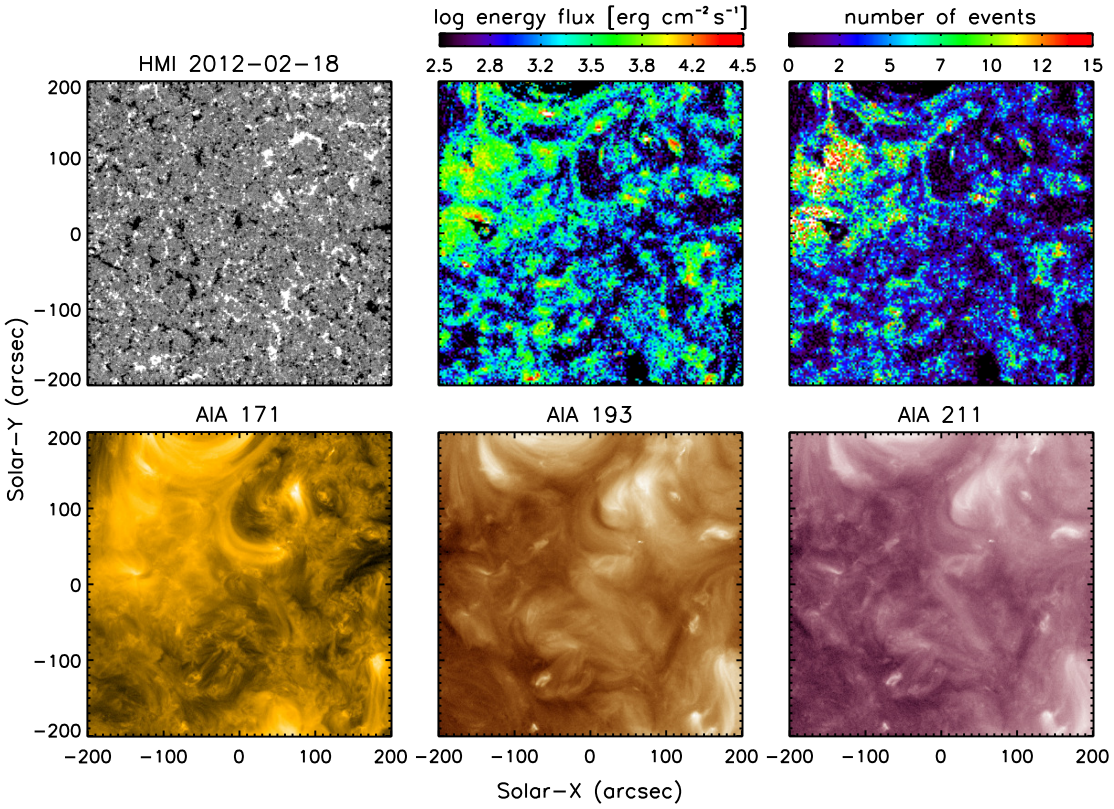

Fig. 6.26.: Same as Figure 6.25.

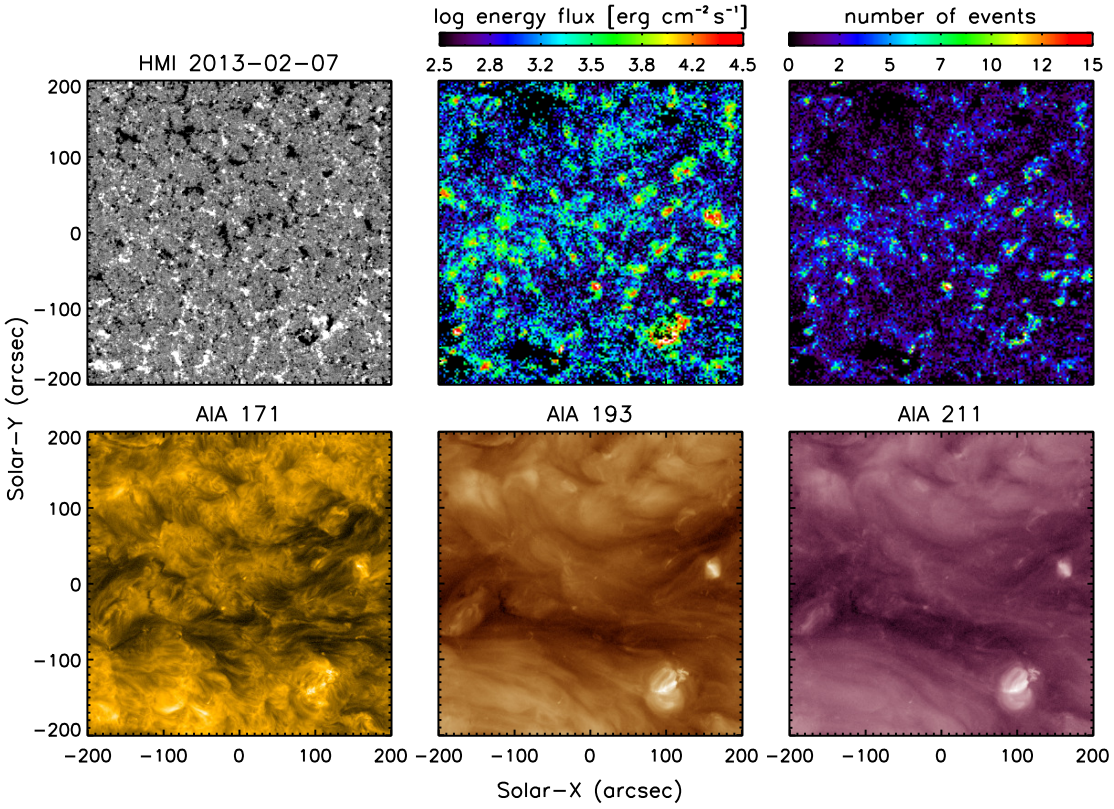

Fig. 6.27.: Same as Figure 6.25.

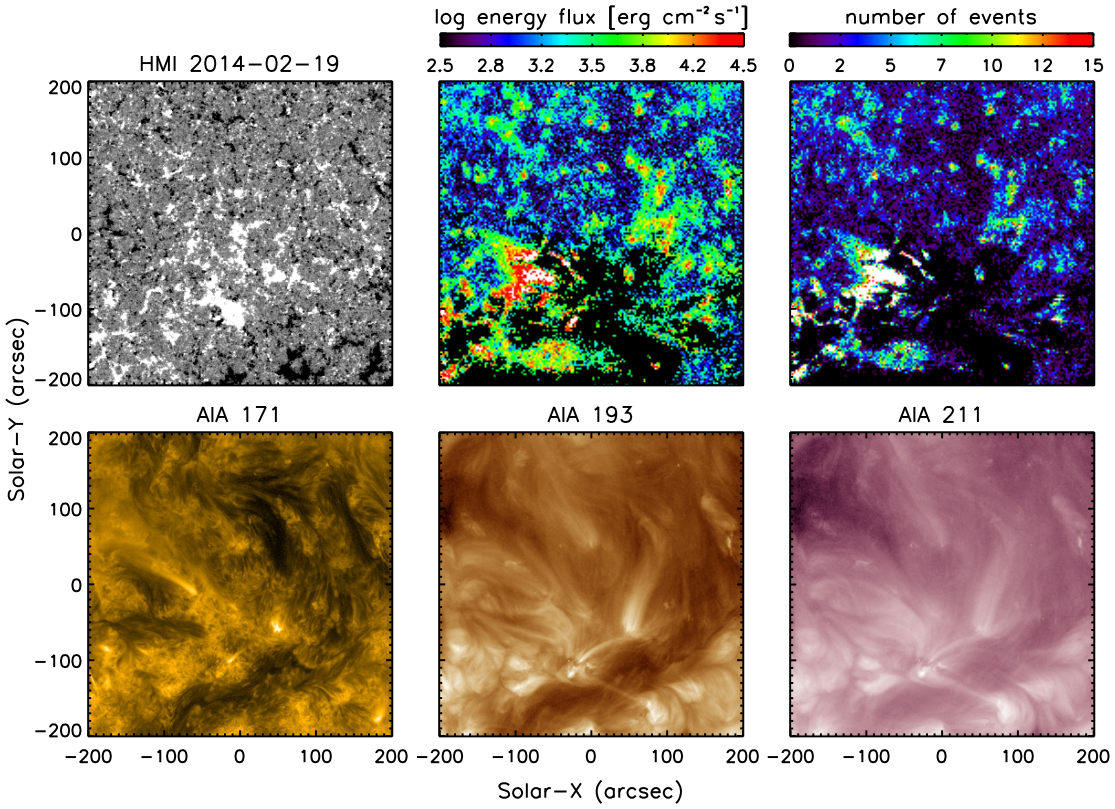

Fig. 6.28.: Same as Figure 6.25.

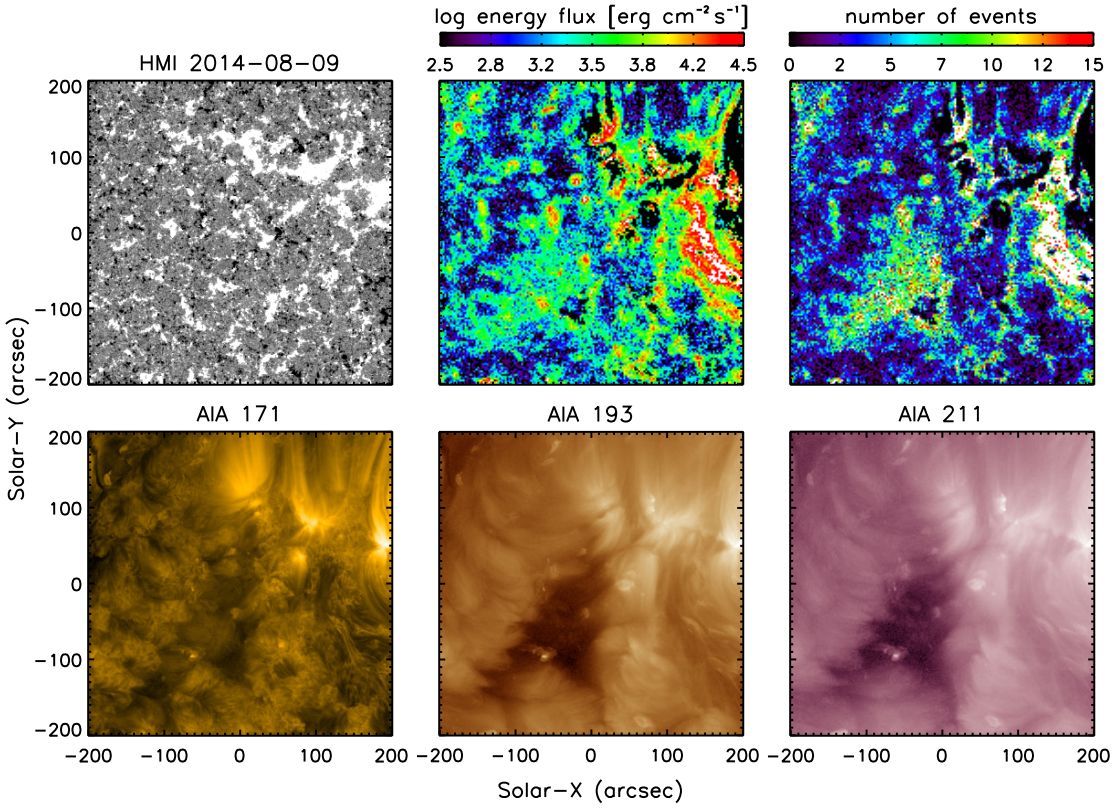

Fig. 6.29.: Same as Figure 6.25.

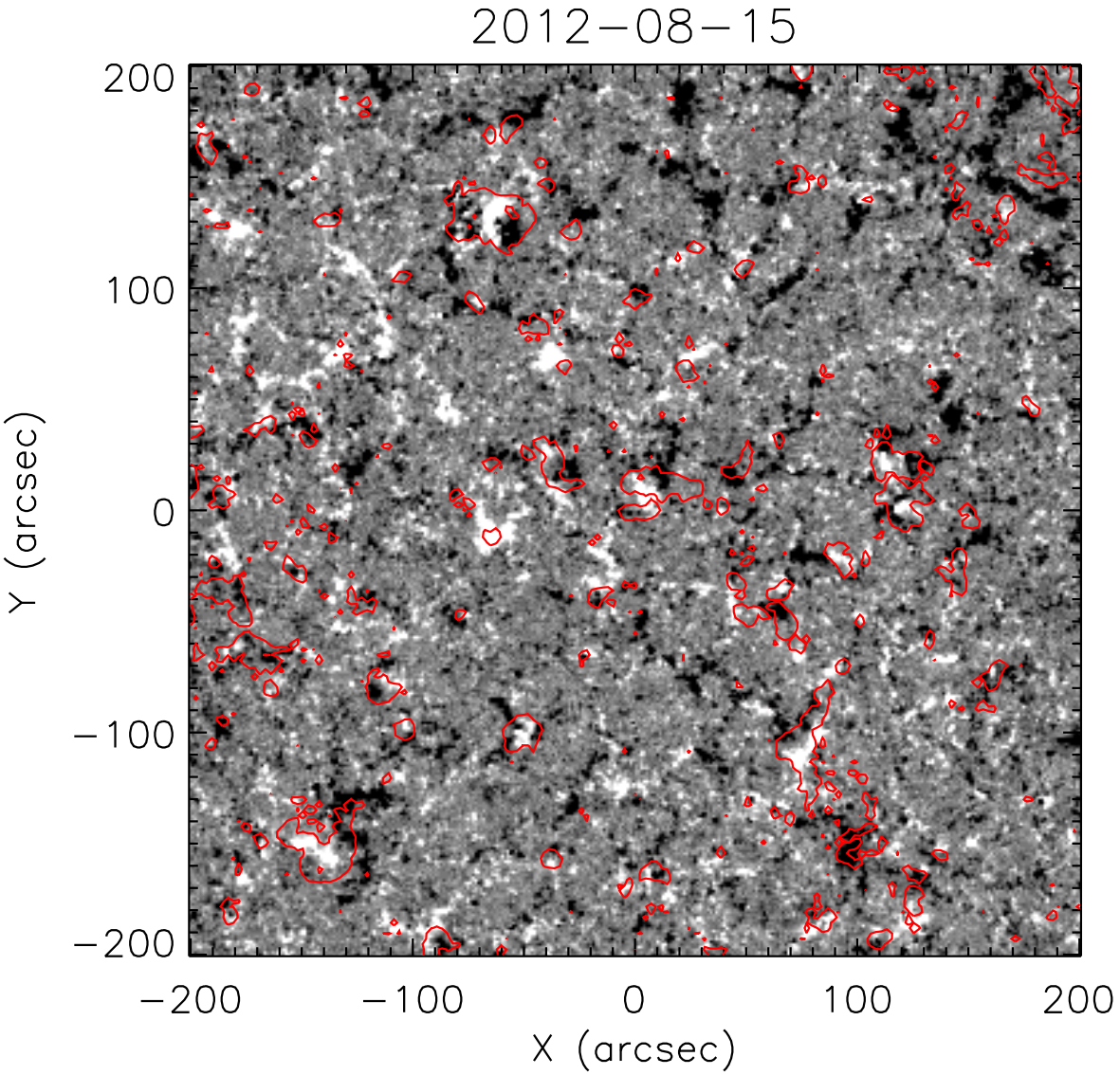

Fig. 6.30.: HMI line-of-sight magnetogram with red contours marking areas that exceed a mean energy flux of $5 \times 10^3\,\mathrm{erg\,cm^{-2}\,s^{-1}}$ over the two hour observation time. Magnetogram is saturated at $\pm 15\,\mathrm{G}$ and the date of the data set is given on top.

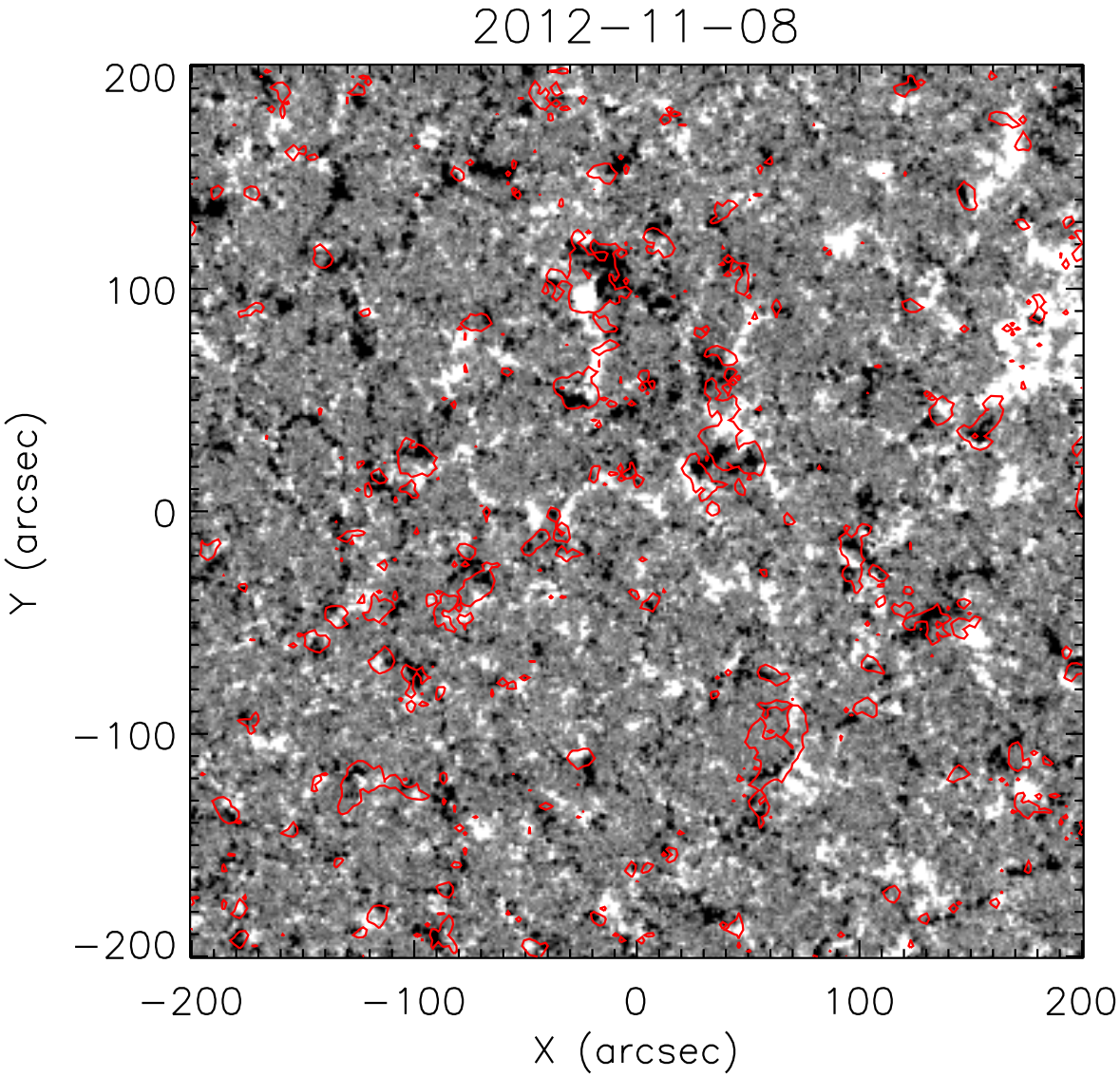

Fig. 6.31.: Same as Figure 6.30.

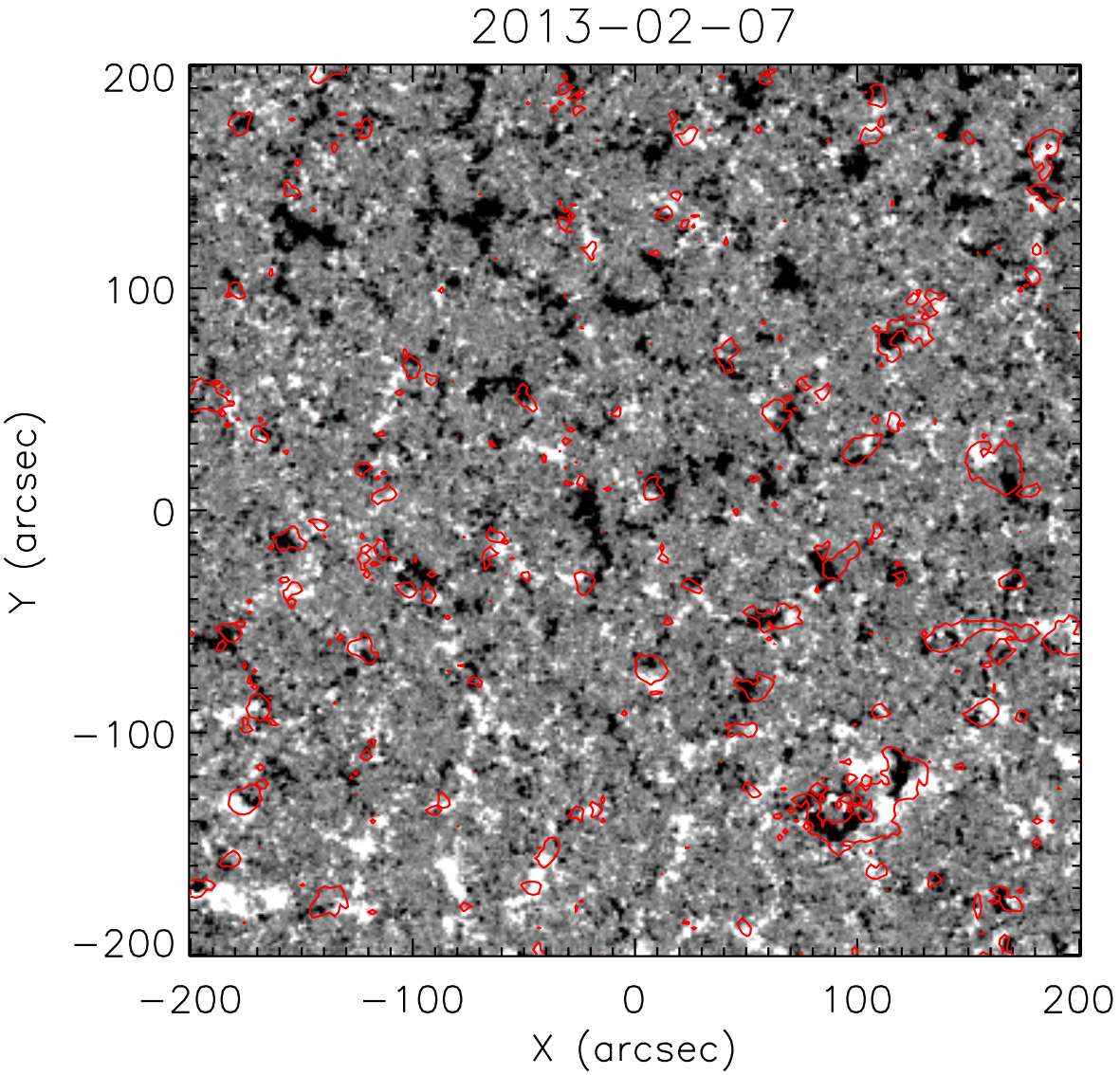

Fig. 6.32.: Same as Figure 6.30.

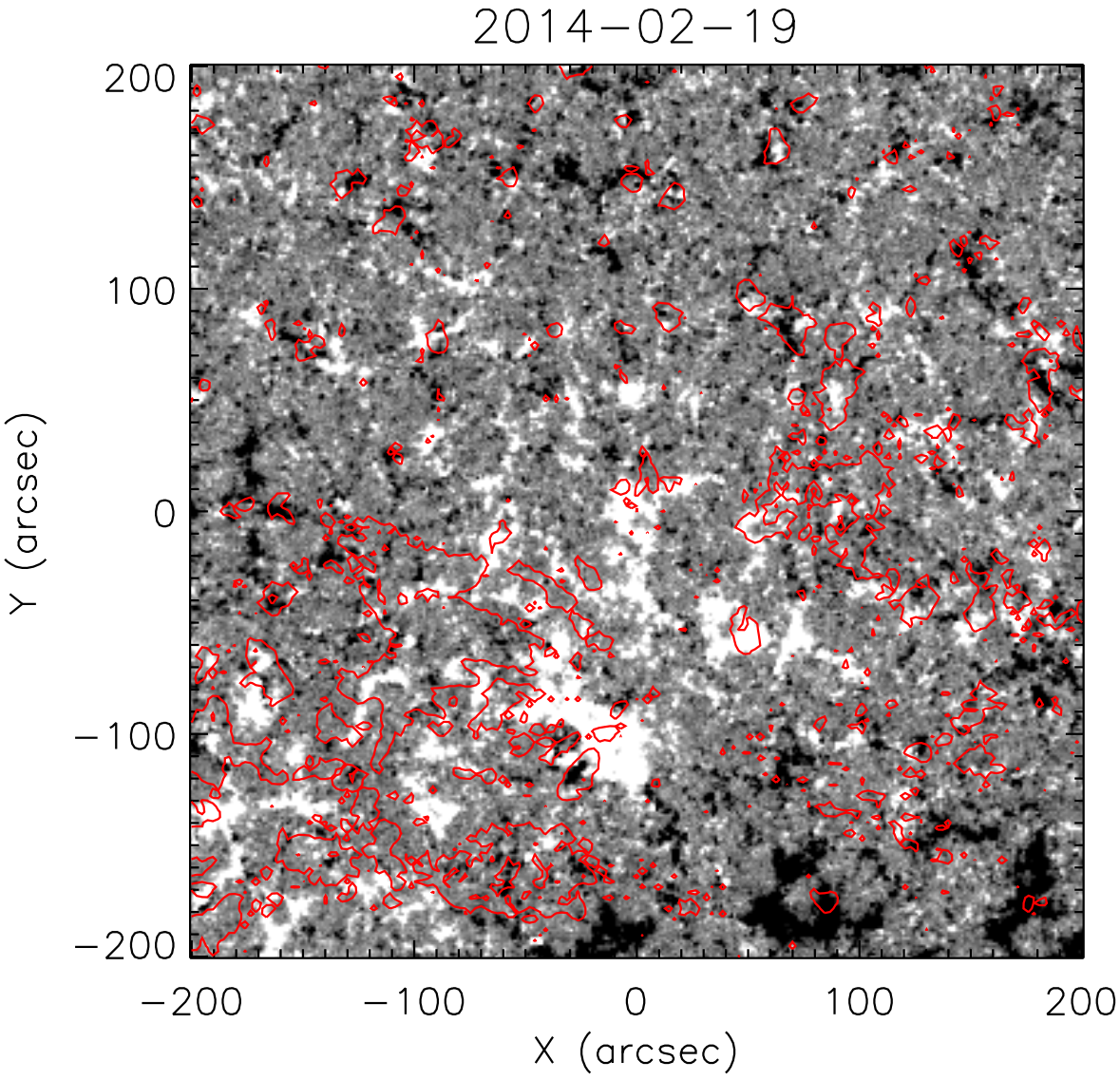

Fig. 6.33.: Same as Figure 6.30.

6.5 Event Combination Results

In this section, we focus on statistics concerning the event areas generated by different methods. Figure 6.34 shows the distribution of areas for each data set analyzed by the reference method. All data set shows a clear maximum at an event size of one pixel and a continuous decrease in frequency for larger event sizes. There are typically about 0.5×10^4 events (70 to $85\,\%$ of total events; see sec. 6.6) that consist of just a single pixel, and this frequency rapidly drops below ten events for areas larger than 20 pixels. The histograms are cut off at a maximum area of 100 pixels. Even larger, likely erroneous event areas may form in some cases, especially if the combination interval is big while the threshold factor is set to a low value. However, such false combinations are very rare compared to the total number of events. The area distributions of the other selected methods discussed here are collectively shown in section A.6 in the appendix.

Figures 6.35, 6.36, and 6.37 present the mean event area found for each dataset and compare the changes from different methods. A larger event detection interval increases the mean event area throughout the data sets and also increases the correlation to the monthly sunspot number. Mean event areas increase as the sunspot number decreases with a maximum correlation of $r = -0.68$ using the detection interval $D = 4$. The detection interval $D = 1$ shows no correlation ($r = -0.08$). Higher threshold factors change the mean event area evolution and reduce the correlation to the sunspot number. As expected, an increase in the combination interval generally increases the mean event area throughout all data sets. The correlation remains similar for all intervals at $r = -0.40$ to -0.47.

The total event area found in each data set and the changes caused by the three free parameters are shown in Figures 6.38, 6.39, and 6.40. The total area is the sum of all individual event areas and, therefore, is not dependent on the event combination. The total area given in pixels is also equal to the number of uncombined events detected. Just like the mean area, it rises with larger event detection intervals. However, a correlation of $r = -0.40$ is already present at the lowest interval ($D = 1$) and then rises to $r = -0.59$ for the highest detection interval ($D = 4$). Contrary to the mean, the total event area decreases significantly with lower threshold factors, while the correlation remains in the range of -0.54 to -0.46.

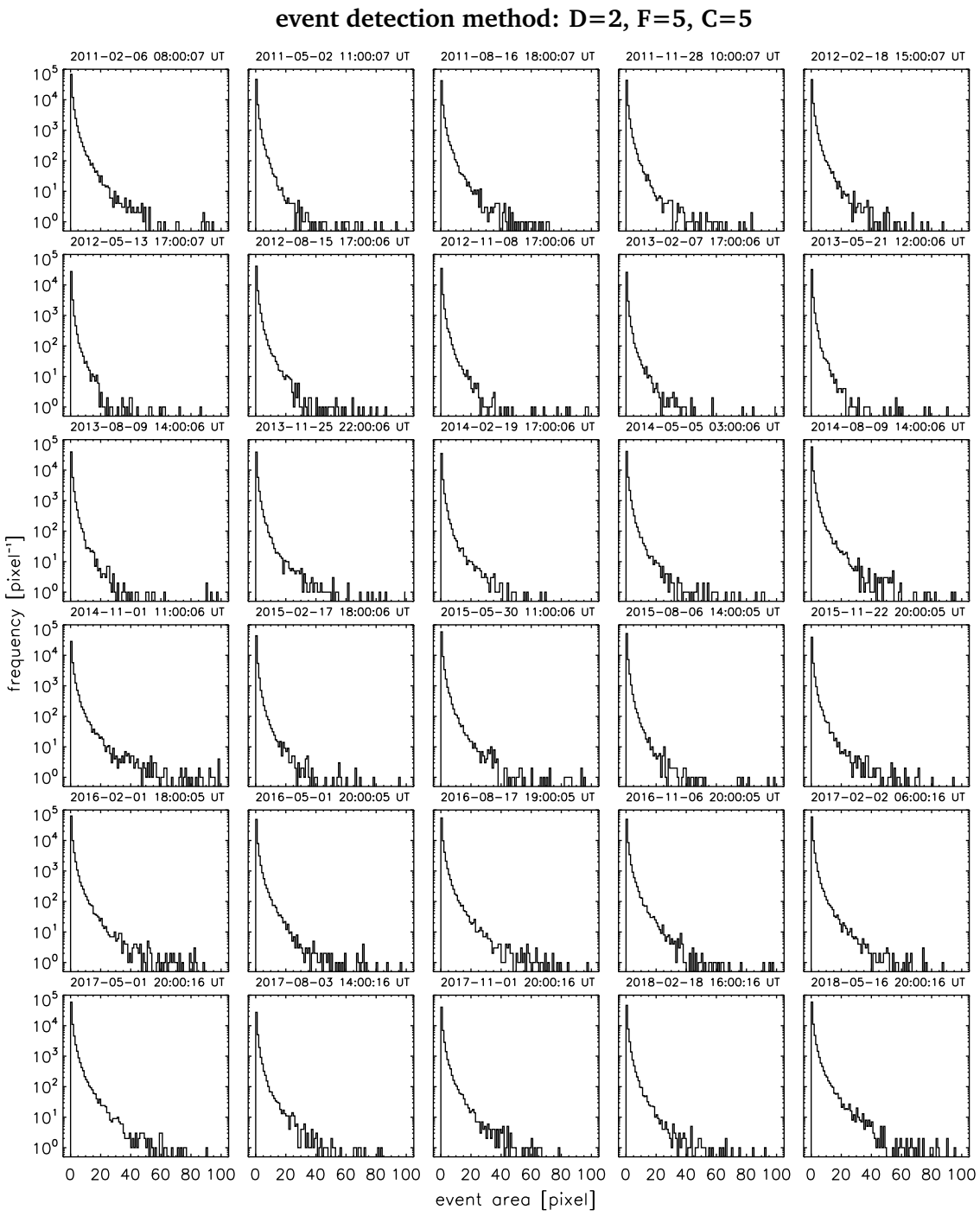

Fig. 6.34.: Event area distribution for each data set. Events where extracted using a detection interval of $D = 2$, a threshold factor of $F = 5$, and a combination interval of $C = 5$. The beginning of each observation series is given on top.

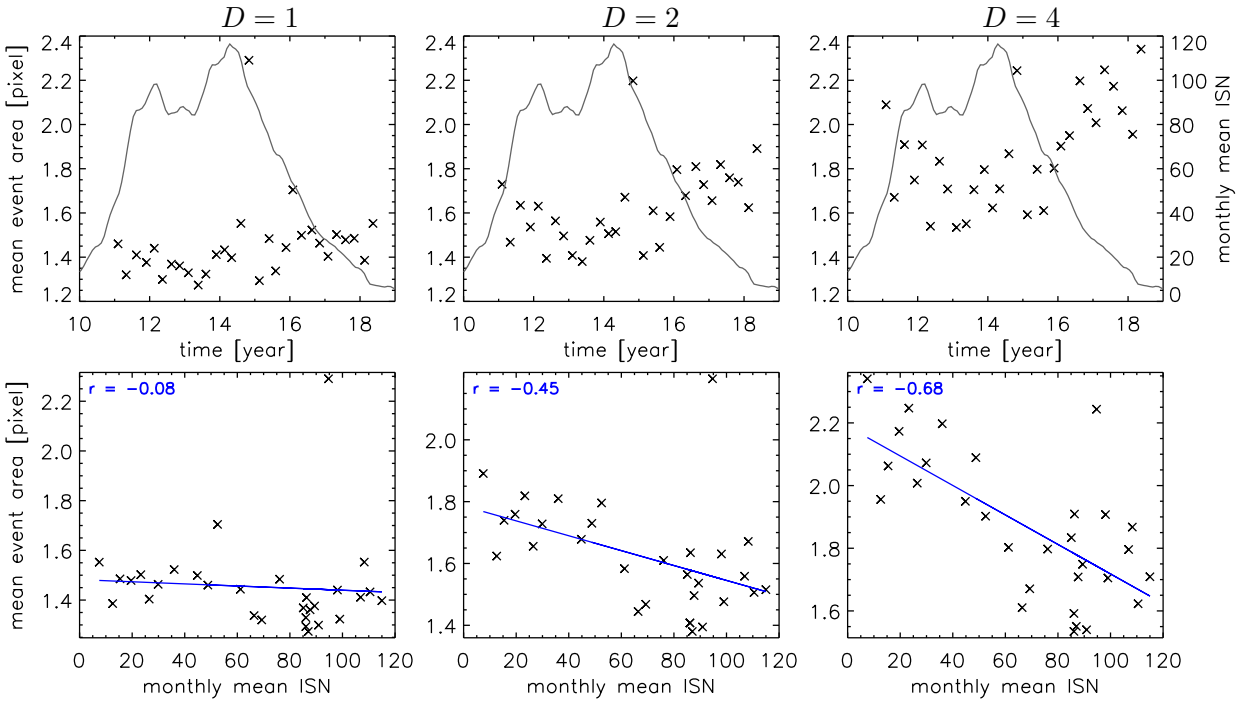

Fig. 6.35.: Mean event area for different detection intervals $D = 1$, 2 and 4 (left to right). The middle panels show results from the reference method. Values extracted for each data set are plotted as a function of time (top row) together with the sunspot number (gray). Correlation to the sunspot number (bottom row), with a linear fit (blue) and correlation coefficient (r) is also shown.

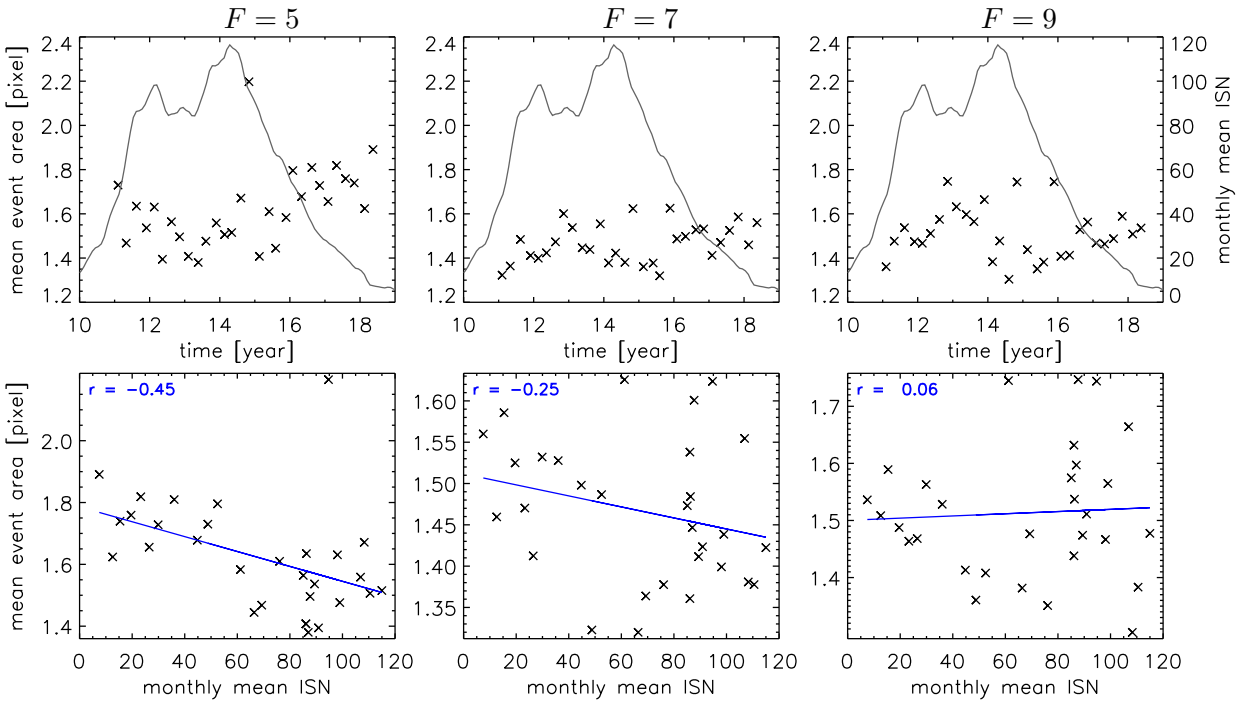

Fig. 6.36.: Same as Figure 6.35 but for different threshold factors $F = 5$, 7 and 9 (left to right). The left panels show results from the reference method.

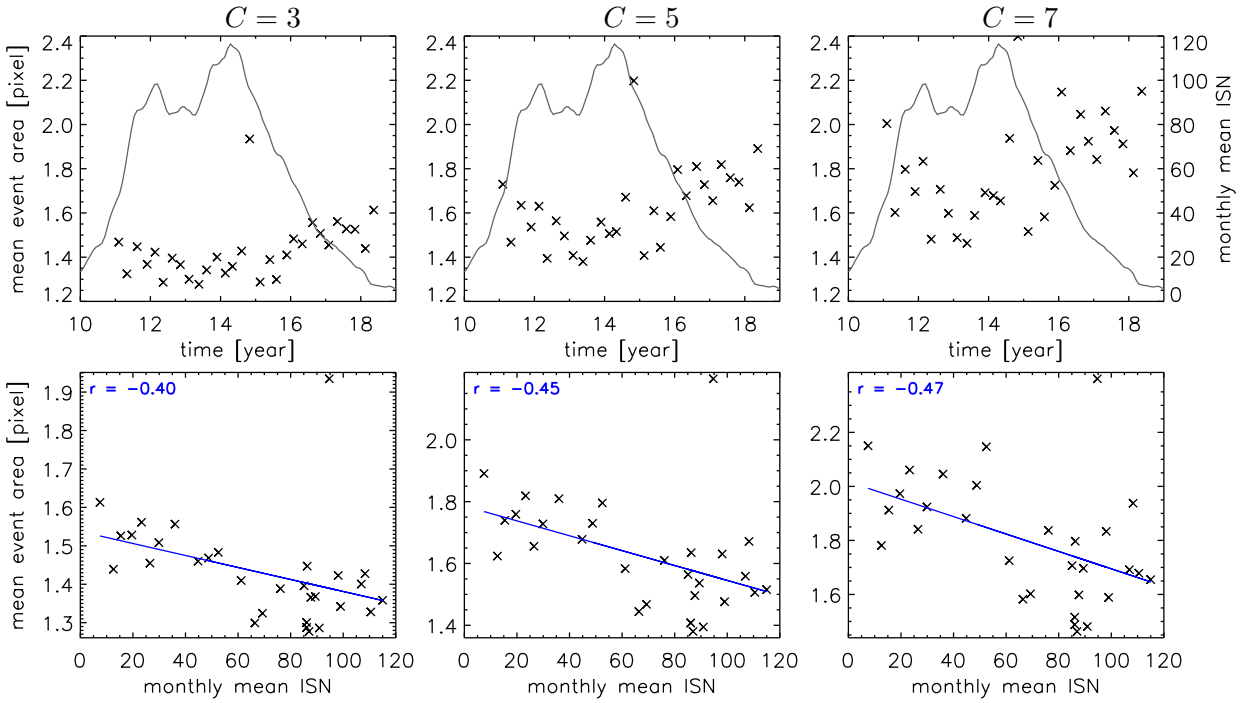

Fig. 6.37.: Same as Figure 6.35 but for different combination intervals $C = 3$, 5 and 7 (left to right). The middle panels show results from the reference method.

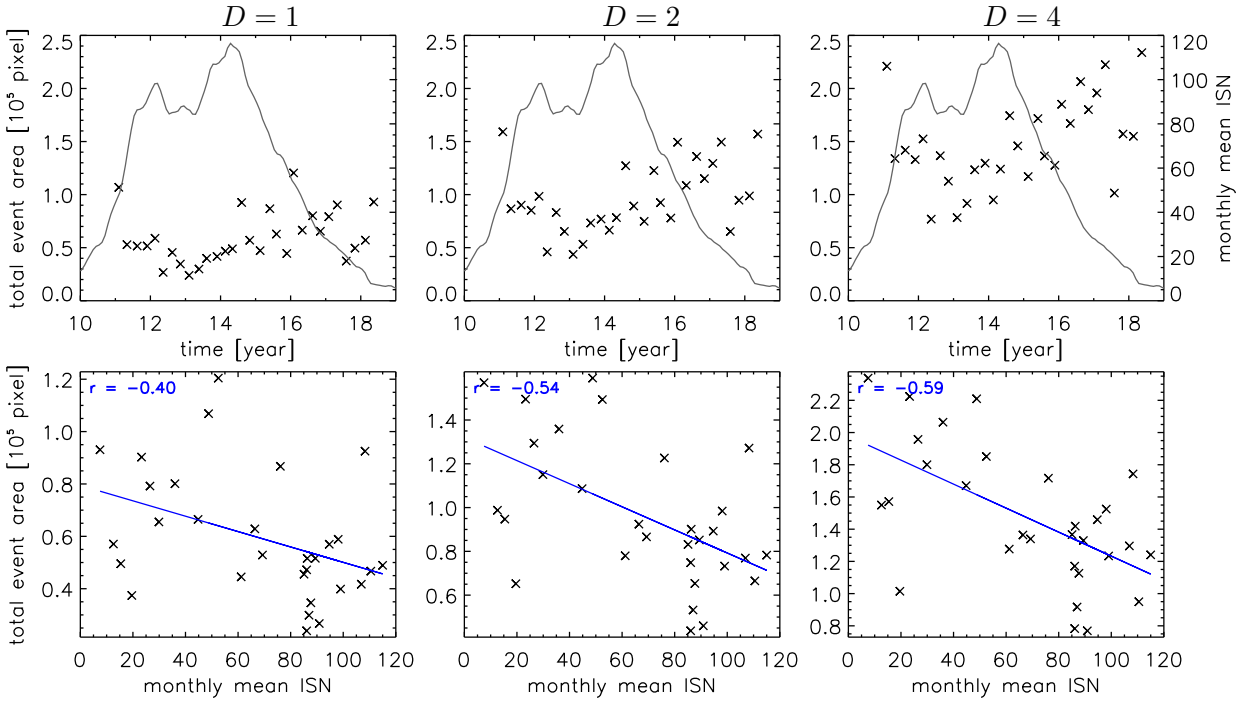

Fig. 6.38.: Total event area for different detection intervals $D = 1$, 2 and 4 (left to right). The middle panels show results from the reference method. Values extracted for each data set are plotted as a function of time (top row) together with the sunspot number (gray). Correlation to the sunspot number (bottom row), with a linear fit (blue) and correlation coefficient (r) is also shown.

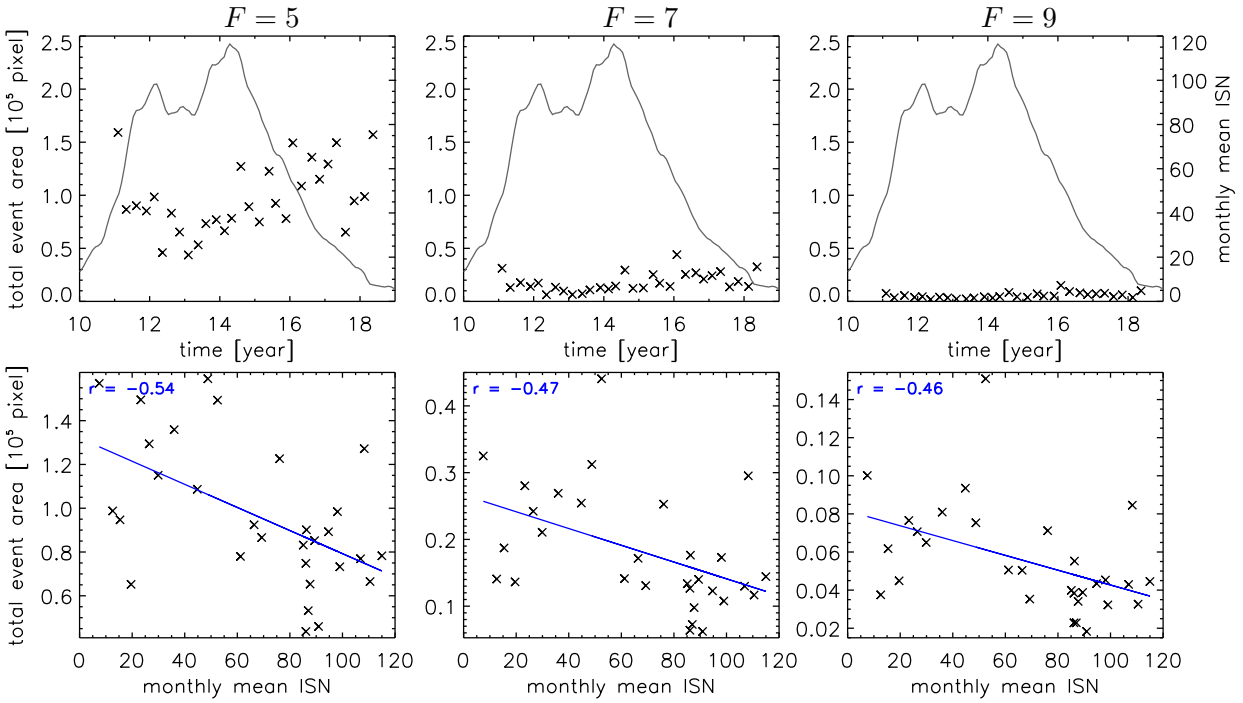

Fig. 6.39.: Same as Figure 6.38 but for different threshold factors $F = 5$, 7 and 9 (left to right). The left panels show results from the reference method.

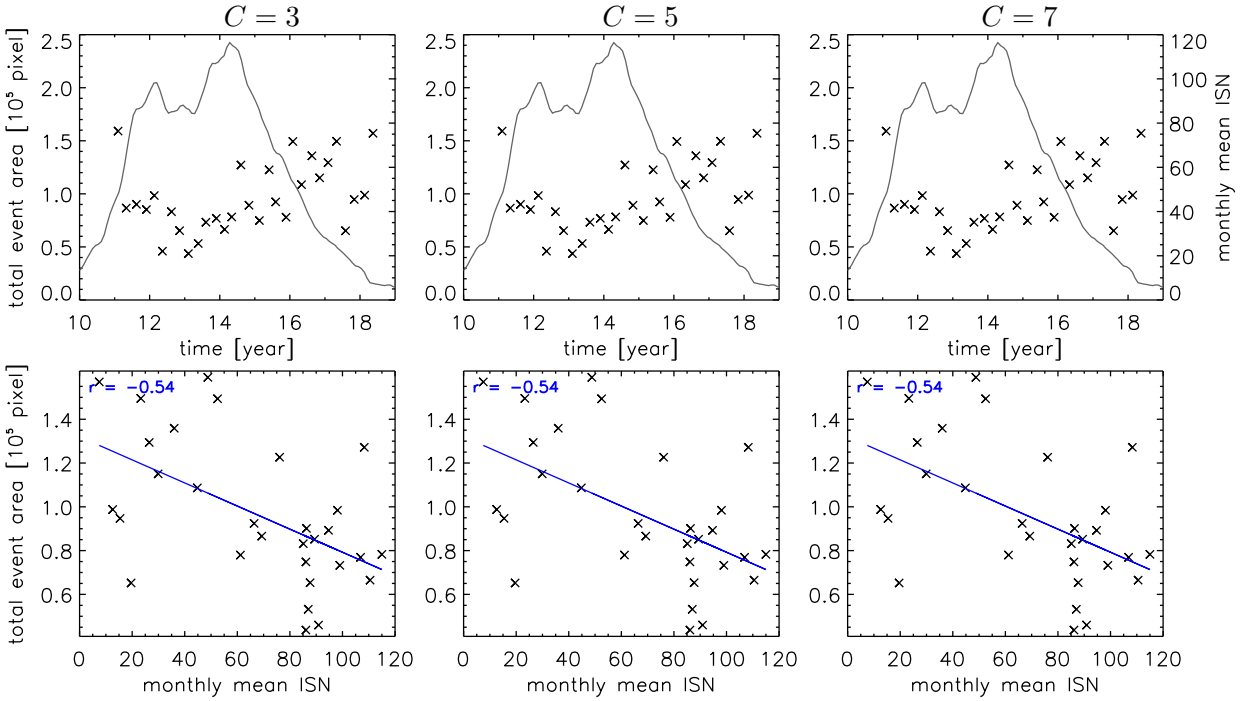

Fig. 6.40.: Same as Figure 6.38 but for different combination intervals $C = 3$, 5 and 7 (left to right). The middle panels show results from the reference method.

6.6 Number of Detected Events

This last section presents the number of detected events after combination and depending on a minimum event area. First, Figures 6.41, 6.42 and 6.43 show the total number of events after combination regardless of their size for all datasets. The number of combined events rises with increased detection intervals, very similar to the number of events before the combination. The inverse correlation to the solar activity increases slightly within the range -0.52 to -0.62. An increased threshold factor significantly decreases the number of combined events and also shows a slight decrease in correlation from -0.60 to -0.48. The number of events decreases for larger combination intervals since more events will be combined. Compared to the threshold factor, the combination interval has, however, only a slight influence on the number of events. The correlation is likewise not affected very much ($r = -0.60$ to -0.63). The trend of less observed events at higher solar activity is present throughout all methods.

To get a better idea of the distribution of different event sizes, we will now look at the fraction of events larger than a given size. Figures 6.44, 6.45, and 6.46 show the relative amount of events larger than one pixel for all datasets, the changes from the variation of different method parameters and their corresponding correlation to the sunspot number. For the reference method, such events that are the result of at least one pixel combination make up between 15 to $30\,\%$ of all detected events. This, of course, implies that 70 to $85\,\%$ of all events are captured by a single pixel. We find that the fraction of combined events rises with larger detection intervals, most likely because of the general increase in detected events and a resulting higher chance of combination. Larger intervals also increase the trend of more combined events at lower sunspot numbers ($r = -0.64$ at $D = 4$). Higher threshold factors reduce this correlation down to $r = -0.10$. We observe an overall increase in combined events for all data sets for larger combination intervals. The evolution over the solar cycle remains very similar between methods, and the trend of more combinations at lower solar activity is sustained, with a correlation of $r = -0.56$ to -0.58 to the sunspot number.

Figures 6.47, 6.48, and 6.49 show the same plots again for the fraction of events larger than 16 pixels. They make up about 0.1 to $0.5\,\%$ of all events found by the reference method. The fraction again rises with lower solar activity ($r = -0.43$) and the trend is stronger for higher detection intervals ($r = -0.71$). Interestingly, higher threshold factors reverse this correlation to $r = +0.32$. Larger combination intervals again result in a larger fraction of the combined events but here also affect the correlation to the sunspot number ($r = -0.14$ to -0.53)

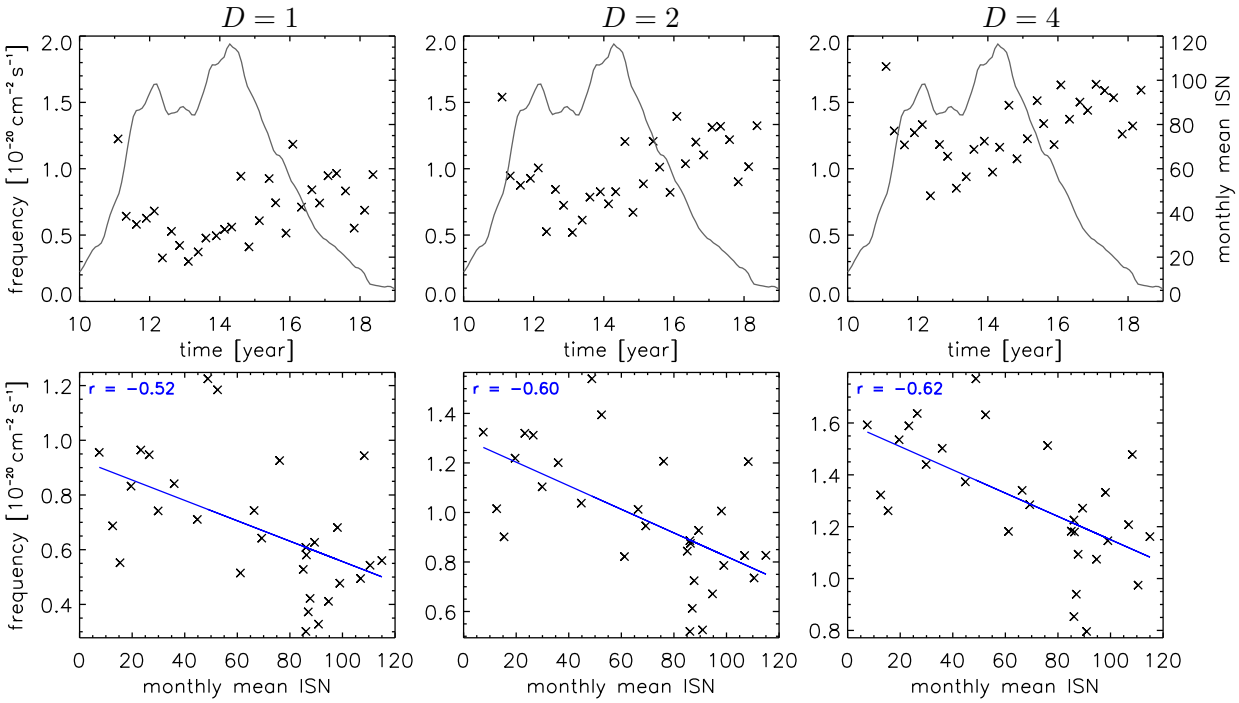

Fig. 6.41.: Total event number for different detection intervals $D = 1$, 2 and 4 (left to right). The middle panels show results from the reference method. Values extracted for each data set are plotted as a function of time (top row) together with the sunspot number (gray). Correlation to the sunspot number (bottom row), with a linear fit (blue) and correlation coefficient (r) is also shown.

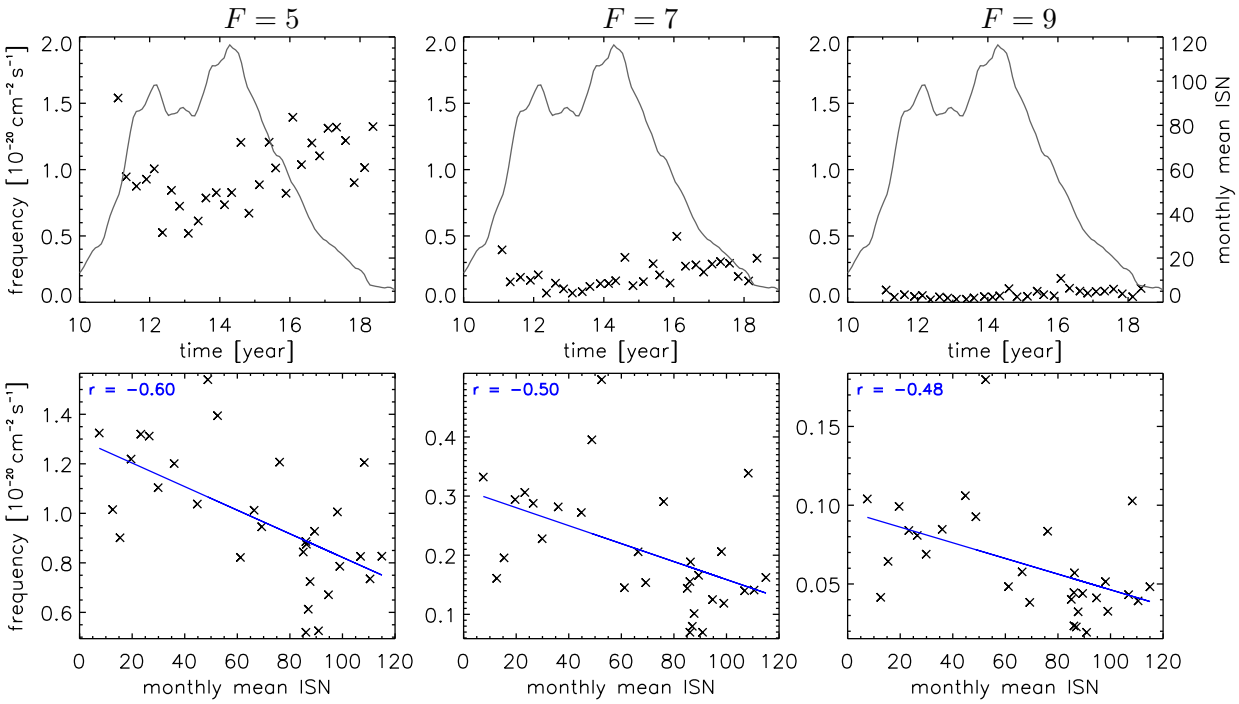

Fig. 6.42.: Same as Figure 6.41 but for different threshold factors $F = 5$, 7 and 9 (left to right). The left panels show results from the reference method.

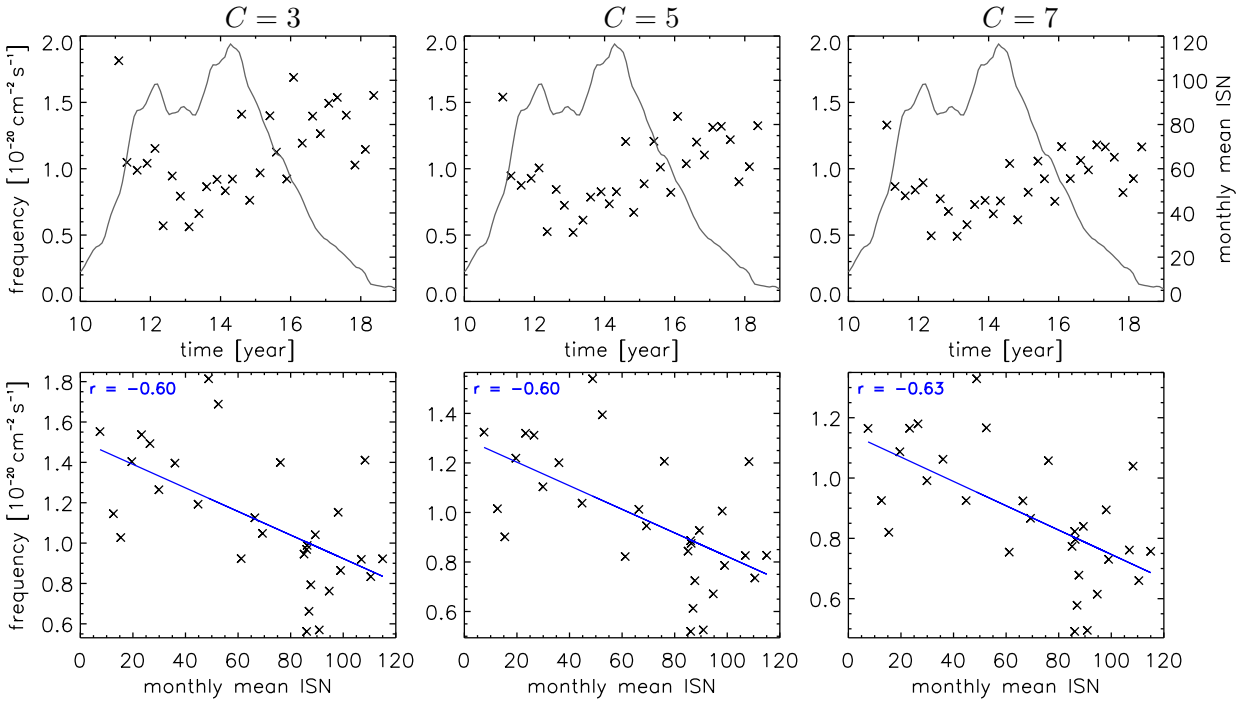

Fig. 6.43.: Same as Figure 6.41 but for different combination intervals $C = 3$, 5 and 7 (left to right). The middle panels show results from the reference method.

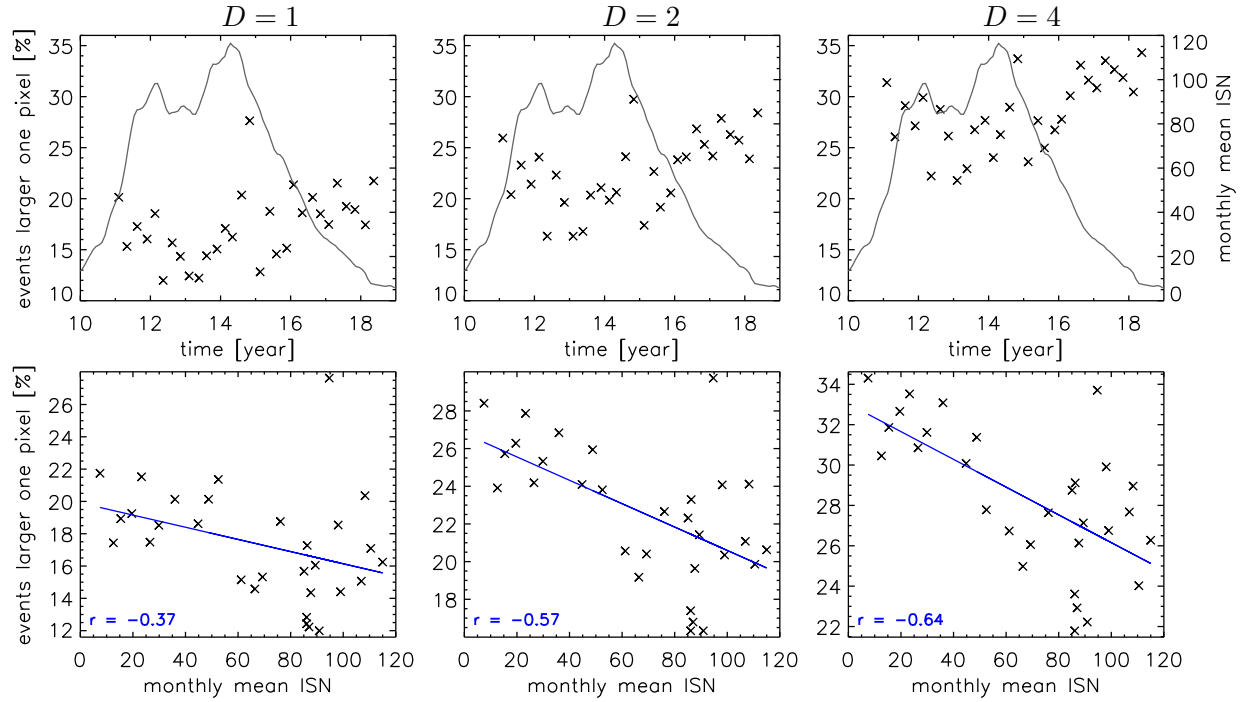

Fig. 6.44.: Events larger than one pixel for different detection intervals $D = 1$, 2 and 4 (left to right). The middle panels show results from the reference method. Values extracted for each data set are plotted as a function of time (top row) together with the sunspot number (gray). Correlation to the sunspot number (bottom row), with a linear fit (blue) and correlation coefficient (r) is also shown.

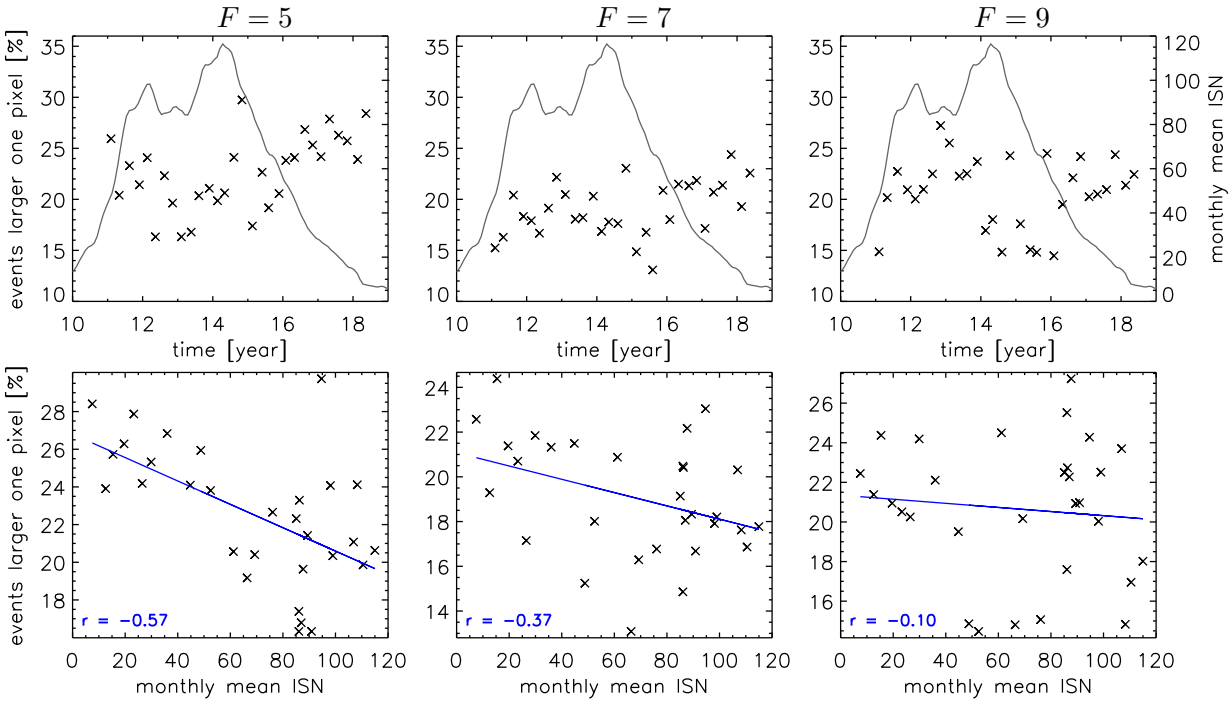

Fig. 6.45.: Same as Figure 6.44 but for different threshold factors $F = 5$, 7 and 9 (left to right). The left panels show results from the reference method.

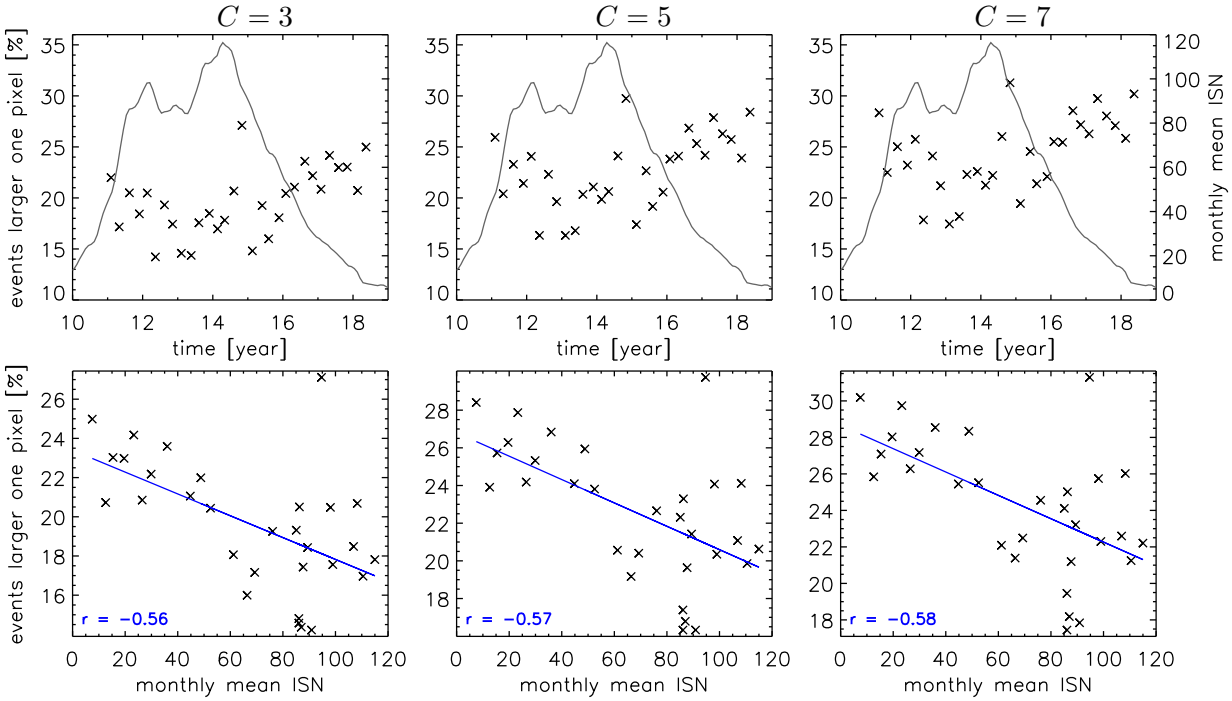

Fig. 6.46.: Same as Figure 6.44 but for different combination intervals $C = 3$, 5 and 7 (left to right). The middle panels show results from the reference method.

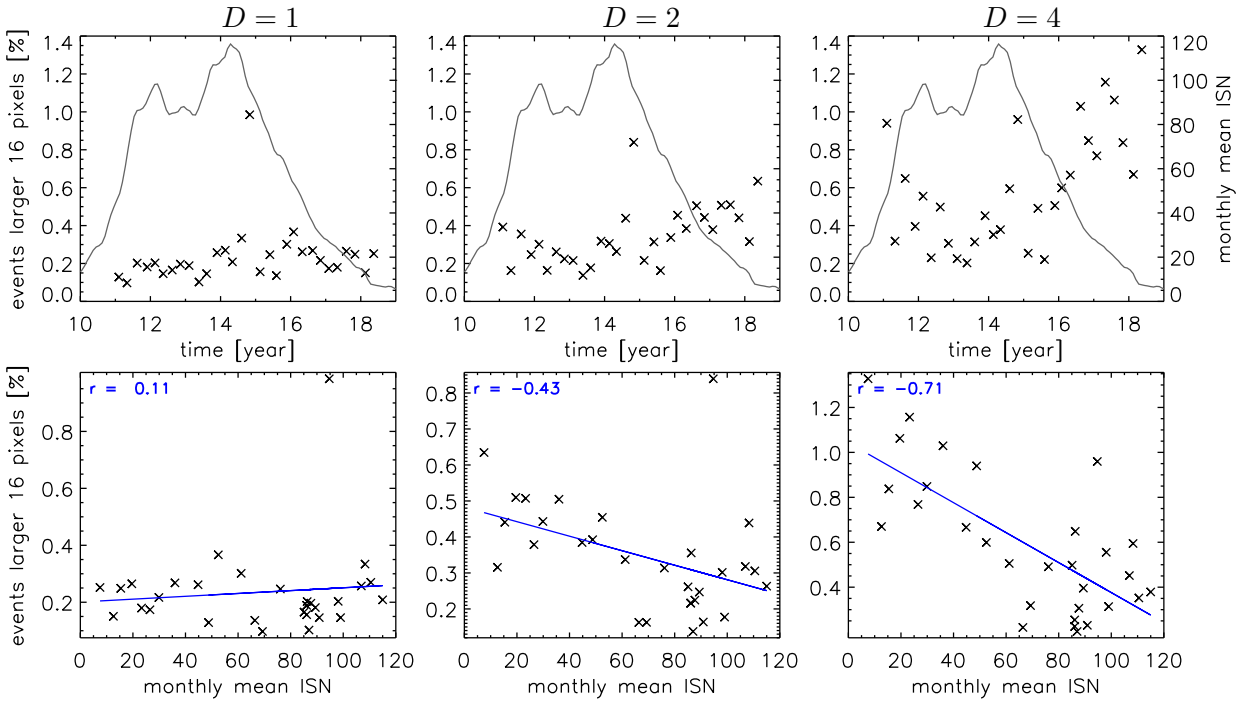

Fig. 6.47.: Events larger than 16 pixel for different detection intervals $D = 1$, 2 and 4 (left to right). The middle panels show results from the reference method. Values extracted for each data set are plotted as a function of time (top row) together with the sunspot number (gray). Correlation to the sunspot number (bottom row), with a linear fit (blue) and correlation coefficient (r) is also shown.

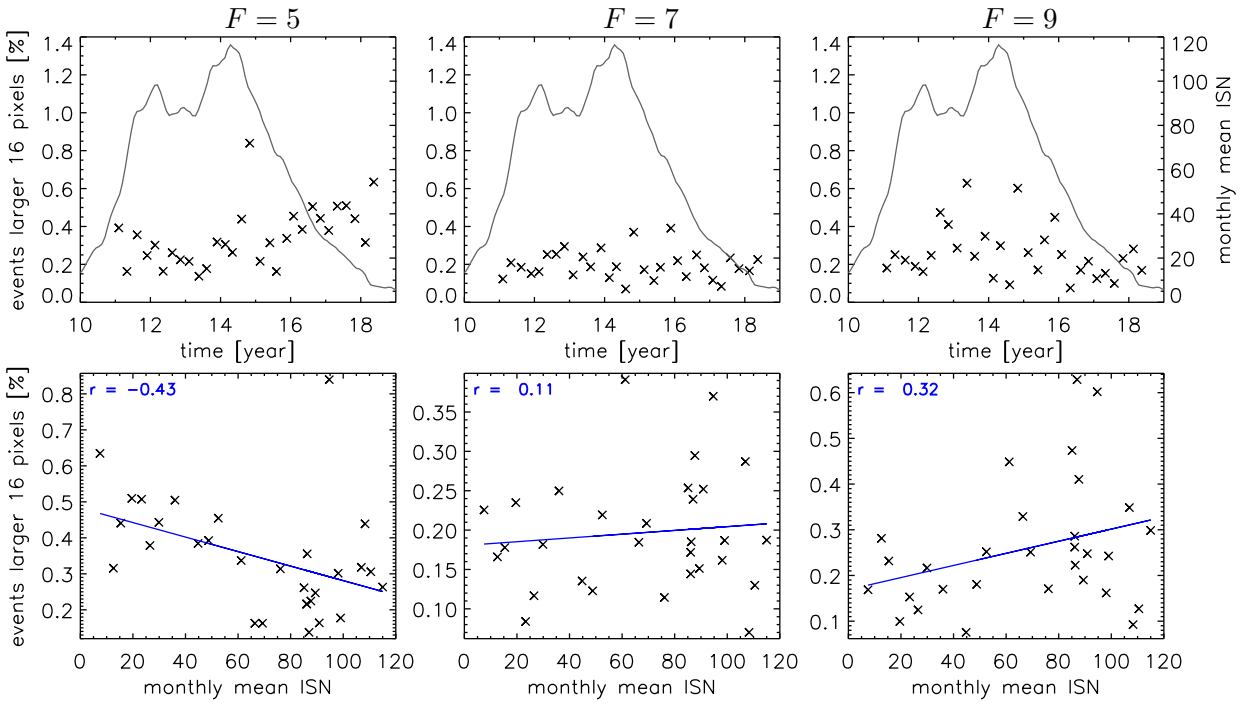

Fig. 6.48.: Same as Figure 6.47 but for different threshold factors $F = 5$, 7 and 9 (left to right). The left panels show results from the reference method.

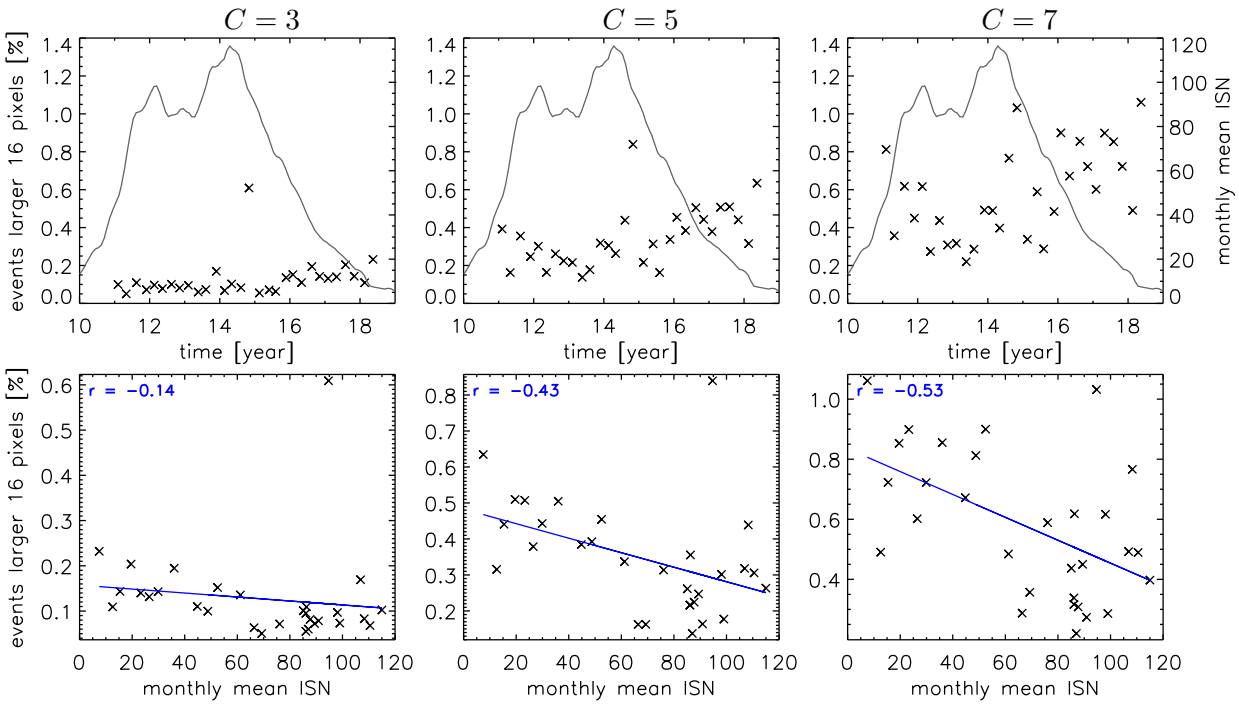

Fig. 6.49.: Same as Figure 6.47 but for different combination intervals $C = 3$, 5 and 7 (left to right). The middle panels show results from the reference method.

7 Summary and Discussion

In this thesis, we extracted the frequency distribution of nanoflares and their characteristics from high spatial and temporal resolution AIA multi-band images using differential emission measure analysis and a tunable event detection algorithm specifically developed for AIA data characteristics. We studied nanoflare energy frequency distributions and other nanoflare characteristics in quiet Sun regions throughout different solar cycle phases. The goal was to determine any changes correlated to the solar activity and study their contribution to coronal heating. To this aim, we studied 30 individual data sets spaced evenly throughout the years 2011 to 2018 to cover a significant portion of solar cycle 24. Strong instrument degradation that started to affect the DEM results of quiet Sun regions in mid-2018 limited the further extent of the observation period. Each individual data set consists of two-hour-long image series in each of the six coronal EUV wavelength channels of AIA with a field-of-view of $400'' \times 400''$ at the solar disk center. The full AIA cadence of 12 seconds was used, but the images were spatially binned by 4×4 pixels, resulting in a resolution of $2.4''$. The DEM inversion code from Hannah and Kontar (2012) was used to reconstruct the DEM profile for each pixel, and subsequently the total emission measure (EM) and EM-weighted temperature from the EUV images. These parameters were then used to calculate for each time step the thermal energy content in each pixel and its evolution.

7.1 Method and Parameters

The developed event detection algorithm searches for local peaks directly in the thermal energy evolution curves of each individual pixel. Three user-supplied parameters tune crucial steps in the algorithm. These are the event detection interval, the event detection threshold, and the event combination interval. The event detection interval influences the search for local peaks by defining an interval given in time-steps (of 12 seconds) in either direction in which a thermal energy value has to be the highest value in the interval in order to be marked as a local peak. The corresponding minimum is defined as the lowest thermal energy value between the current local peak and the previously found local peak, and the energy of a local peak is defined as the difference between the peak value and its corresponding minimum. The second parameter, the threshold factor, sets a lower limit to the

acceptable event energy. The baseline threshold is calculated via the standard deviation of a pixel's noise fluctuations and is then multiplied by the set threshold factor to arrive at the final energy threshold. All events in a pixels time series below this threshold are discarded. Since nanoflares can have larger areas than is covered by a single binned AIA pixel, an algorithm had to be implemented that combines detected events in adjacent pixels if they happen within a defined time interval. This interval is set by the final parameter, the event combination interval, which is given as the number of 12-second time steps in either direction in which events found in adjacent pixels (x and y direction) are combined into one event.

We found event detection intervals of $D = 2$ to 4 time-steps to work well. Detection intervals of $D = 2$ and higher are sufficient in preventing the breakup of events whose rising phase is interrupted by a single low data point, but higher detection intervals may cause an unwanted bias against smaller events. Our recommended threshold factors are in the range of $F = 5$ to 9. Lower factors lead to the detection of noise, especially when combined with low detection intervals, while even higher threshold factors discarded a large portion of the detected events, resulting in bad statistics for the fitted power law. Finally, we found combination intervals of $C = 3$ to 7 produce good results. $C = 3$ already successfully combines most events, while very large events may need a combination interval of $C = 5$ to 7 time-steps to reduce breakup into multiple smaller events. Larger event detection intervals will lead to more erroneous combinations of unrelated events. To investigate the influence of the different parameters, we chose a set of reference parameters ($D = 2$, $F = 5$, $C = 5$) and then varied them one at a time while keeping the other two fixed at the reference values. This approach resulted in seven different sets of parameters that we used to analyze the nanoflare statistics and how it is affected by the parameter settings in the algorithm.

7.2 Frequency Distributions over the Solar Cycle

First, we investigated the nanoflare frequency distribution, arguably one of the most crucial aspects regarding the explanation of coronal heating. The frequency distributions extracted by the method using the reference set of parameters all show a power-law-like distribution over multiple orders of magnitude in thermal energy. They are all characterized by a maximum event frequency at about $1 \times 10^{23}\,\mathrm{erg}$ (cut-off energy) with a sharp drop-off towards the lower energy range. The smallest detected events are usually in the range of $3 \times 10^{22}\,\mathrm{erg}$. We find that all frequency distributions follow a close power-law starting at the cut-off energy and continuing to at least $1 \times 10^{26}\,\mathrm{erg}$, with some distributions extending to even higher energies. Histogram bins at higher energies often only consist of single events and should be

treated carefully because of possible erroneous event combinations. To extract the power-law index from the frequency distributions, we used two different methods. Both fit a linear model to the power-law slope of the frequency distribution in log-log representation by minimizing the chi-square error statistics. The difference lies in the weight of individual histogram bins for the fit. In one method, the data points are weighted according to their Poisson error in each bin, while in the second method, no weights are used, and all data points are treated as equally valid. The former (weighted) method is mostly determined by the energy bins with the highest counts (at lower energies), while energy bins with low counts (high energies) have only a minor influence on the fitted line. This weighted fit may be a valid approach to represent the steepness at lower energies more accurately, but we find that the fit often does not match the determined occurrence frequencies at higher energies. The non-weighted method, on the other hand, produced linear fits that find a common power-law for the whole distribution.

The individual datasets produce power-law indices in the range of 2.02 to 2.38 for the weighted fit and 2.06 to 2.54 for the non-weighted fit. The non-weighted fit is always steeper than the weighted fit from the same data set, suggesting that the observed frequency distribution of lower energies is slightly less steep (smaller power-law index) than the distribution of higher energy events. This is most likely an effect of the limited sensitivity of the AIA instrument for small events. We showed the distribution of the observed standard deviation of individual pixels in Figure 5.12. It shows how our detection method becomes gradually (over one order of magnitude in energy) less sensitive towards smaller events until it reaches the cut-off energy. This implementation will naturally result in a reduced steepness of the observed power-law in the smallest observed events.

The evolution of the power-law index over the solar cycle as extracted by the weighted linear fit shows a correlation to the sunspot number with a coefficient of $r = 0.52$. This correlation is stable against changes to the combination interval and even increases at a larger detection interval. However, the correlation reduces quickly for higher threshold factors and is completely flat at $F = 9$, suggesting that the correlation is an effect of small events only present at lower thresholds. It is therefore likely that the found correlation results from changes in the AIA sensitivity towards small events caused by the changes in solar activity.

A linear fit without weights finds no significant correlation between the power-law index and the sunspot number, with a correlation coefficient of $r = 0.12$ for the distribution extracted with the reference set of parameters. No correlation ($r < 0.17$) is also found for most other parameter combinations, with the exception of a large detection interval ($r = 0.45$ for $D = 4$) and large combination interval ($r = 0.27$ for $C = 7$). We conclude that the observed nanoflare frequency distributions

do not show significant change over the solar cycle, which is consistent with the avalanche model proposed by Lu and Hamilton (1991) and matches observations of the frequency distributions of solar flares in hard X-ray (Crosby et al., 1993) and soft X-ray (Veronig et al., 2002). Any correlations observed by specific parameter combinations of the weighted method are most likely the effect of changes in the AIA data characteristics over the solar cycle and not observations of actual changes to the nanoflare frequency distribution.

7.3 Combined Frequency Distribution

Since we concluded that the power-law steepness is probably not correlated to the solar cycle, we merged the events from all data sets into one histogram to get a combined distribution of nanoflares for the whole observation period. This combined distribution shows a common power-law slope of $\alpha = 2.26$ for the non-weighted fit and the reference set of parameters. The power-law reaches from $1 \times 10^{23}\,\mathrm{erg}$ at the low energy cut-off up to $1 \times 10^{28}\,\mathrm{erg}$, a range of five orders of magnitude in thermal event energy. The weighted linear fit is slightly less steep ($\alpha = 2.18$) and again lacks agreement with the distribution at higher event energies. The lower cut-off of the combined frequency distribution at $1 \times 10^{23}\,\mathrm{erg}$ is expected since all individual distributions also have their cut-off in this range with minimal variation. Individual distributions show a high energy-cutoff of the continuous frequency distribution in the range of 1×10^{26} to $1 \times 10^{27}\,\mathrm{erg}$ with only single, separated events found at even higher energies. These high energy events could have significant uncertainties associated with them since they may heavily depend on accurate event combinations between many pixels, one of the most challenging steps to get right in the event detection algorithm. It is therefore very promising for the developed method that the combined statistics of these large events extend the power-law slope for another order of magnitude, up to $1 \times 10^{28}\,\mathrm{erg}$, consistent in steepness with the lower energy part of the frequency distribution that has much better statistics.

We find that our combined nanoflare frequency distributions using different sets of parameters only show a power-law variation in the range of range of $\alpha = 2.16$ to 2.36 (Figures 6.11, 6.12, and 6.13) The most considerable variations come from the different event combination intervals that change the higher energy range of the distribution. The detection interval changes mainly the lower energy part of the distribution, and the threshold factor equally affects the frequency at all energies. Therefore, we have consistently found a power-law distribution of $\alpha > 2$ that suggests a dominance of lower energy events in the coronal heating process (Hudson, 1991). However, it has to be noted that while we explored a range of different parameters in our detection method, they all rely on other fundamental

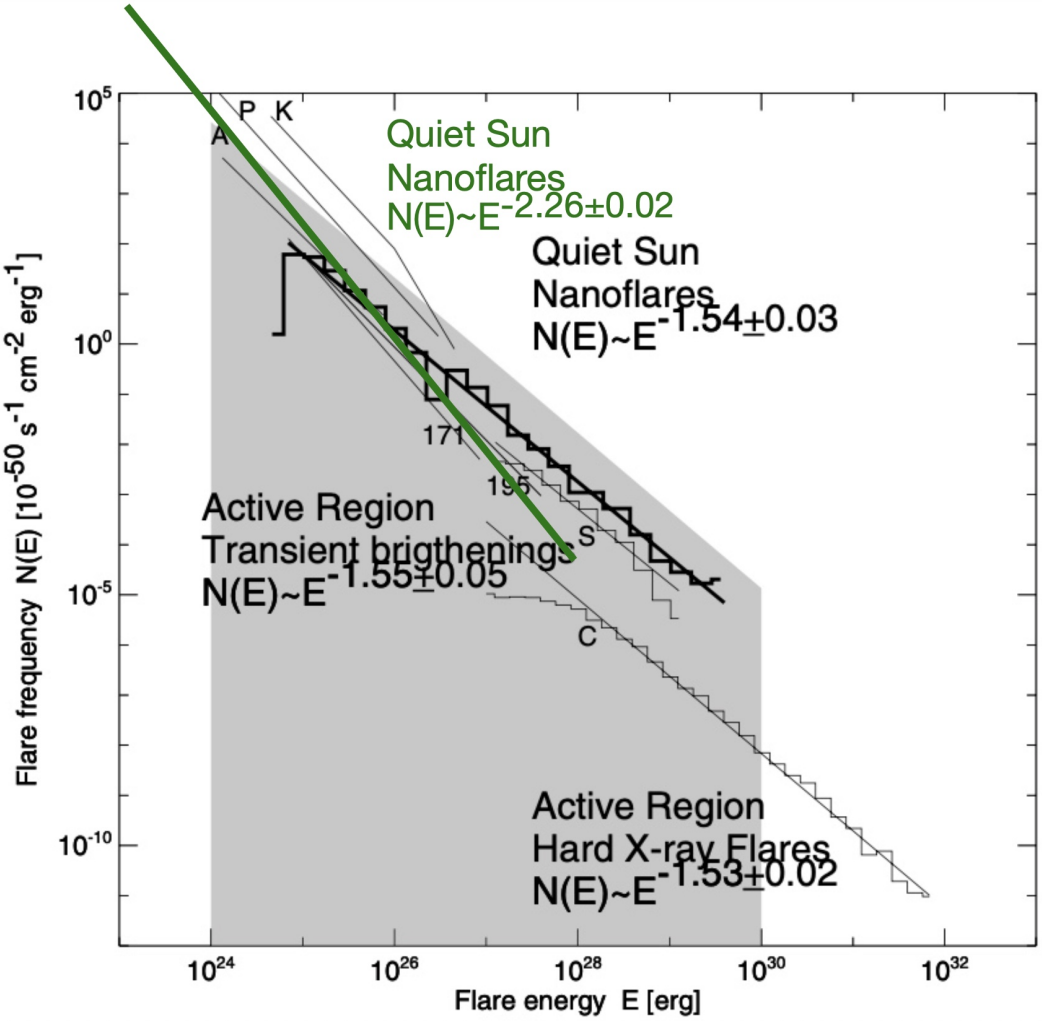

Fig. 7.1.: AIA nanoflare distribution from this study (green) compared to nanoflares in the quiet Sun, active region transient brightenings, and hard X-ray flares derived by the following studies: Krucker and Benz (1998) and Benz and Krucker (2002) (K), Parnell and Jupp (2000) (P), Aschwanden et al. (2000) (A), Shimizu (1995) (S), Crosby et al. (1993) (C) and Aschwanden and Parnell (2002) (171 and 195). The grey area indicates the coronal heating requirement of $P = 3 \times 10^5\,\mathrm{erg\,cm^{-2}\,s^{-1}}$ for quiet Sun regions when a power-law index of $\alpha = 1.54$ (combined slope of all studies) and an energy interval of 10^{24} to $10^{30}\,\mathrm{erg}$ is assumed. Adapted from Aschwanden (2004) (see Fig. 3.7).

assumptions that we did not vary during the final results. These include the thermal energy calculation, the scaling of the events line-of-sight depth relative to the detected area ($h = \sqrt{A}$), the threshold calculation for the event detection, AIA data preparations, and DEM code settings.

Parnell (2004) did an extensive study where she investigated the effects of a broader range of assumptions on the observed frequency distribution. She concluded that the exact determination of frequency distributions by direct observations of

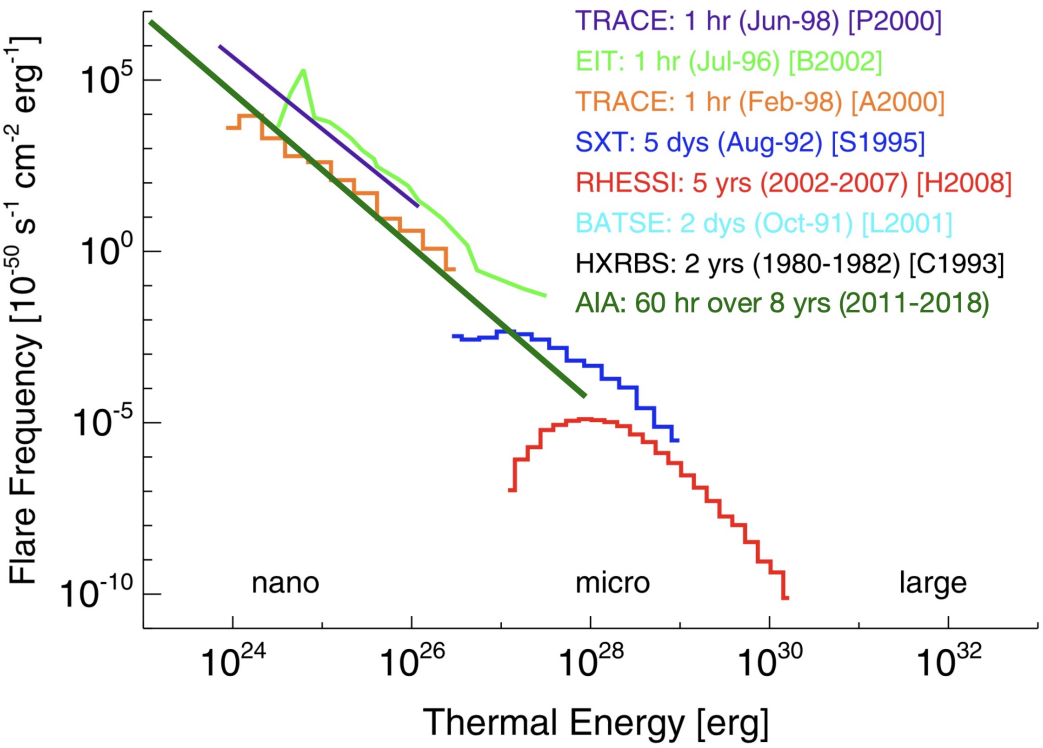

Fig. 7.2.: Comparison of solar flare energy distributions derived by different studies. Shown are EUV nanoflares observed with either SOHO/EIT by Benz and Krucker (2002) or TRACE by Parnell and Jupp (2000) and Aschwanden et al. (2000). Microflares where observed with Yohkoh/SXT by Shimizu (1995) and with RHESSI by Hannah et al. (2008). AIA observations of nanoflares from this study (green) are also shown. Figure adapted from Hannah et al. (2011).

nanoflares is not possible. From this investigation of 1200 differently tuned event detection and power-law extraction methods, all according to physically sensible assumptions, a wide range of different frequency distributions (α =1.5 to 2.6) was found. Of course, the results presented here are subject to the same challenges, and the observed distributions could easily be biased.

Figure 7.1 shows our nanoflare frequency distribution compared to other studies discussed by Aschwanden (2004). While our distribution is similar to the result from Benz and Krucker (2002) who found $\alpha = 2.3 \pm 0.1$ in their nanoflare studies using EIT data and considering the same height model as in this study, our distribution is distinctly steeper than the common power-law proposed by Aschwanden (2004). Another study with similar results to ours was done by Parnell and Jupp (2000), who found a power-law index range of $\alpha = 2.0$ to 2.1 using TRACE data implementing the same height model. Very noticeable is the continuation of our distribution towards lower energies (1×10^{23} erg), which is at least one order of magnitude smaller compared to all other studies shown. This could be a result of the higher

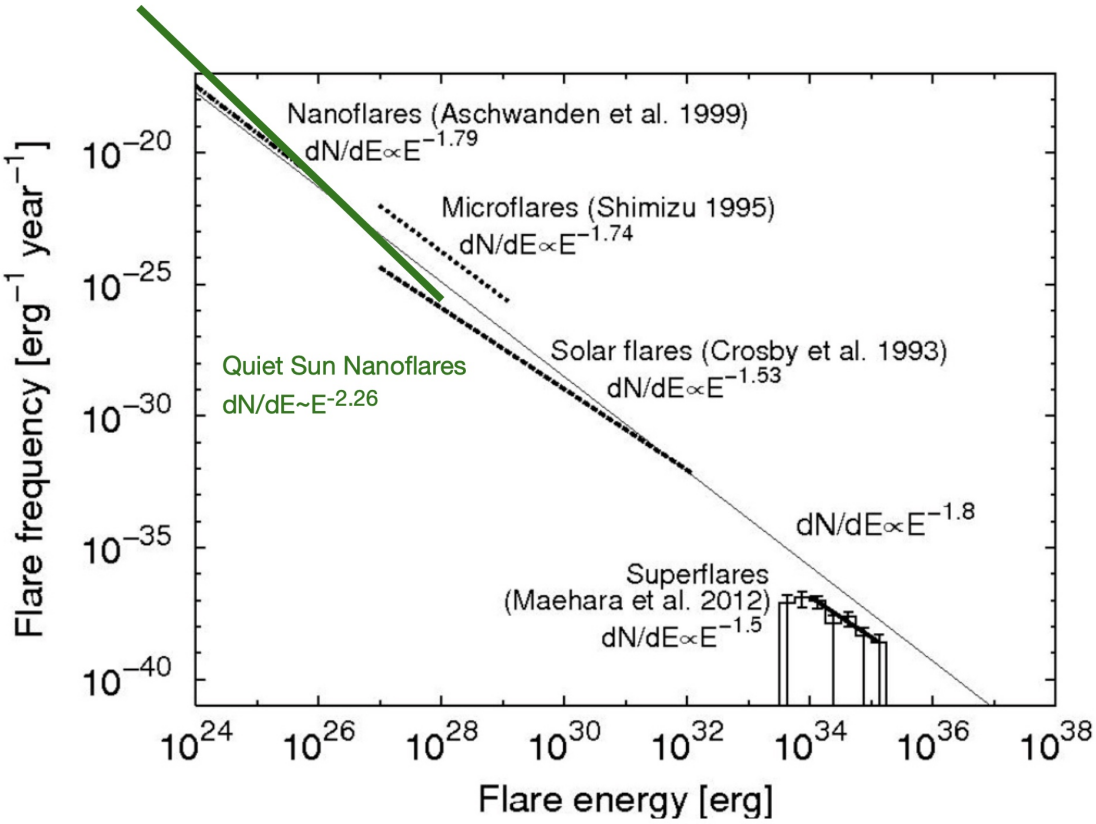

Fig. 7.3.: Combined frequency distributions from solar flares (Aschwanden, 2004; Shimizu, 1995; Crosby et al., 1993) and superflares from Sun-like stars (Maehara et al., 2012). The frequency distribution found by this study using the reference set of parameters are shown in green. Figure adapted from Shibata et al. (2013).

temporal resolution (Parnell and Jupp, 2000)) and the better EM and T resolution due to the use of six EUV wavelength filters and DEM code calculations.

Figure 7.2 is adapted from Hannah et al. (2011) and again shows our combined nanoflare distribution together with solar flare distributions found by other studies. Although there is a significant overlap of the studies shown in Figure 7.1 (only Crosby et al. (1993) is exchanged for the microflare study by Hannah et al. (2008)), in this case, our results fit much better with the suggested common power-law distribution of all studies.

Shibata et al. (2013) again used a relatively low power-law index of $\alpha = 1.8$ to suggest the common distribution of flares that could extend in energy to include the superflares found on Sun-like stars by Maehara et al. (2012). An adaption of the Figure from Shibata et al. (2013) that includes our nanoflare frequency distributions is shown in Figure 7.3. Even with its steeper slope, our derived distribution fits reasonably well within the suggested common power-law.

7.4 Energy Flux and Coronal Heating

We calculated an energy flux for individual data sets of 2×10^3 to $4 \times 10^3\,\mathrm{erg\,cm^{-2}\,s^{-1}}$ by averaging the total detected event energy of a data set over the two hour observation time and observed field-of-view. Our results show no significant correlation between the observed energy flux and the sunspot number, independent of the used algorithm parameters. However, a slight tendency of higher energy flux in the second half of the multi-year observation period is visible. For the combined distribution of all data sets, we derive an energy flux of $3.2 \times 10^3\,\mathrm{erg\,cm^{-2}\,s^{-1}}$. This accounts for only about one percent of the minimum heating rate of $3 \times 10^5\,\mathrm{erg\,cm^{-2}\,s^{-1}}$ required to heat the corona (Withbroe and Noyes, 1977). Krucker and Benz (1998) initially derived a thermal input of $7.1 \times 10^4\,\mathrm{erg\,cm^{-2}\,s^{-1}}$ in their nanoflare study but later corrected these results with the more accurate event depth model ($h = \sqrt{A}$) also used in this study. They arrived at a corrected thermal energy input of about $2.2 \times 10^4\,\mathrm{erg\,cm^{-2}\,s^{-1}}$, which corresponds to $5\,\%$ of the average radiative output they calculated explicitly for the observed field-of-view, and about $5\,\%$ of the minimum requirement introduced by Withbroe and Noyes (1977). Parnell (2004) also report an input power per unit area of $2.9 \times 10^4\,\mathrm{erg\,cm^{-2}\,s^{-1}}$ for the matching height model. Our result is at least a factor of 5 lower than the energy flux estimate of these two studies. Looking at Figures 7.1 and 7.3 we see that our distribution finds lower frequencies for events of all energies compared to both of these studies. On the contrary, Aschwanden et al. (2000) reported an energy flux of $1 \times 10^3\,\mathrm{erg\,cm^{-2}\,s^{-1}}$ in their TRACE observation of EUV nanoflares that is even lower than our results. Although they observed a different power-law index ($\alpha = 1.8$), their overall frequencies for the overlapping energy range are much closer to the ones we observed in this study.

Assuming the nanoflare frequency distribution found by the combined data sets continues to even smaller events, the power-law of $\alpha = 2.26$ would have to be sustained down to energies of $2 \times 10^{19}\,\mathrm{erg}$ in order to account for the coronal heating requirement, i.e. 5 orders of magnitude smaller than the cut-off energy in our study. This estimate is similar to Parnell and Jupp (2000) who derived a minimum required event energy of $3.8 \times 10^{19}\,\mathrm{erg}$ for events with an EM enhancement of at least 3σ. Because of our steep slope ($\alpha > 2$), an extension of the frequency distribution to larger events (above $1 \times 10^{28}\,\mathrm{erg}$) results only in negligible addition to the observed energy flux.

Calculating the actual energy input into the corona from the direct observation of nanoflares is very challenging. The measurement of the thermal energy input through the peak value probably underestimates the energy input since radiation and conduction already reduce the thermal energy during the event. Since the rise time is

similar to the decay time in nanoflares, Benz and Krucker (2002) estimate that about half of the radiative loss occurs before the peak, leading to an underestimate of the thermal energy input by at least a factor of 2. Additional unobserved energy is lost in the isothermal expansion. Benz and Krucker (2002) conclude that the observed energy flux has to be multiplied by a factor of about 3 to include all energies involved during the event process. Using this higher energy flux estimate, our distribution would only have to continue to $1 \times 10^{21}\,\mathrm{erg}$ in order to fulfill the coronal heating requirement.

In addition, there are a number of factors in our event detection and energy calculation that could lead to an underestimate of the observed heating input into the corona. A higher energy flux could either be observed if the overall frequency of all energies is enhanced (rise of the whole distribution) or if the whole distribution is shifted towards higher energies. Our event detection could have a significant influence on the found energy per event because the application of a threshold after the local peak detection leads to generally less energy per event. This is the case because the corresponding minima of local peaks are often higher compared to the minima definition used in Krucker and Benz (1998), and Benz and Krucker (2002). A higher detection interval will generally lower the corresponding minima. This effect of higher observed energy flux with larger event detection intervals can be seen in Figure 6.15, which shows an increase by about a factor of 1.8 when raising the detection interval from $D = 2$ to $D = 4$.

Another factor that could increase the energy per event is the used scaling factor s_{eff} in our energy calculation (see equation 5.4). We used the estimate from Benz and Krucker (2002) ($s_{eff} = 500\,\mathrm{km}$) because of the similar spatial resolution of EIT compared to our binned AIA images, and to make our results more comparable with this specific study. We could have also used the more fundamental energy definition $E_{th} = 3k_B\Delta T\sqrt{\Delta MAgh}$ with the observed line-of-sight depth h and the filling factor q that is usually set to $q = 1$ (Krucker and Benz, 1998; Parnell and Jupp, 2000). Parnell and Jupp (2000) use a simple relation $h = \sqrt{A/k^2}$ and set $k = 1$ which assumes that all events are loops with a length equal to their width. For spatially binned AIA pixels ($2.4''$) this assumption for the event depth results in $h = 1750\,\mathrm{km}$ and would cause an increase in event energies by about a factor 1.9.

Finally, the thresholds we used in the event detection could reduce the overall number of events detected, also leading to reduced energy flux. The effect of different threshold factors on the event frequency of the combined data sets was shown in Figure 6.12. It is clearly visible that a higher threshold reduces the overall frequency distribution while leaving the power-law mostly unchanged. By setting a threshold to reduce the influence of instrument noise on the detections, we are inevitably also limiting the number of detected events and, therefore also the observed energy flux.

This effect can be seen in Figure 6.16 where we found a higher energy flux for lower threshold factors in all individual data sets. We find that the energy flux in each data set increased by at least a factor of 3 when lowering the threshold from $F = 7$ to $F = 5$, hinting at a possible further increase in the derived energy flux at even lower threshold factors. However, we did not use an even lower threshold because it leads to false event detection due to noise and problems with the implemented event combination algorithm.

7.5 Spatial Distribution of Events

We analyzed the spatial distribution of events and energy flux in all data sets and found that both are not distributed evenly across the field-of-view. Instead, flux and activity per pixel form similar clusters with distinct hotspots and extended areas of reduced activity in between. To get the spatial distribution of thermal event energy flux for a data set, we divided the total energy observed in each pixel by the two-hour observation time and the area of a single pixel. From these results we find a difference of about two orders of magnitude (about 4×10^2 to $4 \times 10^4 \,\mathrm{erg\,cm^{-2}\,s^{-1}}$) in energy flux between different regions of the same $400'' \times 400''$ field-of-view. We defined active pixels as all pixels with at least one event during the two-hour observation time. From the results presented in section 6.3 we find that the majority of pixels (at least $60\,\%$) are active in each data set for the reference set of parameters. This is in contrast to Parnell and Jupp (2000), who found that only $16\,\%$ (for 2σ events) of the pixels in their quiet sun observations contain at least one event. As the main reason, the authors give the short observation time of $15\,\mathrm{min}$ and note that Benz and Krucker (1999) found a significantly higher fraction of active pixels in their $42\,\mathrm{min}$ observations. Our high number of active pixels can presumably also be explained by the much longer observation time of two hours per data set. Another factor could be the local threshold we set for each pixel instead of one global value. This increases the sensitivity for small events in dimmer pixels where we would otherwise not find any events.

The fraction of active pixels is also highly dependent on the used threshold factor. Raising the threshold factor to $F = 7$ brings the fraction of active pixels in all data sets down below $50\,\%$ with a large portion of data sets only containing about $20\,\%$ active pixels. The fraction of active pixels is further decreased to $< 20\,\%$ for all data sets at a threshold factor of $F = 9$. We conclude that the number of active pixels will approach a high fraction of the total observed pixels given a long enough observation time and a low enough threshold. However, the immense influence of both factors makes this fraction of active pixels hard to compare between different studies.

We also find that the fraction of pixels considered active in each data set shows a significant ($r < -0.53$) inverse correlation to the sunspot number for all parameter combinations. This could mean that events are spatially more homogeneously distributed during lower solar activity. However, it could also be a result of a change in the AIA data (eg. lower contrast between different regions, degradation of the instrument). The total event frequency also shows an inverse correlation ($r = -0.48$ to -0.63) to the sunspot number for all parameter combinations. Figure 6.18 clearly shows the larger extent of regions with a high number of events (more than seven over two hours) resulting from the combined effect of more active pixels and higher total frequency.

By investigating the spatial distribution of energy flux and event counts per pixel, we find clusters of high activity and high flux (up to $3 \times 10^4\,\mathrm{erg\,cm^{-2}\,s^{-1}}$) surrounded by extended regions of lower activity where the observed flux drops by up to two orders of magnitude. Comparisons with magnetograms from the Helioseismic and Magnetic Imager (HMI) reveal that the high-activity clusters are located mainly in the magnetic network, preferentially in mixed flux regions of opposite polarities.

The frequency distribution of event areas shows a clear peak at an event size of a single pixel with a quick drop-off towards larger areas in all data sets and with all parameter combinations. For the reference parameters, we find a mean area of 1.3 to 1.9 for the different data sets and an inverse correlation ($r = -0.45$) to the sunspot number. The fraction of events larger than one or 16 pixels also shows inverse correlation to the sunspot number with coefficients of $r = -0.57$ and $r = -0.45$, respectively.

8 Conclusions

In this study, we have investigated the frequency distributions of nanoflares and their characteristics in quiet sun regions throughout the years 2011 to 2018 to analyze their energy contribution to coronal heating and detect any changes due to variations in solar activity. We used multi-band EUV images from AIA, differential emission measure analysis, and a threshold-based tunable event detection algorithm specifically developed for AIA data characteristics. In the following, we summarize the main conclusions.

The developed event detection algorithm works very well within the recommended parameter boundaries. It reliably produces nanoflare frequency distributions with continuous power-law slopes over multiple orders of magnitude in thermal event energy (from about 1×10^{23} to $1 \times 10^{26}\,\mathrm{erg}$) for all individual data sets. Non-weighted linear fits to the log-log frequency distribution reveal individual power-law indices in the range of $\alpha = 2.06$ to 2.38 that show no significant correlation to the monthly mean sunspot number. The combined frequency distribution of all data sets, with a total observation time of 60 hours at a 12-second temporal resolution, shows a continuous power-law distribution over five orders of magnitude in thermal event energy (1×10^{23} to $1 \times 10^{28}\,\mathrm{erg\,cm^{-2}\,s^{-1}}$) with a power-law index of $\alpha = 2.26$. We find a power-law index $\alpha > 2$ ($\alpha = 2.16$ to 2.36) for the combined frequency distributions of all investigated method parameter combinations, indicating that the heat input into the corona is dominated by the lower energy part of the distribution. We observed an energy flux in the individual data sets in the range of 2×10^3 to $4 \times 10^3\,\mathrm{erg\,cm^{-2}\,s^{-1}}$ that did not show a significant correlation to the sunspot number, independent of the used set of method parameters. The combined distribution of the reference parameters provides an energy flux of $3.2 \times 10^3\,\mathrm{erg\,cm^{-2}\,s^{-1}}$ that accounts for only about one percent of the required coronal heat input. The observed frequency distribution would have to continue down to events with a thermal energy input of about $2 \times 10^{19}\,\mathrm{erg}$ to balance the total energy loss of the corona if the found energy flux is assumed to be the actual energy flux produced by the events. We discussed energy considerations by Benz and Krucker (2002) and possible biases in the applied event definition and detection that could increase the energy flux and move the required extension of the power-law distribution to higher energies. In addition to the general energy flux considerations, we also investigated its spatial distribution and find large variations of about two orders of magnitude (4×10^2

to $4 \times 10^4\,\mathrm{erg\,cm^{-2}\,s^{-1}}$) between different regions of the same $400'' \times 400''$ field-of-view. Regions with large energy inputs form clusters located preferentially at the boundaries of the magnetic network and are not evenly distributed over the solar disk. Multiple investigated parameters (power-law of small events, fraction of active pixels, events per active pixel, mean size of events, fraction of events larger than one or 16 pixels) show a noticeable change during the second half of the observed timescale with an apparent correlation to the sunspot number. It is unclear whether this is a result of an actual change in the nanoflare distribution or if there is a change in the data quality and characteristics that could cause such behavior.

Bibliography

Arnaud, M. and J. Raymond (1992). „Iron Ionization and Recombination Rates and Ionization Equilibrium“. In: *The Astrophysical Journal* 398, p. 394. DOI: 10.1086/171864 (cit. on p. 23).

Aschwanden, Markus J (2004). *Physics of the solar corona : an introduction*. eng. Springer-Praxis books in geophysical sciences (cit. on pp. 9–16, 18, 22–24, 27, 32, 33, 37, 54, 75, 111–113).

Aschwanden, Markus J. (2001). „An Evaluation of Coronal Heating Models for Active Regions Based on Yohkoh, SOHO, and TRACE Observations“. In: *The Astrophysical Journal* 560.2, pp. 1035–1044. DOI: 10.1086/323064 (cit. on pp. 25, 26).

Aschwanden, Markus J. and Clare E. Parnell (2002). „Nanoflare Statistics from First Principles: Fractal Geometry and Temperature Synthesis“. In: *The Astrophysical Journal* 572.2, pp. 1048–1071. DOI: 10.1086/340385 (cit. on pp. 32, 33, 111).

Aschwanden, Markus J., Ted D. Tarbell, Richard W. Nightingale, Carolus J. Schrijver, Alan Title, Charles C. Kankelborg, Piet Martens, and Harry P. Warren (2000). „Time Variability of the “Quiet” Sun Observed with TRACE. II. Physical Parameters, Temperature Evolution, and Energetics of Extreme-Ultraviolet Nanoflares“. In: *The Astrophysical Journal* 535.2, pp. 1047–1065. DOI: 10.1086/308867 (cit. on pp. 28, 30, 32, 33, 111, 112, 114).

Benz, Arnold O. and Säm Krucker (1999). „Heating events in the quiet solar corona: multiwavelength correlations“. In: *Astronomy and Astrophysics* 341, pp. 286–295 (cit. on p. 116).

Benz, Arnold O. and Säm Krucker (2002). „Energy Distribution of Microevents in the Quiet Solar Corona“. In: *The Astrophysical Journal* 568.1, pp. 413–421. DOI: 10.1086/338807. arXiv: astro-ph/0109027 [astro-ph] (cit. on pp. 32, 33, 54, 55, 64, 111, 112, 115, 119).

Boerner, Paul, Christopher Edwards, James Lemen, Adam Rausch, Carolus Schrijver, Richard Shine, Lawrence Shing, Robert Stern, Theodore Tarbell, Alan Title, C. Jacob Wolfson, Regina Soufli, Eberhard Spiller, Eric Gullikson, David McKenzie, David Windt, Leon Golub, William Podgorski, Paola Testa, and Mark Weber (2012). „Initial Calibration of the Atmospheric Imaging Assembly (AIA) on the Solar Dynamics Observatory (SDO)“. In: *Solar Physics* 275.1-2, pp. 41–66. DOI: 10.1007/s11207-011-9804-8 (cit. on pp. 39, 40).

Carroll, Bradley W. and Dale A. Ostlie (2006). *An introduction to modern astrophysics and cosmology* (cit. on pp. 4–8, 22).

Clette, Frédéric, Leif Svalgaard, José M. Vaquero, and Edward W. Cliver (2014). „Revisiting the Sunspot Number. A 400-Year Perspective on the Solar Cycle“. In: *Space Science Reviews* 186.1-4, pp. 35–103. DOI: 10.1007/s11214-014-0074-2. arXiv: 1407.3231 [astro-ph.SR] (cit. on p. 17).

Close, R. M., C. E. Parnell, D. H. Mackay, and E. R. Priest (2003). „Statistical Flux Tube Properties of 3D Magnetic Carpet Fields“. In: *Solar Physics* 212.2, pp. 251–275. DOI: 10.1023/A:1022961913168 (cit. on p. 34).

Crosby, Norma B., Markus J. Aschwanden, and Brian R. Dennis (1993). „Frequency distributions and correlations of solar X-ray flare parameters“. In: *Solar Physics* 143.2, pp. 275–299. DOI: 10.1007/BF00646488 (cit. on pp. 27, 28, 30–33, 110, 111, 113).

Dahlburg, R. B., J. A. Klimchuk, and S. K. Antiochos (2003). „Coronal energy release via ideal three-dimensional instability three-dimensional instability“. In: *Advances in Space Research* 32.6, pp. 1029–1034. DOI: 10.1016/S0273-1177(03)00305-3 (cit. on p. 31).

Dahlburg, R. B., J. A. Klimchuk, and S. K. Antiochos (2005). „An Explanation for the “Switch-On” Nature of Magnetic Energy Release and Its Application to Coronal Heating“. In: *The Astrophysical Journal* 622.2, pp. 1191–1201. DOI: 10.1086/425645 (cit. on p. 31).

Delaboudinière, J. -P., G. E. Artzner, J. Brunaud, et al. (1995). „EIT: Extreme-Ultraviolet Imaging Telescope for the SOHO Mission“. In: *Solar Physics* 162.1-2, pp. 291–312. DOI: 10.1007/BF00733432 (cit. on p. 54).

Dere, K. P., G. Del Zanna, P. R. Young, E. Landi, and R. S. Sutherland (2019). „CHIANTI—An Atomic Database for Emission Lines. XV. Version 9, Improvements for the X-Ray Satellite Lines“. In: *The Astrophysical Journal Supplement Series* 241.2, 22, p. 22. DOI: 10.3847/1538-4365/ab05cf. arXiv: 1902.05019 [astro-ph.SR] (cit. on p. 23).

Dere, K. P., E. Landi, H. E. Mason, B. C. Monsignori Fossi, and P. R. Young (1997). „CHIANTI - an atomic database for emission lines“. In: *Astronomy and Astrophysics, Supplement* 125, pp. 149–173. DOI: 10.1051/aas:1997368 (cit. on p. 23).

Foukal, Peter V. (2004). *Solar Astrophysics, 2nd, Revised Edition* (cit. on pp. 3, 5, 6, 8, 12, 13, 15, 17).

Handy, B. N., L. W. Acton, C. C. Kankelborg, et al. (1999). „The transition region and coronal explorer“. In: *Solar Physics* 187.2, pp. 229–260. DOI: 10.1023/A:1005166902804 (cit. on p. 54).

Hannah, I. G., S. Christe, S. Krucker, G. J. Hurford, H. S. Hudson, and R. P. Lin (2008). „RHESSIMicroflare Statistics. II. X-Ray Imaging, Spectroscopy, and Energy Distributions“. In: *The Astrophysical Journal* 677.1, pp. 704–718. DOI: 10.1086/529012 (cit. on pp. 112, 113).

Hannah, I. G., H. S. Hudson, M. Battaglia, S. Christe, J. Kašparová, S. Krucker, M. R. Kundu, and A. Veronig (2011). „Microflares and the Statistics of X-ray Flares“. In: *Space Science Reviews* 159.1-4, pp. 263–300. DOI: 10.1007/s11214-010-9705-4. arXiv: 1108.6203 [astro-ph.SR] (cit. on pp. 112, 113).

Hannah, I. G. and E. P. Kontar (2012). „Differential emission measures from the regularized inversion of Hinode and SDO data“. In: *Astronomy and Astrophysics* 539, A146, A146. DOI: 10.1051/0004-6361/201117576. arXiv: 1201.2642 [astro-ph.SR] (cit. on pp. 1, 48, 107).

Hanslmeier, Arnold (2020). *Einführung in Astronomie und Astrophysik*. ger. 4. Aufl. 2020. Berlin, Heidelberg: Springer Berlin Heidelberg (cit. on pp. 3, 6, 7).

Hathaway, David H. (2015). „The Solar Cycle“. In: *Living Reviews in Solar Physics* 12.1, 4, p. 4. DOI: 10.1007/lrsp-2015-4. arXiv: 1502.07020 [astro-ph.SR] (cit. on pp. 6, 15, 17, 18).

Hollweg, J. V. (1981). „Alfven Waves in the Solar Atmosphere - Part Two - Open and Closed Magnetic Flux Tubes“. In: *Solar Physics* 70.1, pp. 25–66. DOI: 10.1007/BF00154391 (cit. on p. 35).

Hollweg, J. V. (1984). „Resonances of coronal loops“. In: *The Astrophysical Journal* 277, pp. 392–403. DOI: 10.1086/161706 (cit. on p. 35).

Hudson, H. S. (1991). „Solar flares, microflares, nanoflares, and coronal heating“. In: *Solar Physics* 133.2, pp. 357–369. DOI: 10.1007/BF00149894 (cit. on pp. 31, 32, 110).

Ionson, J. A. (1982). „Resonant electrodynamic heating of stellar coronal loops - an LRC circuit analog“. In: *The Astrophysical Journal* 254, pp. 318–334. DOI: 10.1086/159736 (cit. on p. 35).

Klimchuk, James A. (2006). „On Solving the Coronal Heating Problem“. In: *Solar Physics* 234.1, pp. 41–77. DOI: 10.1007/s11207-006-0055-z. arXiv: astro-ph/0511841 [astro-ph] (cit. on pp. 24, 26, 31, 34, 35).

Klimchuk, James A. (2015). „Key aspects of coronal heating“. In: *Philosophical Transactions of the Royal Society of London Series A* 373.2042, pp. 20140256–20140256. DOI: 10.1098/rsta.2014.0256. arXiv: 1410.5660 [astro-ph.SR] (cit. on p. 34).

Krucker, Säm and Arnold O. Benz (1998). „Energy Distribution of Heating Processes in the Quiet Solar Corona“. In: *The Astrophysical Journal, Letters* 501.2, pp. L213–L216. DOI: 10.1086/311474 (cit. on pp. 1, 32, 33, 56, 63, 64, 111, 114, 115).

Lemen, James R., Alan M. Title, David J. Akin, et al. (2012). „The Atmospheric Imaging Assembly (AIA) on the Solar Dynamics Observatory (SDO)“. In: *Solar Physics* 275.1-2, pp. 17–40. DOI: 10.1007/s11207-011-9776-8 (cit. on pp. 37, 39, 40).

Lu, Edward T. and Russell J. Hamilton (1991). „Avalanches and the Distribution of Solar Flares“. In: *The Astrophysical Journal, Letters* 380, p. L89. DOI: 10.1086/186180 (cit. on pp. 29–31, 110).

Maehara, Hiroyuki, Takuya Shibayama, Shota Notsu, Yuta Notsu, Takashi Nagao, Satoshi Kusaba, Satoshi Honda, Daisaku Nogami, and Kazunari Shibata (2012). „Superflares on solar-type stars“. In: *Nature* 485.7399, pp. 478–481. DOI: 10.1038/nature11063 (cit. on pp. 28, 30, 113).

Mullan, Dermott J (2009). *Physics of the sun : a first course*. eng. Series in pure and applied physics (cit. on pp. 8, 10–12, 15, 22).

Murdin, Paul (2001). *Encyclopedia of astronomy and astrophysics* (cit. on pp. 6, 8).

Narain, U. and P. Ulmschneider (1996). „Chromospheric and Coronal Heating Mechanisms II“. In: *Space Science Reviews* 75.3-4, pp. 453–509. DOI: 10.1007/BF00833341 (cit. on p. 35).

Parker, E. N. (1957). „Sweet's Mechanism for Merging Magnetic Fields in Conducting Fluids“. In: *Journal of Geophysics Research* 62.4, pp. 509–520. DOI: 10.1029/JZ062i004p00509 (cit. on p. 13).

Parker, E. N. (1972). „Topological Dissipation and the Small-Scale Fields in Turbulent Gases“. In: *The Astrophysical Journal* 174, p. 499. DOI: 10.1086/151512 (cit. on pp. 26, 27).

Parker, E. N. (1983). „Magnetic Neutral Sheets in Evolving Fields - Part Two - Formation of the Solar Corona“. In: *The Astrophysical Journal* 264, p. 642. DOI: 10.1086/160637 (cit. on p. 27).

Parnell, C. E. (2004). „The Role of Dynamic Brightenings in Coronal Heating“. In: *SOHO 15 Coronal Heating*. Ed. by R. W. Walsh, J. Ireland, D. Danesy, and B. Fleck. Vol. 575. ESA Special Publication, p. 227 (cit. on pp. 32, 56, 111, 114).

Parnell, C. E. and I. De Moortel (2012). „A contemporary view of coronal heating“. In: *Philosophical Transactions of the Royal Society of London Series A* 370.1970, pp. 3217–3240. DOI: 10.1098/rsta.2012.0113. arXiv: 1206.6097 [astro-ph.SR] (cit. on pp. 10, 23–26, 32, 34, 35, 54, 56).

Parnell, C. E. and P. E. Jupp (2000). „Statistical Analysis of the Energy Distribution of Nanoflares in the Quiet Sun“. In: *The Astrophysical Journal* 529.1, pp. 554–569. DOI: 10.1086/308271 (cit. on pp. 32, 33, 111–116).

Priest, Eric Ronald (1984). *Solar magneto-hydrodynamics* (cit. on p. 9).

Sakurai, Takashi (2017). „Heating mechanisms of the solar corona“. In: *Proceedings of the Japan Academy, Series B* 93, pp. 87–97. DOI: 10.2183/pjab.93.006 (cit. on pp. 21–25, 31, 35).

Schindler, K. and G. Hornig (2000). „Magnetic Reconnection“. In: *Encyclopedia of Astronomy and Astrophysics*. Ed. by P. Murdin, 2224, p. 2224. DOI: 10.1888/0333750888/2224 (cit. on p. 14).

Schou, J., P. H. Scherrer, R. I. Bush, et al. (2012). „Design and Ground Calibration of the Helioseismic and Magnetic Imager (HMI) Instrument on the Solar Dynamics Observatory (SDO)“. In: *Solar Physics* 275.1-2, pp. 229–259. DOI: 10.1007/s11207-011-9842-2 (cit. on p. 39).

Schrijver, C. J., A. M. Title, K. L. Harvey, N. R. Sheeley, Y. -M. Wang, G. H. J. van den Oord, R. A. Shine, T. D. Tarbell, and N. E. Hurlburt (1998). „Large-scale coronal heating by the small-scale magnetic field of the Sun“. In: *Nature* 394.6689, pp. 152–154. DOI: 10.1038/28108 (cit. on p. 34).

Schwabe, Heinrich (1844). „Sonnenbeobachtungen im Jahre 1843. Von Herrn Hofrath Schwabe in Dessau“. In: *Astronomische Nachrichten* 21.15, p. 233. DOI: 10.1002/asna.18440211505 (cit. on p. 15).

Severino, Giuseppe (2017). *The structure and evolution of the sun*. eng. Undergraduate lecture notes in physics (cit. on pp. 5, 6).

Shibata, Kazunari, Hiroaki Isobe, Andrew Hillier, Arnab Rai Choudhuri, Hiroyuki Maehara, Takako T. Ishii, Takuya Shibayama, Shota Notsu, Yuta Notsu, Takashi Nagao, Satoshi Honda, and Daisaku Nogami (2013). „Can Superflares Occur on Our Sun?“ In: *Publications of the Astronomical Society of Japan* 65, 49, p. 49. DOI: 10.1093/pasj/65.3.49. arXiv: 1212.1361 [astro-ph.SR] (cit. on pp. 28, 30, 31, 113).

Shimizu, Toshifumi (1995). „Energetics and Occurrence Rate of Active-Region Transient Brightenings and Implications for the Heating of the Active-Region Corona“. In: *Publications of the Astronomical Society of Japan* 47, pp. 251–263 (cit. on pp. 28, 30, 32, 33, 111–113).

Su, Yang, Astrid M. Veronig, Iain G. Hannah, Mark C. M. Cheung, Brian R. Dennis, Gordon D. Holman, Weiqun Gan, and Youping Li (2018). „Determination of Differential Emission Measure from Solar Extreme Ultraviolet Images“. In: *The Astrophysical Journal, Letters* 856.1, L17, p. L17. DOI: 10.3847/2041-8213/aab436 (cit. on pp. 47, 48).

Sweet, P. A. (1958). „The Neutral Point Theory of Solar Flares“. In: *Electromagnetic Phenomena in Cosmical Physics*. Ed. by B. Lehnert. Vol. 6, p. 123 (cit. on p. 13).

Thompson, M. J., J. Toomre, E. R. Anderson, et al. (1996). „Differential Rotation and Dynamics of the Solar Interior“. In: *Science* 272.5266, pp. 1300–1305. DOI: 10.1126/science.272.5266.1300 (cit. on p. 7).

Tomczyk, S., S. W. McIntosh, S. L. Keil, P. G. Judge, T. Schad, D. H. Seeley, and J. Edmondson (2007). „Alfvén Waves in the Solar Corona“. In: *Science* 317.5842, p. 1192. DOI: 10.1126/science.1143304 (cit. on p. 35).

Veronig, A., M. Temmer, A. Hanslmeier, W. Otruba, and M. Messerotti (2002). „Temporal aspects and frequency distributions of solar soft X-ray flares“. In: *Astronomy and Astrophysics* 382, pp. 1070–1080. DOI: 10.1051/0004-6361:20011694. arXiv: astro-ph/0207234 [astro-ph] (cit. on pp. 28, 29, 31, 110).

Withbroe, G. L. and R. W. Noyes (1977). „Mass and energy flow in the solar chromosphere and corona.“ In: *Annual Review of Astron and Astrophys* 15, pp. 363–387. DOI: 10.1146/annurev.aa.15.090177.002051 (cit. on pp. 23, 114).

A

Appendix

This appendix contains a collection of additional figures that expand on the selection shown in the main part of this thesis.
Section A.1 contains overviews of the data sets from the three remaining EUV wavelengths used to reconstruct the DEM.
Section A.2 shows examples of the event detection algorithm configured to all parameters discussed in the results.
Nanoflare frequency distributions from all methods are shown depending on the linear fitting method in sections A.3 and A.4.
Additional comparison plots of the HMI line-of-sight magnetogram, the energy flux distribution, the active pixel and event number distribution, and selected AIA images in selected wavelengths (171, 193 and 211 Å) are shown in section A.5.
Finally, the event area histograms from all methods are shown in section A.6.

A.1 AIA EUV Images

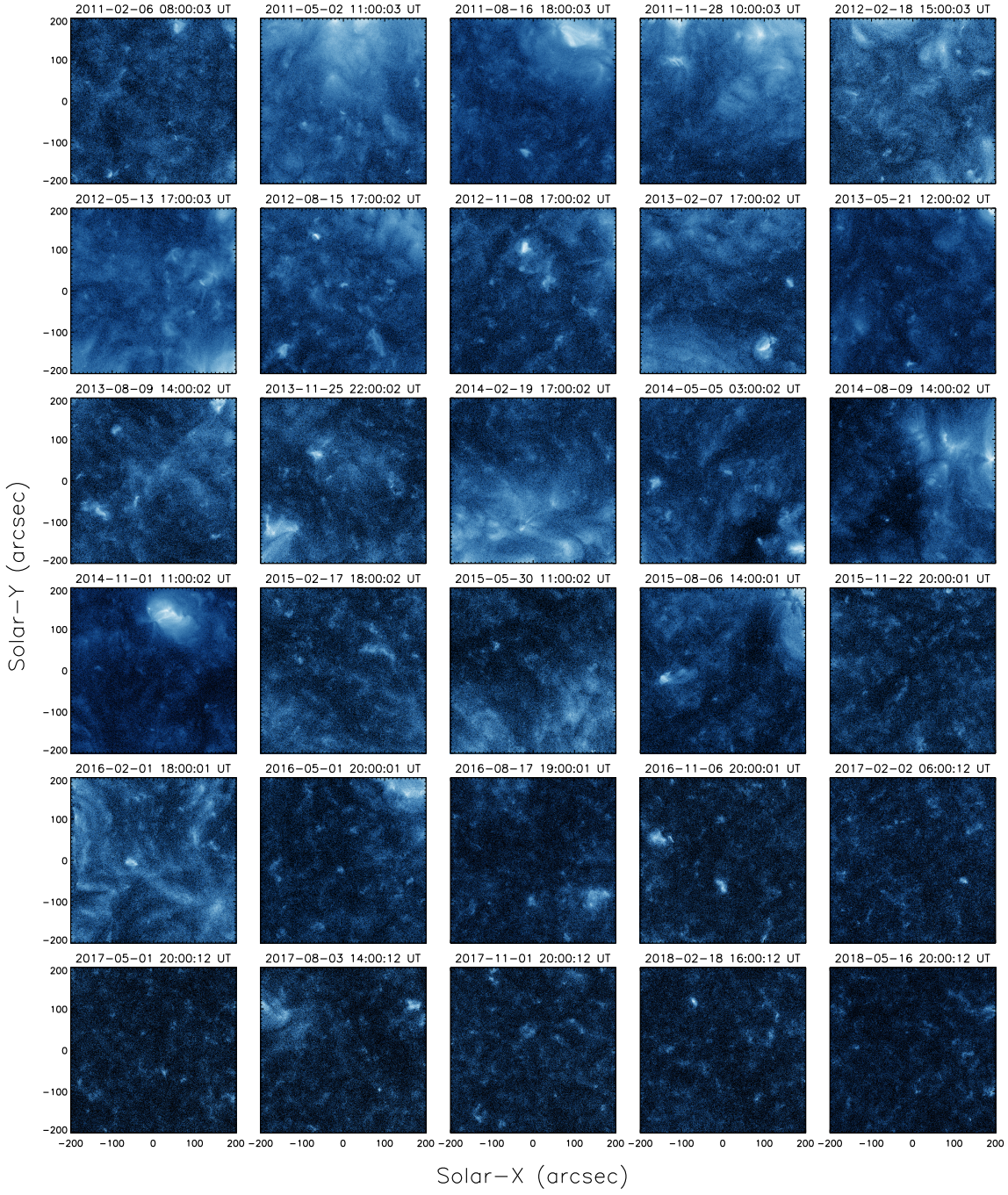

Fig. A.1.: First AIA 335 Å image from each of the data sets. The observation date and time is given on top of each image and marks the beginning of the full two hour data set. All observations are focused on a 400 times 400″ field of view around the solar disk center.

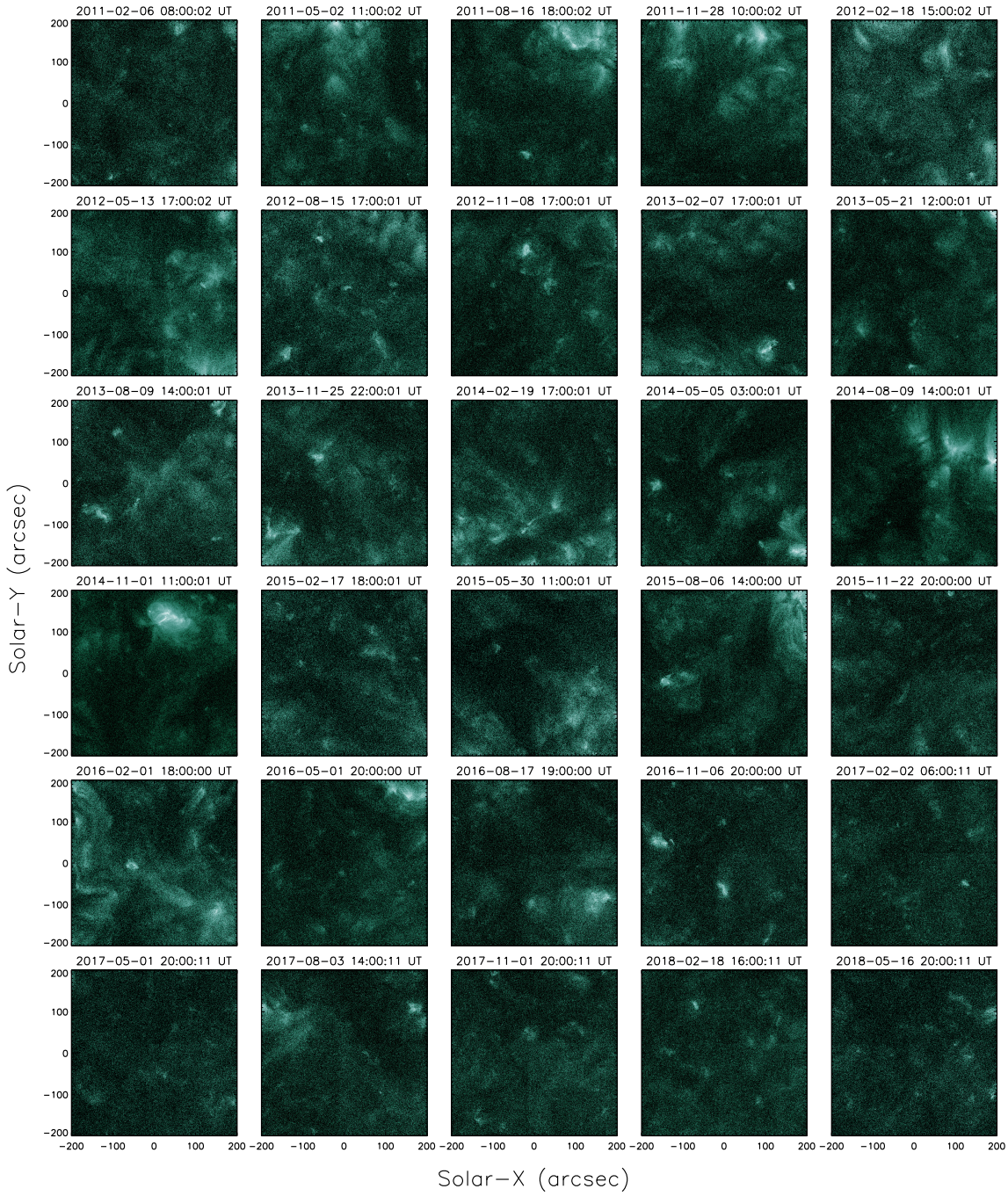

Fig. A.2.: First AIA 94 Å image from each of the data sets. The observation date and time is given on top of each image and marks the beginning of the full two hour data set. All observations are focused on a 400 times 400″ field of view around the solar disk center.

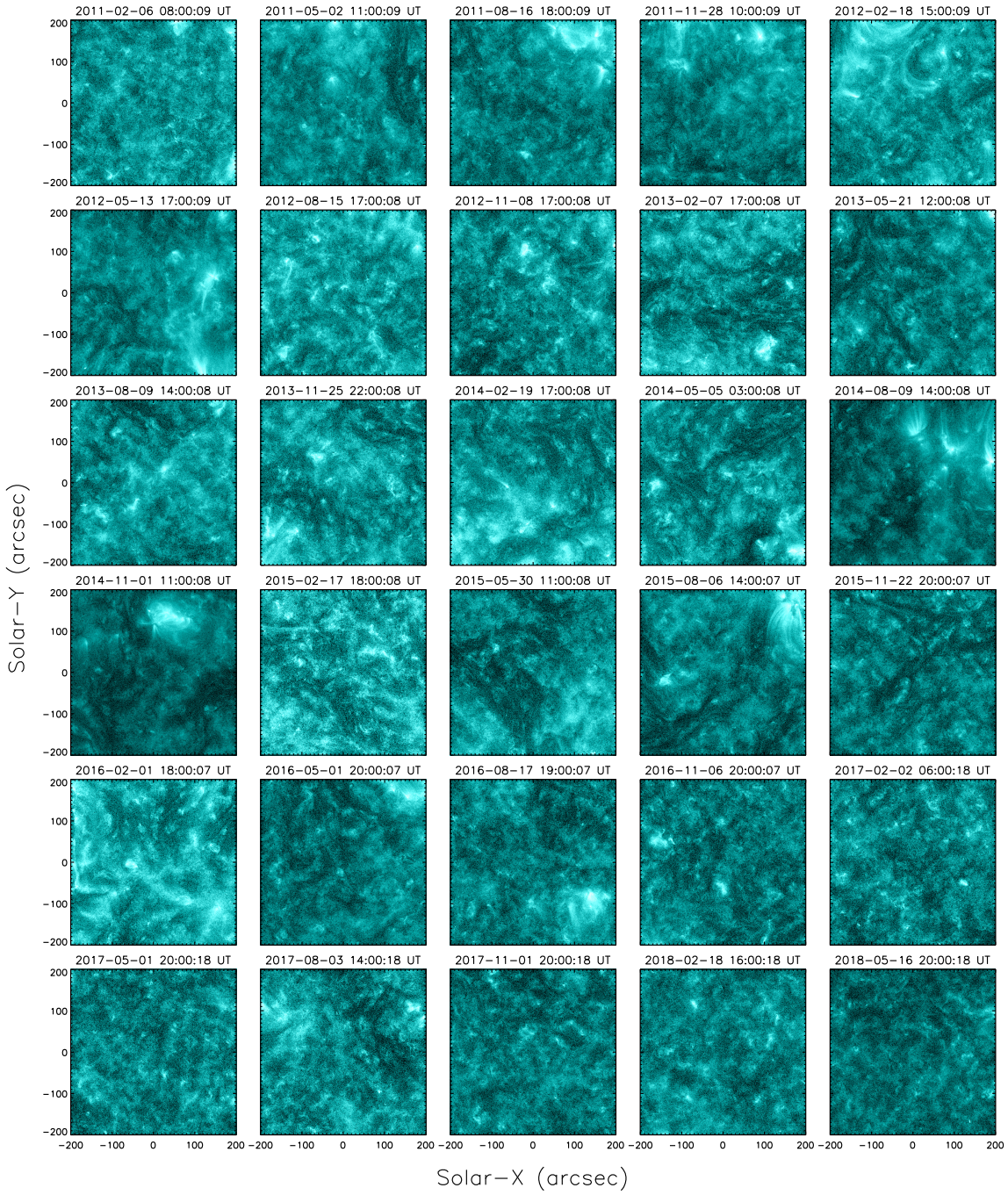

Fig. A.3.: First AIA 131 Å image from each of the data sets. The observation date and time is given on top of each image and marks the beginning of the full two hour data set. All observations are focused on a 400 times 400″ field of view around the solar disk center.

A.2 Event Detection

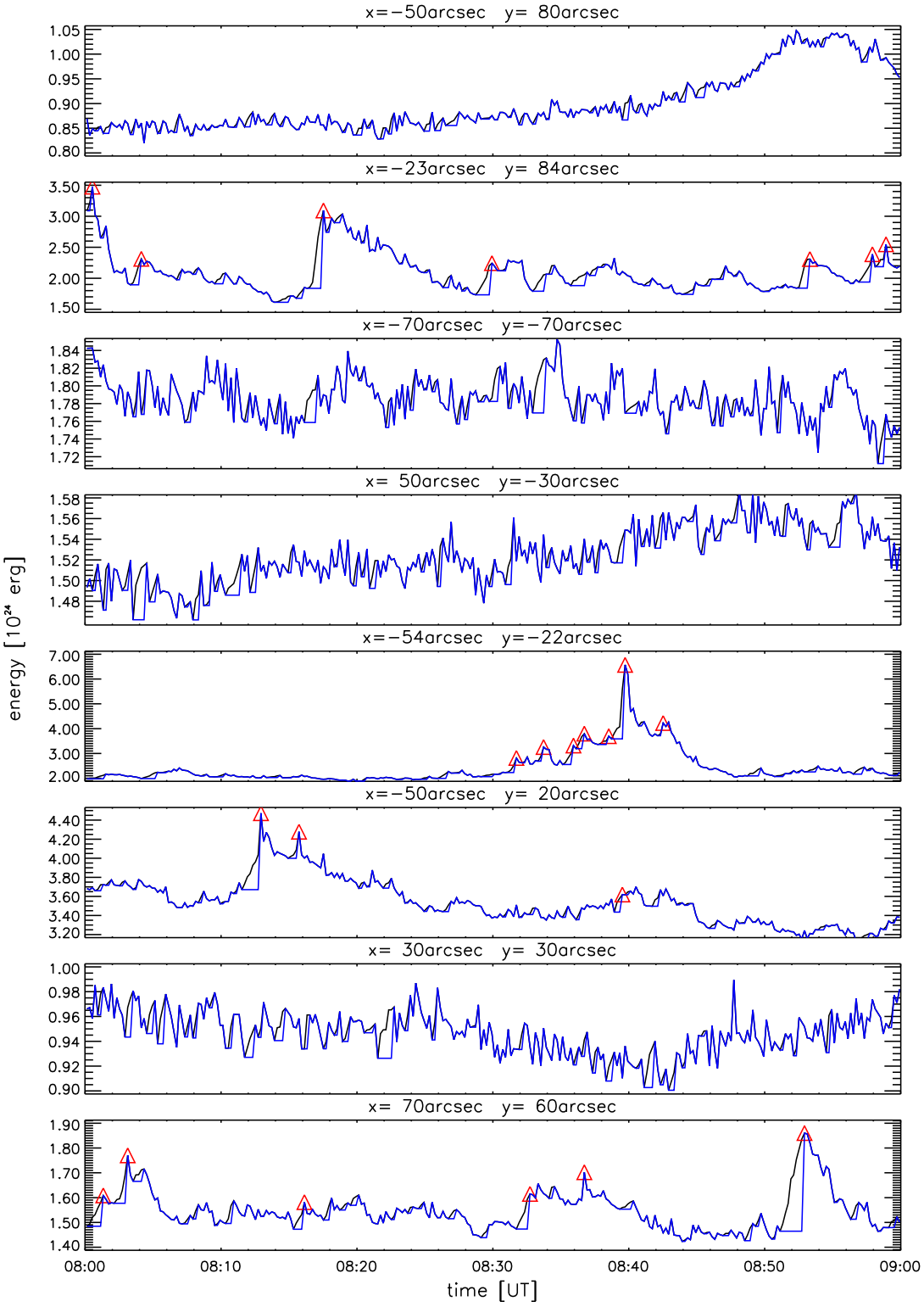

Fig. A.4.: Same as Figure 5.10 but using a detection interval of $D = 1$ and a threshold factor of $F = 5$.

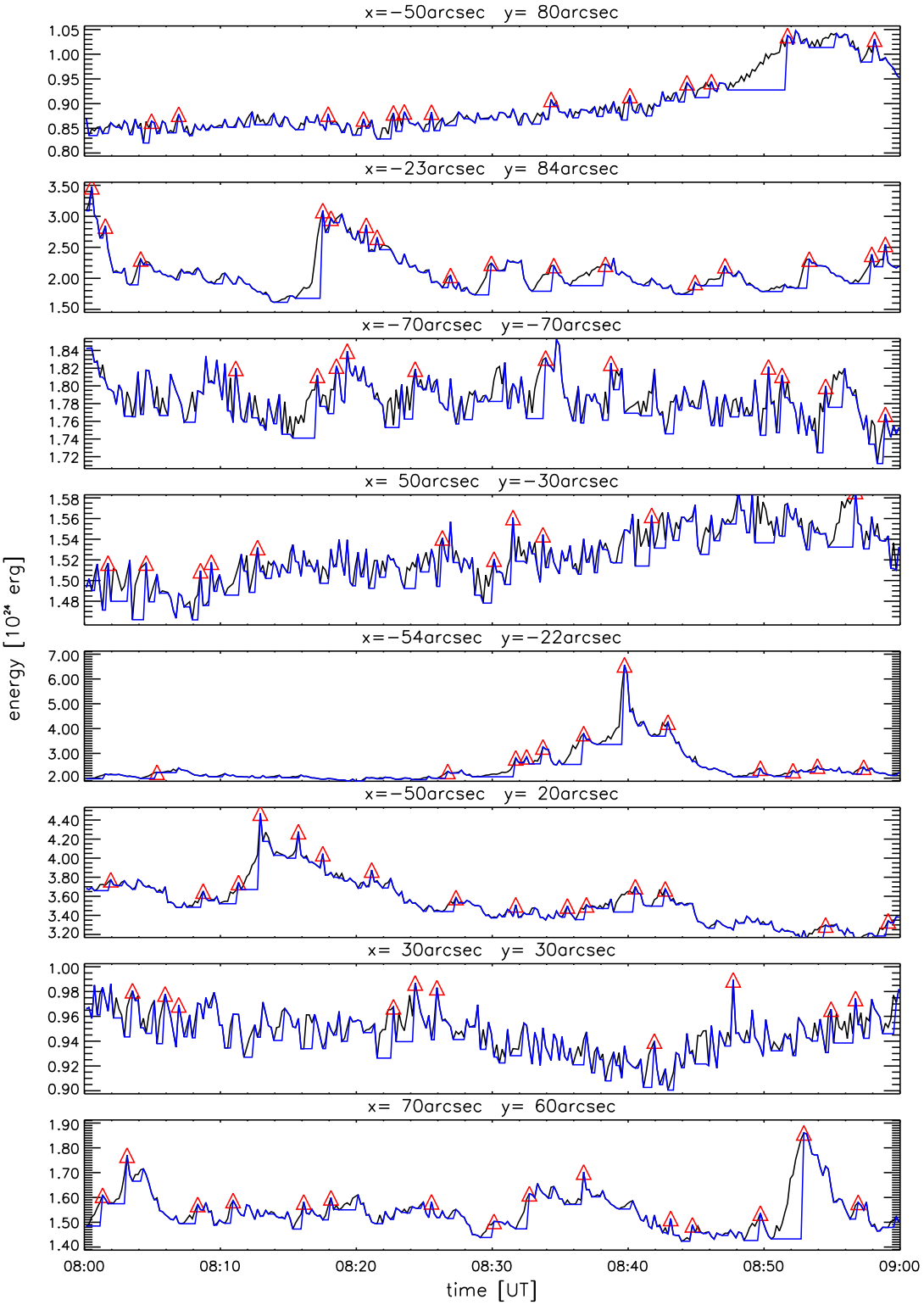

Fig. A.5.: Same as Figure 5.10 but using a detection interval of $D = 2$ and a threshold factor of $F = 3$.

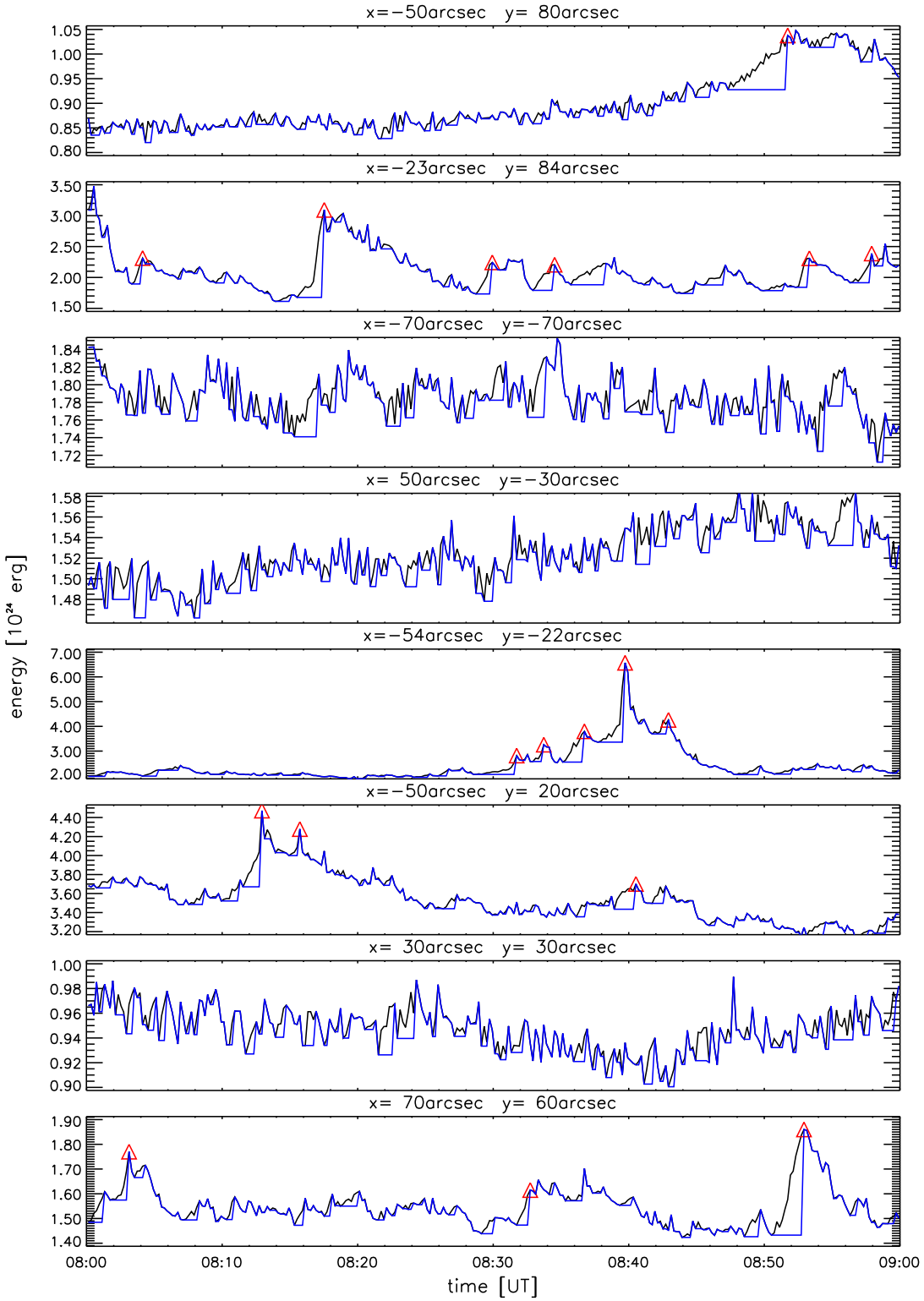

Fig. A.6.: Same as Figure 5.10 but using a detection interval of $D = 2$ and a threshold factor of $F = 7$.

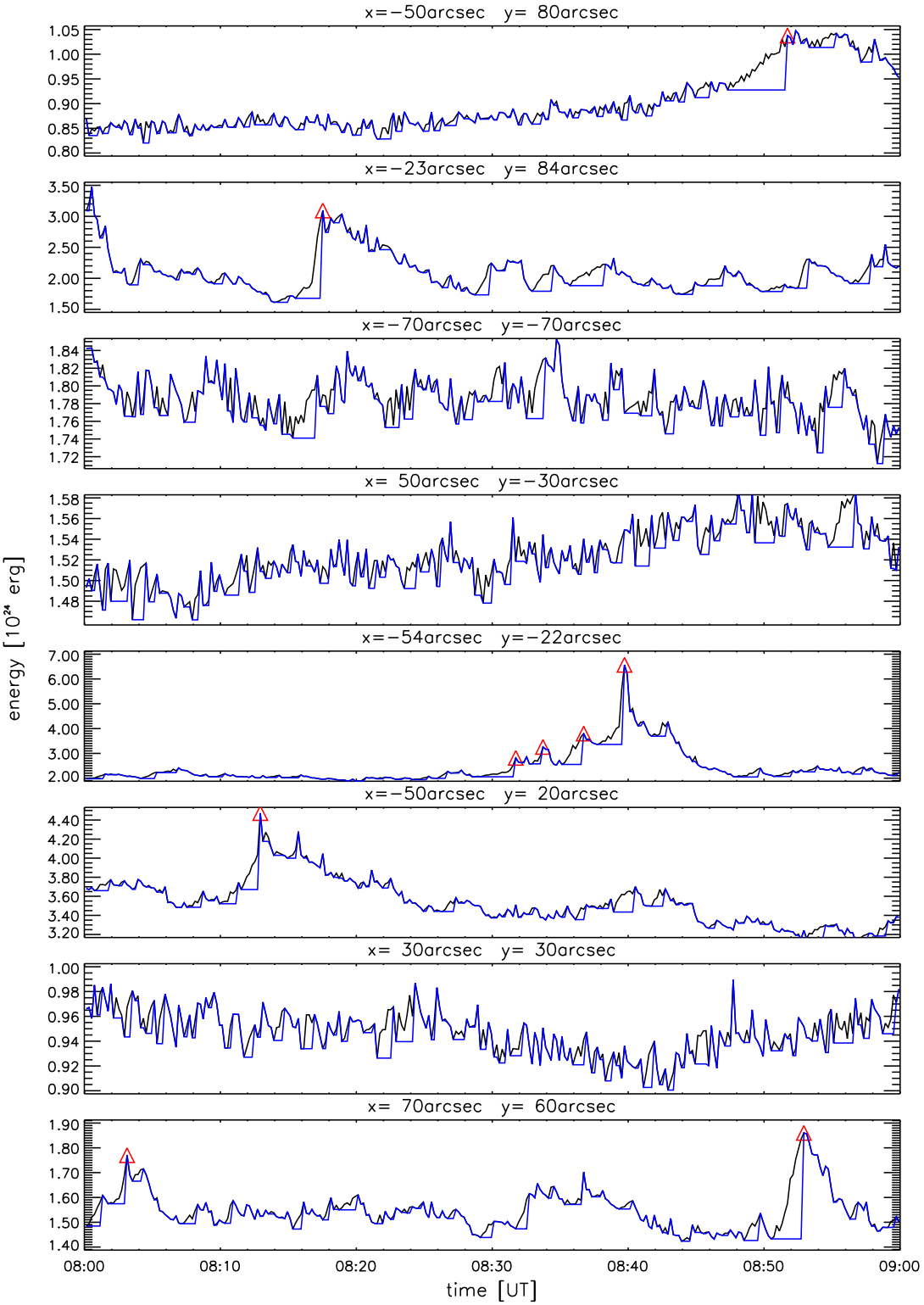

Fig. A.7.: Same as Figure 5.10 but using a detection interval of $D = 2$ and a threshold factor of $F = 9$.

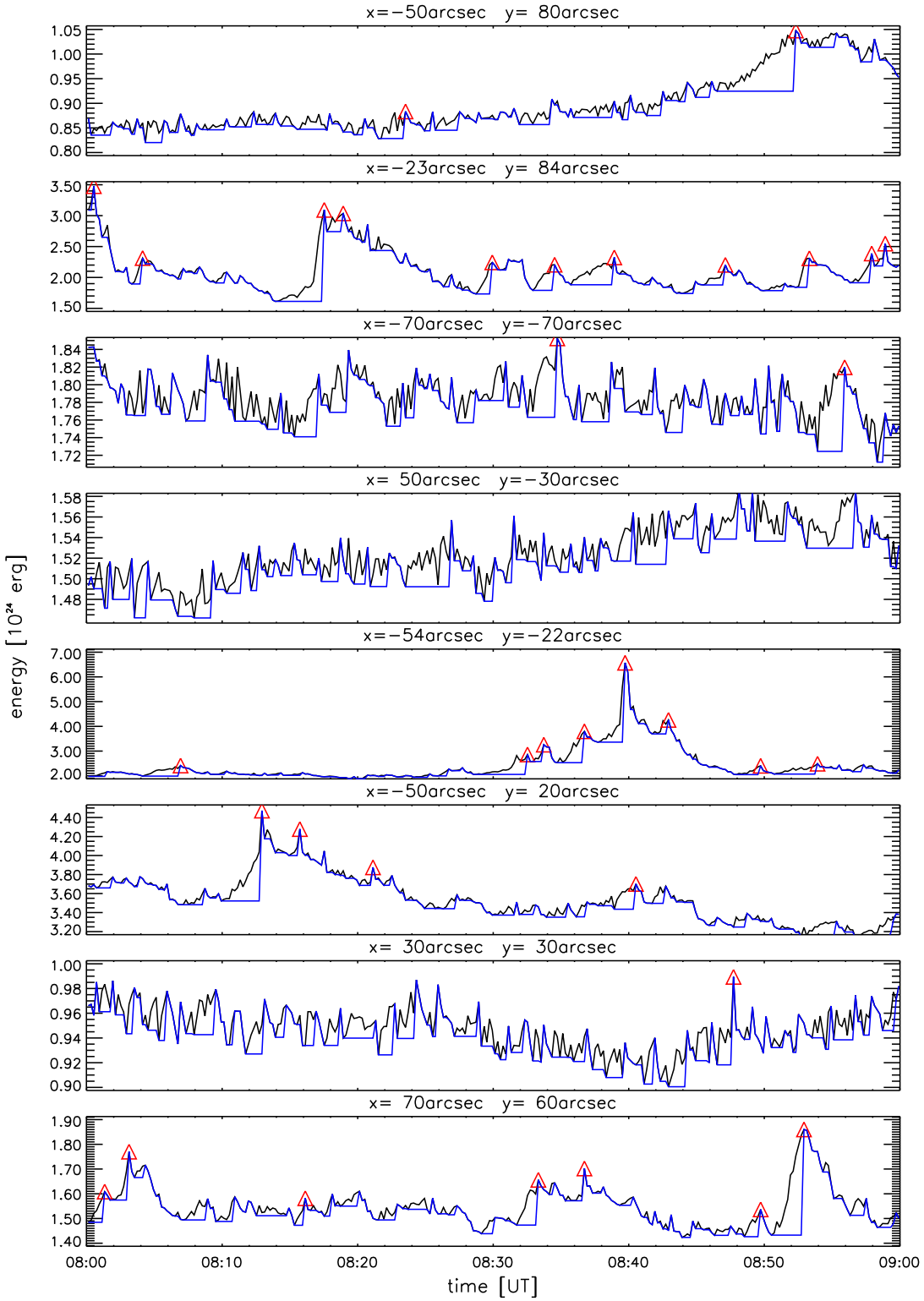

Fig. A.8.: Same as Figure 5.10 but using a detection interval of $D = 4$ and a threshold factor of $F = 5$.

A.3 Power-law Fits with Weights

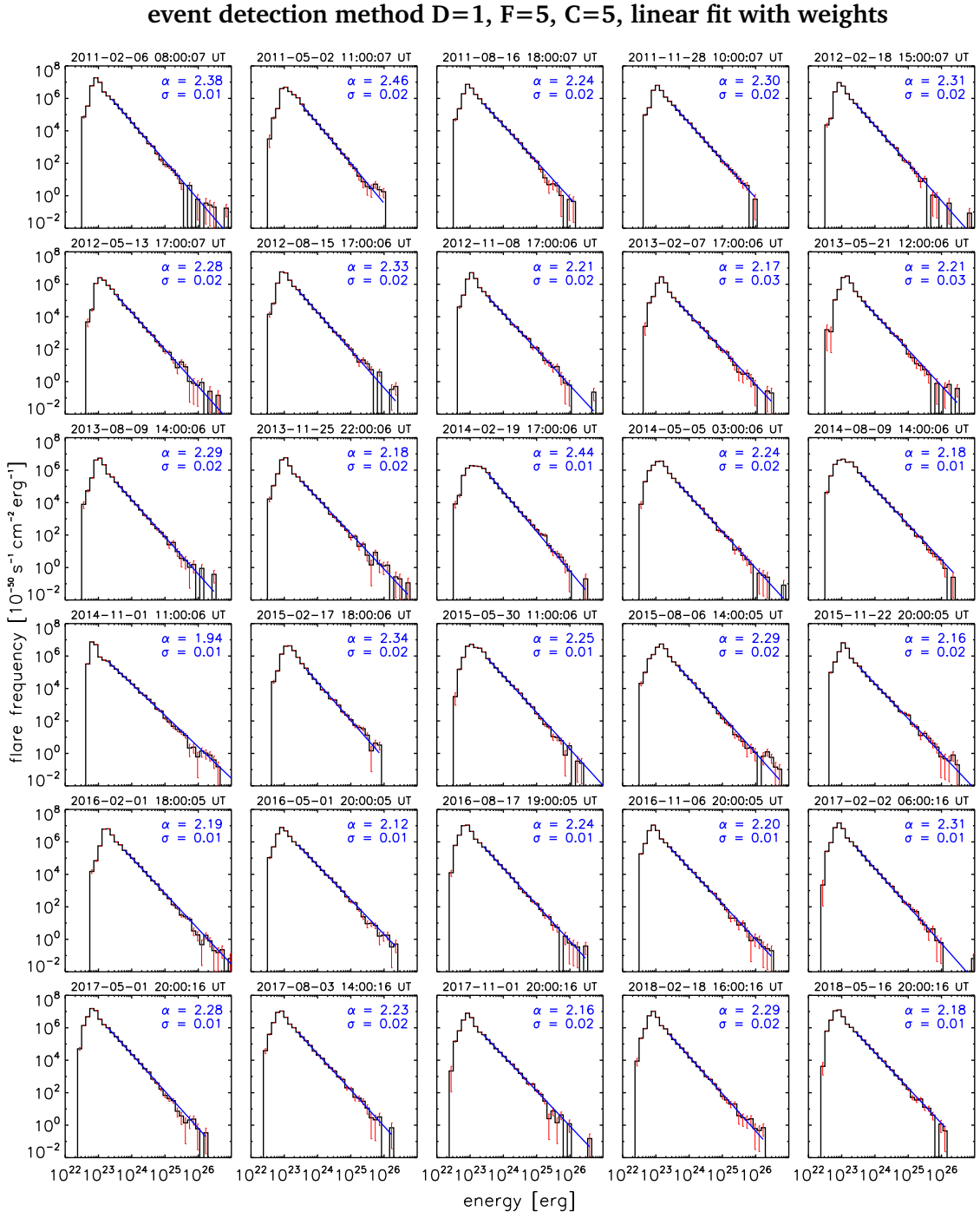

Fig. A.9.: Same as Figure 6.1 but using a detection interval of $D = 1$, a threshold factor of $F = 5$, and a combination interval of $C = 5$.

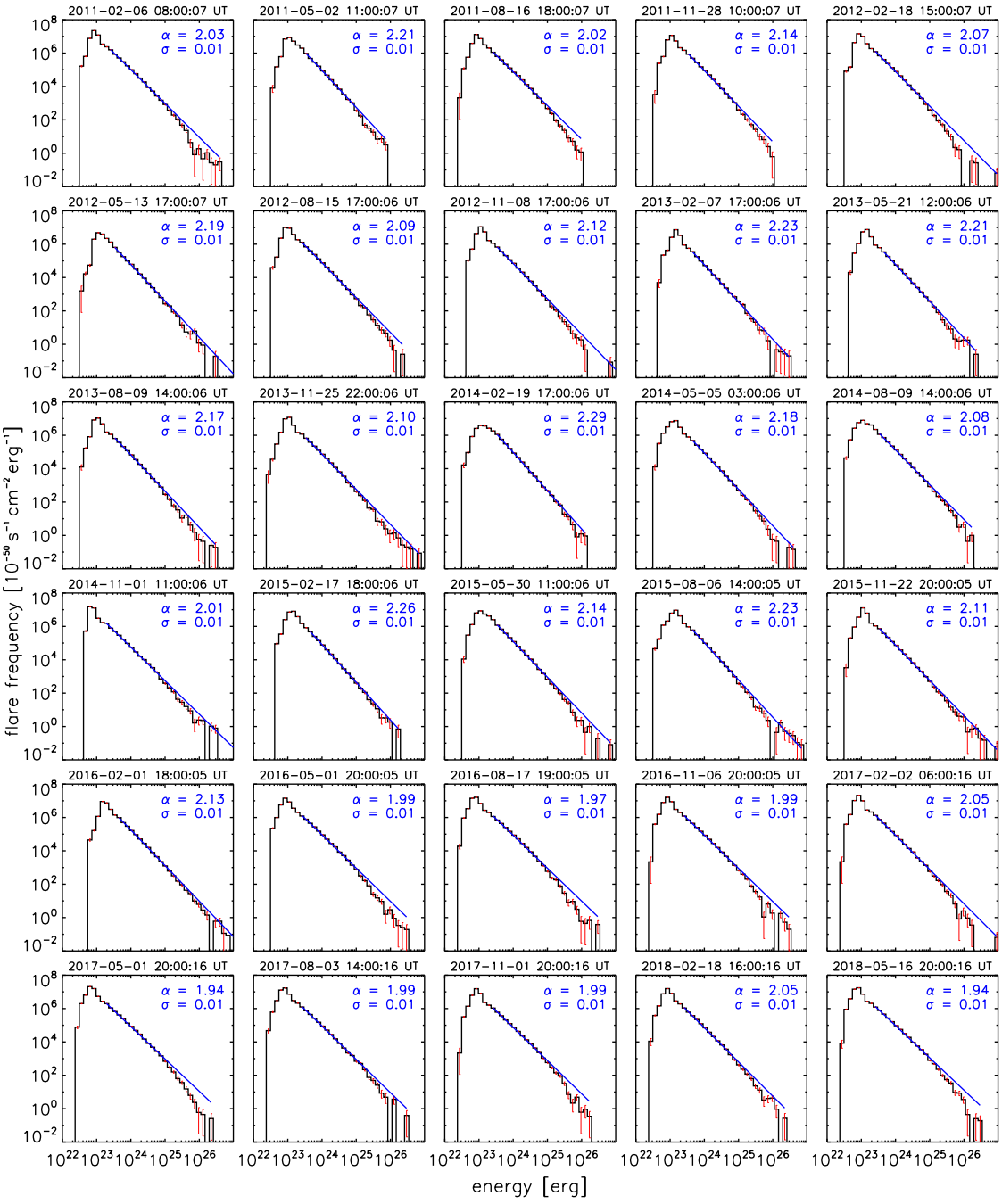

Fig. A.10.: Same as Figure 6.1 but using a detection interval of $D = 4$, a threshold factor of $F = 5$, and a combination interval of $C = 5$.

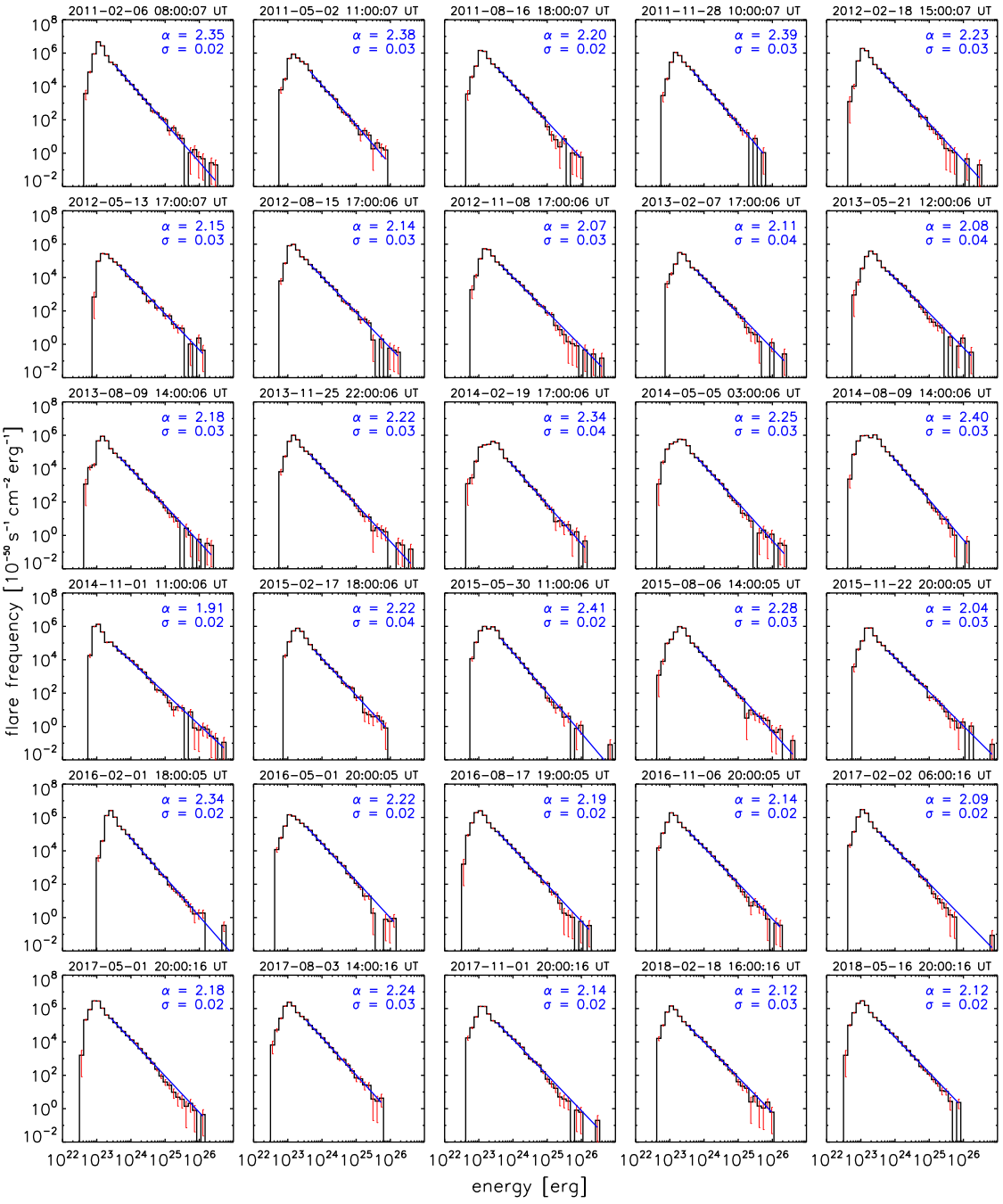

Fig. A.11.: Same as Figure 6.1 but using a detection interval of $D = 2$, a threshold factor of $F = 7$, and a combination interval of $C = 5$.

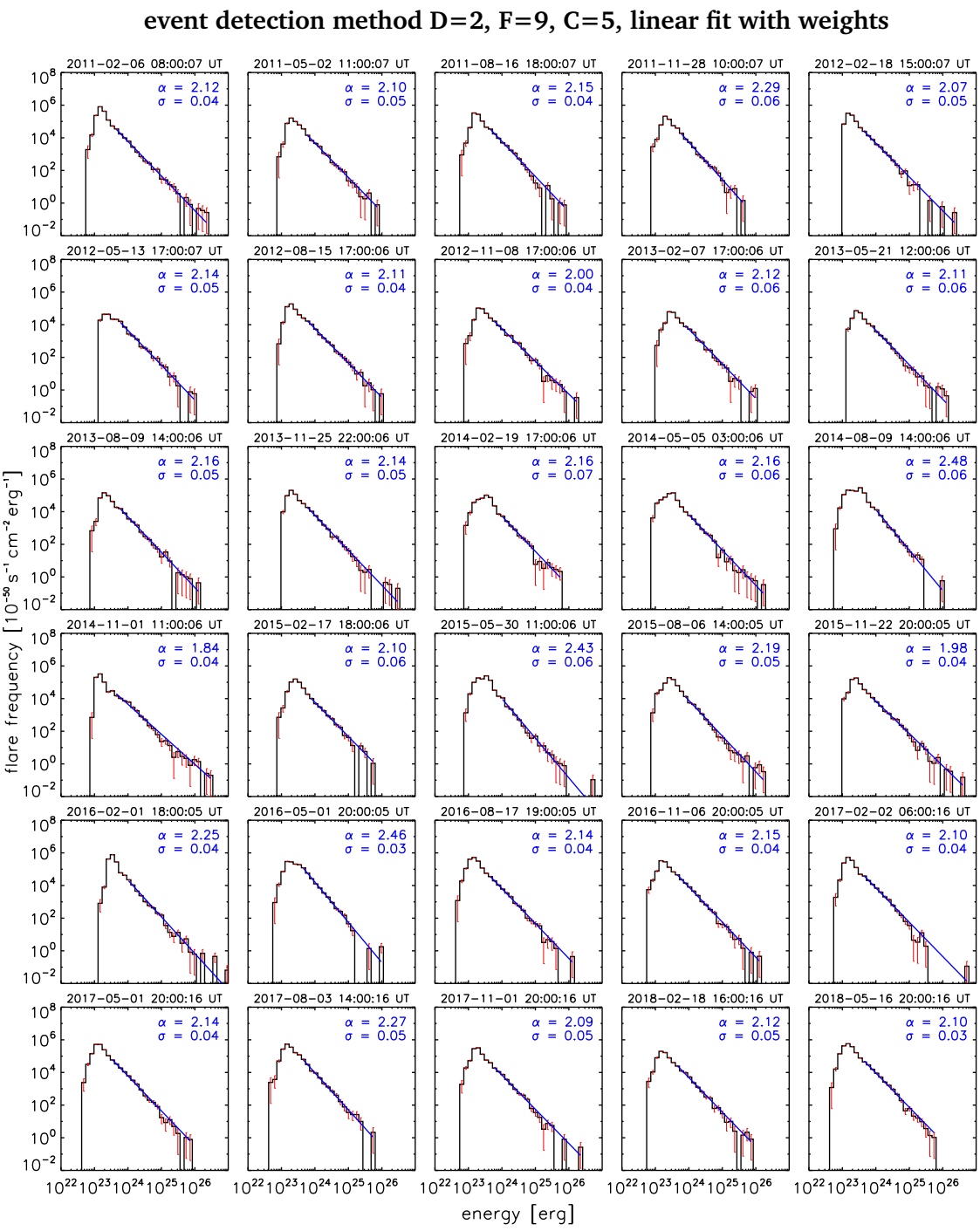

Fig. A.12.: Same as Figure 6.1 but using a detection interval of $D = 2$, a threshold factor of $F = 9$, and a combination interval of $C = 5$.

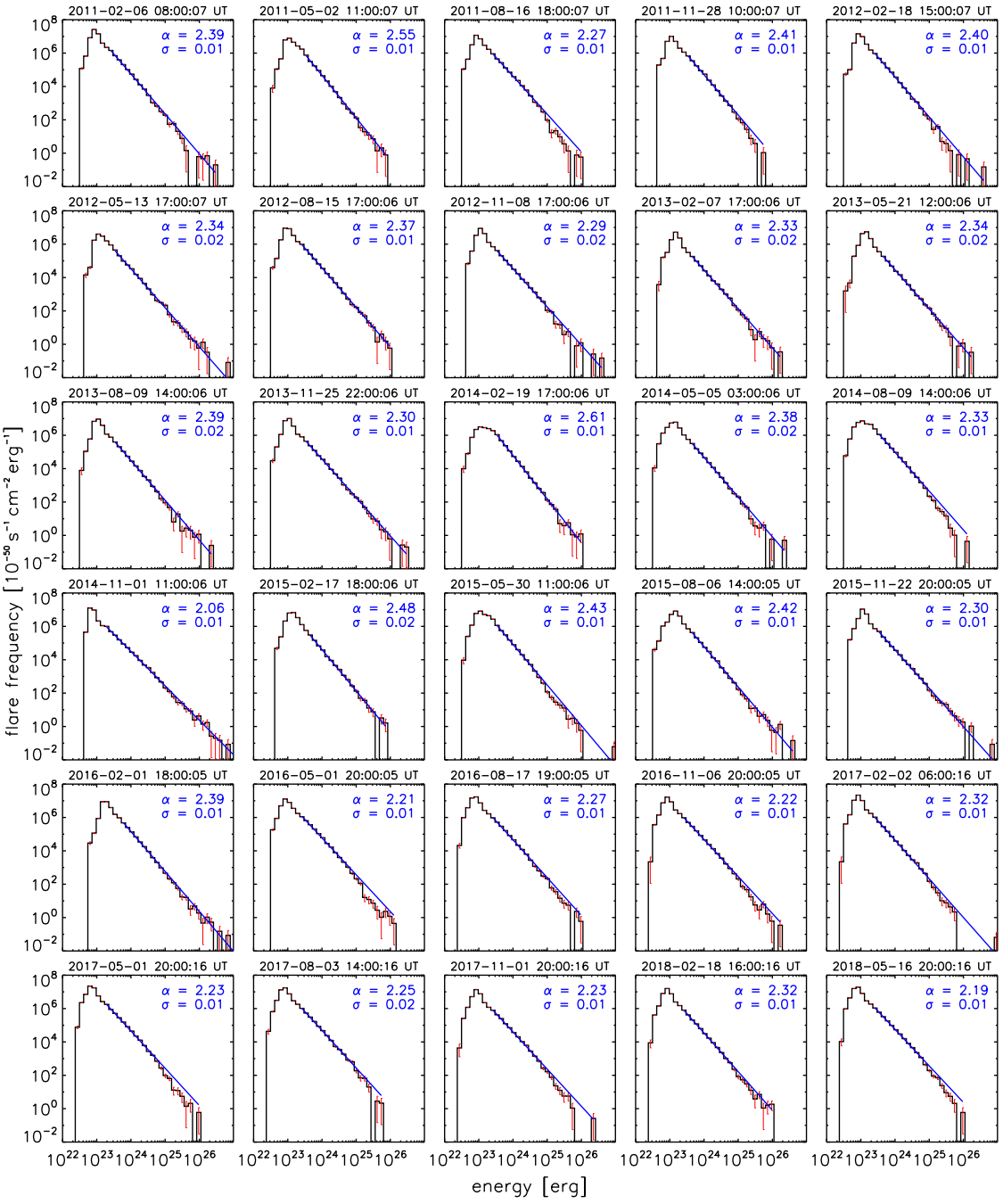

Fig. A.13.: Same as Figure 6.1 but using a detection interval of $D = 2$, a threshold factor of $F = 5$, and a combination interval of $C = 3$.

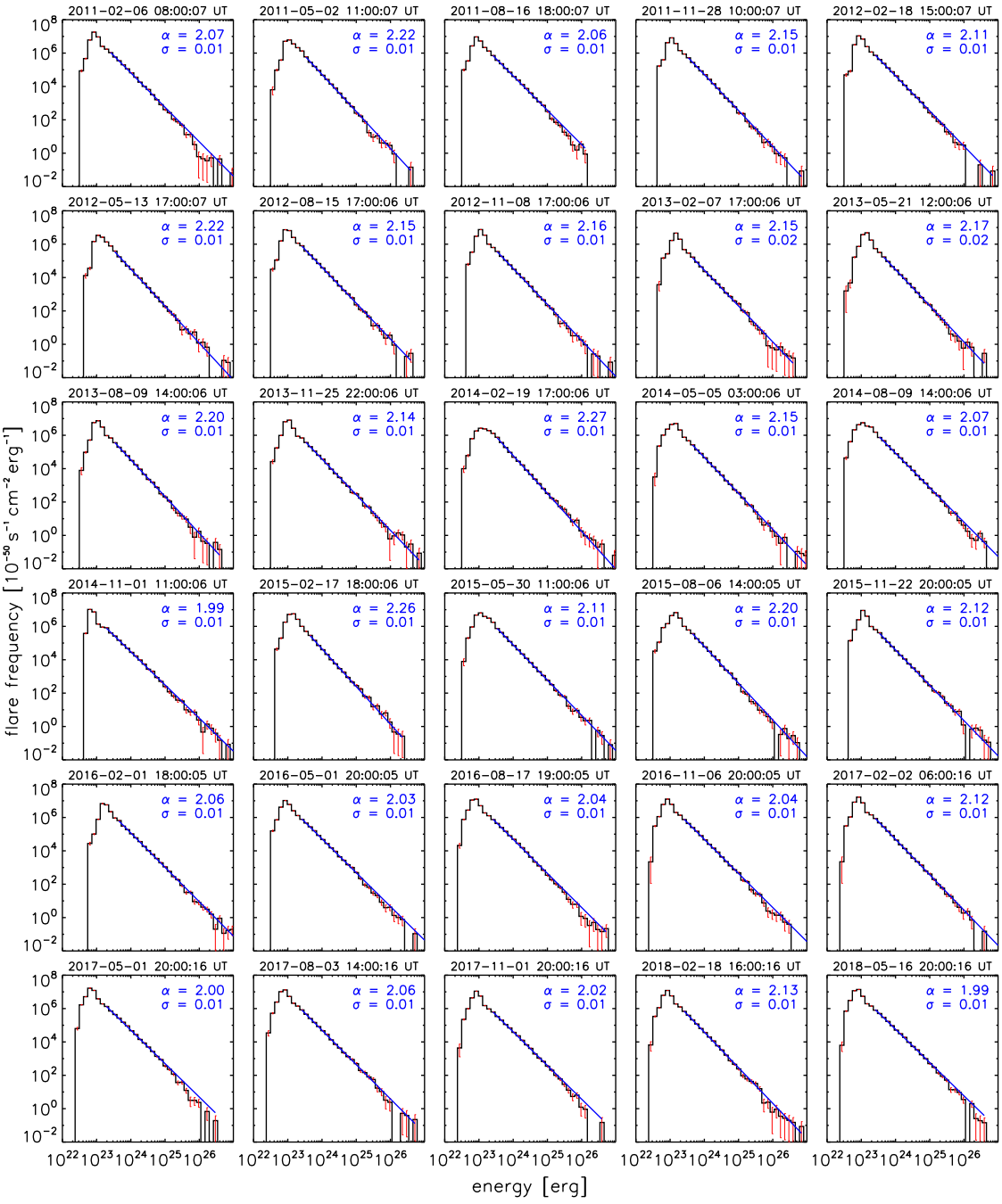

Fig. A.14.: Same as Figure 6.1 but using a detection interval of $D = 2$, a threshold factor of $F = 5$, and a combination interval of $C = 7$.

A.4 Power-law Fits without Weights

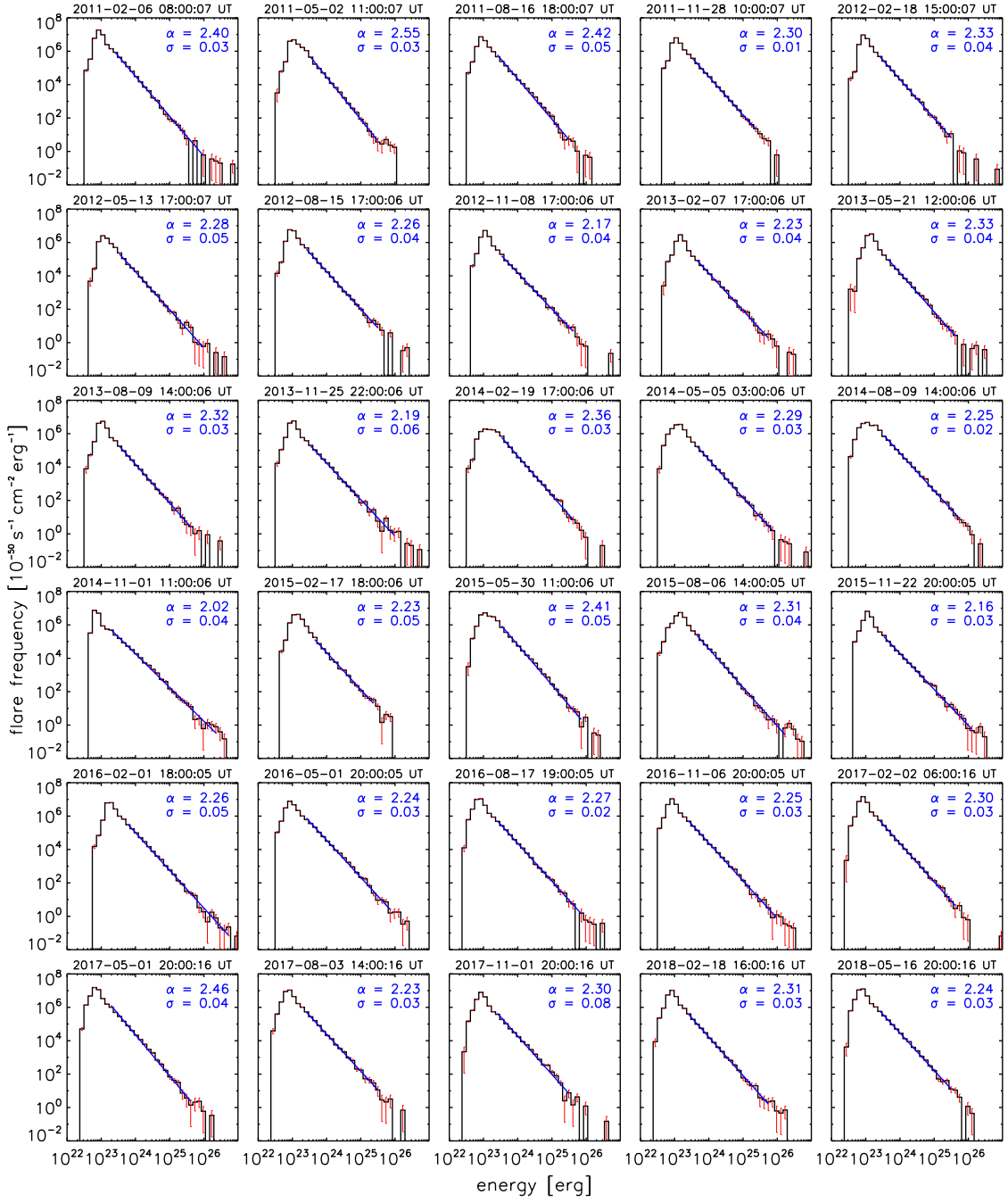

Fig. A.15.: Same as Figure 6.2 but using a detection interval of $D = 1$, a threshold factor of $F = 5$, and a combination interval of $C = 5$.

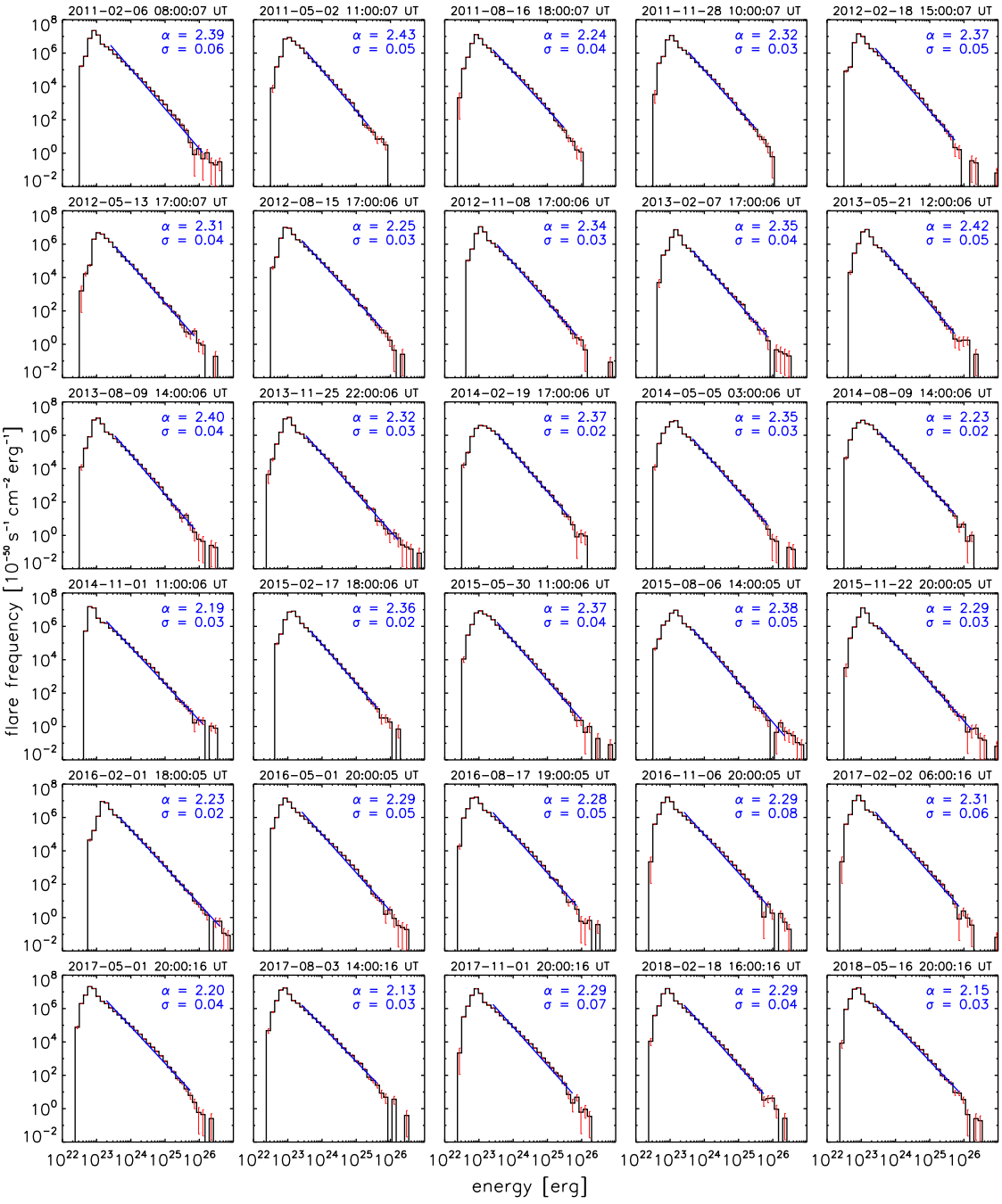

Fig. A.16.: Same as Figure 6.2 but using a detection interval of $D = 4$, a threshold factor of $F = 5$, and a combination interval of $C = 5$.

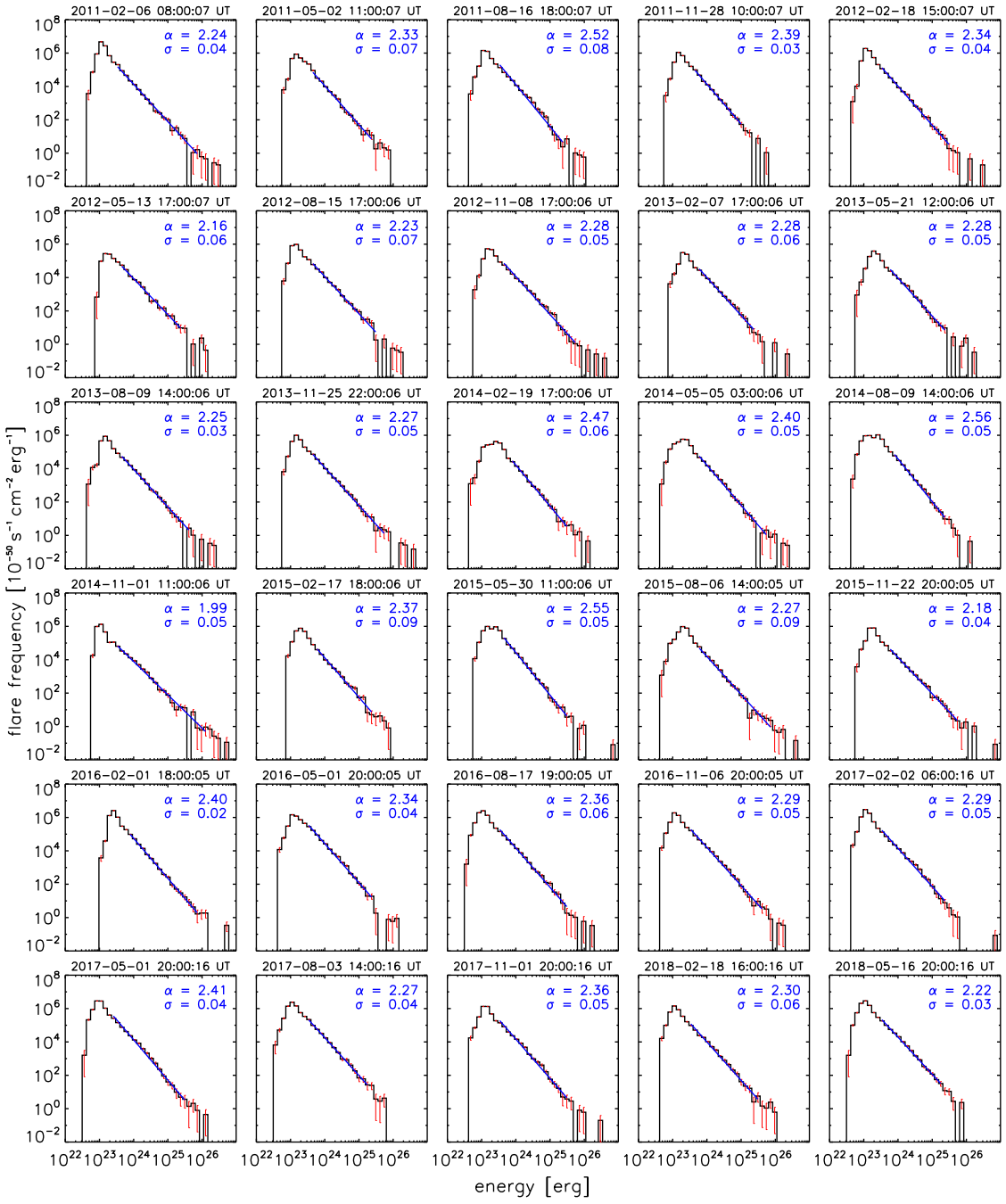

Fig. A.17.: Same as Figure 6.2 but using a detection interval of $D = 2$, a threshold factor of $F = 7$, and a combination interval of $C = 5$.

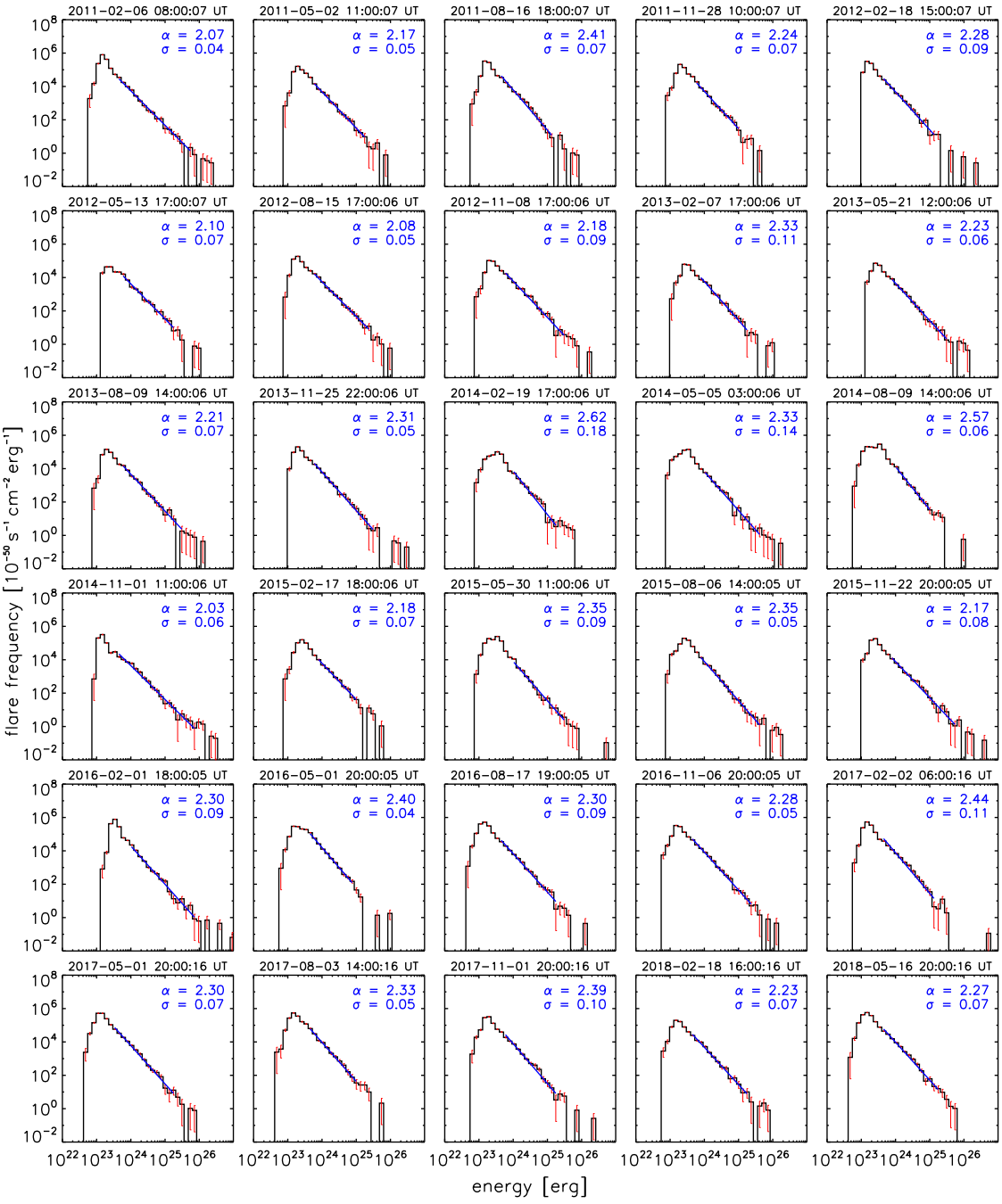

Fig. A.18.: Same as Figure 6.2 but using a detection interval of $D = 2$, a threshold factor of $F = 9$, and a combination interval of $C = 5$.

event detection method: D=2, F=5, C=3, linear fit without weights

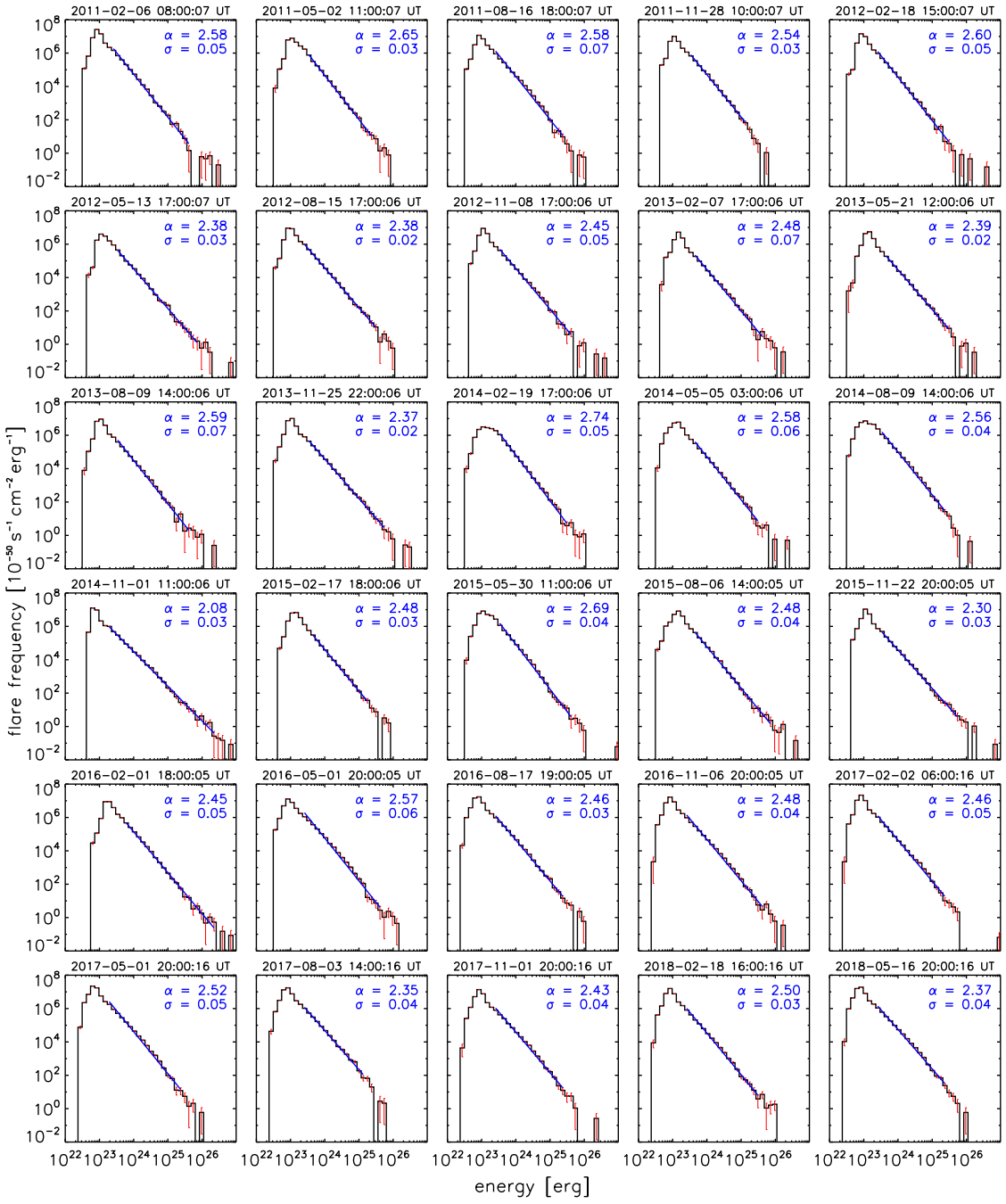

Fig. A.19.: Same as Figure 6.2 but using a detection interval of $D = 2$, a threshold factor of $F = 5$, and a combination interval of $C = 3$.

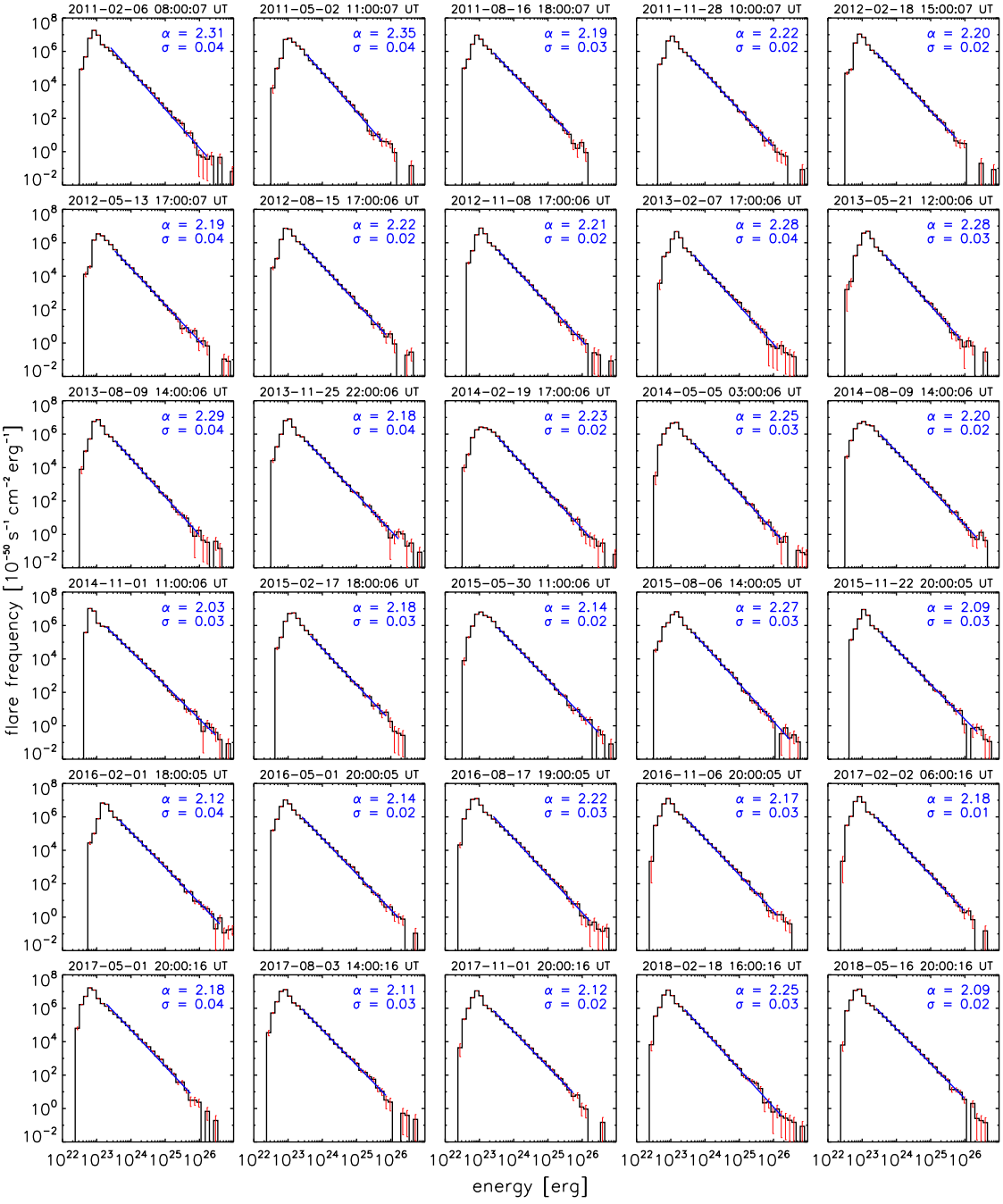

Fig. A.20.: Same as Figure 6.2 but using a detection interval of $D = 2$, a threshold factor of $F = 5$, and a combination interval of $C = 7$.

A.5 Spatial Distribution of Nanoflares

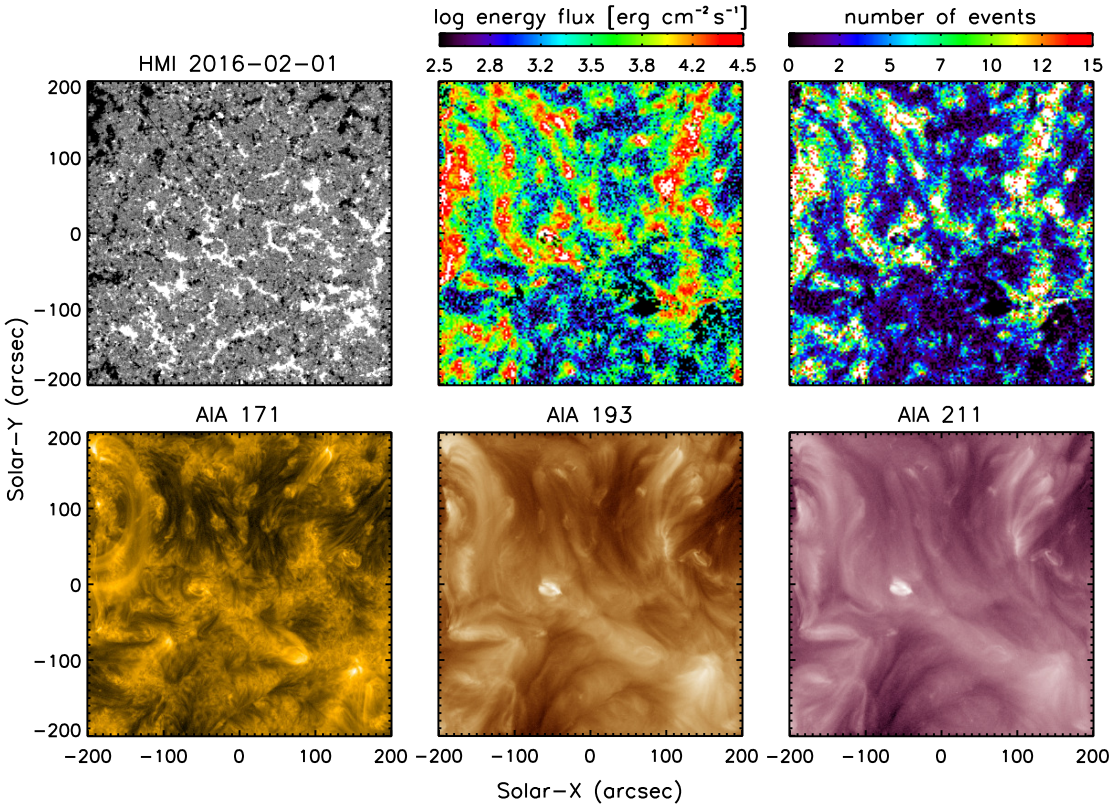

Fig. A.21.: Same as Figure 6.25.

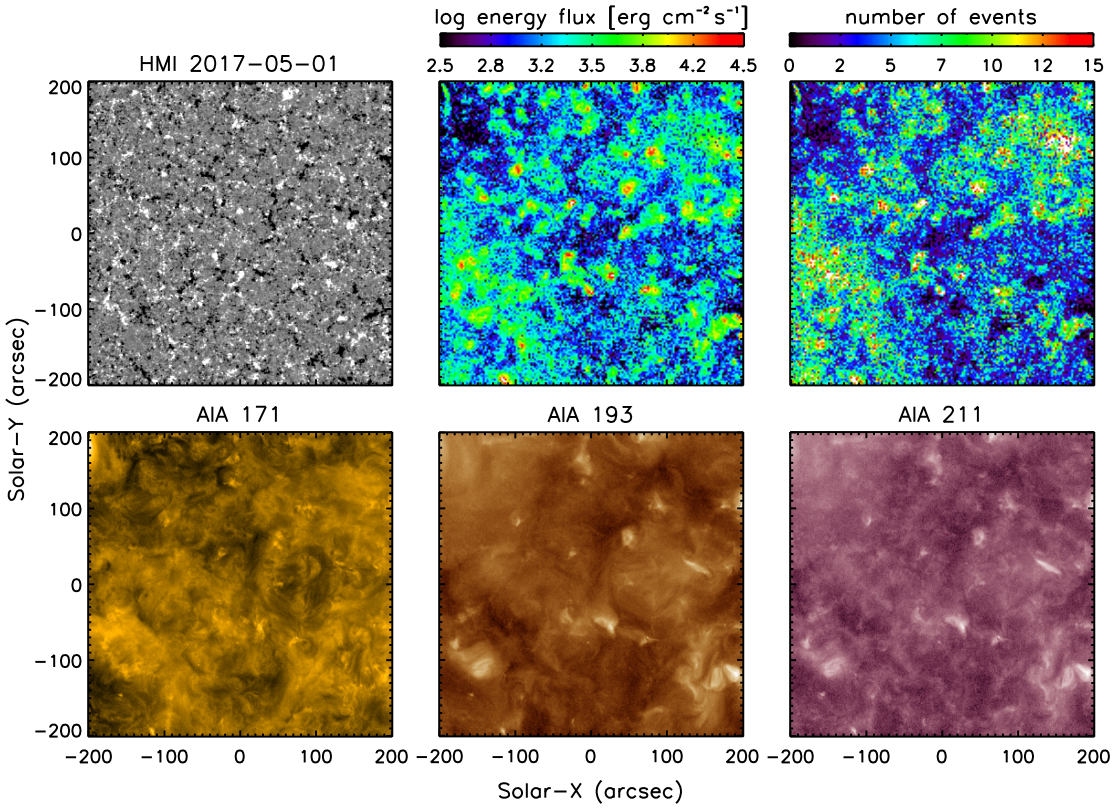

Fig. A.22.: Same as Figure 6.25.

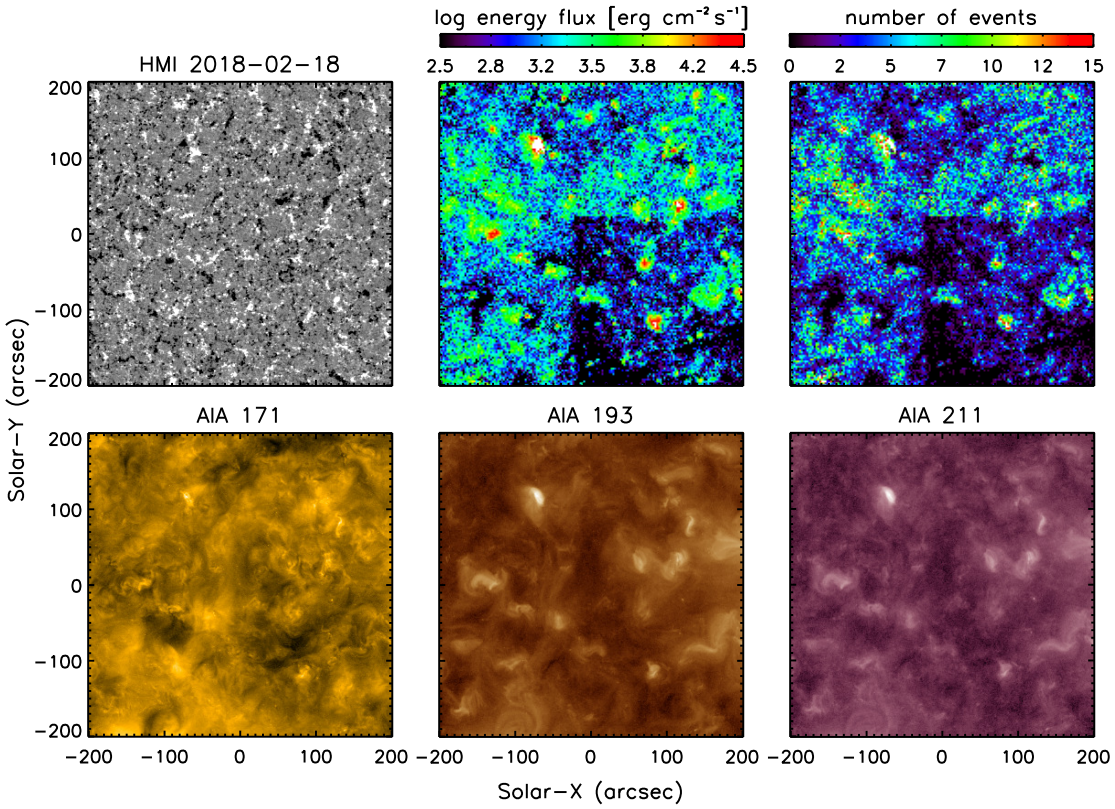

Fig. A.23.: Same as Figure 6.25.

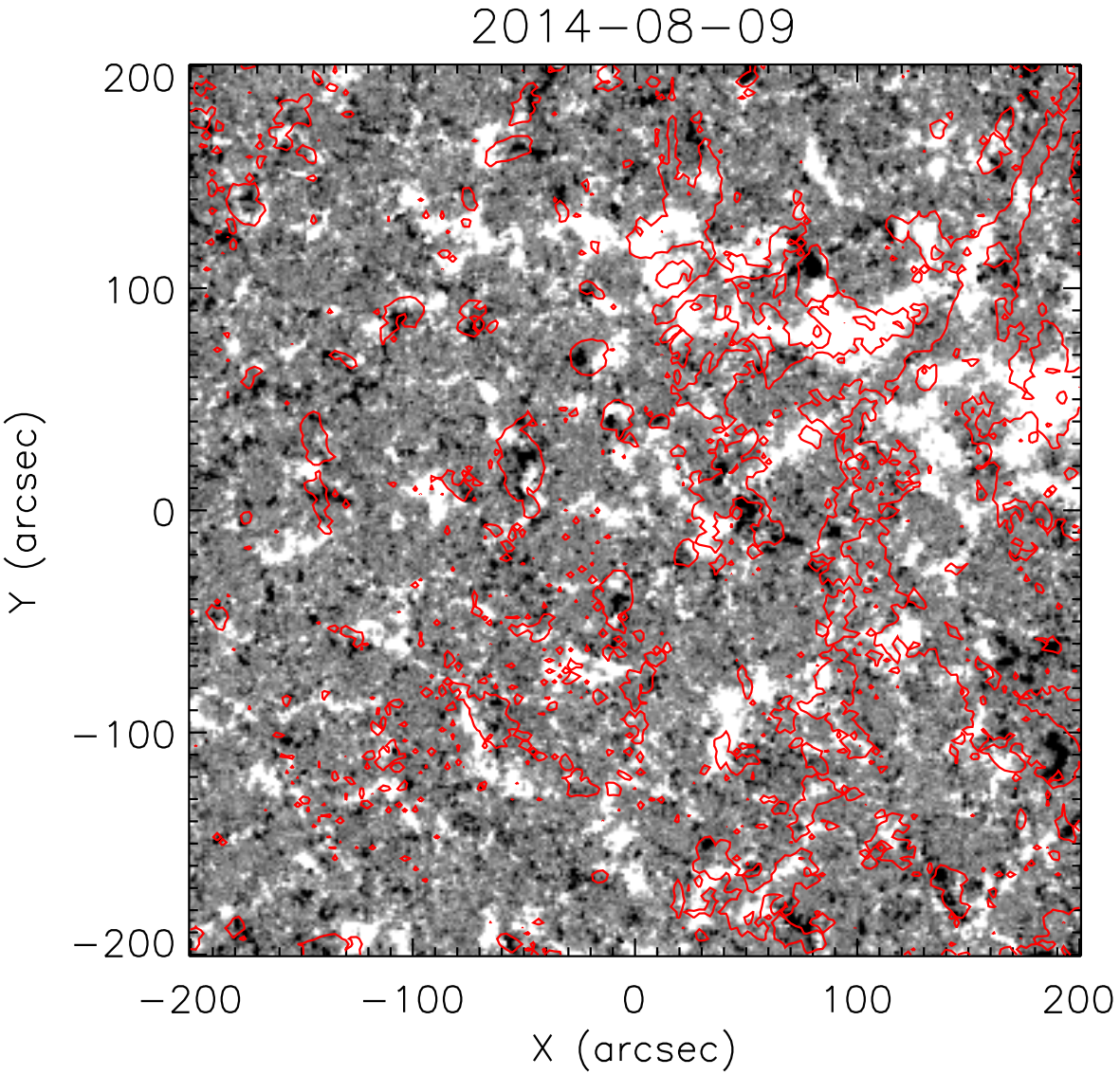

Fig. A.24.: Same as Figure 6.30.

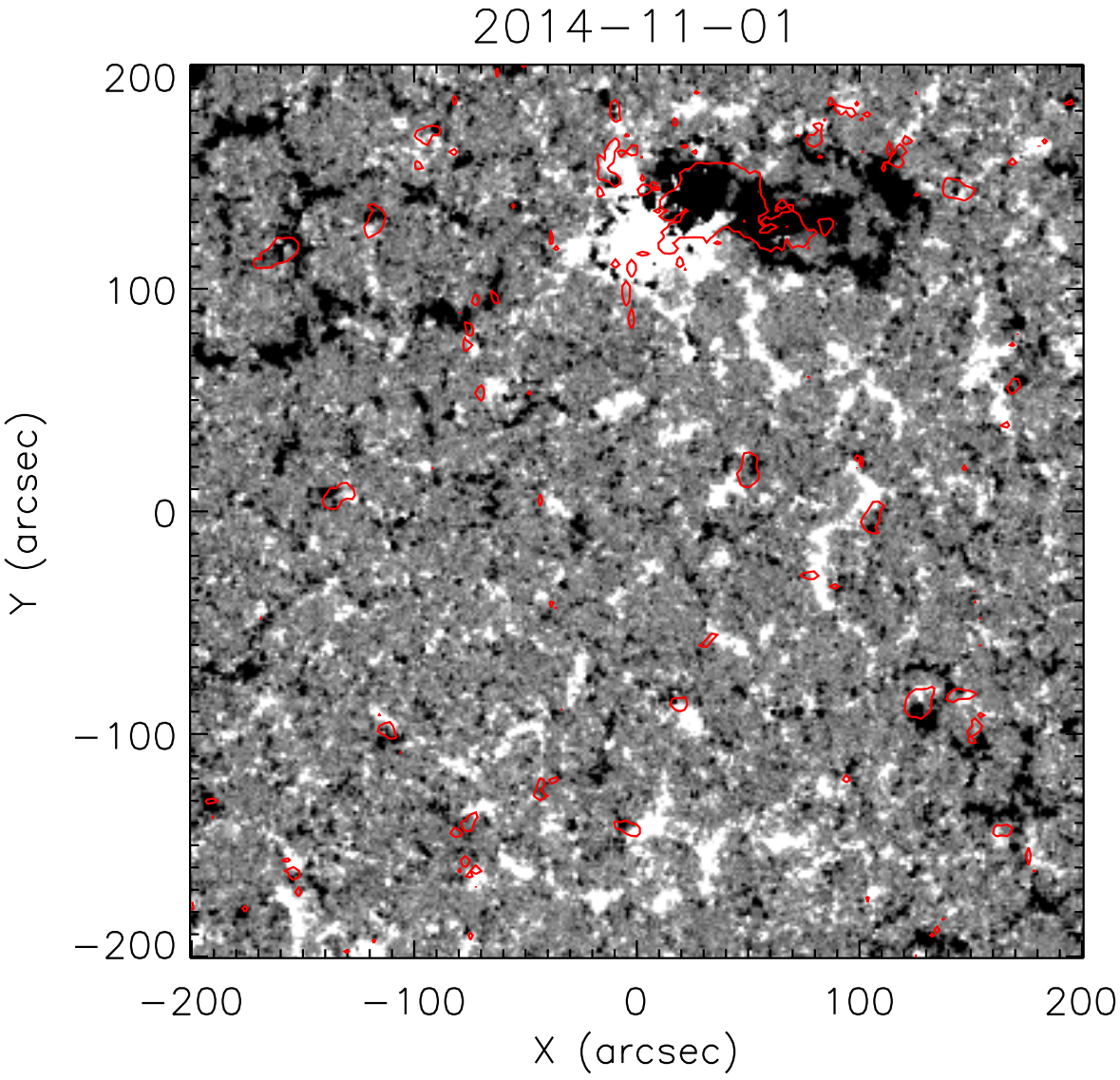

Fig. A.25.: Same as Figure 6.30.

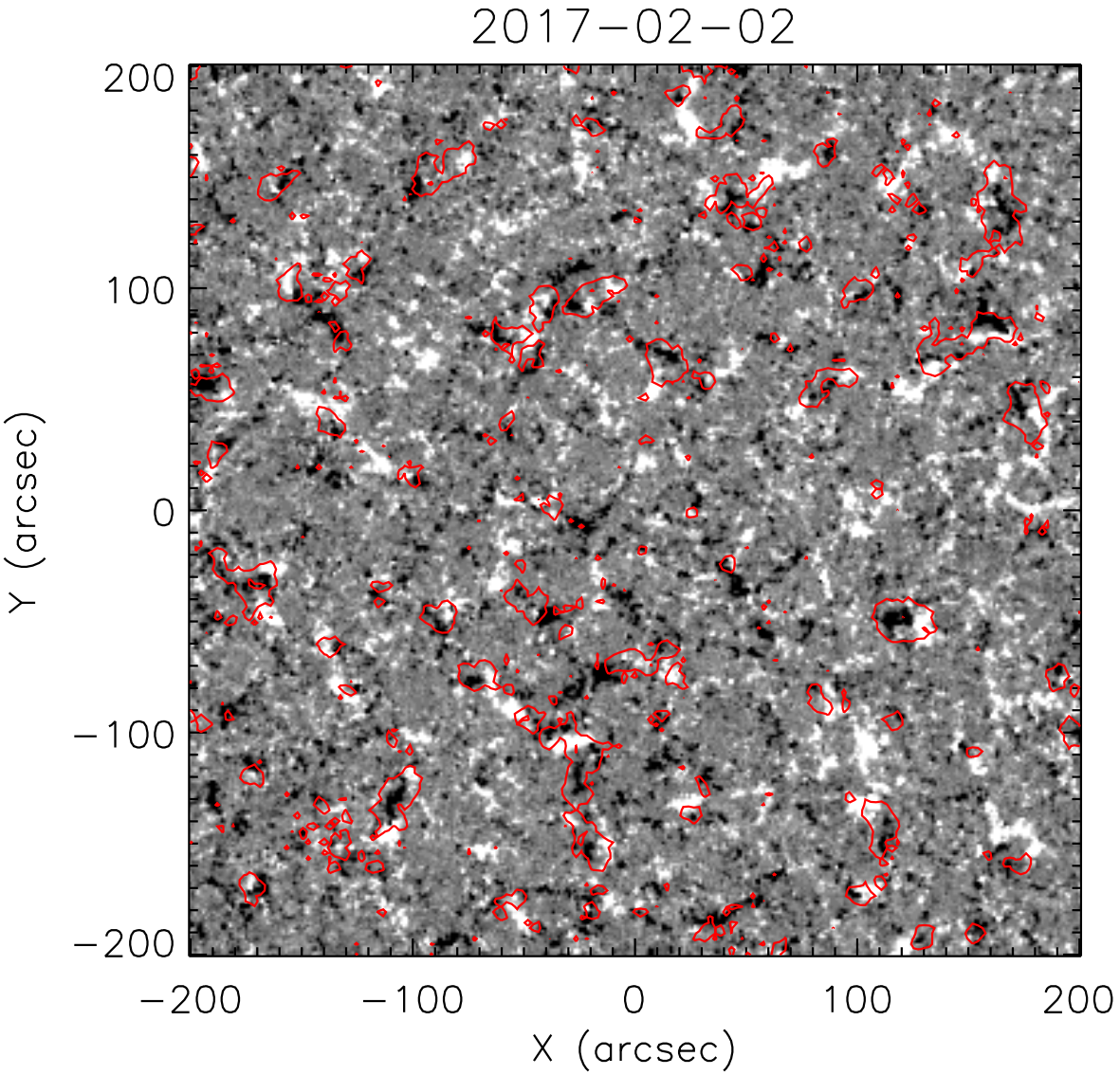

Fig. A.26.: Same as Figure 6.30.

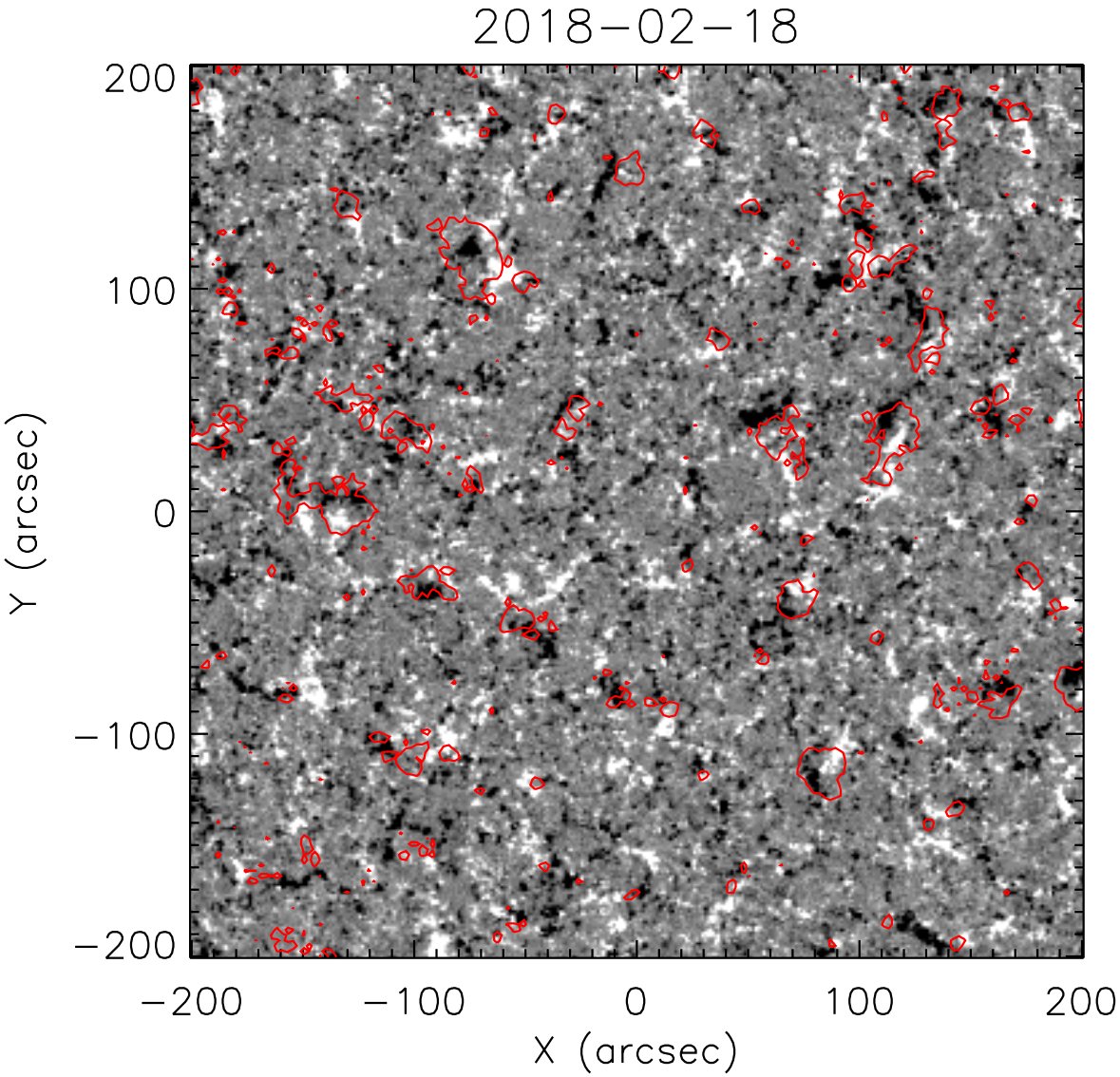

Fig. A.27.: Same as Figure 6.30.

A.6 Event Areas

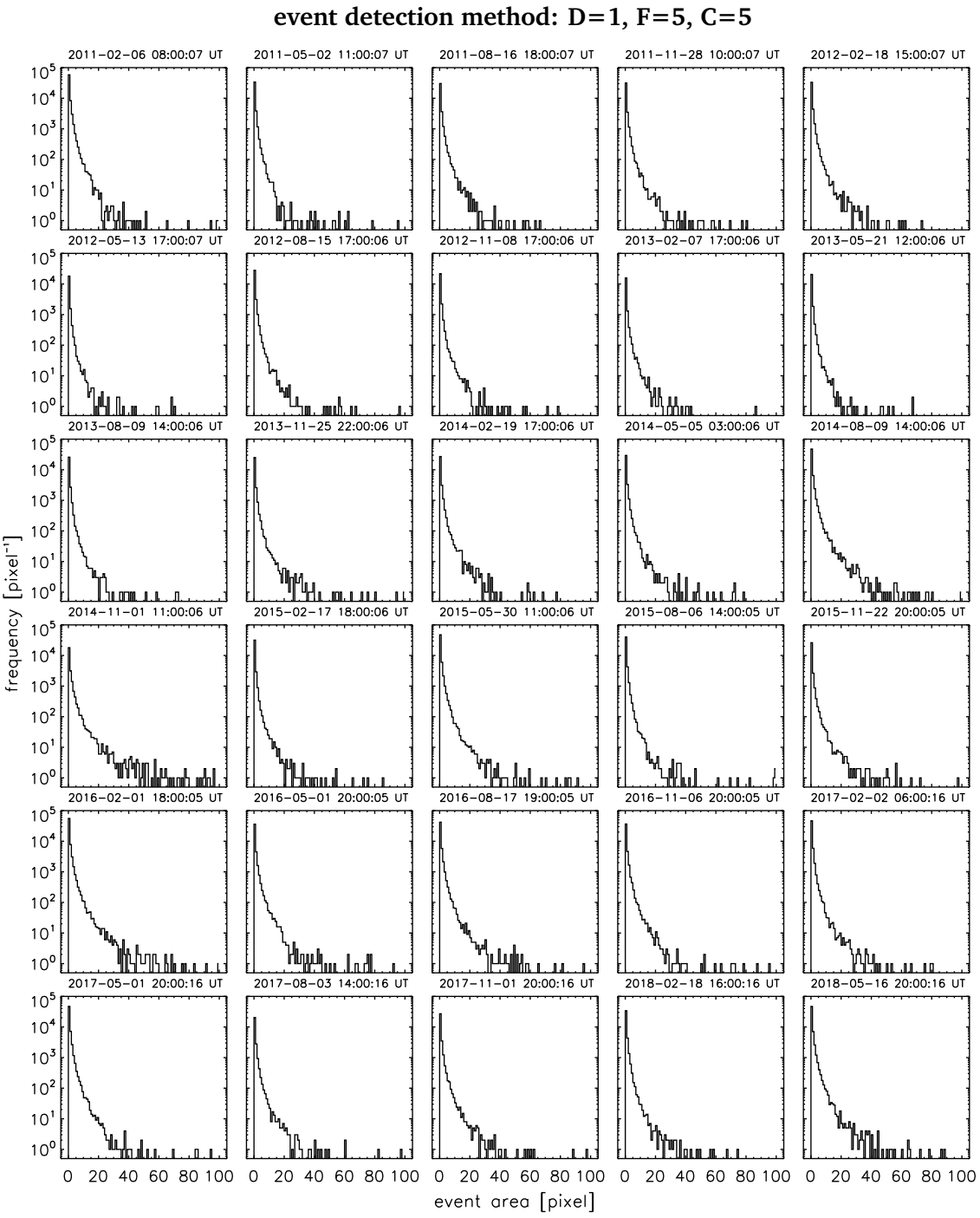

Fig. A.28.: Same as Figure 6.34 but using a detection interval of $D = 1$, a threshold factor of $F = 5$, and a combination interval of $C = 5$.

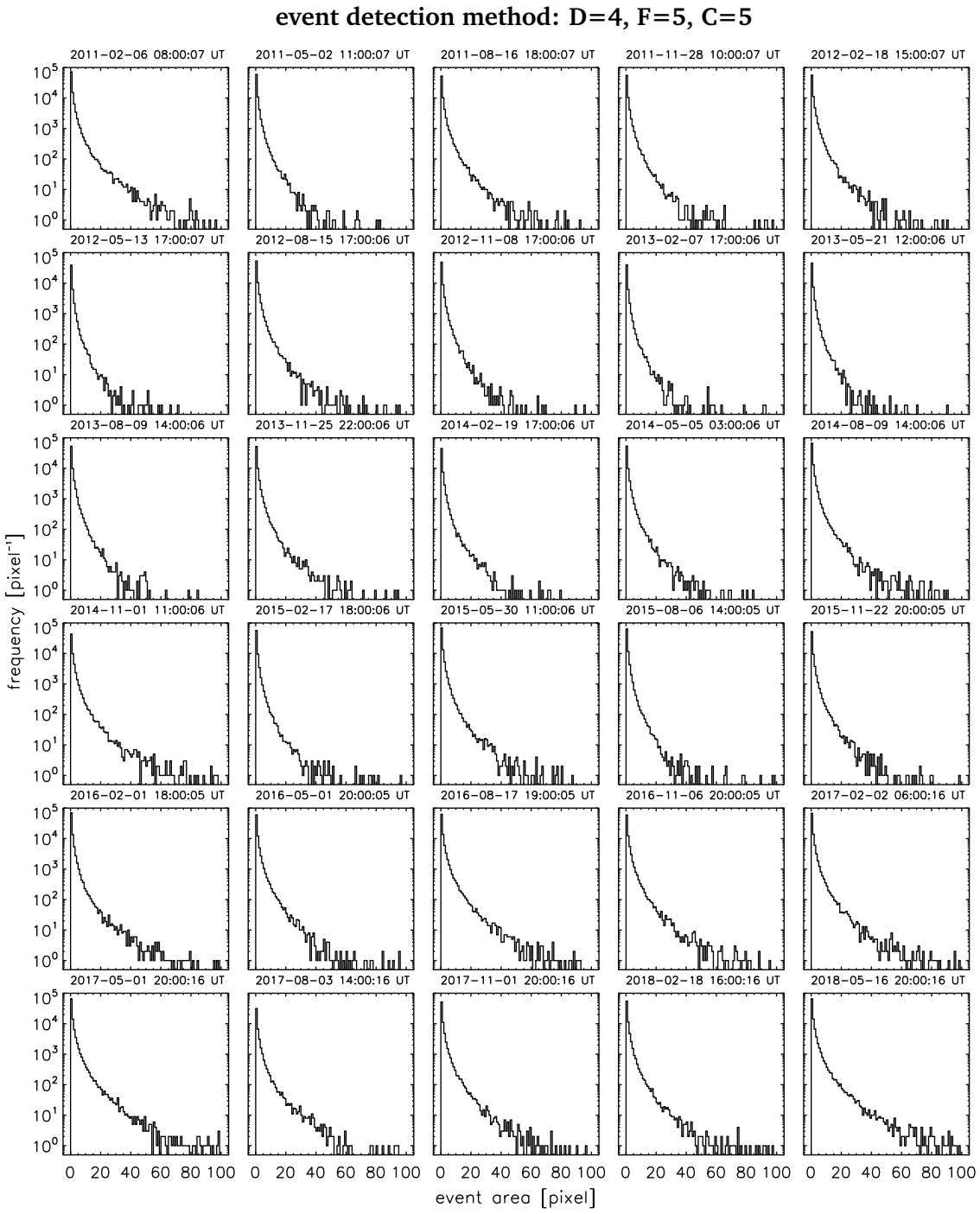

Fig. A.29.: Same as Figure 6.34 but using a detection interval of $D = 4$, a threshold factor of $F = 5$, and a combination interval of $C = 5$.

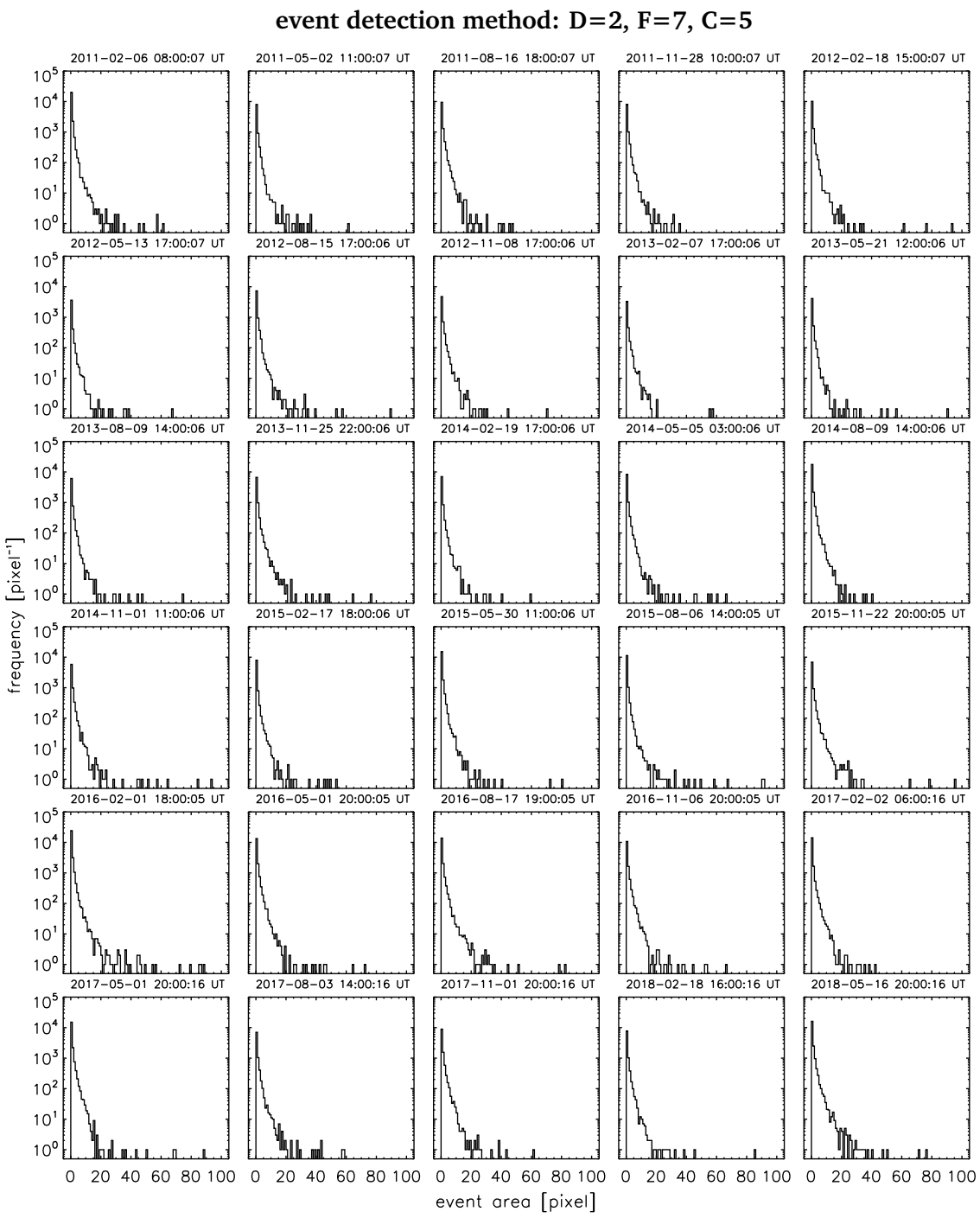

Fig. A.30.: Same as Figure 6.34 but using a detection interval of $D = 2$, a threshold factor of $F = 7$, and a combination interval of $C = 5$.

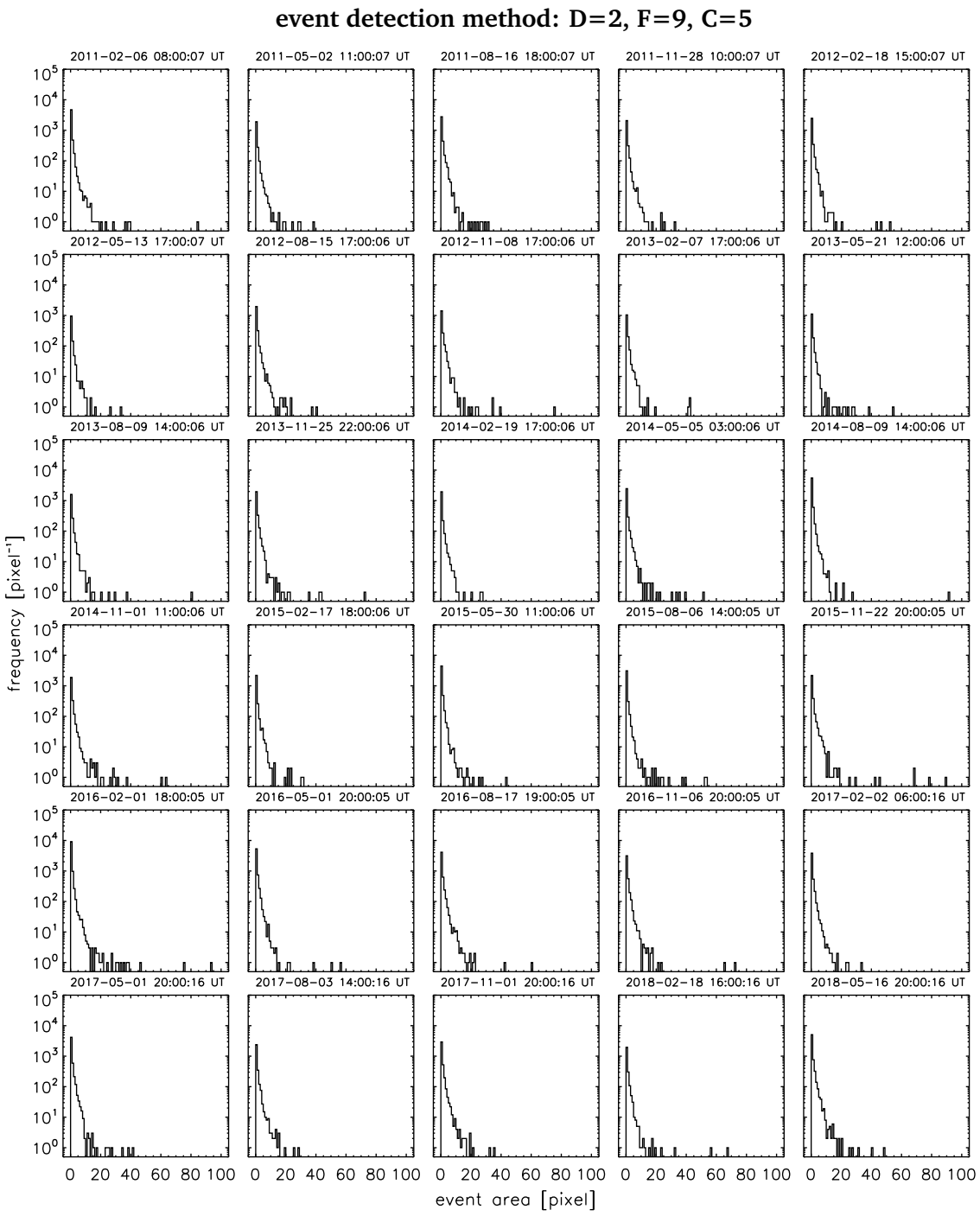

Fig. A.31.: Same as Figure 6.34 but using a detection interval of $D = 2$, a threshold factor of $F = 9$, and a combination interval of $C = 5$.

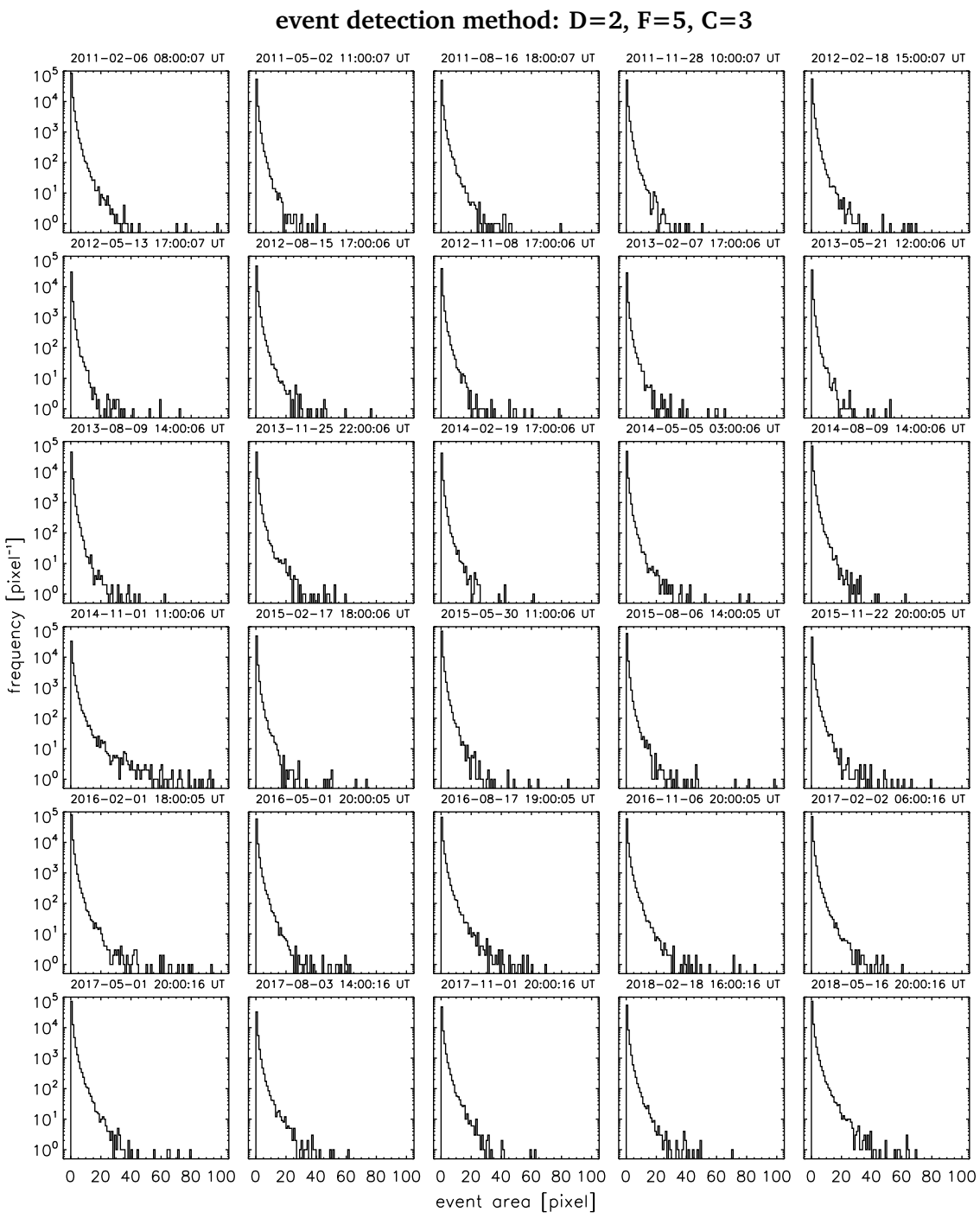

Fig. A.32.: Same as Figure 6.34 but using a detection interval of $D = 2$, a threshold factor of $F = 5$, and a combination interval of $C = 3$.

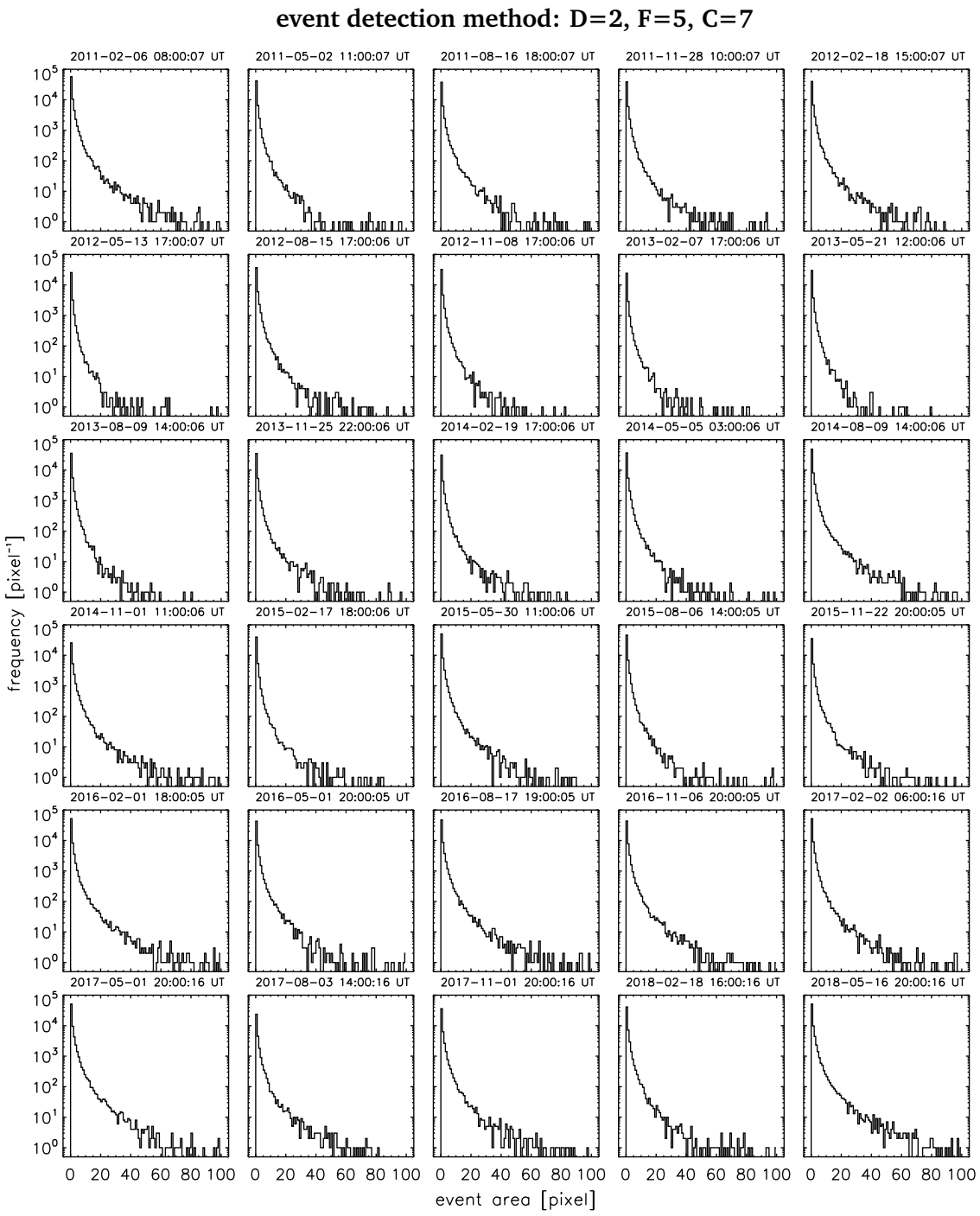

Fig. A.33.: Same as Figure 6.34 but using a detection interval of $D = 2$, a threshold factor of $F = 5$, and a combination interval of $C = 7$.

Colophon

This thesis was typeset with LaTeX 2_ε. It uses the *Clean Thesis* style developed by Ricardo Langner, available at `http://cleanthesis.der-ric.de/`. The design of the *Clean Thesis* style is inspired by user guide documents from Apple Inc.

The template was adapted by Desmond Großman, Stefan Janisch, Lea Schimak and Paul Beck to implement the editorial guidelines of *Astronomy & Astrophysics* and the cooperate-identity guidelines of the University of Graz for the Institute for Physics. This thesis uses the IGAM-template, released on *December 4, 2020*.